Analyses de microvolumes de gaz par spectroscopie Raman : expériences quantitatives et modélisation des mélanges CO -CH -N

Van-Hoan Le

Université de Lorraine, Collégium Sciences et Technologies
Ecole Doctorale SIRENA « Sciences et Ingénierie des Ressources Naturelles »
UMR 7359 GeoRessources

Thèse

Présentée pour l'obtention du grade de
Docteur de l'Université de Lorraine
Mention ''Géosciences''

M. Van-Hoan LE

Analyses de microvolumes de gaz par spectroscopie Raman : expériences quantitatives et modélisation des mélanges CO_2-CH_4-N_2

Raman spectroscopy analyses of microvolumes of gases (CO_2, CH_4 and N_2): from quantitative experiments to theoretical modeling

Soutenance publique le 14 Décembre 2020

Membres du jury :

Rapporteurs :

M. Damien GUILLAUME	Professeur, Université Jean Monnet Saint-Etienne
M. Samuel MARRE	Directeur de recherche, ICMCB - CNRS

Examinateurs :

M. Jacques PIRONON	Directeur de recherche, Université de Lorraine, CNRS
Mme Marta BERKESI	Chargée de recherche, Eötvös Loránd University

Directeurs de thèse :

M. Alexandre TARANTOLA	Maître de conférences, Université de Lorraine
Mme. Marie-Camille CAUMON	Ingénieure de recherche, Université de Lorraine

Invités :

M. Jean-Pierre GIRARD	Expert groupe, TOTAL
M. Alfons van den KHERKHOF	Research scientist, Geoscience Centre, University of Göttingen
Mme Silvia LASALA	Maître de conférences, Université de Lorraine
Mme Odile BARRES	Ingénieure de recherche, Université de Lorraine, CNRS

Remerciements

Ce travail de thèse a été effectué au sein du laboratoire GeoRessouces de l'Université de Lorraine à Vandoeuvre-lès-Nancy. Le projet a pu être réalisé grâce au soutien de l'Institut Carnot ICEEL et du Ministère de la Recherche et de l'Enseignement Supérieur, et par des financements du programme de recherches CRNS-INSU CESSUR.

Je tiens avant tout à exprimer ma plus sincère reconnaissance à Alexandre Tarantola et Marie-Camille Caumon, mes deux directeurs de thèse, pour m'avoir offert l'opportunité d'effectuer ce projet et pour m'avoir accompagné tout en me confiant une grande part d'autonomie. Je souhaite également les remercier pour la véritable envie de me transmettre leurs connaissances et leur vision du travail qui sont le fruit de leurs années d'expérience de recherche. Cette volonté a abouti à un encadrement de qualité irréprochable tout au long de ce doctorat. Un grand merci pour leur patience et leur disponibilité pour répondre rapidement à toutes mes questions, leur rigueur de travail, leur précision et leur exigence dans la rédaction, leur amitié, leur sympathie et leurs encouragements dans les moments difficiles. Sans ces derniers, la réalisation de ce mémoire n'aurait jamais été aboutie !

Mes remerciements les plus sincères vont ensuite à Aurélien Randi pour son accompagnement depuis le début jusqu'à la fin de ce projet. Merci beaucoup pour sa disponibilité pour m'avoir préparé énormément de mélanges de gaz, pour avoir résolu des problèmes qui sont souvent survenus dans le système HPOC (High-Pressure Optical Cell), et pour avoir participé au développement de la nouvelle ligne analytique couplée avec l'analyseur PICARRO (la spectroscopie à cavité optique). Je n'aurais pas pu accomplir mes analyses expérimentales sans son aide et son intervention.

Je voudrais exprimer ma profonde gratitude envers Odile Barres et Jacques Pironon pour avoir toujours soutenu mon projet, pour avoir consacré des heures de discussion sur l'applicabilité de la spectroscopie Infrarouge dans l'étude de la dissolution du CO_2 et CH_4 dans du brouillard d'eau afin d'élargir encore le sujet de ma thèse. Un grand merci à Odile Barres pour son aide durant mes expériences sur les mesures par spectroscopie Infrarouge. Dans

l’aspect financier, je voudrais bien remercier Odile Barres pour sa générosité et sa gentillesse pour avoir acheté des bouteilles de gaz standard étalonnés afin que je puisse tester le domaine de validité de l’analyseur PICARRO dans les analyses isotopiques de $^{13}CO_2$ et $^{13}CH_4$. Bien que cette partie du travail ne soit pas encore totalement aboutie, je les remercie vivement pour leur soutien permanent.

J’adresse aussi mes remerciements à Silvia Lasala et Romain Privat pour les discussions fructueuses sur les propriétés thermodynamiques des mélanges CO_2-N_2. Merci également à Romain Privat pour son cours sur le code Visual Basic et les fonctions avancées d'Excel. Ces derniers m’ont tellement aidé dans le traitement des données Raman.

Je souhaite remercier Catherine Lorgeoux et Héloïse Verron pour leur instruction et leur aide durant mes expériences avec la chromatographie en phase gazeuse.

J’aimerais présenter mes remerciements à tous les membres du comité de suivi individuel de thèse et/ou du jury de la soutenance de ma thèse pour avoir évalué et examiné mes travaux de thèse : Jacques Pironon, Damien Guillaume, Marta Berkesi, Samuel Marre, Silvia Lasala, Odile Barres, Jean-Pierre Girard, et Romain Privat.

Je tiens également à sincèrement remercier l’ensemble du personnel du laboratoire GeoRessouces, notamment Camille Gagny - le secrétariat général, Stéphanie Trombini - l’assistante de direction, Pascale Iracane - la gestionnaire ressources humaine, Aurélie Defeux - le personnel administratif, pour leur aide dans les démarches administratives. Merci également à Zira pour sa bonne humeur et son sourire permanent.

Enfin, je voudrais bien adresser ma gratitude à ma famille, qui a toujours cru en moi et qui me soutient inconditionnellement comme toujours. Un grand merci également à tous mes amis vietnamiens et internationaux, et mes collègues du labo qui me sont chers et qui sont toujours là pour moi, de près ou de loin. Merci beaucoup pour leurs soutiens et leurs encouragements tout au long de ces années, d’avoir partagé avec moi des moments inoubliables au cours de mon séjour à Nancy.

Quê hương là chùm khế ngọt
Cho con trèo hái mỗi ngày
Quê hương là đường đi học
Con về rợp bướm vàng bay
...

Résumé

Les inclusions fluides naturelles peuvent fournir des informations quantitatives précieuses, obtenues par microthermométrie et spectroscopie Raman notamment, pour reconstruire les conditions de circulation des paléofluides. La plupart des données de calibration du signal Raman des gaz ont été établies soit à basse pression, soit sans évaluation des possibles effets de composition. Cependant, les paramètres spectraux sont susceptibles de varier simultanément en fonction de la pression, de la composition et de la température. L'utilisation des données de calibration publiées dans la littérature peut donc entraîner des erreurs significatives, notamment lorsqu'elles sont appliquées aux fluides géologiques qui contiennent généralement plusieurs espèces à des pressions ou densités élevées. CO_2, CH_4 et N_2 sont les espèces gazeuses majoritaires le plus souvent rencontrées dans divers environnements géologiques. Cependant les données de calibration pour une quantification de leurs propriétés *PVX* ne sont pas encore complètement établies.

L'objectif central de ce travail de thèse est d'apporter des données d'étalonnage du signal Raman des gaz CO_2, CH_4, N_2 et de leurs mélanges, sur une gamme de pression de 5 à 600 bars, afin de pouvoir déterminer simultanément les propriétés *PVX* à une température fixée. Plusieurs étapes expérimentales et analytiques ont été réalisées : (i) évaluer les effets de la composition et de la pression sur la variation de la section efficace du CO_2 et du CH_4, (ii) identifier les paramètres spectraux les plus pertinents pour des analyses quantitatives, (iii) établir des données de calibration et estimer leurs incertitudes sur les mesures, et (iv) appliquer les données de calibration à des inclusions fluides naturelles, puis comparer les résultats avec ceux obtenus par microthermométrie pour validation. Pour cela, des mélanges de gaz ont été préparés et comprimés par le biais d'un mélangeur (GasMix AlyTech^{TM}) couplé avec un système de pressurisation développé au laboratoire GeoRessources. Des analyses *in situ* Raman des mélanges de gaz ont été réalisées dans des conditions contrôlées en utilisant le système HPOC (High-Pressure Optical Cell) couplé avec un microcapillaire transparent placé sur une platine microthermométrique (Linkam CAP500$^{®}$). Les propriétés *PVX* des inclusions fluides à 22 ou 32 °C peuvent donc être déterminées à partir de nos équations d'étalonnage avec une incertitude de < 1 mol%, ~ ± 20 bars et ~ ± 0,02 g·cm^{-3} pour la composition, la pression et la densité, respectivement.

Un autre objectif du projet est, d'un point de vue théorique physico-chimique, d'interpréter les tendances de variation de la position du pic du CH_4 et N_2 pour une compréhension approfondie. Deux modèles théoriques, i.e., le potentiel de Lennard-Jones 6-12 (LJ) et le modèle « Perturbed hard-sphere fluid » (PHF) ont été utilisés afin de (1) évaluer quantitativement la contribution des forces d'interaction intermoléculaire attractives et répulsives par rapport aux décalages des bandes de CH_4 et N_2, et (2) estimer la variation de la longueur de la liaison C-H des molécules de CH_4 en fonction de la pression (densité). Un modèle prédictif a également été proposé pour prédire la tendance de la variation de la position du pic du CH_4 jusqu'à 3000 bars en fonction de la composition des mélanges CH_4-N_2 et CH_4-CO_2. L'applicabilité de nos données d'étalonnage dans d'autres laboratoires, ou pour des mélanges de gaz contenant une faible quantité d'une autre espèce (e.g., H_2, H_2S) est discutée et évaluée. Des nouvelles données d'étalonnage universelles applicables dans d'autres laboratoires sont fournies. Un programme de calcul « FRAnCIs » avec une interface utilisateur a été développé pour rendre l'utilisation de nos données d'étalonnage (76 équations de régression polynomiale au total) accessibles au plus grand nombre.

Mots clés : Spectroscopie Raman, Fluides géologiques, Gaz, Thermodynamique, Densimètre, Baromètre, Interactions intermoléculaires, HPOC Système, Interface utilisateur, FRAnCIs.

Abstract

Quantitative knowledge of species trapped within fluid inclusions provides key information to better understand geological processes as well as to reconstruct the conditions of paleofluid circulation. However, most of the quantitative calibration data of the Raman signal of gases were established either at low pressure or without evaluating the composition effect. Nevertheless, the spectral parameters are subject to vary simultaneously as a function of pressure, density, composition, and temperature. Using the previously published data can therefore lead to non-quantified errors, especially when applied to geological fluids containing generally several substances at elevated pressure and density. CO_2, CH_4, and N_2 are among the most dominant gas species omnipresent in various geological environments, but their quantitative *PVX* calibration data are not fully established yet.

The aim of this work is to provide accurate calibration data for the simultaneous determination of *PVX* properties of pure gases or any binary and ternary mixtures of CO_2, CH_4, and N_2 over 5 to 600 bars at a fixed temperature, directly from Raman spectra. Several experimental and analytical steps were conducted : (i) reevaluate the composition and pressure dependence of the RRSCS of CO_2 and CH_4 (relative to N_2), (ii) figure out the most pertinent spectral parameters for quantitative measurements, (iii) establish regression calibration equations and estimate their uncertainties, and (iv) apply the calibration data to natural fluid inclusions and compare the obtained results to that determined by microthermometry for validation. For this, gas mixtures were prepared and compressed using a mixer (GasMix AlyTech™) coupled with a homemade pressurization system. Raman *in situ* analyses of gas mixtures were performed at controlled conditions using an improved HPOC system (High-Pressure Optical Cell) with a transparent microcapillary containing the prepared gas mixtures, placed on a heating-cooling stage (Linkam CAP500®). Overall, the *PVX* properties of fluid inclusions determined from our calibration equations at 22 or 32 °C have accuracies of about < ± 1 mol%, ~ ± 20 bars, and ~ ± 0.02 g·cm^{-3} for molar proportion, pressure and density, respectively.

The ensuing aim of the project is, from a theoretical physico-chemical point of view, to interpret the variation trends of the peak position of the CH_4 and N_2 ν_1 band for an in-depth understanding. Two theoretical models, i.e., Lennard-Jones 6-12 potential energy approximation (LJ) and Perturbed hard-sphere fluid model (PHF) were involved to quantitatively assess the contribution of the attractive and repulsive intermolecular interaction forces to the pressure-induced frequency shifts, as well as to estimate the bond length change of the CH_4 and N_2 ν_1 bands. A predictive model was also provided to predict the variation trend of the CH_4 ν_1 band over a pressure range up to 3000 bars as a function of composition within CH_4-N_2 and CH_4-CO_2 mixtures. Furthermore, the applicability of our calibration data to other laboratories and apparatus and to gas mixtures that contain a small amount of other species (e.g., H_2, H_2S) was discussed and evaluated. New universal calibration data applicable within other laboratories (i.e., other instruments) were then provided. A computer program, named "FRAnCIs" was also developed to make the application of our calibration data (i.e., 76 regression polynomial equation in total), including the automatic selection of an adequate equation for a specific analysis and the calculation of the combined uncertainty of the final results, as convenient as possible via a user-friendly interface.

Keywords: Raman spectroscopy, Geological fluids, Gas, Thermodynamics, Densimeter, Barometer, Intermolecular interaction, High-Pressure Optical Cell System, User Interface, FRAnCIs.

Table of contents

Introduction

1. Contexte général de la thèse

1.1. Intérêt géologique de l'analyse quantitative des fluides géologiques

Les fluides géologiques sont omniprésents dans toutes les enveloppes terrestres et sont considérés comme les principaux vecteurs de chaleur et de matière au sein de la lithosphère (Poty, 1967; Fyfe et al., 1978; Etheridge et al., 1983). La composition de ces fluides témoigne directement de leur source et des différentes interactions fluides-roches. Certains de ces fluides sont directement accessibles avec de possibles prélèvements pour des analyses chimiques, e.g., eau de pluie, eau de bassins, geyser (Truesdell and Thompson, 1982; Herczeg et al., 1991; Gemery-Hill et al., 2007), fumeurs noirs (Gamo et al., 2001), surveillance de sites industriels pour détection de fuites (Taquet et al., 2013), … Il est également possible de rencontrer des traces de circulations de fluides dans les roches qui sont trouvées sous forme de petites inclusions contenant des mélanges plus ou moins complexes. Comprendre et reconstruire la composition et la densité de ces paléofluides peut permettre de reconstruire l'histoire géologique d'un site d'étude particulier avec de vastes domaines d'investigation, e.g., bassins (Kiipli et al., 2009), métallogénie et tectonique (Wang et al., 2003; Gasquet et al., 2005; Yang et al., 2011), etc.

Les fluides géologiques contiennent généralement des mélanges d'eau plus ou moins salés (Na, Ca, K, Mg, Cl …) et de gaz (hydrocarbonés ou non) avec des compositions chimiques très variées (e.g., systèmes purs, binaires, ternaires, voire plus complexes) en fonction de la nature de leur environnement géologique. Dans le cadre de ce travail de thèse, nous étudierons essentiellement les systèmes constitués de CH_4, CO_2 et N_2 qui sont les espèces non-aqueuses majoritaires dans de nombreux environnements géologiques (Van den Kerkhof, 1988) tels que : les bassins sédimentaires (e.g. Roedder, 1979a; Burruss, 1981; Benson and Cole, 2008), des roches diagénétiques ou métamorphiques (e.g. Poty et al., 1974; Mullis, 1979; Touret, 2001; Tarantola et al., 2007), des environnements magmatiques-hydrothermaux (e.g. Seitz et al., 1993) ou des gisements métalliques par exemple (e.g. Roedder, 1979b, 1984; Diamond, 1990; Bodnar et al., 2014).

Les inclusions fluides sont des microcavités, dont la taille varie de quelques micromètres (µm) jusqu'à quelques dizaines de µm, voire, plus rarement, quelques centaines de µm, observées à l'intérieur de minéraux. Ces objets géologiques sont les témoins de circulations de

fluides au sein de la lithosphère. Le piégeage des fluides peut avoir lieu pendant la croissance du cristal hôte ou après sa formation, suite à l'effet d'un événement postérieur (épisode(s) de déformation par exemple (Roedder, 1984)). Il y a donc la possibilité d'avoir plusieurs générations d'inclusions fluides coexistant au sein d'un même échantillon. Comme les inclusions fluides sont isolées hermétiquement de leur environnement par le minéral hôte, elles sont considérées, en première approximation, comme des systèmes isoplèthes (chimie constante) et isochores (volume constant) depuis le moment du piégeage (Roedder, 1979a), et apportent ainsi des contraintes essentielles sur la reconstruction des conditions *PT* de circulation des paléofluides. À température ambiante, les inclusions fluides peuvent se présenter sous forme monophasée (liquide ou gaz), biphasée (liquide et gaz ou deux liquides immiscibles), triphasée ou encore polyphasée (une phase aqueuse saturée en une ou plusieurs phases solides et une phase gazeuse, par exemple).

En première approximation, les propriétés des inclusions fluides, telles que le volume, la composition chimique, la densité, la salinité, la signature isotopique, etc., sont considérées comme inchangées depuis sa formation (selon le postulat de Sorby (1858)). Ces dernières propriétés reflètent donc, théoriquement, les conditions physico-chimiques au moment du piégeage, et sont dès lors liées intrinsèquement à l'environnement et/ou à l'événement géologique survenu à un certain moment de l'histoire du cristal hôte. Par ailleurs, les inclusions fluides sont naturellement des systèmes diathermes, c'est à dire que la température à l'intérieur est la même que celle de l'environnement immédiat (roche hôte durant l'histoire géologique ou au sein des platines microthermométriques qui permettent les observations de transitions de phases).

Concrètement, la composition des fluides peut renseigner sur l'environnement chimique dans les conditions de formation de la roche (e.g. Claypool and Mancini, 1989; Mullis, 1987; Mullis et al., 1994; Tarantola et al., 2007, 2009). La densité ($g \cdot cm^{-3}$) ou le volume molaire ($cm^3 \cdot mol^{-1}$) est le paramètre clé qui va permettre de contraindre, pour un système chimique donné, les conditions de pression et température (*PT*) pendant le piégeage du paléofluide considéré. En effet, pour une composition chimique fixée (système isoplèthe avec XH_2O, $XNaCl$, XCO_2, …), comme il est de prime abord considéré qu'il n'y a pas d'échange de matière entre le contenu de l'inclusion et l'environnement, et que le volume est inchangé depuis le piégeage, les inclusions fluides ne peuvent évoluer que le long de droites monovariantes, dans l'espace *PT*, appelées isochores par analogie, et dont la pente est régie par la densité (ou volume molaire) du fluide. La signature isotopique de fluide (généralement exprimée par les valeurs

δD (ou δ^2H), $\delta^{13}C$, $\delta^{18}O$) permet de renseigner, discuter, et contraindre l'origine et les éventuelles interactions fluides-roches (e.g. Sharp, (2009)). Autrement dit, les inclusions fluides enregistrent des informations précieuses sur l'histoire des paléocirculations de fluides. L'étude qualitative et quantitative des inclusions fluides est alors incontournable pour recueillir ces informations uniques, et est de ce fait une branche essentielle de la pétrologie et de la minéralogie. Grâce à ces informations, nous pouvons mieux comprendre les processus géologiques ayant eu lieu dans le passé en établissant la relation chronologique entre les minéraux, en définissant les générations de paléofluides, les interactions fluides-roches (Mullis, 1975; Roedder, 1984; Mullis et al., 1994), ou encore nous pouvons restituer partiellement l'histoire d'une formation des gisements métallifères ou la précipitation des minéraux (e.g. Edmond et al., 1979; Dill et al., 1994; Fu et al., 2016). Ainsi, la source des fluides minéralisateurs, les conditions *PT* de transport de matières et de précipitation des éléments peuvent être mis en évidence, aidant ainsi à améliorer l'efficacité de la prospection, l'exploration et l'exploitation des gisements d'intérêt économique par exemple.

1.2. Vue globale sur le développement des méthodes d'analyse des inclusions fluides

Cette section n'a pas pour objectif de fournir une étude bibliographie exhaustive sur l'histoire de la recherche sur les inclusions fluides naturelles, mais seulement un récapitulatif des découvertes charnières ainsi que des travaux remarquables dans la discipline. L'objectif est donc de donner une vue globale sur le développement des différentes techniques permettant d'en tirer tout type d'informations avec des applications géologiques.

En effet, les études primitives des inclusions fluides ont commencé dès le début du XIX^{ème} siècle. Davy (1822) a essayé pour la première fois de déterminer la composition chimique des inclusions fluides piégées dans du quartz en broyant les cristaux dans différentes solutions (i.e., eau, mercure, pétrole…), puis en observant et décrivant le comportement des bulles de gaz libérées. Brewster, un des pionniers qui a le plus étudié les inclusions fluides à cette époque, a pu identifier deux liquides immiscibles (H_2O et CO_2) dans certains inclusions fluides, et a constaté le phénomène de décrépitation en raison de la dilatation du fluide des inclusions lors d'un échauffement (Brewster, 1823, 1826). Le comportement de la phase solide dans l'inclusion fluide lors des changements de la température a été étudié pour la première fois par Brewster (1845). Treize ans plus tard, Sorby (1858) a pu décrire le premier principe essentiel de la thermométrie pour l'étude des inclusions fluides, y compris la détermination de la température de cristallisation des minéraux, et puis d'une manière ou d'une autre partiellement

mettre en relation les informations acquises depuis ses expériences avec la formation de certaines roches en les utilisant comme un géothermomètre naturel. Cependant, en raison de la performance limitée des instruments et/ou le fait que le fluide piégé a souvent été considéré comme un système pur (probablement dû au manque de modèles théoriques de thermodynamique concernant l'eau, les gaz et leurs mélanges, les solutions salées, etc., (Bowen, 1928; Kennedy, 1950)), leurs toutes premières observations et premiers essais de caractérisation ont souvent conduit à des résultats très variables. Ces derniers rendent alors leur utilisation très douteuse. Malgré une modeste incertitude, ces études pionnières ont établi le fondement pour le développement des méthodes analytiques des inclusions fluides, et avant les principes initiaux de la microthermométrie, technique toujours le plus largement utilisée à l'heure actuelle.

Il faut noter également que pour mieux interpréter les processus et les événements géologiques du passé, différents types d'information potentiellement intéressants, qui sont préservés par les inclusions fluides (e.g., les propriétés *PVX*, la salinité, la composition isotopique…) devraient être tous recueillis avec la meilleure précision possible et combinées lors de l'interprétation. Cela nécessite non seulement une étude microthermométrique mais aussi d'autres techniques modernes alors que les techniques analytiques disponibles jusqu'au milieu du XX^{ème} siècle ne le permettaient pas. Par conséquent, la recherche sur les inclusions fluides n'a que très peu été développée et appliquée jusqu'aux années 1950 où ce domaine va à nouveau attirer l'attention de la communauté scientifique, notamment dans l'exploration minière et pétrolière (Lemmlein, 1929; Ermakov, 1950; Smith, 1953; Deicha, 1955). Un grand nombre d'articles ont été successivement publiés par des chercheurs du monde entier suite, à la fois, au développement des modèles thermodynamiques, à l'introduction des nouvelles techniques analytiques de haute sensibilité, et aux améliorations dans la fabrication des instruments de plus en plus performants et précis (cf. Touret (1984), Chou (2012), Dubessy et al. (2012) et la revue de Kesler et al. (2013)).

En effet, la seconde moitié du XX^{ème} siècle a vu l'essor de la technique de microthermométrie qui a eu alors un développement considérable. Roedder n'a pas été le premier à introduire le prototype de la platine microthermométrique, mais le premier fournissant une description complète pour détailler cette technique (Roedder, 1962). Malgré des limitations techniques de la platine au départ (la température minimale atteinte n'est que −35 °C par exemple), il a pu ensuite améliorer et adapter l'appareil pour mieux refroidir en plongeant dans un bain de glace d'acétone (– 79 °C) ou par un flux d'azote liquide (– 196 °C).

Les premiers résultats concernant l'application de l'appareil à différents types de gisements minéralisés sont ensuite publiés par Roedder (1963, 1965, 1967, 1971), et synthétisés dans Roedder (1984). Des nouveaux modèles thermodynamiques, y compris des équilibres L-V, des connaissances sur la formation, la stabilisation et la dissociation des hydrates de gaz, etc., ont été introduits par le biais des équations d'état (Chueh and Prausnitz, 1967; Soave, 1972; Lee and Kesler, 1975; Peng and Robinson, 1976; Angus et al., 1976, 1978, 1979) ou sous forme de diagrammes de phases mettant en relation les propriétés de *PVTX* (Burruss, 1981; Darimont and Heyen, 1988; van den Kerkhof, 1990; Diamond, 1992; Thiéry et al., 1994a, 1994b; Bakker et al., 1996; Bakker, 1997). Il est incontestable que ces derniers ont été cruciaux pour une meilleure interprétation des transitions de phases observées, et donc ont permis d'étendre significativement l'applicabilité de la microthermométrie. De plus, de nouvelles générations de platines microthermométriques ont été développées et commercialisées (Poty et al., 1974; Werre, 1979; Shepherd, 1981), permettant de simplifier le protocole d'analyse et aussi de minimiser l'incertitude des mesures. Tout cela fait de la microthermométrie une technique standardisée, pratique et indispensable pour l'analyse des inclusions fluides.

Cependant, il reste encore les limitations inhérentes à la microthermométrie (voir la section 2 – « Problématique » en bas). La microspectroscopie Raman a été développée et utilisée, à partir des années 1970, de façon complémentaire à la microthermométrie pour combler ces limitations (Wang and Wright, 1973; Wright and Wang, 1974; Rosasco et al., 1975; Rosasco and Roedder, 1979; Dubessy et al., 1982; Pasteris et al., 1986, 1988; Dubessy et al., 1989). Malgré les capacités potentielles très prometteuses, l'application de la spectroscopie Raman reste restreinte principalement aux analyses qualitatives, et reste peu appliquée aux analyses quantitatives en dehors de certains systèmes simples. Comme l'effet (signal) Raman est extrêmement sensible à divers paramètres instrumentaux et aux conditions de mesures, l'analyse quantitative à haute précision nécessite strictement un processus de calibration assez complexe et minutieux. Une étude bibliographique plus complète de cette technique sera présentée dans un chapitre dédié, i.e., Chapitre 1 – État de l'art.

La spectroscopie infrarouge est une autre méthode de spectroscopie vibrationnelle qui s'applique en partie à l'analyse des espèces hydrocarbonées ou fluorescentes pour lesquelles la spectroscopie Raman n'est pas efficace. D'autres techniques non-destructives permettant des analyses multi-élémentaires et d'éléments en traces peuvent également être citées tels que le PIXE (Particle-induced X-ray Emission) (Ryan et al., 1991), le SRXRF (Synchrotron Radiation X-ray Fluorescence) (Frantz et al., 1988), etc.

Vis-à-vis des techniques destructives, Roedder (1958) a réalisé les premières analyses géochimiques (en déterminant quantitativement les ions présents dans la phase aqueuse d'inclusions fluides piégés dans du quartz) de gisements hydrothermaux par le biais de la technique appelée «crush-leach». Cette technique a été encore développée pour réduire la quantité d'échantillon à écraser (jusqu'à 2 g) et améliorer la limite de détection (Bottrell et al., 1988; Banks and Yardley, 1992). L'ICP-MS (Inductively Coupled Plasma - Mass Spectrometry) couplée à l'ablation laser, et la LIBS (Laser Induced Breakdown Spectroscopy) sont aussi des techniques destructives qui sont largement utilisées pour déterminer la composition élémentaire et les éléments présents en traces dans les inclusions fluides sur une très large gamme de concentration (jusqu'à l'ordre des ppb). Quelques études représentatives peuvent être citées ici comme Wilkinson et al. (1994), Irwin et Roedder (1995), et Shepherd et Chenery (1995) pour l'ICP-MS, ou Fabre et al. (1999, 2002) pour la LIBS. La signature isotopique des fluides peut aussi être obtenue par différentes techniques en broyant une petite quantité de l'échantillon hôte (1-2 g), par exemple la ligne d'extraction couplée avec la spectroscopie de masse (Kasemann et al., 2001; Tarantola et al., 2007) ou la CRDS (Cavity-Ring-Down Spectroscopy) (Arienzo et al., 2013; Affolter et al., 2014; Uemura et al., 2016). L'inconvénient majeur de certaines de ces techniques destructives, notamment le crush-leach et l'analyse isotopique, en plus de détruire l'échantillon, est le fait d'analyser un mélange de différentes générations d'inclusions fluides car nécessitant une masse d'échantillon importante généralement supérieure à 1 g.

2. Problématique

Actuellement, la microthermométrie est toujours la méthode non-destructive la plus pratique à manipuler et la plus couramment utilisée pour l'analyse des inclusions fluides. Elle est basée sur l'observation de la température des transitions de phases des différents constituants piégés dans l'inclusion. Les données obtenues sont ensuite interprétées en utilisant des abaques (i.e., des diagrammes de phases *PT* ou *XT*) et/ou une équation d'état adéquate pour estimer le volume molaire (la densité) et la composition chimique totale, incluant la salinité, de l'inclusion fluide. Bien que cette méthode et les interprétations quantitatives des observations ait été grandement améliorées (voir le texte au-dessus), son applicabilité est encore restreinte par quelques limitations inhérentes. Par exemple, il est difficile, voire impossible, d'observer exactement les transitions de phases dans les inclusions de très petite taille (< 5 µm) ou de faible densité (Kawakami et al., 2003; Rosso and Bodnar, 1995; Yamamoto et al., 2002). De plus, cette méthode n'est pas non plus applicable, de manière

quantitative, aux inclusions de compositions complexes (par exemple avec plus de deux sels ou plus de deux composés volatiles) avec un nombre d'observations de transitions de phase insuffisant pour contraindre complètement le système thermodynamiquement. En effet, par exemple, les diagrammes de phases *VX* des systèmes de CO_2-N_2 et CH_4-CO_2 sont disponibles dans la littérature (Burruss, 1981; Thiéry et al., 1994a), permettant ainsi de déterminer la composition et la densité à partir des températures de fusion et d'homogénéisation de la phase volatile de l'inclusion fluide. Cependant, l'incertitude des résultats dérivés de ces diagrammes de phases est souvent inconnue.

D'autre part, ce type de diagrammes de phases pour des mélanges CH_4-N_2 et CO_2-CH_4-N_2 n'est pas disponible. Par conséquent, la composition actuelle de ces systèmes est souvent simplifiée en considérant des systèmes purs ou en négligeant l'existence d'un (ou certains) constituant(s) afin de pouvoir appliquer les modèles thermodynamiques disponibles. La formation d'hydrates de gaz (e.g., CH_4, CO_2) impacte également sur les températures des transitions de phases mesurées. Cela peut donc de nouveau générer des erreurs sur les données obtenues ainsi que pour leur interprétation quantitative (Seitz et al., 1987; Diamond, 1992, 1994).

Pour toutes ces raisons, les études quantitatives de reconstruction de composition et de densité des inclusions fluides ne sont généralement accomplies qu'en combinant la microthermométrie avec la microspectroscopie Raman.

Théoriquement, la spectroscopie Raman est à l'heure actuelle la seule méthode permettant une analyse ponctuelle à la fois non-destructive, qualitative, quantitative et localisée avec une taille du point d'analyse qui peut être réduite jusqu'à 1 µm. Les questions qui se posent ici sont alors:

- *Est-ce que la spectroscopie Raman peut remplacer entièrement la microthermométrie, ou au moins, dans certains cas précis ?*
- *Est-ce que les incertitudes des mesures réalisées par spectroscopie Raman sont meilleures ou comparables à celles de l'analyse par microthermométrie ?*

3. Objectifs et démarches de la thèse

L'objectif principal de cette thèse est d'apporter des données d'étalonnage du signal Raman des mélanges de gaz de CO_2, CH_4 et N_2 couvrant toute échelle de composition (c.à.d., allant de gaz purs à des mélanges binaires et ternaires). Ces nouvelles données permettent de

déterminer directement et simultanément les propriétés *PVX* de l'inclusion fluide à température fixée uniquement à partir de mesures Raman. Pour cela, plusieurs tâches ont été réalisées :

(i) **Évaluer les valeurs relatives de la section efficace (RRSCS) des gaz** : le RRSCS est un paramètre physique reflétant l'efficacité de la diffusion Raman de chaque mode de vibration des molécules, ce qui est traduit sur le spectre Raman par l'intensité ou l'aire des pics d'intérêt. Ce paramètre est donc utilisé pour déterminer la composition (fractions molaires) de chacun des composés du mélange gazeux à partir de l'intensité du signal mesurée par spectroscopie Raman. Seule la section efficace absolue de N_2 a été fidèlement établie par Murphy et al. (1969), Fouche and Chang (1971a), Penney et al. (1972) et Fenner et al. (1973). Pour les autres gaz, seule la section efficace relative (RRSCS) à celle du N_2 a été mesurée. Les valeurs des sections efficaces relatives des gaz couramment rencontrés dans les fluides géologiques tels que CO_2, CH_4, ainsi que O_2, H_2 et CO, ont été publiées il y a environ cinquante ans par Penney et al. (1972) et Fenner et al. (1973). Ces valeurs ont été rassemblées par Schrötter and Klockner (1979) avec une discussion complète, fournissant ainsi une base de données pour l'analyse quantitative. Cependant, ces valeurs ont été utilisées jusqu'à l'heure actuelle avec une incertitude peu ou pas connue (cf. les revues de Burke (2001) et Frezzotti (2012)). Il convient de garder à l'esprit que toutes ces anciennes données ont été déterminées à partir de gaz à faible densité et à température ambiante, i.e., des conditions non représentatives de la plupart des fluides géologiques. Certains travaux ont montré qu'elles peuvent varier avec la température (Schrötter and Klöckner, 1979), la pression et/ou la composition (Wopenka and Pasteris, 1986; Dubessy et al., 1989; Seitz et al., 1993, 1996). Au vu de l'ancienneté des données dans la littérature et de la sensibilité de ces paramètres à la réponse de l'instrument, il est donc nécessaire de les réévaluer dans des mélanges gazeux et à des pressions (densités) élevées pour connaître leur domaine de validité afin d'assurer une meilleure incertitude et donc améliorer la qualité des mesures lors de l'étude des fluides géologiques.

(ii) **Identifier les marqueurs spectroscopiques les plus pertinents pour des analyses quantitatives** : Evaluer l'effet du changement de la pression, de la densité et de la composition (et éventuellement de la température) sur la variation de tous les paramètres spectraux Raman (y compris les déplacements en nombre d'onde de la position des pics, la séparation entre les pics, la largeur du pic à mi-hauteur, les rapports des aires ou des intensités des pics…) afin de choisir les paramètres quantitatifs les plus pertinents et fiables. La reproductibilité est aussi un facteur très important à prendre en compte pour ce type de mesure

quantitative. Ceci est fait par la répétition des mesures à différentes périodes et/ou éventuellement par l'élaboration et l'utilisation de standards de type microcapillaires scellés pour pouvoir calibrer ponctuellement ou quotidiennement le signal Raman afin d'assurer une pérennité dans le temps de nos étalonnages.

(iii) **Estimer l'incertitude et le domaine de validité des mesures :** la gamme de notre calibration sera comprise entre 5 et 600 bars couvrant ainsi le domaine de la majeure partie des inclusions fluides à température ambiante. Les données de calibration obtenues seront fournies, sous forme d'équations de régression polynomiale, pour différents domaines de pression (ou densité) et de composition afin de minimiser l'incertitude des mesures. L'incertitude finale des mesures sera évaluée en prenant en compte la propagation de toutes les sources d'erreurs majeures, y compris les incertitudes dans la mesure de paramètres spectraux (i.e., l'aire ou la position des pics…) et les incertitudes provenant des équations de régression.

(iv) **Tester les étalonnages sur des inclusions fluides naturelles pour validation** : les données de calibration seront ensuite appliquées pour analyser une série d'inclusions fluides naturelles dans différents contextes tels que des bassins faiblement métamorphisés de la partie externe des Alpes Centrales (inclusions fluides à CH_4), le métamorphisme alpin (inclusions fluides à CH_4-CO_2 et CO_2-N_2), ou des ressources avec l'exemple du gisement W-Sn de Panasqueira au Portugal (inclusions fluides à CO_2-CH_4-N_2). Les résultats obtenus par spectroscopie Raman seront comparés avec ceux obtenus par microthermométrie pour validation de la méthode.

(v) **Modéliser la variation des paramètres spectraux :** un autre objectif de cette thèse est, d'un point de vue théorique physico-chimique, d'interpréter la tendance de la variation du paramètre spectral choisi pour les mesures quantitatives (i.e., la variation relative de la position du pic) sous l'effet du changement de pression (densité) et de la composition à l'échelle moléculaire. Cela est fait par des calculs des contributions des forces d'interaction intermoléculaire (répulsives et attractives) et ainsi que de la variation de la longueur des liaisons entre les atomes par le biais de modèles théoriques. Un modèle prédictif sera également fourni et discuté afin d'estimer la tendance de la variation de la position du pic du CH_4 (pour le CH_4 pur ainsi que pour les mélanges CH_4-N_2 et CH_4-CO_2) sur une gamme de pression plus large que la gamme parcourue lors de nos études expérimentales (jusqu'à 3000 bars).

(vi) **Développer un programme de calcul** avec une interface utilisateur pour faciliter l'accès au plus grand nombre aux nouvelles données de calibration.

Une discussion concernant l'applicabilité des données de calibration (qui sont intégrées dans le programme de calculs) à un autre spectromètre Raman ou à un autre laboratoire, ainsi que la possibilité de les extrapoler à d'autres systèmes gazeux sera présentée dans les chapitres 3 et 5.

4. Organisation du manuscrit

Après une **introduction** qui présente successivement (i) le contexte dans lequel la thèse s'inscrit en soulignant les intérêts géologiques de l'analyse quantitative des inclusions fluides, (ii) la problématique sur l'aspect méthodologique, et (iii) les objectifs et les démarches de la thèse, le manuscrit est constitué de 5 chapitres :

Le chapitre 1 propose une synthèse bibliographique récapitulant les études réalisées depuis les années 1970 sur la section efficace et l'analyse quantitative par spectroscopie Raman de gaz et de mélanges de gaz CO_2, CH_4 et N_2 qui sont couramment rencontrés dans les inclusions fluides naturelles. Ceci permet d'avoir une vue globale sur cette technique analytique et sur les variations des différents paramètres spectraux en fonction de la température, de la pression, de la densité, et donc permet de définir les conditions des expériences à mener et les paramètres spectraux les plus pertinents.

Le chapitre 2 est dédié spécifiquement aux mélanges binaires CO_2-N_2 dont les données de calibration au Raman n'ont jamais été publiées dans la littérature jusqu'à ce travail. Le protocole expérimental, allant de la préparation des mélanges à différentes concentrations, et la vérification de la composition par chromatographie en phase gazeuse (GC), jusqu'au traitement des spectres Raman obtenus sera décrit. Ensuite, nous présenterons le jeu de données de calibration du signal Raman de ce mélange pour toute composition sur une gamme de pression de 5 à 600 bars. Les analyses seront principalement réalisées à 32 °C (au-dessus du point critique du CO_2 pur à 31.05 °C) pour éviter les situations en domaine biphasé. Quelques analyses, pour certains mélanges avec un point critique moins élevé, ont été également réalisées à 22 °C pour comparaison et évaluer l'effet de la température sur les paramètres d'intérêt. L'étalonnage est ensuite validé par l'analyse quantitative de la composition et de la densité d'inclusions fluides naturelles provenant des Alpes Centrales, comparées avec celles obtenues à partir des transitions de phases observées en microthermométrie. Le contenu de ce chapitre a été publié le 17 octobre 2019 dans la revue Analytical Chemistry (Le et al., 2019).

Dans **le chapitre 3**, nous suivrons une procédure similaire à celle du chapitre 2 pour établir et valider des données de calibration, mais cette fois en généralisant la méthode en l'étendant à d'autres mélanges, i.e., les mélanges binaires dans les systèmes CH_4-N_2 et CH_4-CO_2 et les mélanges ternaires dans le système CO_2-CH_4-N_2. Une partie de ce chapitre sera consacrée à une discussion sur l'applicabilité de nos données de calibration aux autres laboratoires en comparant nos résultats avec ceux publiés récemment dans la littérature. Le contenu de ce chapitre a été publié le 20 juillet 2020 dans la revue Chemical Geology (Le et al., 2020).

Le **chapitre 4** est consacré à détailler les interprétations de la variation de la position des pics de CH_4 et N_2 en fonction de la pression (densité) et de la composition en utilisant deux modèles théoriques « Lennard-Jones 6-12 potential energy approximation » et « Perturbed Hard-Sphere Fluid ». Des modèles prédictifs sont ensuite proposés pour décrire l'évolution de la position du pic de CH_4 en fonction de la pression (densité) et de la composition dans les mélanges CH_4-N_2 et CH_4-CO_2. Ce chapitre est rédigé sous forme d'article pour être soumis dans la revue Physical Chemistry.

Lamadrid et al. (2018) ont proposé un modèle prédictif pour déterminer directement par spectroscopie Raman la fugacité des gaz (CH_4, CO_2 et N_2) dans certains mélanges. Grâce à nos données de calibration, nous avons pu réviser ce modèle et fournir des données d'étalonnage pour le même objectif, mais avec une meilleure applicabilité et incertitude. Comme ces données d'étalonnage de la fugacité ne sont pas en lien concret avec l'objectif principal du chapitre 4, elles seront placées dans la partie annexe. Le but est ici d'illustrer une des applications potentielles de nos données de calibration, au-delà du développement des densimètres et baromètres.

Dans le **chapitre 5**, l'applicabilité des données d'étalonnage obtenues dans ce travail aux autres laboratoires (ou autres spectromètres Raman) est discutée. Pour cela, l'ensemble de nos données d'étalonnage est révisé, comparé et/ou combiné avec celles publiées dans la littérature afin (i) d'évaluer la reproductibilité de la mesure des paramètres spectraux quantitatifs choisis, et (ii) d'examiner la possibilité d'extension des données d'étalonnage à plus haute pression (densité) et/ou à température plus élevée. Ensuite, les nouvelles données d'étalonnage qui sont applicables dans d'autres laboratoires seront fournies, tout en définissant le domaine de validité optimal avec un minimum d'incertitude lors de l'utilisation.

Au total 76 équations de régression polynomiale sont fournies pour différentes gammes de composition-pression et température. Ces équations permettent de déterminer les propriétés

PVX de tous les systèmes gazeux de CH_4, CO_2, et N_2 (purs, binaires et ternaires) directement à partir des données Raman. Il n'est donc pas pratique de sélectionner manuellement une équation d'étalonnage pour chaque analyse spécifique. De plus, l'estimation de l'incertitude globale du résultat final (pressure ou densité) est assez fastidieuse à réaliser. Pour ce faire, nous avons développé le programme de calcul **FRAnCIs** (**F**luids : **R**aman **An**alysis **C**omposition of **I**nclusion**s**) qui permet rapidement et facilement de calculer les propriétés *PVX* ainsi que les incertitudes associées via une interface utilisateur qui intègre ainsi toutes nos données d'étalonnage. Enfin, nous discuterons sur la possibilité d'application des données d'étalonnage développés dans cette étude, qui ont été spécifiquement établies pour les systèmes CO_2-CH_4-N_2, à un autre système contenant une faible quantité d'un autre constituant tels que H_2, H_2S, O_2…

Le manuscrit se terminera par une conclusion générale soulignant tous nos résultats et des perspectives pour des développements futurs pouvant potentiellement intéresser la communauté scientifique.

Chapter 1: État de l'art sur l'analyse quantitative des propriétés *PVX* des gaz et des mélanges gazeux par spectroscopie Raman

En premier lieu, le principe de la diffusion Raman, les modes de vibration des molécules CO_2, CH_4 et N_2 ainsi que la description et l'interprétation générales de ces spectres Raman seront brièvement rappelées.

Ensuite, un récapitulatif sur la détermination de la section efficace - un paramètre physique qui reflète l'efficacité de l'effet Raman selon les modes de vibration actives en Raman, sera présenté. La détermination de la composition relative du mélange gazeux en utilisant les valeurs de la section efficace disponible dans la littérature, et l'incertitude de mesures sera détaillée et discutée.

Enfin, les données sur les étalonnages du signal Raman des gaz CO_2, CH_4 et N_2 et éventuellement de leurs mélanges, publiés dans la littérature depuis les années 1970 jusqu'à ce travail, seront rassemblées et discutées. Ces données d'étalonnage sont généralement fondées sur la variation des différents paramètres spectraux (e.g., la position, le rapport d'aire ou d'intensité des pics, …) en fonction de la pression, de la densité, de la température et de la composition chimique.

1. Généralités sur les spectres Raman de N_2, CH_4 et CO_2

1.1. Principe de la diffusion Raman

Lorsqu'un faisceau laser monochromatique est envoyé sur la matière, plusieurs phénomènes d'interaction sont possibles selon le rapport entre la taille de l'objet diffusant et la longueur d'onde, e.g., la transmission, la réflexion, la réfraction, l'absorption et la diffusion, etc. Dans le cas de l'effet Raman, c'est le phénomène de diffusion qui entre en jeu. La Figure 1-1a illustre trois phénomènes de diffusion différents qui sont induits lors de l'interaction photon-matière.

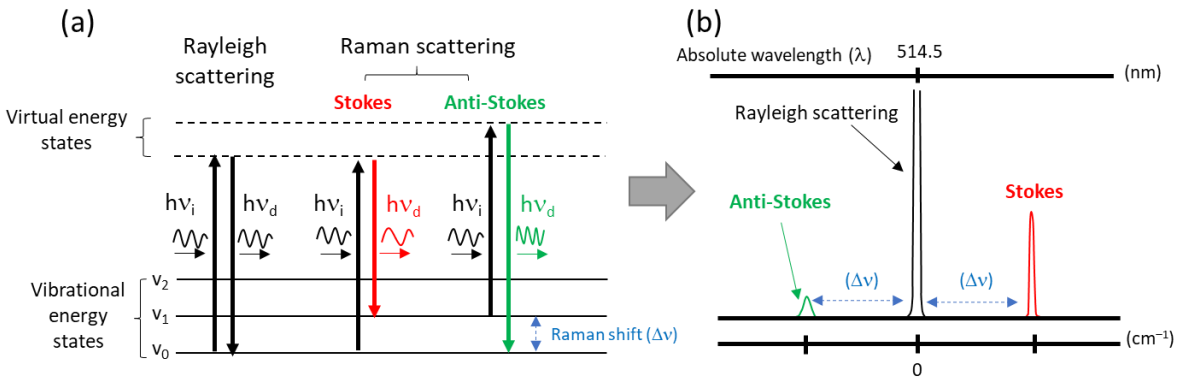

Figure 1-1: (a) Représentation des transitions énergétiques d'un mode de vibration de la molécule induites par l'interaction photon-matière, et des différents phénomènes de diffusion. (b) Exemple d'un spectre Raman obtenu par un laser de λ = 514.5 nm. Les trois pics reportés sur le spectre Raman correspondent à trois phénomènes de diffusion. La raie Rayleigh la plus instense induite par la diffusion élastique (e.g., pas de modification d'énergie) se situe à 0 cm^{-1}. Les deux raies Stokes et Anti-Stokes moins intenses, induites par la diffusion inélastique, se situent à $\pm$ $\Delta\nu$ cm^{-1}, avec $\Delta\nu$, le déplacement Raman (ou Raman shift), la différence entre la fréquence du photon incident et celle du photon diffusé. Comme la différence d'énergie entre le photon incident et le photon diffusé correspond à l'énergie d'une transition d'état de vibration de la molécule, le deplacement Raman $\Delta\nu$ caractérise donc le mode de vibration et la nature chimique de la molécule associée.

En effet, l'énergie du rayonnement d'excitation $E_i = h\nu_i$ (où ν_i est la fréquence du photon incident et *h* est la constante Planck) mise en jeu dans la diffusion Raman est largement supérieure aux niveaux d'énergie vibrationnelle de la molécule, mais généralement inférieure à celle de l'énergie des niveaux électroniques (E_1, E_2, …). Lors de l'interaction avec le photon incident d'énergie E_i, la molécule est alors excitée à un niveau d'énergie virtuel instable, puis redescend (désexcite) immédiatement à un niveau d'énergie de vibration plus bas en émettant un photon diffusé d'énergie E_d (Figure 1-1a).

Le processus le plus probable est celui où la molécule retourne à son niveau d'énergie initial en émettant un photon diffusé ayant la même énergie (fréquence) que celle du photon incident ($E_i = E_d$) : c'est la diffusion élastique, nommée la diffusion Rayleigh. La molécule n'a donc subi aucune modification d'énergie. Avec une très faible probabilité, le rayonnement incident peut être diffusé inélastiquement avec un changement d'énergie (fréquence). Ce changement d'énergie est égal à la différence énergétique entre deux états vibrationnels d'un mode de vibration donnée de la molécule (Figure 1-1a). Deux cas sont donc possibles :

Dans le cas où la molécule retourne à un niveau d'énergie vibrationnelle plus haut que le niveau initial (la probabilité est environ 1 sur 10^7 des cas) en émettant un photon diffusé ayant une énergie inférieure à celle du photon incident ($E_d < E_i$), c'est-à-dire que le photon incident cède une part de son énergie à la molécule : c'est la diffusion Raman Stokes. La molécule descend à un niveau d'énergie plus bas que le niveau initial (environ 1 sur 10^9 des cas) en émettant un photon ayant une énergie supérieure à celle du photon incident ($E_d > E_i$), i.e., la molécule cède une part de son énergie au photon diffusé : c'est la diffusion Raman Anti-Stokes. Il est à noter que seuls les modes de vibration induisant une variation de la polarisabilité totale de la molécule lors de la transition énergétique sont actifs en Raman, c'est-à-dire que la dérivée de la polarisabilité de la molécule par rapport à la coordonnée de vibration $\left(\frac{\partial \alpha}{\partial u}\right)_0$ est non nulle. D'après les règles de sélection, tous les modes de vibrations totalement symétriques sont actifs en Raman.

En général, le spectre Raman reporte la différence entre la fréquence du photon incident (radiation d'excitation) et celle du photon diffusé, appelée le déplacement Raman $\Delta\nu$, exprimée en nombre d'onde (cm^{-1}). Le déplacement $\Delta\nu$ est mesuré relativement à la raie Rayleigh située à 0 cm^{-1} (Figure 1-1a et b). Théoriquement, le $\Delta\nu$ ne dépend pas de la fréquence de la radiation d'excitation mais dépend du mode de vibration considéré, et donc de la nature chimique de la molécule associée. C'est-à-dire que si on change la fréquence du laser d'excitation tout en conservant le même échantillon, la position de la raie reportée sur le spectre Raman reste inchangée. Cette caractéristique du spectre Raman est donc utilisée pour les analyses d'identification (qualitatives).

Il est à noter également qu'un mode de vibration donné existe à la fois sur les deux domaines Stokes et Anti-Stockes du spectre Raman à une même valeur absolue du déplacement Raman $\Delta\nu$ (Figure 1-1b). Cependant, l'intensité de la raie reportée sur le domaine Anti-Stokes est beaucoup plus petite que celle de la raie reportée sur le domaine Stockes en raison d'une

très faible probabilité de la diffusion Anti-Stokes par rapport à celle de la diffusion Stokes (conséquence de la loi de Boltzman). C'est aussi la raison pour laquelle les raies reportées dans la partie Stokes sont préférentiellement utilisées dans les analyses Raman classiques afin de gagner en intensité du signal.

1.2. Modes de vibration et spectres Raman du N_2, CH_4 et CO_2

Le nombre de modes de vibration d'une molécule est égal à 3N-5 pour les molécules linéaires ou 3N-6 pour les molécules non-linéaires, où N est le nombre d'atomes. Ainsi, la molécule diatomique symétrique N_2 ne possède qu'un seul mode de vibration d'élongation symétrique actif en Raman mesurée à ~ 2331 cm^{-1} (dénoté ν_1) (Figure 1-2a). Le spectre Raman du N_2 (mesuré à température ambiante et à environ 1 bar) est alors caractérisé par un seul pic à environ 2331 cm^{-1} (Figure 1-3).

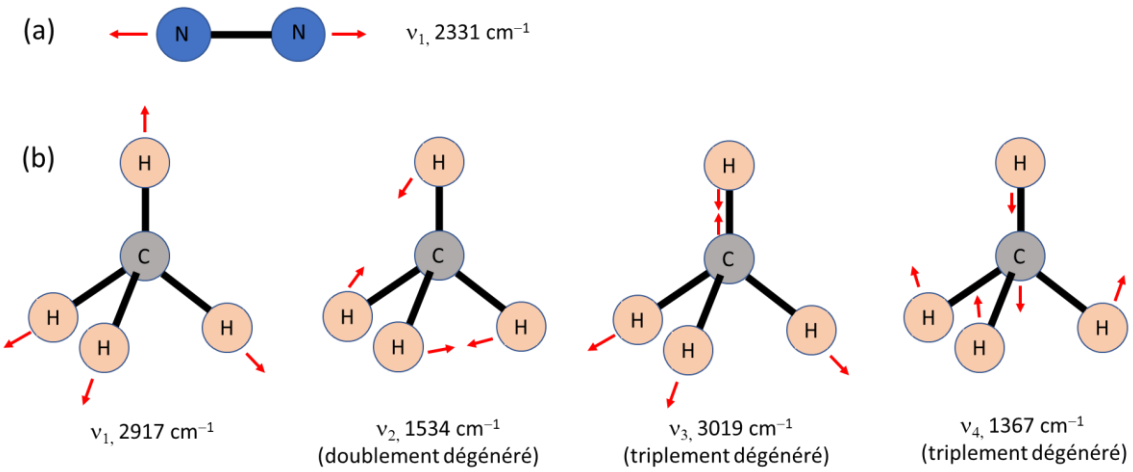

Figure 1-2: Représentation schématique des mouvements des modes de vibration fondamentaux de la molécule (a) N_2 et (b) CH_4. La molécule N_2 présente un seul mode de vibration d'élongation totalement symétrique (ν_1). La molécule CH_4 présente neuf modes de vibration : un mode d'élongation symétrie (ν_1), deux modes doublement dégénérés de déformation d'angle (ν_2), trois modes triplement dégénérés d'élongation antisymétrique (ν_3), et trois modes triplement dégénérés de déformation antisymétrique (ν_4).

La molécule tétraédrique symétrique CH_4 possède neuf modes de vibration dont un mode d'élongation symétrique ν_1 à ~ 2917 cm^{-1}, deux modes de déformation d'angle ν_2 à ~ 1534 cm^{-1} (doublement dégénérés), trois modes d'élongation antisymétrique ν_3 à ~ 3019 cm^{-1} (triplement dégénérés), et trois modes de déformation antisymétrique ν_4 à ~ 1367 cm^{-1} (triplement dégénérés) (Figure 1-2) (Thomas and Welsh, 1960). Tous les modes de vibration fondamentaux du CH_4 entrainent une variation de la polarisabilité totale de la molécule pendant

la vibration, et sont donc tous actifs en Raman. La raie située vers 2917 cm^{-1}, correspondant au mode de vibration ν_1, est la plus intense. Cette raie est donc souvent étudiée dans les analyses qualitatives et/ou quantitatives (voir la section suivante). Les raies des autres modes de vibration du CH_4 (ν_2, ν_3 et ν_4), sont de très faible intensité, comparées à celle de la raie ν_1 (Figure 1-3).

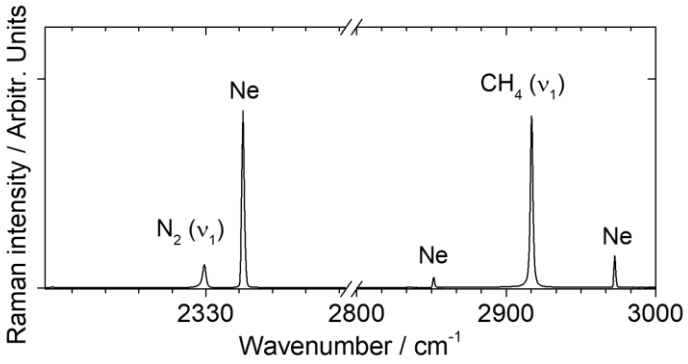

Figure 1-3: Exemple de spectre Raman du N_2 et CH_4 enregistrés à ~ 150 bars et à 32 °C par un laser d'excitation à 514 nm. Les spectres du N_2 et du CH_4 sont caractérisés par une raie à ~ 2331 cm^{-1} et ~ 2917 cm^{-1}, respectivement, correspondant au mode de vibration d'élongation symétrique ν_1. Les autres modes de vibration du CH_4 (ν_2, ν_3, ν_4), bien qu'ils soient actifs en Raman, sont généralement très peu visibles parce que leurs intensités sont beaucoup trop faibles par rapport à celle de la raie ν_1 du CH_4. Les émissions du néon ont été simultanément enregistrées avec les spectres du N_2 et CH_4 pour l'étalonnage en nombres d'onde.

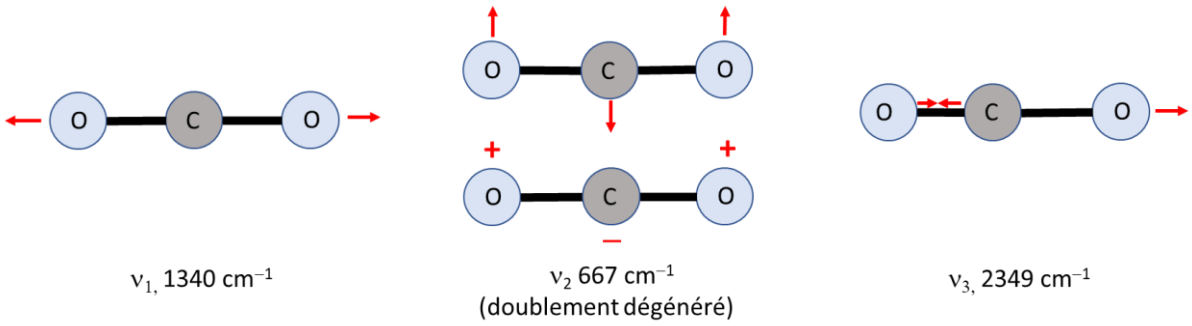

Figure 1-4: Représentation schématique des mouvements des modes de vibration fondamentaux de la molécule de CO_2. Elle possède quatre modes de vibration : un mode d'élongation symétrique ν_1 à 1340 cm^{-1}, deux modes de déformation d'angle ν_2 à 667 cm^{-1} (doublement dégénérés) et un mode d'élongation antisymétrique ν_3 à 2349 cm^{-1}.

La molécule CO_2 comprend trois atomes reliés linéairement par des liaisons doubles. Elle possède quatre modes de vibrations fondamentales dont un mode d'élongation symétrique ν_1 à

~ 1340 cm^{-1}, deux modes de déformation d'angle ν_2 vibrant dans deux plans perpendiculaires à ~ 667 cm^{-1} (doublement dégénérés), et un mode d'élongation antisymétrique ν_3 à ~ 2349 cm^{-1} (Figure 1-4) (Gordon and McCubbin, 1966). Les règles de sélection prévoient qu'un seul mode de vibration fondamental ν_1 est actif en Raman. Les autres modes (ν_2 et ν_3) ne sont pas actifs en Raman, mais visibles en spectroscopie infrarouge.

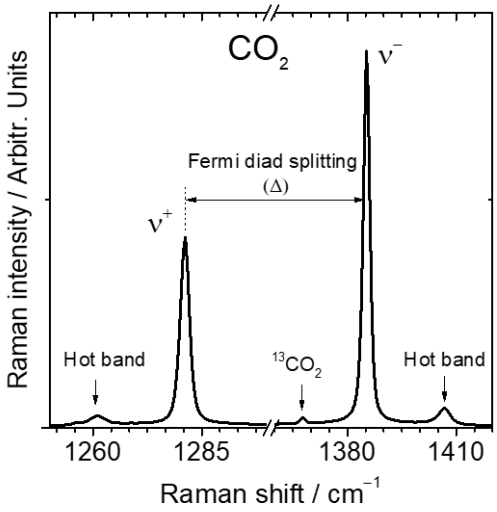

Figure 1-5: Exemple d'un spectre Raman du CO_2 enregistrés à ~ 100 bars et à 32 °C par un laser d'excitation à 514 nm.

Malgré un seul mode ν_1 théoriquement prévu, le spectre Raman du CO_2 se présente sous forme de deux raies intenses situées à environ 1388 et 1285 cm^{-1}, et dénotées ν^+ et ν^-, respectivement (Figure 1-5). Ceci est expliqué par l'effet de résonance de Fermi qui a lieu lorsque les énergies de transition (ou les fréquences) de deux modes de vibrations sont proches (Fermi, 1931). Pour le cas du CO_2, le mode de vibration fondamental ν_1 et l'harmonique d'ordre 2 du mode ν_2 (e.g., $2\nu_2$), qui possèdent presque la même énergie (ν_1 = 1340 cm^{-1}, et $2\nu_2 = 2\times667$ = 1334 cm^{-1}) et la même symétrie (Σ_g^+), sont mis en jeu (Herzberg, 1945). Par conséquent, ces deux états de vibration (ν_1 et $2\nu_2$) se perturbent et résultent en une division en deux raies ν^+ et ν^- à des positions comme précitées, appelées le doublet de Fermi (Fermi, 1931; Gordon and McCubbin, 1966). Par ailleurs, deux raies situées de part et d'autre du doublet Fermi à 1409 et 1265 cm^{-1} sont aussi observées sur le spectre du CO_2, nommées bandes chaudes. Ces raies peuvent également être expliquées par l'effet de résonance de Fermi dû à la perturbation entre deux états de vibration ($\nu_1 + \nu_2$) et ($3\nu_2$) d'une faible proportion de molécules déjà excitées, et non pas de molecules qui sont à l'état fondamental comme dans le cas de la perturbation entre

états ν_1 et $2\nu_2$. Une autre raie située à 1370 cm^{-1} est attribuée au signal de l'isotope de $^{13}CO_2$. En général, ces trois dernières raies (bandes chaudes et isotope) sont de très faible intensité et ne présentent pas d'intérêt réel dans des mesures de pression, densité ou de composition isotopique.

2. Section efficace - un paramètre pour déterminer la composition (mol%)

Fondamentalement, l'aire d'un pic reportée sur le spectre Raman est proportionnelle au nombre de molécules présentes dans le volume analysé défini par le laser d'excitation. Selon la théorie de la polarisation de Placzek (1934), la relation entre l'aire d'un pic Raman et la concentration *absolue* d'un constituant gazeux peut être exprimée par la formule suivante (Wopenka and Pasteris, 1986) :

$$A = \int_{\nu_1}^{\nu_2} \sigma_a(\nu_0 - \nu_{vib}; \nu) d\nu N(V) I(\nu_0) \Omega_c \qquad 1.1$$

Où :

- A : l'aire du pic reporté sur le spectre Raman.
- ν_0 : le nombre d'onde absolue de la radiation d'excitation (cm^{-1}).
- ν_{vib} : la fréquence vibrationnelle de la molécule (exprimée en nombre d'onde, cm^{-1}).
- $\sigma_a(\nu_0 - \nu_{vib}; \nu)$: la section efficace absolue du mode de vibration de la molécule gazeuse (ν_{vib}) par rapport à la radiation d'excitation (ν_0) (voir texte en bas).
- $N(V)$: le nombre de molécules présentes dans le volume analysé.
- $I(\nu_0)$: l'irradiance de l'échantillon, i.e., la puissance du faisceau laser diffusé par l'échantillon par unité de surface.
- Ω_c : l'angle solide de la collection des photons diffusés par l'échantillon.

Une fois que toutes les variables de l'Equation 1.1 sont connues, la concentration *absolue* des gaz peut être théoriquement calculée à partir de l'aire des pics Raman. Cependant, pratiquement, cela est impossible pour plusieurs raisons (Dhamelincourt et al., 1979; Wopenka and Pasteris, 1986) :

(i) L'irradiance à la surface de l'échantillon peut être estimée, mais pas l'irradiance exacte diffusée par l'inclusion fluide considérée. En effet, la fraction réelle de l'irradiance de l'inclusion fluide, qui est recueillie par le détecteur du spectromètre, est impossible à quantifier correctement du fait de la variation de la réfraction et de

la réflexion aux différentes interfaces le long du faisceau du laser diffusant. De plus, les caractéristiques d'absorption du minéral hôte sont différentes d'un échantillon à l'autre. La variété des propriétés optiques (e.g., la taille, la forme, la couleur, l'orientation cristallographique et la profondeur par rapport à la surface de l'échantillon, etc.,) de chaque échantillon naturel rend aussi difficile la mesure de son irradiance exacte.

(ii) La dérive spontanée de la réponse instrumentale d'un jour à l'autre.

(iii) Les sections efficaces *absolues* des gaz sont encore peu ou pas connues dans la littérature du fait de la complexité et de la difficulté de leur détermination. Seule celle de l'azote a été fidèlement déterminée (voir le texte en bas).

Pour rappel, la section efficace (RSCS - Raman Scattering Cross-Section) est un paramètre physique traduisant l'efficacité de l'effet Raman (i.e., la diffusion inélastique causée par l'interaction entre le photon d'excitation et la matière analysée) par rapport à chaque espèce chimique, ou plus spécifiquement par rapport à chaque mode de vibration actif en Raman. En raison de la complexité de la détermination de la RSCS *absolue*, seule celle de l'azote a été soigneusement mesurée par différentes techniques (Fouche and Chang, 1971b; Penney et al., 1972; Fenner et al., 1973; Hyatt et al., 1973; Schrötter and Klöckner, 1979). L'azote a été utilisé comme un gaz standard parce qu'il est non-réactif et peut donc facilement être mélangé avec d'autres gaz afin de déterminer les valeurs des sections efficaces *relatives* (Schrötter and Klöckner, 1979).

Plusieurs types de RSCS peuvent être trouvés dans la littérature. La RSCS *absolue* et la RSCS *absolue différentielle* ($cm^2 \cdot sr^{-1}$) sont des valeurs mesurées pour un angle solide complet ($\Omega_c = 4\pi$) ou pour un certain angle solide Ω_c, respectivement (cf. Equations 4.7 et 4.8 de Schrötter and Klöckner 1979). De plus, la RSCS *absolue différentielle* varie également en fonction de la longueur d'onde d'excitation, i.e., par un facteur exponentiel de $(\nu_0 - \nu_{vib})^4$. En normalisant la RSCS *absolue différentielle* avec ce dernier facteur, on obtient la RSCS *absolue différentielle normalisée* ($cm^6 \cdot sr^{-1}$) qui est indépendante de la fréquence du laser d'excitation. Malgré l'utilisation de conditions de mesures (température, pression) et de configurations instrumentales identiques dans différents laboratoires (spectromètre, laser d'excitation, les configurations de l'accumulation des spectres, etc.), les valeurs de la RSCS *absolue différentielle* $\frac{d\sigma}{d\Omega}$ et de la RSCS *absolue différentielle normalisée* $\frac{d\sigma}{d\Omega} \cdot (\nu_0 -$

$2331\ cm^{-1})^4$ du N_2 sont légèrement différentes et ont toujours été reportées avec une incertitude relative variant de ~ 2 à 33% (cf. Table 1-1).

Table 1-1: Valeurs absolues différentielles[(a)] et valeurs absolues différentielles normalisées[(b)] de la section efficace Raman du mode de vibration d'élongation symétrique du N_2. [(*)]

Longueur d'onde d'excitation (nm)	(a) $\frac{d\sigma}{d\Omega}$ (10^{-32} $cm^2 \cdot sr^{-1}$)	(b) $\frac{d\sigma}{d\Omega} \cdot (\nu_0 - 2331\ cm^{-1})^4$ (10^{-48} $cm^6 \cdot sr^{-1}$)	Références
632.8	21 ± 3	6.4 ± 1	(Kamiyama et al.,1974)
514.5	44 ± 17 43 ± 2 42 ± 2 43.2 ± 0.8	5.1 ± 2 5.0 ± 0.3 4.9 ± 0.3 5.05 ± 0.11	(Fouche and Chang, 1972) (Penney et al., 1972) (Hyatt et al., 1973) (Klöckner, 1977)
488.0	33 ± 11 43 54 ± 3 55.8 ± 2	3.0 ± 1 4.0 ± 1 5.0 ± 0.3 5.13 ± 0.2	(Fenner et al., 1973) (Fenner et al., 1973) (Hyatt et al., 1973) (Klöckner, 1977)
457.9	76 ± 5 73.7 ± 3	5.2 ± 0.4 5.09 ± 0.25	(Hyatt et al., 1973) (Klöckner, 1977)
435.8	92 ± 10	5.1 ± 0.5	(Murphy et al., 1969)
363.8	204 ± 25	5.1 ± 0.6	(Klöckner, 1977)
351.1	243 ± 30	5.2 ± 0.7	(Klöckner, 1977)
	Valeur moyenne	5.05 ± 0.08	

[*] Les valeurs de la RSCS sont citées de Schrötter and Klöckner (1979).

[(a)] Les valeurs de la RSCS *différentielle* ont été mesurées pour un certain angle solide.

[(b)] Les valeurs de la RSCS *différentielle normalisée* ont été normalisées par un facteur de $(\nu_0 - \nu_{vib})^4$.

Une fois que la RSCS *absolue* du N_2 est mesurée, la RSCS *relative* des autres gaz peut alors être mesurée relativement par rapport à la valeur RSCS *absolue* du N_2, dénotée par RRSCS (Relative Raman Scattering Cross-Section) (ou σ). Pour comparer les RRSCS (σ) ayant été déterminées sous des longueurs d'onde d'excitation différentes, on peut les convertir à la RRSCS *indépendante de la longueur d'onde*, notée Σ. La relation entre Σ, σ et la longueur d'onde d'excitation est exprimée par l'Equation 1.2, dans laquelle Σ_i et σ_i sont les RRSCSs du mode de vibration i, ν_0 est le nombre d'onde absolue de la radiation d'excitation (cm^{-1}), *h* est la constante de Planck ($6.626 \cdot 10^{10}$ $cm \cdot s^{-1}$), *c* est la vitesse de la lumière ($cm \cdot s^{-1}$), *k* est la

constante de Boltzmann ($1.381 \cdot 10^{-16}$ erg·K^{-1}), et T est la température (K) (Schrötter and Klöckner, 1979; Garcia-Baonza et al., 2012).

$$\Sigma_i = \sigma_i \left[\frac{(\nu_0 - \nu_i)^{-4}}{(\nu_0 - 2331)^{-4}}\right] \times \left[1 - \exp\left(-\frac{hc\nu_i}{kT}\right)\right] \quad 1.2$$

Bien que la détermination de la concentration *absolue* (i.e., nombre exact de molécules présentes dans le volume diffusant) ne puisse pas aboutir par le biais de l'Equation 1.1 comme expliqué ci-dessus, la détermination de la concentration *relative* (fraction molaire) est toujours possible par l'utilisation de l'Equation 1.3 dans laquelle i est le nombre d'espèces présentes dans le mélange ; X_i, A_i, σ_i et ζ_i sont respectivement la fraction molaire (mol%), l'aire d'un (ou des) pic(s), la RRSCS et la fonction de réponse de l'instrument par rapport à l'espèce i donnée ; F_i est le facteur de quantification Raman incorporé σ_i et ζ_i (Wopenka and Pasteris, 1987). Le rapport du F-factor de deux constituants d'un système binaire donné peut être exprimé par l'Equation 1.4 ce qui ne dépend que des aires des pics et des proportions molaires.

$$X_i = \frac{\left(\frac{A_i}{\sigma_i \zeta_i}\right)}{\sum_1^i \left(\frac{A_i}{\sigma_i \zeta_i}\right)} = \frac{\left(\frac{A_i}{F_i}\right)}{\sum_1^i \left(\frac{A_i}{F_i}\right)} \quad 1.3$$

$$\text{F} - \text{factor ratio} = \frac{F_1}{F_2} = \frac{A_1 X_2}{A_2 X_1} \quad 1.4$$

Il est à noter que pour pouvoir mesurer la composition *relative* d'un mélange avec la meilleure précision possible, toutes les espèces considérées devraient être présentes dans une même phase de l'inclusion fluide. Aussi, les paramètres d'acquisition du spectre Raman (i.e., la focalisation et la position du spot laser, intensité, etc.) devraient être maintenus constants durant tout le temps d'acquisition de l'analyse. Comme chaque spectromètre Raman a sa propre valeur de la fonction de réponse instrumentale ζ_i, la calibration de cette dernière devrait être individuellement réalisée pour chaque spectromètre. Par rapport au spectromètre disponible dans notre laboratoire GeoRessouces (LabRam HR, Horiba Jobin-Yvon), la fonction de réponse de l'instrument ζ_i a été calibrée en éclairant l'appareil avec une lampe blanche de spectre d'émission continue connu (e.g., Raman Calibration Accessory, Kaiser Optical System, Inc) (Dubessy et al., 2012). Après la calibration de l'appareil, les valeurs de ζ_i vis-à-vis de chaque gaz sont donc considérées comme identiques. La variable ζ_i dans l'Equation 1.3 peut alors être éliminée.

Les valeurs de la RRSCS (σ) des gaz peuvent ensuite être déterminées par le biais de l'Equation 1.3 en analysant des mélanges de gaz (i.e., dans lesquels le gaz d'intérêt est mélangé avec N_2) par un spectromètre Raman bien calibré, et sous des conditions de mesure bien définies et contrôlées. Les RRSCS (σ) des gaz couramment rencontrés dans les fluides géologiques ont été fournies dans la littérature pour différentes longueurs d'onde d'excitation. Elles sont reportées avec une incertitude variant de 5 à 20% (Schrötter and Klöckner, 1979; Wopenka and Pasteris, 1986; Dubessy et al., 1989; Burke, 2001). D'ailleurs, il est à noter ici que les valeurs de Σ ne devraient être utilisées que pour comparer les valeurs de la RRSCS précédemment mesurées par des longueurs d'onde d'excitation différentes (Dubessy et al., 1989). Dubessy et al. (1989) ont constaté que l'utilisation des valeurs de Σ reportées dans la littérature, qui ont été converties (calculées) par l'Equation 1.2, pour la détermination de la composition *relative* (en utilisant l'Equation 1.3) peut peut-être entrainer des erreurs jusqu'à 2 mol% , d'après les résultats expérimentaux de Wopenka et Pasteris (1986, 1987). L'utilisateur devrait donc bien comprendre les différentes « types » de sections efficaces disponibles dans la littérature afin de les utiliser correctement pour avoir le moins d'erreur possible.

La limitation et l'incertitude de mesures de la composition *relative* par le biais de l'Equation 1.3 ont été évaluées en considérant plusieurs sources d'erreur potentielles (Pasteris et al., 1986; Wopenka and Pasteris, 1986, 1987; Seitz et al., 1987; Dubessy et al., 1989; Seitz et al., 1993, 1996). Premièrement, la différence (jusqu'à 10%) de la RRSCS publiées dans de nombreux articles est due à la sensibilité de la réponse des différents instruments ainsi qu'à la différence dans les configurations d'analyse choisies.

Deuxièmement, les valeurs de RRSCS (σ) disponibles dans la littérature ont été déterminées à faible pression (~1 - 15 bars) et à température ambiante, conditions loin d'être représentatives de la plupart des inclusions fluides naturelles. Quelques travaux ont montré une variation significative en fonction de la pression du rapport de RRSCS, et du rapport d'aire du pic ou de F-facteur (un paramètre de quantification incorporant la RRSCS et la fonction de réponse instrumentale ζ, cf. Equations 1.3 et 1.4) du CH_4/CO_2 (Wopenka and Pasteris, 1986; Seitz et al., 1987, 1996) ou du CH_4/N_2 (Chou et al., 1990; Seitz et al., 1993) (Figure 1-6). Des résultats expérimentaux montrent que ces rapports augmentent avec la pression (la densité), surtout à des faibles pressions (de 0 à ~ 100 bars), et puis restent stables jusqu'à 3000 bars (Fabre and Oksengorn, 1992). Cependant, l'auteur n'a pas précisé si l'aire du pic du N_2 présent dans l'atmosphère a été soustraite ou non (Seitz et al., 1993). Seitz et al. (1996) a aussi

remarqué que seule l'aire du pic du CO_2 à 1388 cm^{-1} (et la RRSCS correspondant) devrait être utilisée pour mesurer la proportion molaire (mol%) du mélange CO_2-CH_4 du fait que le rapport des aires des pics CH_4/CO_2 est presque constant (Figure 1-6b) lorsque la pression est > ~100 bars. Cette dernière remarque est cependant en désaccord avec Dubessy et al. (1989) qui ont souligné que l'utilisation de la somme de deux pics du CO_2 et la somme de ses RRSCSs pour mesurer la composition donne une meilleure exactitude.

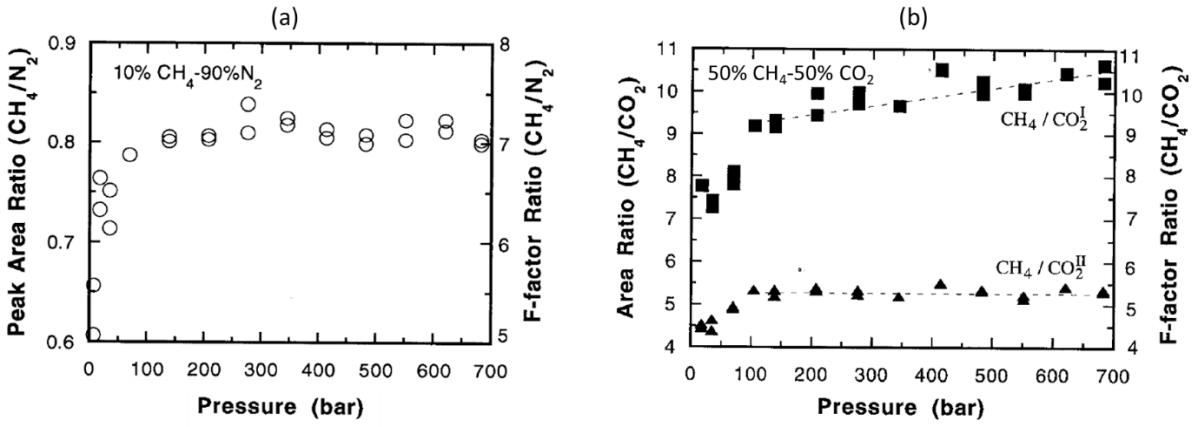

Figure 1-6: Variation du rapport d'aire du pic et de F-facteur du mélange (a) CH_4/N_2 et (b) CH_4/CO_2 en fonction de la pression. Les rapports d'aire du pic ou de F-facteur du CH_4 par rapport à celle du CO_2 ont été mesurées séparément pour deux pics du CO_2 (e.g., ν^+ à 1388 cm^{-1} et ν^- à 1285 cm^{-1}) (Seitz et al., 1993, 1996).

Troisièmement, la reproductibilité et la dérive du spectromètre Raman, i.e., la variation des résultats obtenus lors de la répétition de la mesure sur un même échantillon dans la même session d'analyse ou sur des périodes différentes. En général, selon les évaluations de Wopenka et Pasteris (1987), l'exactitude dans la mesure de la composition a pu atteindre un ordre de ~ ± 2 mol%. Cette dernière est assez faible et en général satisfaisante dans la plupart des cas des mesures quantitatives de la composition du mélange de gaz. Cependant, elle peut entraîner des erreurs importantes dans des mesures quantitatives de la pression ou de la densité (voir la section suivante).

Par ailleurs, les possibles effets de l'indice de réfraction, du champ interne et particulièrement de la composition sur la variation de la RRSCS (ou bien le rapport d'aire des pics ou le rapport de F-facteurs) ne sont toujours pas fermement confirmés. De plus, au vu de l'ancienneté des données disponibles dans la littérature (qui ont été déterminées il y a environ 50 ans et jamais réévaluées depuis) et de la sensibilité de ces paramètres à la réponse de l'instrument, il est donc nécessaire de réévaluer les valeurs de la RRSCS des gaz tout en

vérifiant l'effet de la composition et de la pression. Ceci permet de réduire encore l'incertitude de la RRSCS et donc d'améliorer la qualité des mesures lors de l'étude des inclusions fluides naturelles.

3. Données d'étalonnage du signal Raman des gaz N_2, CH_4 et CO_2

Il est connu que les paramètres du spectre Raman des molécules gazeuses (i.e., le décalage du pic, la variation de la largeur à mi-hauteur du pic ou du rapport d'aire/intensité) varient en fonction des conditions de mesure telles que la pression, la densité, la température et la composition (*PVTX*) (Dubessy et al., 2012; Long, 2002). En conséquence, la détermination des propriétés *PVTX* de gaz ou des mélanges gazeux est théoriquement possible une fois que le signal Raman des constituants analysés est correctement étalonné sous des paramètres instrumentaux bien définis et des conditions de mesure bien contrôlées. En effet, la variation des paramètres spectraux des gaz les plus communément rencontrés dans les fluides géologiques (e.g., CO_2, CH_4, N_2, …) en fonction de la pression, de la densité et/ou éventuellement de la température a fait l'objet de nombreuses études à partir des années 1970 (cf. les revues de Burke (2001) et Frezzotti (2012)). Les configurations, le domaine de densité et de pression utilisées dans les travaux remarquables réalisés depuis 1970s jusqu'à ce jour pour fournir les données d'étalonnage pour les systèmes CH_4, CO_2 et N_2, sont présentés dans la Table 1-2.

Wang and Wright (1973) ont étudié la dépendance à la densité de la position et de la largeur à mi-hauteur (FWHM, Full Width at Half Maximum) du pic du mode de vibration d'élongation symétrique ν_1 du N_2 (situé à ~ 2331 cm^{-1}) à travers des mesures expérimentales, sur une gamme de densité comprise entre 0 et ~ 600 amagat à 300 K (e.g., 0.04 et 0.58 $g{\cdot}cm^{-3}$ à 27 °C) (Figure 1-7). Les résultats obtenus montrent qu'il n'y a pas de différence entre les données déduites des spectres Raman polarisés et dépolarisés. D'ailleurs, ils montrent aussi une diminution linéaire de la position du pic du N_2 lors de l'augmentation de la densité (Figure 1-7a). L'amplitude du décalage du pic du N_2 pour la gamme de densité étudiée est environ 2 cm^{-1}. La FWHM du pic du N_2 diminue aussi avec l'augmentation de la densité (Figure 1-7b). Cependant, ces premières données de calibration sont fortement dispersées, indiquant une incertitude importante dans la mesure de la position exacte du pic du N_2.

Table 1-2: Récapitulation des études sur l'étalonnage du signal Raman des gaz CH_4, CO_2 et N_2.

Références	Gaz	Laser (nm)	T (°C)	ρ (g·cm^{-3})	P (bar)
Wang and Wright (1973)	N_2	488	27	0.04-0.058	-
Wang and Wright (1973)	CO2	488	40	0.03-1.05	-
Rosasco et al. (1975)	CH_4	514	-	-	-
Dhamelincourt et al. (1979)	CH_4	514	-160 à 30.2		1-70
Garrabos et al. (1980)	CO_2	514	40	0-0.66	-
Fabre and Couty (1986)	CH_4	514	20	0-4.5	0-3000
Fabre and Oksengorn (1992)	CH_4-N_2	488	22	-	0-3000
Seitz et al. (1993)	CH_4-N_2	514	23	-	0-700
Seitz et al. (1996)	CH_4-CO_2	514	23	-	0-700
Thieu et al. (2000)	CH_4	514	25	0.02-0.31	34-721
Hansen et al. (2001)	CH_4	514	-	-	0-400
Lu et al. (2007)	CH_4	532	22	-	1-650
Lin et al. (2007)	CH_4	514	22	0-0.29	1-600
Wang et al. (2011)	CO_2	532	21	-	22-357
Fall et al. (2011)	CO_2	514	-10 à 35	-	10-300
Zhang et el. (2016)	CH_4	532	25, 100, 160, 200	0-0.38	1-1500
Lamadrid et al. (2018)	CO_2-CH_4-N_2	514	22-23	-	10-500
Fang et el. (2018)	CH_4	532			
Sublett et al. (2019)	CO_2, CH_4, N_2	514	-160 à 45	-	
Wang et al. (2019)	CO_2	514/532	25 et 40	-	5-500

La variation de l'asymétrie du pic du N_2 a aussi été étudiée et évaluée en fonction de la densité (Musso et al., 2002, 2004). En effet, le pic du N_2 est légèrement asymétrique à faibles pressions (densité) (Bendtsen, 1974) et devient symétrique à partir d'environ 30 - 50 bars. Il n'est donc pas efficace d'utiliser ce paramètre pour des mesures quantitatives de densité ou de

pression. Parmi les paramètres spectraux mentionnés ci-dessus, la position du pic du N_2 semble donc être un des paramètres quantitatifs les plus prometteurs.

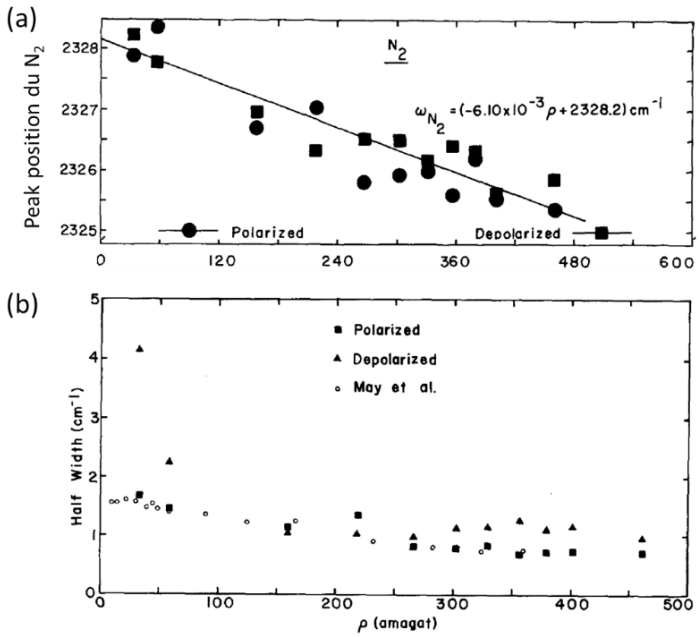

Figure 1-7: Variation (a) de la position du pic du N_2 (ν_1 à ~ 2331 cm^{-1}) et (b) de la largeur à mi-hauteur du pic du N_2 en fonction de la densité (modifié depuis Wang and Wright, 1973). Les analyses ont été faites avec une longueur d'onde du laser de 488 nm à 300 K.

La variation de la position du pic du mode de vibration d'élongation symétrique ν_1 du CH_4 (situé à ~ 2917 cm^{-1}) en fonction de la pression et/ou de la température a aussi été étudiée par de nombreux auteurs (Rosasco et al., 1975; Dhamelincourt et al., 1979; Fabre and Couty, 1986; Fabre and Oksengorn, 1992; Thieu et al., 2000; Lin et al., 2007a; Caumon et al., 2014; Zhang et al., 2016). En général, le pic ν_1 du CH_4 se décale vers les bas nombres d'onde lors de l'augmentation de la densité ou de la pression (Figure 1-8a). À une pression donnée, la position du pic du CH_4 diminue avec l'augmentation de la température (Figure 1-8b). L'amplitude du décalage du pic du CH_4 est assez importante, e.g., une diminution de ~ 7 cm^{-1} (de ~ 2918 à 2911 cm^{-1}) lorsque la densité augmente de ~ 0 à ~ 0.3 $g{\cdot}cm^{-3}$ (i.e. de ~ 0 à ~ 600 bars) (Figure 1-8a). Cette sensibilité avec la densité et la pression de la position du pic du CH_4 en font un paramètre spectral très prometteur pour le développement des densimètres ou des baromètres. Les courbes d'étalonnage publiées dans la littérature sont en général en bon accord au niveau de la tendance de variation de ce paramètre (Figure 1-8a). Pourtant, les densités calculées pour une position du pic donnée en utilisant ces courbes d'étalonnage sont bien différentes, avec un écart variant jusqu'à 0.1 $g{\cdot}cm^{-3}$.

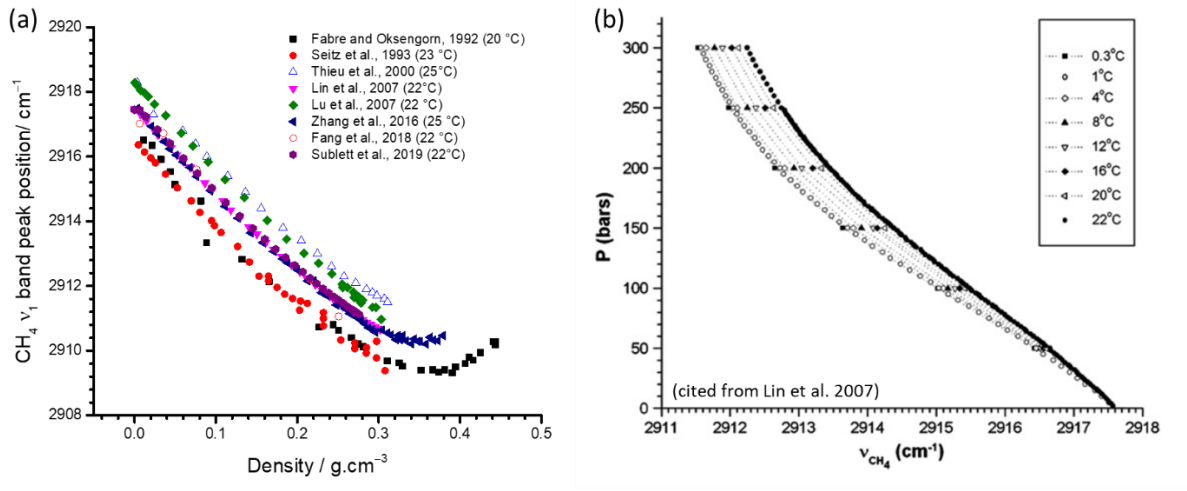

Figure 1-8: Variation de la position du pic du CH_4 (ν_1 à 2917 cm^{-1}) en fonction (a) de la densité ou (b) de la pression et température.

En effet, les courbes d'étalonnage fournies par différents auteurs sont reportées de manières parallèles (Figure 1-8a). Plusieurs raisons potentielles peuvent y être attribuées. Par exemple, la différence dans la procédure de la correction de la position « exacte » du pic du CH_4. En effet, Fabre and Couty (1986) ont utilisé une seule émission d'argon à 2912.8 cm^{-1} alors que Thieu et al. (2000) ont utilisé deux émissions du néon à 2852.6 et 2973.3 cm^{-1} (pour des mesures réalisées avec un laser d'excitation de 514 nm). Ces deux dernières valeurs légèrement différentes par rapport à celles utilisées dans l'étude de Lin et al. (2007a), e.g., 2851.38 et 2972.44 cm^{-1} respectivement, même si ces auteurs ont utilisé les mêmes émissions de référence. De même, Lu et al. (2007) ont utilisé une autre émission du laser He-Ne à 2992.52 cm^{-1} pour la correction de la position du pic du CH_4, etc. La température utilisée lors de ces études n'est pas non plus identique (Table 1-1) alors que l'effet de la température sur la variation des différentes paramètres spectraux n'est pas clairement établi dans la littérature.

Le parallélisme des courbes d'étalonnage publiées dans la littérature suggère également une erreur systématique de type instrumentale, i.e., la dérive spontanée du spectromètre et du système optique, la différence entre la réponse du spectromètre des différents laboratoires (même si les étalonnages ont été réalisés en utilisant le même type d'instruments et les même configurations). Tout cela signifie qu'on est vraiment à la limite de sensibilité de la technique. Pour des mesures quantitatives à plus haute précision, toutes les sources d'erreur (et leurs propagations d'erreur) devraient être prises en compte. Il est aussi nécessaire de réaliser un étalonnage du signal Raman propre à chaque laboratoire, ou de trouver un paramètre quantitatif

plus pertinent. Une procédure d'étalonnage plus efficace est aussi requise afin de pouvoir unifier des données d'étalonnage fournies par différentes équipes de chercheurs.

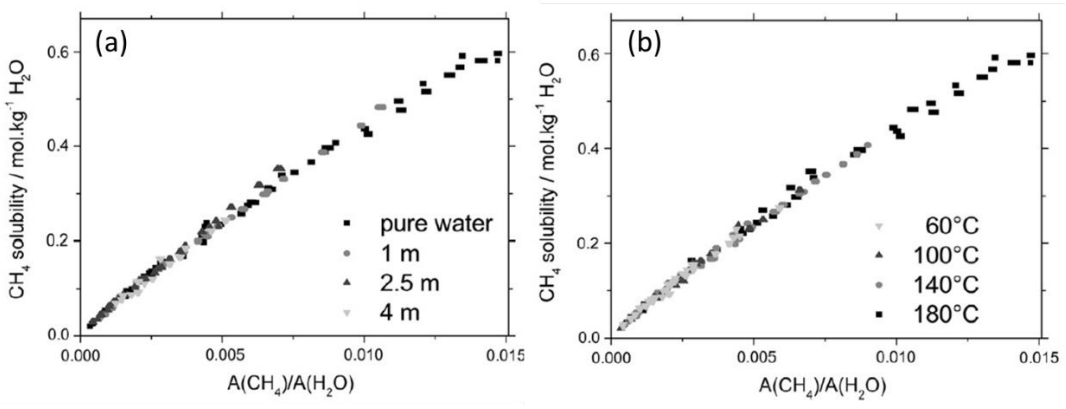

Figure 1-9: Variation de la solubilité du CH_4 dans l'eau (mol.kg^{-1} H_2O) en fonction (a) de la salinité (NaCl, mol.kg^{-1}) et/ou (b) de la température (°C). Les diagrammes sont cités depuis Caumon et al. (2014).

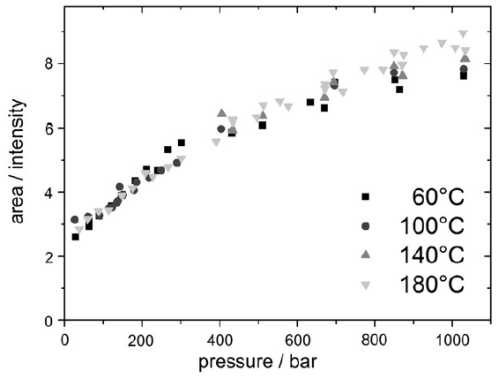

Figure 1-10: Variation du pic du CH_4 (ν_1 à 2917 cm^{-1}) en fonction de la pression et de la température (Caumon et al., 2014).

La quantité du CH_4 non-dissout ou dissout dans l'eau peut aussi être déterminée en étalonnant le signal de son pic. En effet, Caumon et al. (2014) ont établi des données d'étalonnage mettant en évidence la corrélation entre la solubilité du CH_4 (mol.kg^{-1} H_2O) et les rapports d'aires des pics de CH_4 et H_2O en fonction de la salinité et de la température (Figure 1-9). Ces étalonnages ont été ensuite appliqués avec succès à une série d'inclusions fluides naturelles piégées dans du quartz provenant de la partie externe des Alpes Centrales (Suisse). En général, les données d'étalonnage indiquent bien que le rapport d'aire CH_4/H_2O augmente de façon quasi-linéaire avec la concentration du CH_4. Cette dernière observation est en bon accord avec les travaux antérieurs (Dubessy et al., 2001; Lu et al., 2008; Faulstich et al., 2013).

L'effet de la salinité ou de la température sur ces courbes d'étalonnage n'a pas été observé (Caumon et al., 2014). Les résultats obtenus montrent que le rapport aire/intensité A/I augmente continuellement avec la pression, et est très peu sensible à la température jusqu'à 700 bars (Figure 1-10). Néanmoins, les auteurs ont également souligné une incertitude assez importante lors de l'utilisation du rapport A/I pour des mesures quantitatives, e.g., jusqu'à ~ ± 50 bars lorsque la pression totale est de ~ 400 bars. L'augmentation continue du FWHM du pic du CH_4 avec la pression a aussi été observée jusqu'à 3000 bars dans différentes études (Rosasco and Roedder, 1979; Fabre and Oksengorn, 1992; Zhang et al., 2016). Cependant, ce paramètre présente une reproductibilité modeste, ce qui entraine une différence importante entre les données reportées dans la littérature (Zhang et al., 2016). La FWHM du pic du CH_4, tout comme pour le N_2, n'a donc que rarement été utilisée pour des mesures quantitatives de haute précision.

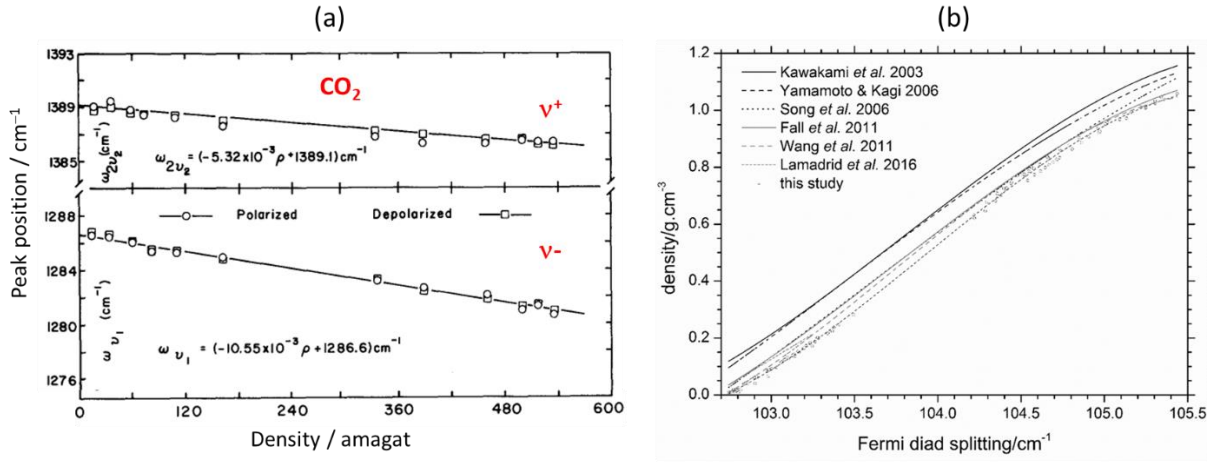

Figure 1-11: (a) Variation des deux pics principaux du CO_2 (ν^+ à 1388 cm^{-1} et ν^- à 1285 cm^{-1}) en fonction de la densité (amagat). Les mesures ont été réalisées à 40 °C par l'excitation d'un laser à 488 nm (Wright et Wang (1973)). (b) Variation du doublet de Fermi du CO_2 (cm^{-1}) en fonction de la densité ($g \cdot cm^{-3}$) et comparaison de certains densimètres publiés dans la littérature (Boulliung et al., 2017).

Vis-à-vis du CO_2, la variation de plusieurs paramètres spectraux de ses deux pics principaux (ν^+ à ~ 1388 et ν^- à ~ 1285 cm^{-1}) a été étudiée. Wright and Wang (1973) ont analysé du CO_2 à 40 °C (au-dessus du point critique du CO_2 pur à 31.05 °C) pour une gamme de densité comprise entre 15 et 534 amagat (e.g., entre 0.03 et 1.05 $g \cdot cm^{-3}$) (Figure 1-11a). Les résultats expérimentaux montrent que les deux pics ν^+ et ν^- du CO_2 se décalent linéairement vers les bas nombres d'onde lors de l'augmentation de la densité. Les amplitudes du décalage de ces pics ν^+ et ν^- sont 3.3 cm^{-1} et 5.9 cm^{-1}, respectivement. Comme les amplitudes du décalage de

ces deux pics du CO_2 ne sont pas identiques, le doublet de Fermi du CO_2 (i.e., l'écart entre ces deux pics, dénoté Δ) varie en fonction de la densité (pression).

La variation du Δ en fonction de la pression (densité) et/ou de la température ainsi que la bonne reproductibilité dans la mesure du Δ a aussi été confirmée par de nombreux groupes de recherche. En général, le Δ augmente avec l'augmentation de la densité (ou pression) (Figure 1-11b) et de la température (Wang et al., 2011, 2019; Yuan et al., 2017). Plusieurs densimètres du CO_2 pur basés sur la variation du Δ ont été établis (Figure 1-11b) (Garrabos et al., 1980, 1989; Rosso and Bodnar, 1995; Kawakami et al., 2003; Yamamoto and Kagi, 2006; Wang et al., 2011; Fall et al., 2011; Yuan et al., 2017; Wang et al., 2019). Il est à noter que les courbes d'étalonnage du Δ du CO_2 publiées dans la littérature sont légèrement décalées l'une par rapport à l'autre (Figure 1-11b), c'est-à-dire que le même phénomène est constaté pour les différents densimètres fondés sur la variation de la position du pic du CH_4 (Figure 1-8a). La variation du rapport A/I de ces deux pics ν^+ et ν^- du CO_2 a aussi été calibrée, et peut être utilisée pour la détermination de la densité des inclusions fluides (Garrabos et al., 1980). Cependant, les résultats dérivés à partir de la variation de ce paramètre possèdent une incertitude beaucoup plus élevée que ceux dérivés à partir de la variation du Δ (Garrabos et al., 1980).

Il est important de noter que tous les paramètres spectraux dépendent également de la composition du mélange de gaz analysé en raison de la modification des interactions moléculaires. En effet, l'influence de la composition sur la variation des paramètres spectraux a été observée depuis longtemps pour certains mélanges à travers des analyses expérimentales, e.g., le mélange CO_2-CH_4 (Seitz et al., 1996, 1987), le mélange CH_4-N_2 (Fabre and Couty, 1986; Chou et al., 1990; Fabre and Oksengorn, 1992; Seitz et al., 1993) ou les mélanges du CH_4 avec N_2, H_2 ou Ar (Seitz et al., 1993) (Figure 1-12). Ces études montrent clairement que l'effet de la présence d'une autre substance sur la variation des paramètres spectraux est significatif et ne peut pas être négligé, surtout pour une analyse quantitative requérant une haute précision telle que l'étude des inclusions fluides. Ainsi, toutes les données d'étalonnage, qui ont été établies sans évaluation de l'effet de composition, ne sont valides que pour les systèmes de gaz pur. L'application de ces étalonnages aux inclusions fluides naturelles, qui contiennent des mélanges gazeux, peut entrainer des erreurs importantes. Néanmoins, très peu de travaux ont pu fournir des étalonnages complets du signal Raman qui couvrent toutes les gammes de composition de mélanges gazeux binaires ou ternaires à CH_4, CO_2 et N_2 avec une incertitude satisfaisante.

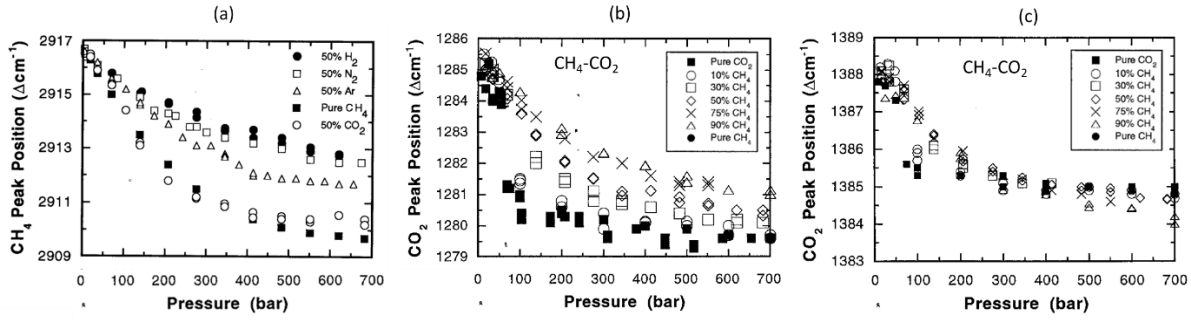

Figure 1-12 : (a) Comparaison de la variation de la position du pic ν_1 du CH_4 en fonction de la pression dans le CH_4 pur et dans des mélanges binaires à une proportion 1:1 de CH_4-H_2, CH_4-N_2, CH_4-Ar et CH_4-CO_2. (b) et (c) Variation de la position du pic ν_1 du CH_4 en fonction de la pression et de la proportion molaire dans les mélanges CH_4-N_2 et CH_4-CO_2, respectivement (Seitz et al., 1993, 1996).

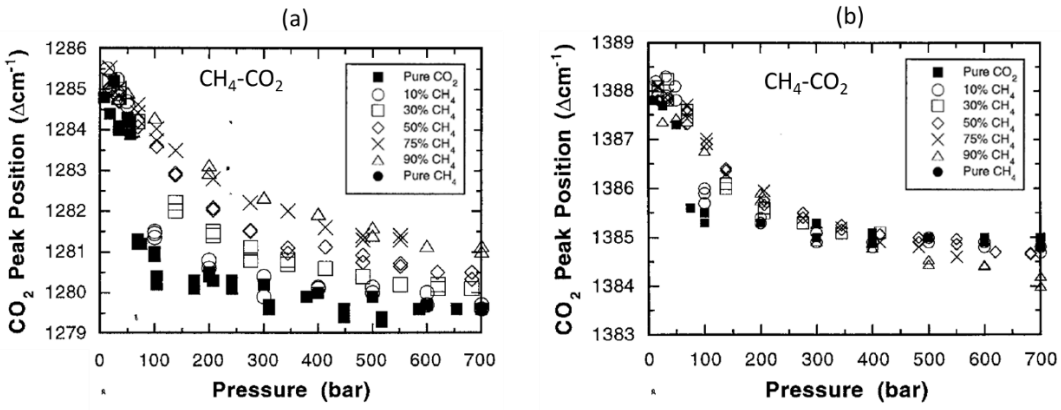

Figure 1-13 : Variation de la position du pic (a) ν^- et (b) ν^+ du CO_2 en fonction de la pression et de la proportion molaire dans les mélanges CH_4-CO_2 (Seitz et al., 1996)

Parmi les données de calibration ayant pris en compte l'effet de la composition, celles publiées dans Seitz et al. (1993, 1996) sont les plus complètes établies pour les mélanges binaires CH_4-N_2 et CH_4-CO_2 (Figure 1-12 et Figure 1-13). Dans ces études, l'auteur a étudié l'évolution des différents paramètres spectraux en fonction de la variation à la fois de la pression (densité) et de la composition de mélanges CH_4-N_2 et CH_4-CO_2 sur toute la gamme de composition. Leurs résultats expérimentaux ont montré non seulement l'effet significatif de la composition chimique (Figure 1-12a), mais également de la variation de la proportion molaire des constituants du mélange (Figure 1-12b et c). Concrètement, les variations de la position du pic ν_1 du CH_4 dans les mélanges CH_4-N_2 et CH_4-CO_2 sont complètement différentes (Figure 1-12b et c). En effet, l'amplitude du décalage du pic ν_1 du CH_4 augmente graduellement avec l'augmentation de la pression totale et de la diminution de la proportion molaire du CH_4 dans le mélange CH_4-N_2 (Figure 1-12b). Dans les mélanges CH_4-CO_2, la variation du pic ν_1 du

CH_4 est bien moins affectée lors de la variation de la teneur en CO_2 que dans le cas présenté dans la Figure 1-12c.

De manière similaire, la variation de la position de deux pics principaux du CO_2 (ν^- et ν^+) en fonction de la pression et de la composition du mélange CH_4-CO_2 a aussi été étudiée et reportée dans Seitz et al. (1996). Les pics ν^+ et ν^- se comportent différemment lors de la variation des proportions molaires du mélange CH_4-CO_2 (Figure 1-13a et b). D'autres paramètres spectraux tels que le rapport de la FWHM du pic du CH_4/N_2 ou CH_4/CO_2, le rapport A/I du pic ν_1 du CH_4 et du N_2 ont été également étudiés en fonction de la pression et/ou de la densité (Seitz et al., 1993, 1996). En général, les résultats expérimentaux montrent que ces paramètres (FWHM, rapport A/I) sont bien moins efficaces (moins bonne reproductibilité) que la variation de la position du pic ν^+ et ν^- ou du doublet de Fermi Δ pour des mesures quantitatives de pression ou de densité.

Bien que la tendance de la variation des paramètres spectraux du CH_4, CO_2 et N_2 dans les mélanges CH_4-CO_2 et CH_4-N_2 soient bien confirmée dans les travaux de Seitz et al. (1993, 1996), leurs données d'étalonnages sont, cependant, très dispersées (Figure 1-12 et Figure 1-13). L'utilisation de ces données d'étalonnage pour déterminer la pression (densité) des inclusions fluides peut donc entrainer des résultats aberrants. D'ailleurs, la variation du doublet de Fermi Δ, qui est le paramètre le plus utilisé pour l'établissement des densimètres (ou des baromètres) pour le CO_2 pur, n'est jamais reportée pour les mélanges CH_4-CO_2. A notre connaissance, les données d'étalonnage complètes pour les mélanges binaires CO_2-N_2 et ternaires CH_4-CO_2-N_2 ne sont pas encore disponibles. Lamadrid et al. (2018) a récemment reporté la variation des pics du CH_4, CO_2 et N_2 dans le mélange ternaire, mais pour une seule composition (e.g., 15, 15, 75 mol% pour CH_4, CO_2 et N_2, respectivement), ce qui ne couvre pas tous les cas possibles des fluides géologiques. L'objectif de ce projet est donc de fournir des étalonnages complets du signal Raman de CH_4, CO_2 et N_2 pour toutes les compositions des mélanges binaires et ternaires avec la meilleure incertitude possible.

analytical chemistry

Article

Cite This: *Anal. Chem.* 2019, 91, 14359−14367

pubs.acs.org/ac

Chapter 2: Quantitative measurements of composition, pressure, and density of micro-volumes of CO_2-N_2 gas mixtures by Raman spectroscopy

Article soumis le 20 juin 2019 et publié le 17 octobre 2019

dans Journal of Analytical Chemistry.

DOI : /10.1021/acs.analchem.9b02803

Van-Hoan Le* [a], Marie-Camille Caumon [a], Alexandre Tarantola [a], Aurélien Randi [a], Pascal Robert [a] and Josef Mullis [b]

[a] *Université de Lorraine, CNRS, GeoResssources Laboratory, BP 70239, F-54506 Vandoeuvre-lès-Nancy, France*

[b] *Department of Environmental Sciences, University of Basel, Bernoullistrasse 32, 4056, Basel, Switzerland*

Chapter 2, entitled "*Quantitative measurements of composition, pressure and density of micro-volumes of CO_2-N_2 gas mixtures by Raman spectroscopy*", has been published in the revue of Analytical Chemistry on 17 October 2019.

In the previous chapter (**Chapter 1**), the calibration data of the Raman signal of gases (CO_2, CH_4, and N_2) published in the literature since the 1970s has been collected and reviewed (i) to have a global vision about selecting spectral parameters the most adequate for quantitative measurements (i.e., the variation of peak positions) and (ii) to point out some problems that are still questionable or unclear, e.g., the effect of composition, pressure, density and/or temperature, as well as the influence of the instrumental configurations on the variation behavior of different spectral parameters, e.g., the RRSCS and the peak position.

This chapter is dedicatedly focused on studying the variation of the spectral parameters of CO_2-N_2 mixtures, whose calibration data has never been published in the literature so far. A complete experimental protocol, from (i) the gas mixture preparation and (ii) the verification of the composition by gas chromatography, to (iii) the performance of the *in-situ* Raman analyses of gas mixtures and the data processing, is successively described.

The CO_2-N_2 mixtures are thereby analyzed under controlled *PTX* conditions (e.g., over 5-600 bars at 22 or 32 °C) to figure out the most reliable parameters for the development of densimeters and barometers. The effects of composition, pressure, and density on the variation of Raman spectra of CO_2 and N_2 were accurately studied. New regression polynomial calibration equations are given with their respective accuracy for different *PVX* domains. The obtained calibration data is also validated with an application to natural fluid inclusions by comparing the obtained Raman results with those derived from microthermometry data.

Abstract

Quantitative analysis of gases by Raman spectroscopy is based on relative Raman scattering cross-sections (RRSCS) and the evolution of different spectral parameters (peak position, peak area, peak intensity, etc.). However, most of the calibration data were established at low pressure (low density) and without evaluating the effect of the composition. Using these data may lead to considerable errors, especially when applied to gas mixtures at high pressure as found in natural fluid inclusions. The aim of this study is to reevaluate the RRSCS of CO_2 and to establish new calibration data based on the variation of CO_2 Fermi diad splitting as a function of pressure (density) and composition over a pressure range of 5 to 600 bars at 22 and 32 °C. A high-pressure optical cell system (HPOC) and a heating-cooling stage were used for Raman in-situ analyses at controlled *PTX* conditions. Our experimental results show that the RRSCS of CO_2 varies slightly with pressure but can be considered constant over the studied pressure range. It can be used to measure the proportion of CO_2 in gas mixtures with an uncertainty of about ± 0.5 mol%. Different polynomial equations were provided to calculate pressure and density of CO_2-N_2 gas mixtures with an uncertainty of ~ ± 20 bars or 0.01 g.cm^{-3}. A comparison of *PVTX* properties of natural CO_2-N_2 fluid inclusions hosted in quartz from the Central Alps (Switzerland) obtained by Raman measurement and as derived from phase transition temperatures by microthermometry experiments shows comparable values.

Keywords: Raman spectroscopy, Mixtures, Fluids, Calibration, Phase Transition.

1. Introduction

The exploration of the Raman effect by C.V Raman in 1928 provided a new way for non-destructive analyses of materials under different phase states (solid, liquid and gaseous) to get qualitative and quantitative information (after establishing calibration data). The sensitivity of Raman spectroscopy covers a wide concentration range, down to very low concentration (D'Orazio and Hirschberger, 1983; Petrov and Matrosov, 2016), even to sub-ppm levels (Hanf et al., 2014, 2015). Raman spectroscopy has been widely used for gas analysis in various domains of investigation such as monitoring of polluted air (Inaba and Kobayasi, 1969) or automobile exhaust gases (D'Orazio and Hirschberger, 1983), fuel gas analysis (Kiefer et al., 2008; Buric et al., 2009; Petrov et al., 2019), diagnosis and monitoring of disease states by human breath analysis (Hanf et al., 2014, 2015; Bögözi et al., 2015), controlling and monitoring of fruit ripening (Jochum et al., 2016), analyzing of gas bubbles appearing as defects inside industrial glasses to optimize production process (Pedeche et al., 2003). Other applications can also be found in the field of environmental gas sensing, e.g. monitoring of geological storage site of CO_2 (Taquet et al., 2013), investigation of biological and/or geochemical gas exchange and migration processes within the different compartment (groundwater, subsurface, surface, atmosphere) (Jochum et al., 2015, 2017; Keiner et al., 2015; Sieburg et al., 2017, 2018). All applications mentioned above relate exclusively to the analysis of immense and/or small volume of gas at relatively low pressure (< few dozen bars). The present study is dedicated to another case of extreme conditions: the analysis of gas mixtures in micro-volumes at relatively high pressure (up to 600 bars). The main application is the study of fluid inclusions naturally trapped in minerals.

Fluid inclusions (FIs) are small cavities in minerals containing a micro-volume of a geological fluid trapped during or after crystal growth. They are the most reliable relicts recording information about the conditions of crystal formation as well as of paleo-fluid circulations. A quantitative knowledge (composition, pressure, and density) of these fluids provides key information to better understand geological processes, to reconstruct the conditions of paleo-fluid circulations and thereafter for further application such as natural resources exploration (Roedder, 1984). CO_2 and N_2 are among the most common gases present in a large variety of geological fluids (Roedder, 1984; Van den Kerkhof and Thiéry, 2001).

The observation of phase transitions during microthermometry experiments is currently the standard method to investigate fluid inclusion properties. However, some limitations appear

when FIs are of small size (< 5 µm), of complex composition or of low density without any observable phase transitions (Rosso and Bodnar, 1995; Yamamoto et al., 2002, 2007; Kawakami et al., 2003; Song et al., 2009). Raman spectroscopy is a complementary method to microthermometry as it can offer fast (from a few seconds to a few minutes), high resolution (down to ~ 1 μm^2) and simultaneous non-destructive, qualitative and quantitative analyses (Burke, 2001; Dubessy et al., 2012; Frezzotti et al., 2012). Several applications of Raman spectroscopy dedicated to the investigation of FIs have been carried out by different research teams since the 1970s (cf. reviews by Burke (2001) and Frezzotti et al. (2012)). The determination of the composition, pressure, and density of gas mixtures using Raman spectroscopy requires the knowledge of the Raman scattering cross-section (RSCS) and the behavior of Raman spectral features (peak position, peak area/intensity ratio…) as a function of pressure, density, temperature, and composition (Burke, 2001; Frezzotti et al., 2012).

RSCS is a specific parameter related to the probability of Raman scattering effect for each vibration. It can be used to determine the concentration of molecules (Wopenka and Pasteris, 1986). Due to the difficulty of the determination of absolute values of RSCS, only that of N_2 was carefully determined by different techniques (Fouche and Chang, 1971b; Penney et al., 1972; Fenner et al., 1973; Schrötter and Klöckner, 1979). Relative RSCS (RRSCS) values of common gaseous species found in fluid inclusions (CO_2, CO, CH_2, O_2, H_2S…) were then measured relatively to RSCS of N_2 with an accuracy varying from 5 to 20 % (Burke, 2001; Schrötter and Klöckner, 1979). However, all published data of RRSCS were determined at room temperature and 1 - 5 atm whereas, according to Wopenka et Pasteris (1986) and Seitz et al (1993, 1996). RRSCS may not just vary as a function of wavelength and temperature (Schrötter and Klöckner, 1979), but also as a function of pressure and composition due to changes in molecular interaction (Dubessy et al., 1989). Moreover, although many improvements in Raman instruments were made, the RRSCS data were never reevaluated since the 1970s.

The variations of the peak positions of Raman bands of N_2 and CO_2 as a function of pressure (or density) were also separately investigated (Wang and Wright, 1973; Wright and Wang, 1974; Garrabos et al., 1989; Rosso and Bodnar, 1995; Kawakami et al., 2003; Song et al., 2009; Fall et al., 2011; Wang et al., 2011; Lamadrid et al., 2018), showing the applicability for pressure and density monitoring. Indeed, the Fermi diad splitting (distance between the two main peaks) of CO_2 was used to develop densimeters for pure CO_2 or CO_2-rich fluid inclusions (Garrabos et al., 1989; Rosso and Bodnar, 1995; Kawakami et al., 2003; Yamamoto and Kagi,

2006; Song et al., 2009; Fall et al., 2011; Wang et al., 2011; Lamadrid et al., 2017). Nevertheless, the variation of peak positions as well as of CO_2 Fermi diad splitting are subject to change as a function of pressure, density, temperature (Fall et al., 2011; Wang et al., 2011) but also composition (Seitz et al., 1993, 1996; Wang et al., 2011). The inappropriate use of calibration data obtained from pure gas for analyzing gas mixtures may, therefore, lead to an over/underestimation of density (Wang et al., 2011) or pressure (Lamadrid et al., 2018). Thus, the effect of composition, pressure, density, and temperature on Raman spectral features should be simultaneously taken into account upon any quantitative analysis. The experimental data of Seitz et al. (1993, 1996) revealed the variation trends of different Raman spectral features of CO_2 and N_2 as a function of composition (when mixed with CH_4) but the results were quite scattered due to the use of low spectral resolution (~ 5 cm^{-1}). Consequently, no robust calibration with uncertainty analysis was given.

The present work aims (1) to reevaluate the dependence of RRSCS of CO_2 on pressure and composition by using nowadays performance instruments and (2) to establish a new Raman calibration methodology for composition, pressure, and density measurement of any CO_2-N_2 gas mixtures. Data acquisition was done thanks to the combination of an improved HPOC system (Chou et al., 2005; Chou, 2012; Caumon et al., 2014) and a heating-cooling stage to control the *PT* conditions during experiments and to collect numerous data points for statistical purposes. CO_2-N_2 gas mixtures of different compositions were analyzed by Raman spectroscopy at 22 °C (room temperature) and 32 °C (just above the critical point of pure CO_2 in order to avoid any V-L phase transition for any CO_2-N_2 mixture composition) over the pressure range 5-600 bars. The relationships between the variation of Raman spectral parameters with pressure (or density) and composition were evaluated to determine the most reliable quantification parameters. Finally, the composition, density, and pressure of natural FIs hosted in quartz from the Central Alps (Switzerland) (Mullis et al., 1994) were obtained with these calibration data, and subsequently compared with microthermometry data.

2. Materials and methods

2.1. Gas mixtures preparation

CO_2-N_2 binary mixtures of different compositions were prepared from high-purity commercial N_2 and CO_2 gases (99.99 % purity, Air Liquide™) at low pressure (< 10 bars) by a gas mixer (GasMix AlyTech™). They were subsequently compressed up to 120 - 150 bars using a home-made compressor system and stored in a stainless-steel reservoir. The

composition of the prepared gas mixtures was controlled by gas chromatography (GC) to ensure there was no significant modification during the compression step. The GC was calibrated by measuring several times a commercial CO_2-N_2 gas mixture (Air Liquide^{TM}), yielding a standard deviation of about 0.4 mol%. The final composition of the prepared gas mixtures was the average of three GC measurements with a standard uncertainty $\sim \frac{0.4}{\sqrt{3}} \approx 0.3$ mol% (1σ). The compositions of the CO_2-N_2 gas mixtures used in this study were 10.5, 30.1, 50.3, 60.9, 70.5, 80.1, and 88.6 mol% CO_2.

2.2. Pressurization system

The reservoir containing the gas mixture was connected to an improved HPOC system, which consists of several valves, stainless steel microtubes and a pump Figure 2-1 (Chou et al., 2005; Chou, 2012; Caumon et al., 2014). One end of the HPOC system was equipped with a manual screw pressure generator. The other end was coupled with a fused silica capillary (FSC) of 200 µm of internal diameter sealed at one end by a hydrogen flame (Caumon et al., 2014, 2013). Two pressure transducers were set on the fixed part and on the movable part of the HPOC system to monitor pressure (± 1 bars) inside the whole system. The FSC was set on a customized heating-cooling stage (Linkam CAP500) previously calibrated by measuring the triple point of distilled water (0.0 °C) and of a pure CO_2 standard sample (–56.6 °C) to maintain the temperature at 22.0 and 32.0 ± 0.1 °C. The system was evacuated for a minimum of 30 minutes to remove any other gases before loading the investigated gas mixture. Thereby, the gas mixtures were analyzed by Raman spectroscopy through the microcapillary at controlled *PT* conditions.

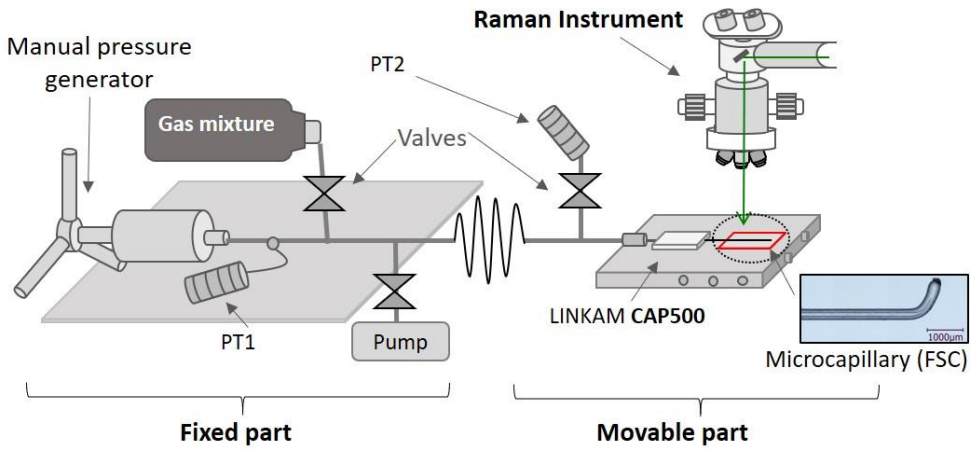

Figure 2-1: Sketch of the HPOC system coupled with a transparent fused silica capillary (FSC) set on a Linkam CAP500 heating-cooling stage. The system consists of a fixed part composed of a manual

pressure generator, a pressure transducer (PT1), valves, microtubes, and a pump to purge the system. The movable part connects the system with the heating-cooling stage. It is also equipped with valves and another pressure transducer (PT2).

2.3. Raman instruments and analysis

Raman measurements were performed using a LabRAM HR spectrometer (Horiba Jobin-Yvon®) equipped with an 1800 groove·mm^{-1} grating with an aperture of confocal hole and slit set at 1000 µm and 200 µm, respectively, giving a spectral resolution of about 1.67 cm^{-1} (fitted FWHM of Neon peak at 2348 cm^{-1}). The excitation radiation was provided by an Ar^+ laser (Stabilite 2017, Spectra-Physics) at 514.53 nm with a power of 200 mW, focused on the FSC by a ×20 objective (Olympus, NA = 0.4). Each measurement was repeated six times successively at the same *PTX* conditions for statistical purposes. A spectrum was recorded before loading any gas mixture into the microcapillary to measure the contribution of atmospheric N_2 for peak area correction (1989). The same configuration (excitation wavelength, hole, slit, grating) was used for Raman analyses of natural FIs, except the use of a ×50 objective (Olympus, NA = 0.5). To minimize the error due to the subtraction of the N_2 peak area, the intensity of the N_2 band within FI should be 3 or 4 times higher than that of ambient N_2. Thus, the acquisition time ranged from 5 to 30 seconds per accumulation (with 10 accumulations per measurement) depending on the density, size, shape, and depth of FIs.

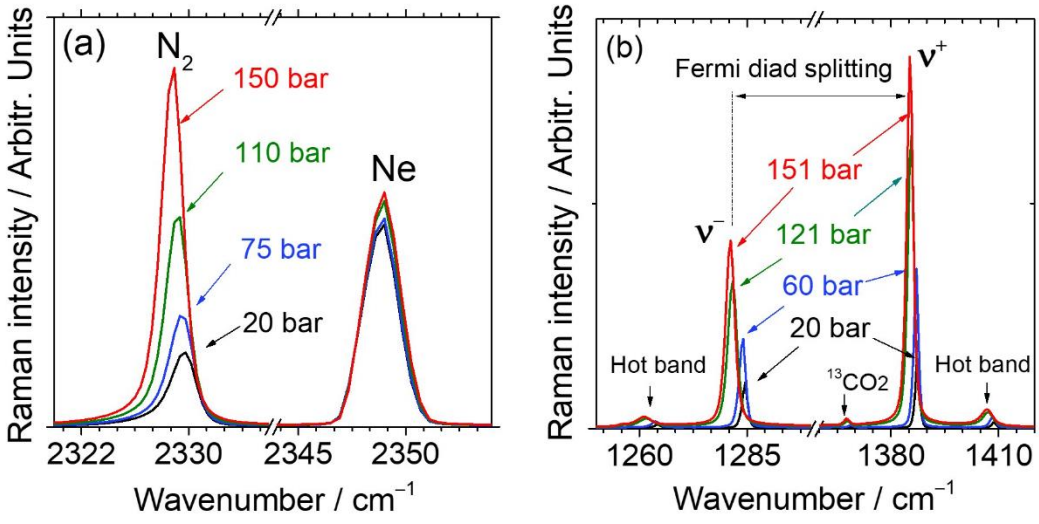

Figure 2-2: Evolution of (a) N_2 and (b) CO_2 Raman spectra with pressure. Both gases show a downshift with increasing pressure. The signal of neon (Ne) was simultaneously recorded with N_2 spectra for wavenumber calibration.

The Raman spectrum of N_2 characterized by a peak at ~ 2331 cm^{-1} was simultaneously recorded with Ne peak at ~ 2348 cm^{-1} (Figure 2-2a) for wavelength calibration (McCreery, 2005). As the N_2 band is not symmetrical (due to the asymmetric distribution of $\Delta J = 0$ transition in the Q-branch (Bendtsen, 1974)), the spectra of N_2 were fitted by an asymmetrical Gaussian-Lorentzian function using the peak fitting tool of LabSpecs 6 software (Horiba) after baseline subtraction. The peak position of N_2 was then corrected by that of Ne using Equation 2-1, where ν_{N_2} and ν_{Ne} are the fitted peak positions of N_2 and Ne, respectively, and 2348.4318 cm^{-1} the reference peak position of Ne cited from NIST webbook (Kramida et al., 2018).

$$\nu_{N_2(cor)} = \nu_{N_2} + (2348.4318 - \nu_{Ne}) \qquad 2\text{-}1$$

CO_2 has four vibrational modes: symmetrical stretching (ν_1), asymmetrical stretching (ν_3) and a doubly degenerated bending mode (ν_{2a} and ν_{2b}). Only the ν_1 mode (~ 1333 cm^{-1}) is Raman-active. However, the experimental spectrum of CO_2 presents two strong bands because of Fermi resonance (Fermi, 1931) taking place between the excited vibrational states ν_1 and the first overtone of ν_2 ($2\nu_2 = 2 \times 667 = 1334\ cm^{-1}$). As these two excited states have nearly the same energy level, they perturb each other and cause a division into two peaks at higher (1388 cm^{-1}) and lower (1285 cm^{-1}) wavenumbers. This phenomenon is known as the Fermi diad splitting, resulting in two bands denoted ν^+ and ν^-, respectively. Moreover, the spectrum of CO_2 has also two low-intensity bands at 1409 cm^{-1} and 1265 cm^{-1}, known as hot bands. Another weak band at 1370 cm^{-1} corresponds to the signal of $^{13}CO_2$ (Figure 2-2b). Extended interpretation of spectral features of CO_2 can be found in literature (Placzek, 1934). Raman spectra of CO_2 were fitted by symmetric Gaussian-Lorentzian function using LabSpec 6 (Horiba) after baseline subtraction. Final values of spectral parameters were the mean of 6 measurements, yielding an uncertainty of about ± 0.4 % (1σ) for peak area values, about ± 0.01 cm^{-1} (1σ) for peak position and ± 0.015 cm^{-1} for CO_2 Fermi diad splitting (1σ) (see Supporting Information for detailed uncertainty calculations).

The Raman spectra of CO_2 and N_2 were recorded in two different spectral ranges (1100 to 1580 cm^{-1} and 2100 to 2525 cm^{-1}, respectively) with different instrumental efficiency of the spectrometer (Dubessy et al., 2012). All the Raman spectra were thus corrected using an ICS function (Intensity Correction System) integrated into LabSpec6 software to normalized instrument response with wavelength. The calibration was done using a white lamp of known emission (Raman Calibration Accessory, Kaiser Optical Systems, Inc.) (Dubessy et al., 2012).

As a result, the instrumental efficiencies at the wavelength of CO_2 and N_2 peaks (ζ_{CO_2} and ζ_{N_2}) can be considered identical.

2.4. Microthermometry measurements

Microthermometry is a standard method to determine *PVTX* proprieties of natural FIs. It is based on the determination of phase transition temperatures of geological fluid trapped within inclusions. In the present work, microthermometry measurements of natural FIs were made using a THMSG600 heating-cooling stage coupled with an Olympus BX50 microscope. The stage was calibrated at ± 0.1 °C using standard inclusions against the melting point of pure CO_2 (–56.6 °C) and of pure H_2O (0.0 °C). Herein, the melting temperature T_m(car) and the homogenization temperature T_h(car) of the volatile carbonic phase containing the CO_2-N_2 mixtures trapped within FIs were measured. These phase transition temperatures were then used to determine the composition and density of FIs using the *VX* diagram of Thiéry et al. (1994a).

2.5. GERG-2004 equation of state

GERG-2004 equation of state (EoS) is used to calculate (i) the pressure within natural FIs at a given temperature from density-composition properties derived from microthermometry results and (ii) the density of gas mixtures during Raman measurements (for a given composition, pressure and temperature). The GERG-2004 EoS is known as the most accurate available EoS at the *P* and *T* conditions of interest. Concerning the CO_2-N_2 gas mixtures, the EoS is fitted from 823 experimental data points, covers the entire composition range (from 1 to 98 mol% in CO_2) and large pressure and temperature ranges (1 to 2740 bars and –63 to 400 °C). The uncertainties in density are shown to be less than 0.1 % when pressure < 350 bars or less than 0.5 % when pressure < 700 bars in the vapor region, about 0.1 - 0.5 % in the liquid region and less than 3 % in the two-phase region. This model is integrated into REFPROP software (Lemmon et al., 2013).

2.6. Natural fluid inclusions

A prismatic quartz crystal (Mu 147.2) found in late Alpine tension gashes from the Central Alps (Switzerland) (Mullis et al., 1994) was used for its CO_2-N_2 natural fluid inclusions. At room temperature, the 2 to 30 µm large FIs are either monophasic (liquid CO_2+N_2) or biphasic (liquid H_2O + vapor CO_2-N_2) (Figure 2-3). 15 FIs from 4 different zones were selected to be analyzed by Raman spectroscopy and microthermometry for comparison.

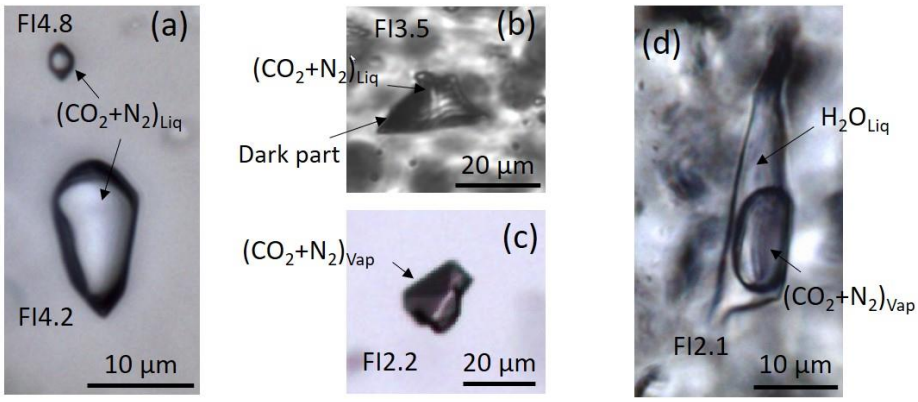

Figure 2-3: Examples of selected FIs of sample Mu 147.2 (transmitted plane-polarized light at room temperature): (a), (b) and (c) monophasic FIs from zones 4, 3 and 2 containing a CO_2-N_2 liquid phase; (d) two-phase FI containing H_2O (liquid) and a bubble of CO_2-N_2 vapor.

3. Results and discussion

3.1. Mixture composition: Evaluation of the RRSCS CO_2

The RRSCS of the two main bands of CO_2 (σ_{CO_2}) were calculated at different composition and pressure conditions with the use of Equation 2-2 (Wopenka and Pasteris, 1986), where A_{CO_2} is the peak area of ν^+ or ν^- band, A_{N_2} is the peak area of the N_2 band, C_{CO_2} and C_{N_2} are the concentration (mol%) of CO_2 and N_2, respectively.

$$\sigma_{CO_2} = \frac{A_{CO_2} \cdot C_{N_2}}{A_{N_2} \cdot C_{CO2}} \qquad 2\text{-}2$$

Figure 2-4a shows the variation of the RRSCS of the upper band (σ_{ν^+}) and the lower band (σ_{ν^-}) as a function of pressure and composition. Both RRSCS are somewhat perturbed at low pressure (< ~ 80 bars), probably due to a significant change of molecular interaction effect (Seitz et al., 1993, 1996). Above ~ 80 bars, σ_{ν^+} increases slightly whereas σ_{ν^-} decreases slightly with increasing pressure. Indeed, from 5 to 600 bars, the RRSCS value only increases by 0.05 (σ_{ν^+}) or decrease by 0.1 (σ_{ν^-}), resulting in a difference of only ~ 0.2 mol% CO_2. Figure 2-4b shows the evolution of the sum of the two RRSCS of CO_2 ($\sigma_{\nu^+} + \sigma_{\nu^-}$) as a function of pressure and composition. A slight perturbation was also observed at a low pressure-range. Above 80 bars, it remains nearly constant up to 600 bars for every composition.

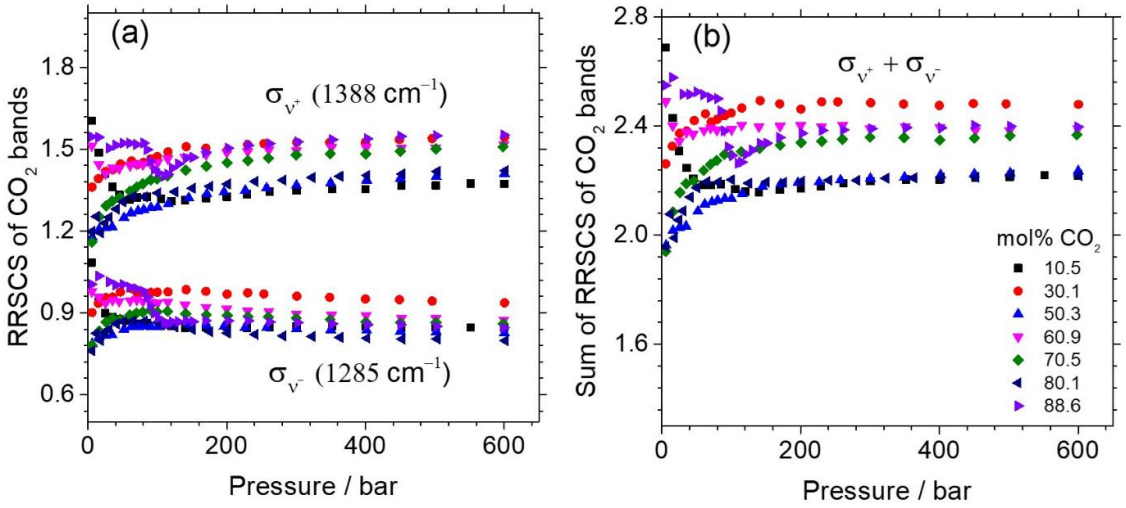

Figure 2-4: Variation as a function of pressure and composition of (a) the RRSCS of the two bands of CO_2 (σ_{v+} at 1388 cm^{-1} and σ_{v-} at 1285 cm^{-1}) and (b) their sum ($\sigma_{v+} + \sigma_{v-}$).

A small shift with composition is observed but without a clear correlation (Figure 2-4a,b). The shifts are quite small, which is probably due to the small error on the measured composition of gas mixtures and to the sensitivity of the Raman spectrometer. Indeed, each gas mixture was analyzed on a different day, and there is always a fluctuation in the instrumental efficiency from day to day (known as instrumental and random errors).

Table 2-1: RRSCS of the two bands of CO_2 (v^+ and v^-) and their sum [a].

	This study	*(Fouche and Chang, 1971b)*	*(Penney et al., 1972)*	*(Fenner et al., 1973)*
λ (nm)	514	514	514	488
Pressure (bar)	5-600	2.35	-	≤ 1
σ_{v+}	1.40 ± 0.03	1.5	1.37 ± 0.1	1.4
σ_{v-}	0.89 ± 0.02	1	-	0.89
$\sigma_{v+} + \sigma_{v-}$	2.29 ± 0.04	2.5	-	2.29

[a] *Values in literature were obtained at low pressure (1-5 atm) and room temperature. Our data are obtained in the pressure range 5 - 600 bars at 32 °C.*

Dubessy et al. (1989) stated that the sum of two RRSCS of CO_2 should always be preferred for the determination of gas mixture composition because it is constant with pressure. However, Seitz et al. (1996) showed in figure 5 that it was advantageous to use σ_{v+} only rather than the sum of the two for determining the composition of gas mixtures. According to our statistical analyses, the small variations of σ_{v+} and σ_{v-} with pressure are negligible. We can, therefore,

conclude that σ_{ν^+}, σ_{ν^-} and their sum are all almost constant for every gas mixture concentration over the studied pressure range and can be therefore be used to determine the composition of the gas mixture. However, the small variations of σ_{ν^+} and σ_{ν^-} may become significant at very high pressure. The sum of the two RRSCS of CO_2 should, therefore, be used in preference to avoid any effect of pressure. The averaged values calculated from the experimental data (a population of 160 data points) are 1.40 ± 0.03, 0.89 ± 0.02 and 2.29 ± 0.04, for ν^+, ν^- and the sum $\nu^+ + \nu^-$, respectively (uncertainties at 1σ). The values are in good agreement with the data from literature but are given with better accuracy (Table 2-1).

3.2. Effect of composition, pressure, and density on Raman spectral features of N_2 and CO_2

3.2.1. Variation of the N_2 peak position at 32 °C

The downshift of the N_2 band as a function of pressure and composition is shown in Figure 2-2a and Figure 2-5. The uncertainty of the corrected peak position of N_2 (± 0.01 cm^{-1}) is too small to be shown in Figure 2-5. At low pressure, the N_2 peak position seems to converge to the same value (~ 2330 - 2330.5 cm^{-1}) for all gas compositions that is in agreement with Lamadrid et al.(2017) A drastic downshift is reported from 5 to 200 bars, especially for the gas mixtures dominated by CO_2. Above 200 bars, it becomes less sensitive to pressure, even becoming nearly constant for gas mixtures dominated by CO_2. This stepwise behavior can be explained by the variation of the density of the gas mixtures. For example, the density of the mixture at 11.4 mol% N_2 increases drastically from 5 to 200 bars then reaches a plateau until 600 bar (cf. Figure S. 2-1). Figure 2-5 shows that the peak positions of N_2 also vary with the composition of gas mixtures. In general, the presence of CO_2 causes a greater downshift of the N_2 peak position than that of pure N_2 at the same pressure. For instance, a downshift of about 2 cm^{-1} is observed for pure N_2 at 600 bars, whereas it is about 3.4 cm^{-1} for a gas mixture of 11.4 mol% N_2.

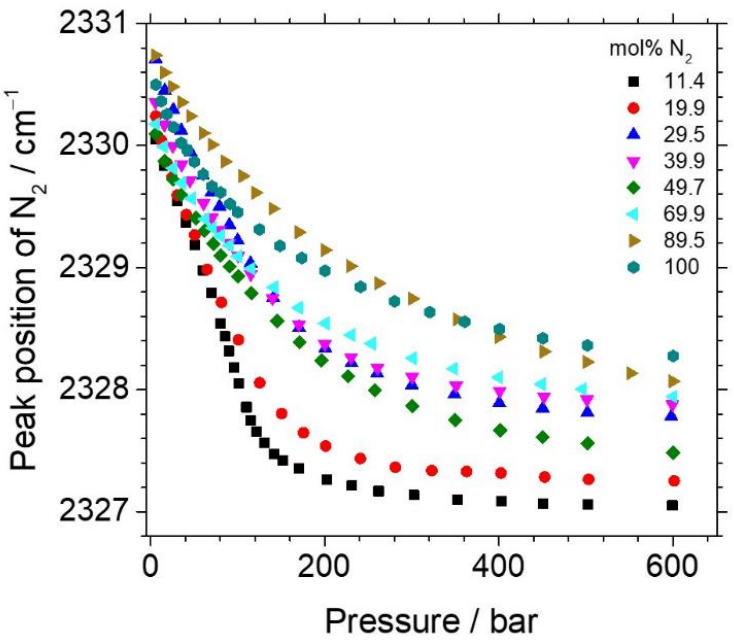

Figure 2-5: Variation of the fitted peak position of N_2 (corrected from Ne peak position) at 32 °C as a function of pressure and composition (mol% N_2) of gas mixtures.

Besides, some curves relative to samples at different N_2 concentrations are superimposed or overlap each other (100 and 89.5 mol% N_2 or 29.5, 39.9 and 69.9 mol% N_2), indicating that the variation of the peak position of N_2 as a function of composition is not significant enough to be distinguished for some composition-pressure ranges. Moreover, for unknown reasons, the 89.5% N_2 curve shows an abnormal behavior whereas the corresponding associated curve of the Fermi diad splitting of CO_2 (the curve of 10.5 mol% CO_2 in Figure 2-6) evolves as expected. The modest reproducibility of the N_2 peak position despite wavelength calibration by Ne may be linked to small day-to-day variation in the shape and the position of the neon band because of variations in the positioning of the neon lamp in the optical path of the Raman spectrometer. Thus, a higher-accurate method to wavelength correction is required to use the N_2 peak position as a reliable quantitative parameter. After all, we can only conclude here the global variation trend of the N_2 peak position with a significant effect of the composition and pressure.

3.2.2. Variation of the CO_2 Fermi diad splitting at 32 °C

Figure 2-2b shows typical Raman spectra of CO_2 and the downshift of CO_2 peaks with increasing pressure. The two bands of CO_2 were investigated by measuring the distance between them (Fermi diad splitting), so there was no need for absolute wavelength calibration of the spectrometer.

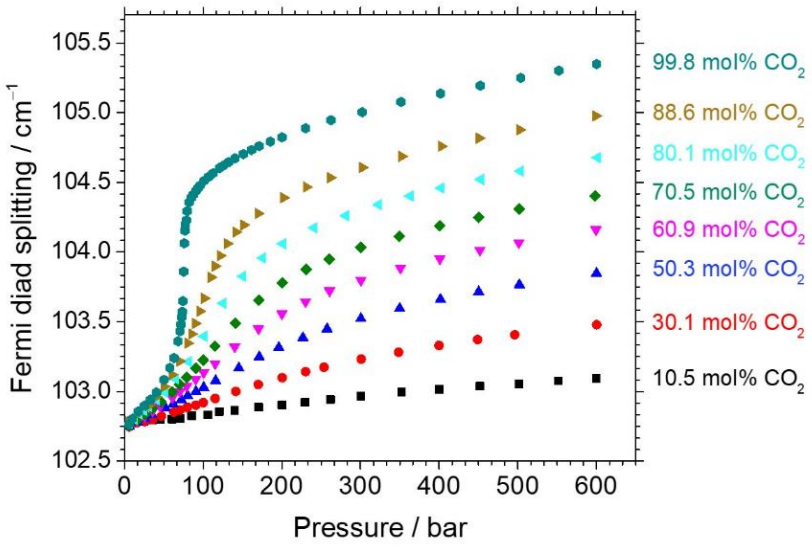

Figure 2-6: Evolution of the Fermi diad splitting as a function of composition and pressure of different CO_2-N_2 gas mixtures at 32 °C. Uncertainties of Fermi diad splitting (± 0.015 cm^{-1} at 1σ) and of pressure (± 1 bar) are smaller than the data dot size.

Figure 2-6 represents the variation of the Fermi diad splitting of CO_2 at 32 °C as a function of pressure and composition of the CO_2-N_2 gas mixture. At low pressure, the Fermi diad splitting value is nearly identical (~ 102.762 cm^{-1}) for any composition. At higher pressure, an effect of the gas mixture composition is clearly observed. In general, the presence of N_2 reduces the magnitude of the variation of the Fermi diad splitting. For example, at 600 bars, the Fermi diad splitting shifts down from 105.348 cm^{-1} (for pure CO_2) to 103.093 cm^{-1} (for the gas mixture at 10.5 mol% CO_2). This trend is relatively similar to that observed for CO_2 mixed with CH_4 (Seitz et al., 1996). The repeatability and the reproducibility of the relationship between Fermi diad splitting, pressure, and composition of the gas mixture are much better than the peak position of N_2 (Figure 2-5). The Fermi diad splitting of CO_2 can thus be used as an accurate parameter to determine the pressure of CO_2-N_2 gas mixtures.

The Fermi diad splitting of CO_2 can also be used for the determination of the density of CO_2-N_2 gas mixtures. For this, the density of every gas mixtures at given *PT* conditions presented in Figure 2-6 was calculated by the GERG-2004 EoS. The resulting relationship between Fermi diad splitting of CO_2, density, and composition of gas mixtures (at 32 °C) is presented in Figure 2-7. The Fermi diad splitting increases with the density of the gas mixture and the content of CO_2. Note that the shape of the curve with 99.8% CO_2 is relatively irregular between 103.7 and 104.3 cm^{-1} (0.3 - 0.7 $g{\cdot}cm^{-3}$). This is likely due to the proximity with the

critical temperature of CO_2 (31.05 °C) where a small temperature fluctuation may result in a significant variation of density.

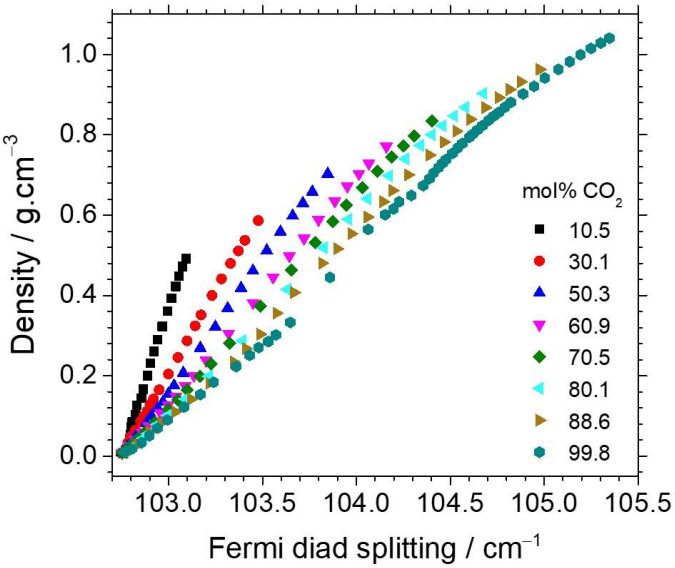

Figure 2-7: Evolution of the Fermi diad splitting of CO_2 as a function of composition and density of CO_2-N_2 gas mixtures at 32 °C. The density was calculated at given temperature, pressure, and composition by the GERG-2004 EoS. Uncertainty on density is smaller than data dot size.

Overall, the data of the present study are in good agreement with recently published densimeters of pure CO_2 (Fall et al., 2011; Wang et al., 2011). It also agrees well with the previous investigations regarding the Fermi resonance of CO_2: (i) with increasing pressure, the Fermi resonance interaction reduces through a decrease of the anharmonic coupling constant (k_{122}), resulting in an increase of the separation between the unperturbed levels (ν_1 and $2\nu_2$) as well as the Fermi diad splitting (Olijnyk et al., 1988; Hacura et al., 1990; Hacura, 1997), and (ii) while increasing the content of N_2, the reduction of the Fermi resonance becomes smaller (so the Fermi diad splitting still increases but with a smaller magnitude) in comparison with that of pure CO_2 in the same conditions (Hacura, 1997).

3.2.3. Effect of temperature on the Fermi diad splitting of CO_2

The effect of temperature on the variation of CO_2 Fermi diad splitting of CO_2-N_2 gas mixtures was also analyzed conducting experiments at 22 °C. At this temperature, a V-L phase transition is observed for any gas mixture containing > ~ 92 mol% CO_2 (Figure 2-8a).The results are compared with those obtained at 32 °C in Figure 2-8b,c. In general, the magnitude of the variation of the CO_2 Fermi diad splitting at 32 °C is smaller than that at 22 °C at the same pressure (Figure 2-8b) but identical at the same density (Figure 2-8c). A large gap appears

at ~60 bars on the curve of pure CO_2 at 22°C (< T_c = 31.05 °C) due to the vapor-liquid phase transition. Indeed, at this condition (22 °C and 60 bars), CO_2 is in the two-phase LV domain (Figure 2-8a), and thus both liquid and vapor phases coexist in the microcapillary. Pressure remains constant at ~60 bars until the vapor phase is completely converted to liquid. As a result, no data point can be recorded within the density range ~ 0.2 g·cm^{-3} (vapor state) to ~ 0.7 g·cm^{-3} (liquid state). At 32 °C, there is no phase transition (supercritical state) for any CO_2-N_2 gas mixture (Figure 2-8a) and data points can be collected over the entire density range. Therefore, only the data acquired at 32 °C were fitted to provide calibration equations. These equations must be used at 32 °C only for pressure determination but can be used (at least) in the range 22 - 32 °C for density determination of any gas composition above the critical temperature (Figure 2-8b, c).

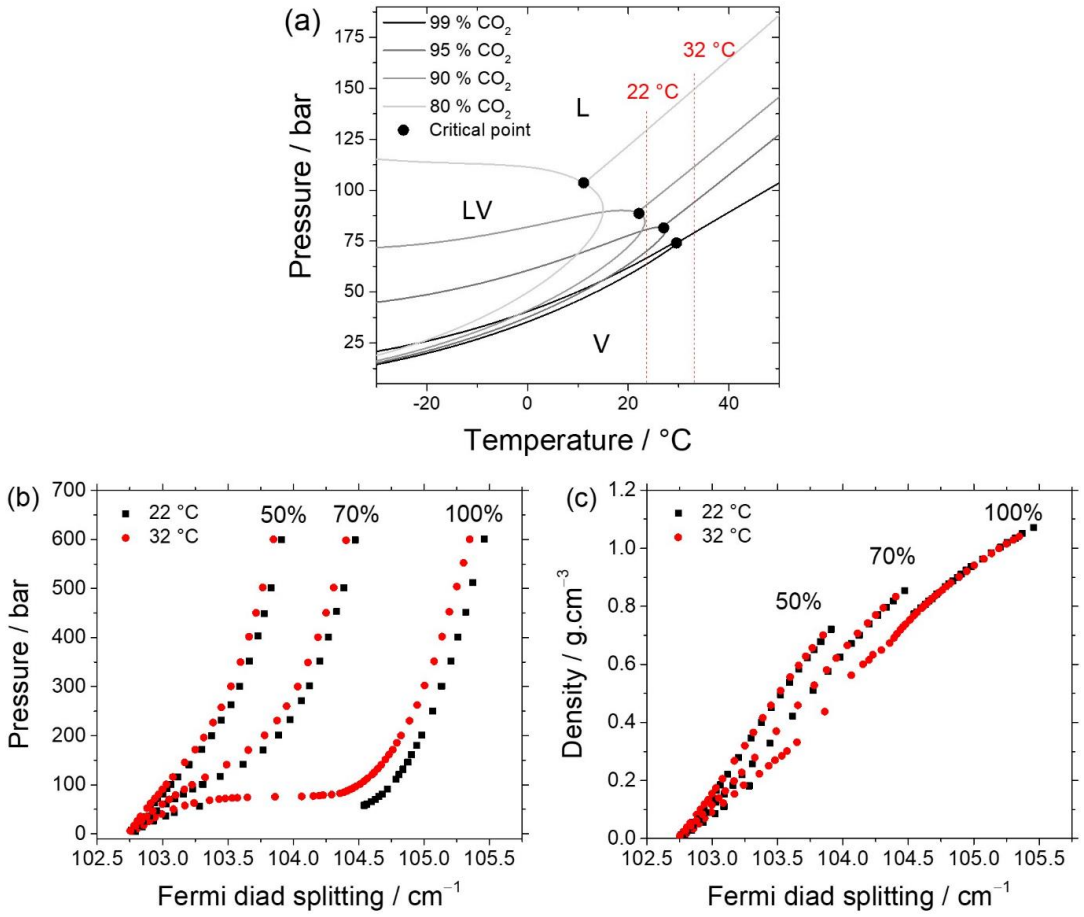

Figure 2-8: (a) Phase diagrams of CO_2-N_2 gas mixtures exported from data calculated by REFPROP. L: liquid-phase domain; V: vapor-phase domain and LV: biphasic liquid-vapor domain. Only critical isochores are drawn for each mixture. (b) and (c) Comparison between the evolution of Fermi diad splitting of pure CO_2 and CO_2-N_2 mixtures (50 and 70 mol% CO_2) as a function of pressure and density at 22 and 32 °C.

3.2.4. Calibration equations to determine the pressure and density of CO_2-N_2 gas mixtures

According to the whole data set shown in Figure 2-5, Figure 2-6 and Figure 2-7, the Fermi diad splitting of CO_2 appears as the most reliable quantitative parameter for determining pressure and density of CO_2-N_2 gas mixtures. Data obtained at 32 °C were fitted to provide calibration equations. In order to minimize uncertainties on the calculated pressure and density, the calibration data were fitted separately for five smaller pressure-composition (*PX*) domains (Figure 2-9). Regions (a) and (b) cover the pressure range 5 to 600 bars and the composition range 50 - 100 mol% CO_2 and 10 - 50 mol% CO_2, respectively. Regions (c) and (d) cover only the low-pressure range (5 - 150 bars) and the composition range 50 - 100 mol% CO_2 and 10 - 50 mol% CO_2, respectively.

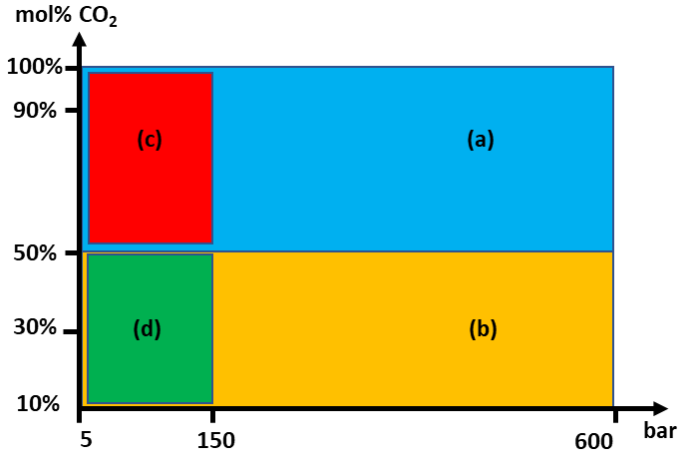

Figure 2-9: Pressure-composition (*PX*) domains for application of polynomial equations a, b, c, and d. Experimental data were fitted within each *PX* domain to provide the best-fitting polynomial equation to minimize uncertainties on the calculated pressure and density.

Third-order polynomial equations linking pressure or density to the CO_2 Fermi diad splitting and the composition of gas mixtures were computed for each *PX* domain. The general form of the calibration polynomial is given in Equation 2-3, where C_{CO2} and Δ are defined by Equations 2-4 and 2-5 respectively. Fitting by a higher-order polynomial does not lead to substantial improvements in the qualitative of measurement. The coefficients (p_{ij}, a, b, std_a, std_b, with $(i + j) \leq 4$) of each calibration equations are listed in Table S. 2-2 (for pressure determination) and Table S. 2-3 (for density determination) in Supporting Information.

$$\text{Pressure (or density)} = \sum_{i=0}^{3}\sum_{j=0}^{4} p_{ij}\left(C_{CO_2}\right)^{i}(\Delta)^{j} \qquad 2\text{-}3$$

$$C_{CO_2} = \frac{\text{Molar proportion of } CO_2 - a}{\text{Std\_a}} \quad 2\text{-}4$$

$$\Delta = \frac{\text{Fermi diad splitting} - b}{\text{Std\_b}} \quad 2\text{-}5$$

Two main error sources contribute to the final uncertainty of the calculated pressure and density. The first source is directly associated with the uncertainty of the Fermi diad splitting (± 0.015 cm^{-1}) and of the measured composition of the gas mixture (calculated from RRSCS and peak areas with Equation 2-2). As the regression calibration equations are not linear, the uncertainty of the first error source is not constant but varies with the composition of the gas mixture and the CO_2 Fermi diad splitting. The second error source is related to how well the best-fitted calibration equations reproduce the pressure and the density from a given CO_2 Fermi diad splitting and gas mixture composition. The uncertainty of each calibration equation was derived from its prediction bounds (at 1σ) and reported in the last row of Table S. 2-2 and Table S. 2-3. The ultimate uncertainty on measured pressure or density will be the sum of these two error sources, as reported by Fall et al (2011) and Wang et al (2011) for pure CO_2.

3.3. Investigation of CO_2-N_2 natural fluid inclusions

The calibrations data described above were applied to 15 natural CO_2-N_2 fluid inclusions trapped within a quartz sample from the Central Alps (Switzerland). Composition, pressure, and density were compared with those derived from microthermometry.

Each FI was analyzed three times by microthermometry to determine the melting temperature T_m(car) and the homogenization temperature of the volatile phase T_h(car). These phase transition temperatures were subsequently reported in the *VX* diagram of Thiéry et al. (1994a) to calculate the composition and molar volume (density) of the fluid inclusion. As the uncertainties arising from this *VX* diagram are unknown, only the uncertainty of ± 0.1 °C of the heating-cooling stage to T_m(car) and T_h(car) is considered. This uncertainty of ± 0.1 °C can cause either significant or insignificant error depending on the region in the *VX* diagram. For example, the slopes of the T_h(car) lines are less steep in the vapor field than in the liquid field (Figure 8b in (Thiéry et al., 1994a)). In this domain, an uncertainty of ± 0.1 °C in T_m(car) can result in a variation of up to 5 mol% in composition and up to 0.09 $g \cdot cm^{-3}$ in density. The second source of error may be an error in graphical reading. Detailed microthermometry results of each FI were reported in Table S. 2-1 (Supporting Information).

The selected FIs were also analyzed three times by Raman spectroscopy. The averaged values of the peak position and peak area of CO_2 and N_2 bands were used to calculate composition, pressure, and density through Equations 2-2 to 2-5. The composition of the FIs was calculated by the RRSCS of the two CO_2 bands and their sum for comparison. The difference between these three values is always less than 1 mol% CO_2. Detailed measurements of each FI are presented in Table S. 2-4 (Supporting Information).

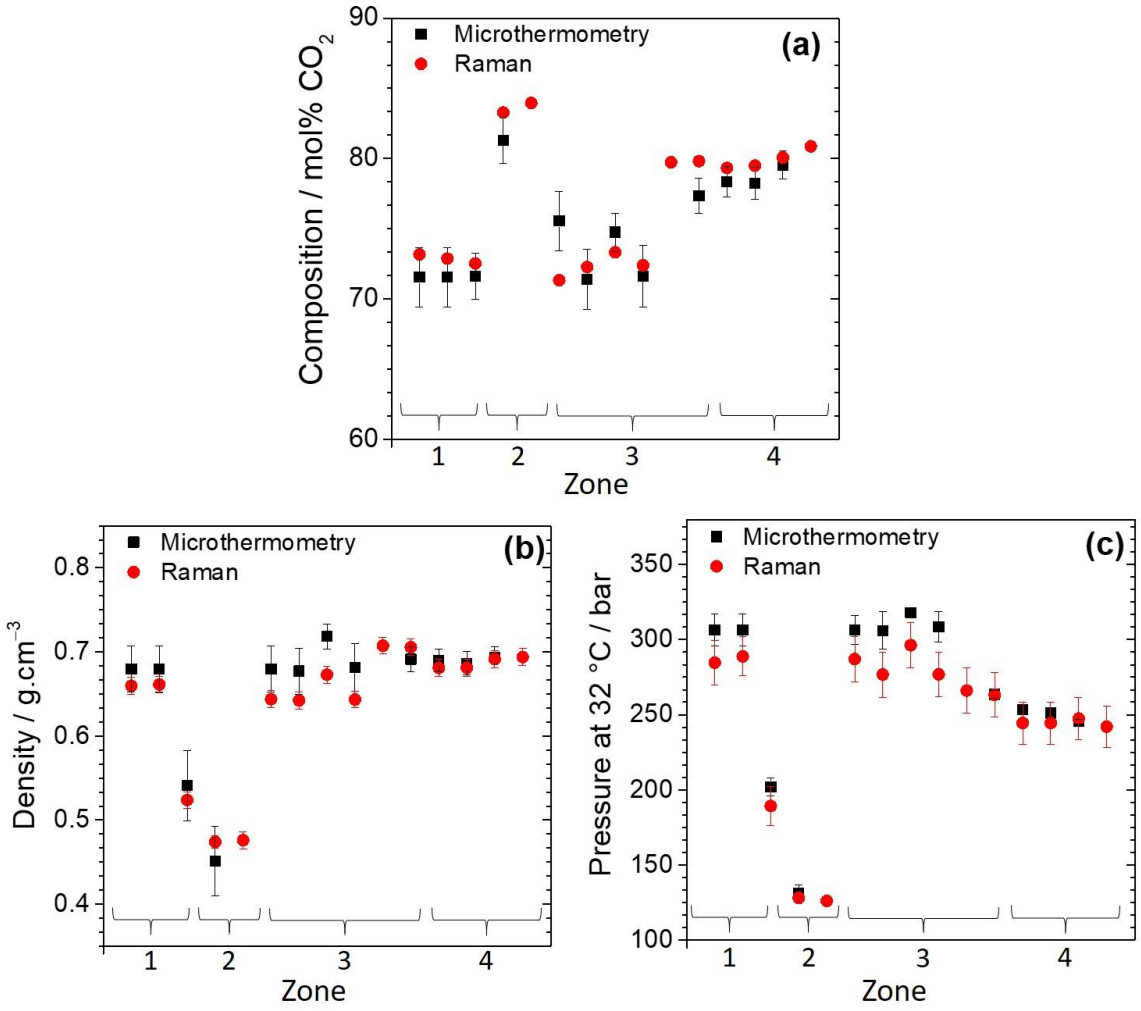

Figure 2-10: Comparison after analysis of the volatile phase of selected FIs by Raman and microthermometry of the (a) composition, (b) density, and (c) pressure at 32 °C.

Figure 2-10 presents a comparison between Raman and microthermometry results. The uncertainty of Raman measurements on composition (< 0.5 mol% CO_2) and density (< 0.01 g·cm^{-3}) is slightly better than that derived from microthermometry measurements (ranging from ~1 to 2.2 mol% for composition, and from 0.01 to 0.04 g·cm^{-3} for density). Uncertainty on measured pressure at 32 °C from microthermometry (varying from 2 to 11 bars, Figure

2-10c) is equivalent to that from Raman (~ 15 bars when pressure > 150 bars, and ~ 3 bars when pressure < 150 bars).

Overall, the results derived from the two methods are close and comparable with a relative difference varying from 0.1 - 7 % coming from the error sources mentioned above, but also from the unknown error of the thermodynamic models of Soave-Redlich-Kong (1972) and Lee-Kesler (1975) used for the construction of the *VX* diagram of Thiéry et al. (1994a) According to Mullis et al.(1994), the trapping temperature of the geological fluid where Mu 147.2 sample was collected was about 400 °C. Thereby, the trapping pressure (the pressure at trapping temperature) of the geological fluid determined using GERG-2004 EoS is about 1610 ± 20 bars (calculated from Raman results) or 1770 ± 20 bars (calculated from microthermometry results). The difference of density leads to a difference of only 160 bars (9 %) which is of no consequence on geological interpretation.

Raman spectroscopy may be more efficient than microthermometry in some cases. For example, FI4.8 is too small (< 2 µm, Figure 2-3a) to observe any phase transition with good accuracy. Concerning FI3.5, T_h(car) could not be determined precisely because the vapor bubble was located in the dark part of the inclusion at a temperature close to homogenization (Figure 2-3b). Similarly, FI2.2 could not be analyzed by microthermometry because of bad optical conditions (color, contrast, etc.). These three FIs could, however, be analyzed by Raman spectroscopy. Another disadvantage of microthermometry method (using *VX* diagram of Thiéry et al. (1994a)) appears when clathrate is formed and remains above T_h(car), meaning that a part of CO_2 is still trapped inside the clathrate structure, and thus could lead to an underestimation of the CO_2 quantity while using only T_h(car) (Diamond, 1992; Bakker, 1997). The latter problem is not encountered by Raman spectroscopy at 22 and 32 °C.

4. Conclusion

The use of an improved HPOC system consisting of an FSC coupled with a heating-cooling stage and a Raman spectrometer makes it possible to investigate the behavior of CO_2-N_2 mixtures at controlled pressure and temperature conditions. The experiments can be easily repeated several times for statistical purposes as well as repeatability and reproducibility test. A complete calibration of the Raman signals of CO_2-N_2 mixtures was thus performed for the first time. The Fermi diad splitting of CO_2 was linked to pressure or density for any CO_2-N_2 gas mixture in the range 22 - 32 °C. It was also demonstrated that the RRSCS of CO_2 does not depend on composition but slightly on pressure or density. However, this effect is negligible

in the studied pressure range (< 600 bars). Thus, accurate RRSCS values of the two vibration modes of CO_2 and their sum can be either used to determine the composition of CO_2-N_2 gas mixtures with an uncertainty of about ± 0.5 mol%. The pressure and the density of CO_2-N_2 binary gas mixtures can be henceforth calculated by using regression calibration equations that were validated by successful application to natural fluid inclusions from the Central Alps, Switzerland. A detailed comparison was made indicating that Raman spectroscopy is a powerful alternative tool to the microthermometry, providing not only *PVX* information with comparable accuracy (even better in some cases) but also handling cases for which microthermometry cannot be applied. This study shows the applicability of Raman spectroscopy for gas analysis purposes at extreme conditions (very small object at high pressure) and can be easily extended to any gas mixture.

Acknowledgments

This work is a part of the thesis of Van-Hoan Le (Université de Lorraine) who acknowledges the French Ministry of Education and Research and the ICEEL Institut Carnot. The work benefited financial support from CNRS-INSU CESSUR program. The authors are sincerely thankful to Catherine Lorgeoux and Héloïse Verron for their instruction during the Gas Chromatography measurement part, to Silvia Lasala and Romain Privat for a fruitful discussion about the thermodynamic properties of the CO_2-N_2 system. Two anonymous reviewers are acknowledged for their thorough re-view and their insightful comments and suggestions.

Appendix: Supporting Information

- S-1 Correlation between pressure and density of CO_2-N_2 gas mixtures
- S-2 Uncertainty of microthermometry measurements
- S-3 Coefficients of regression calibration equations
- S-4 Uncertainty of CO_2 Fermi diad splitting
- S-5 Uncertainty on the determination of composition (at 1 σ)
- S-6 Uncertainty of pressure and density measured by Raman spectroscopy

---

S-1 Correlation between pressure (bar) and density (molecular number/cm^{-3}) of CO_2-N_2 gas mixtures

Figure S. 2-1 represents the variation of the density of CO_2-N_2 gas mixtures as a function of pressure and composition. The density was calculated by GERG-2004 EoS at given *PTX* conditions.

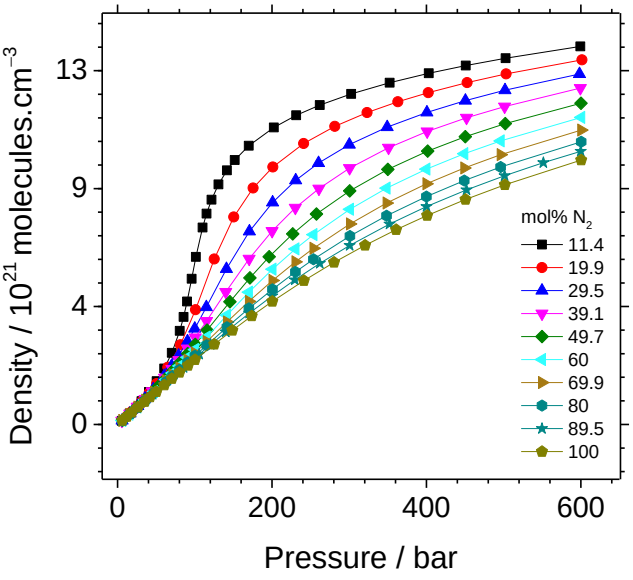

Figure S. 2-1 Correlation between the pressure and the density of CO_2-N_2 gas mixtures (at 32 °C)

S-2 Uncertainty of microthermometry measurements

The uncertainty of microthermometry measurements is related to the uncertainty of the melting temperature T_m(car) and the homogenization temperature T_h(car) of the volatile carbonic phase (± 0.1°C). We assumed that the measured density and composition follow a rectangular distribution as illustrated by Figure S. 2-2, where a and b are the min and max of

the measured density and pressure, respectively. The average value is $m = \frac{(a+b)}{2}$ and the standard uncertainty $1\sigma = \frac{(b-a)}{2\sqrt{3}}$.

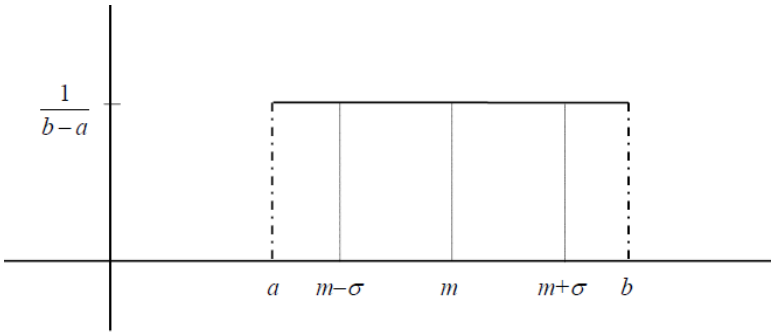

Figure S. 2-2: Probability density function of rectangular distribution

Table S. 2-1 listed all results of microthermometry measurements. In the following, we detailed an example of uncertainty determination for fluid inclusion 3.4 (FI3.4, Figure 2-3) which have T_m(car) = – 59.5 ± 0.1 °C and T_h(car) = – 10.5 ± 0.1 °C. Since the uncertainty of ± 0.1°C of T_h(car) causes a very small difference that cannot be distinguished on the *VX* diagram of Thiéry et al. (1994), we consider therefore only two extrema of results calculated from the variation of ± 0.1 °C of T_m(car). Thereby:

- At T_m(car) = – 59.5 + 0.1 = – 59.4 °C and T_h(car) = – 10.5 °C, the molar proportion of CO_2 in volatile phase = 75.4 mol% and the density = 54.8 cm^3.mol = 0.73 g·cm^{-3}.
- At T_m = – 59.5 – 0.1 = – 59.6 °C and T_h(car) = – 10.5 °C, the molar proportion of CO_2 in volatile phase = 67.8 mol% and the density = 61.5 cm^3.mol = 0.63 g·cm^{-3}.

The average value composition of $CO_2 = \frac{(75.4 + 67.8)}{2} = 71.6$ (mol%). The uncertainty of composition $= \frac{(75.4 - 67.8)}{2\sqrt{3}} = \pm 2.2$ (mol%).

The average value of density $= \frac{(0.731 + 0.632)}{2} = 0.68$ (g·cm^{-3}). The uncertainty of density $\frac{(0.73 - 0.63)}{2\sqrt{3}} = \pm 0.03$ (g·cm^{-3}).

The pressure of FIs was calculated from the two extrema values of composition and density by GERG-2004 EoS (at 32 °C):

- At composition = 75.4 mol% CO_2 and density = 0.731 g·cm^{-3}, the calculated pressure = 326 bars.

- At composition = 67.8 mol% CO_2 and density = 0.632 g·cm^{-3}, the calculated pressure = 291 bars.

Therefore, the average value of pressure $= \frac{(326 + 291)}{2} = 309$ bars and its uncertainty (1σ) $= \frac{(326 - 291)}{2\sqrt{3}} = \pm 11$ bars.

Table S. 2-1: Microthermometry results

FI name	T_m(car)(1) (°C)	T_h(car) (2) (°C)		Composition (3) (mol% CO_2)	Density (4) (g·cm^{-3})	Pressure (5) (bar)
1.1	– 59.5	– 9.9	L	71.6 ± 2.1	0.68 ± 0.03	307 ± 10
1.2	– 59.5	– 9.9	L	71.6 ± 2.1	0.68 ± 0.03	307 ± 10
1.4	– 59.0	1.1	V	70.2 ± 1.4	0.52 ± 0.03	200 ± 9
2.1	– 58.0	14.5	V	81.3 ± 1.6	0.45 ± 0.04	131 ± 6
2.2	?	?	V	?	?	?
3.1	– 59.5	– 9.9	L	71.6 ± 2.1	0.68 ± 0.03	307 ± 10
3.2	– 59.5	– 9.7	L	71.4 ± 2.1	0.68 ± 0.03	306 ± 10
3.3	– 59.4	– 9.8	L	74.8 ± 1.4	0.72 ± 0.02	318 ± 4
3.4	– 59.5	– 10.5	L	71.6 ± 2.2	0.68 ± 0.03	309 ± 11
3.5	– 59.1	?	?	?	?	?
3.6	– 59.1	– 3.7	L	77.4 ± 1.2	0.69 ± 0.02	264 ± 3
4.2	– 59.0	– 2.2	L	78.4 ± 1.1	0.69 ± 0.01	254 ± 2
4.4	– 59.0	– 1.9	L	78.2 ± 1.1	0.69 ± 0.01	251 ± 2
4.5	– 58.9	– 0.7	L	79.6 ± 1.0	0.69 ± 0.01	246 ± 2
4.8	?	?	?	?	?	?

T_m(Car)(1) (°C) and T_h(Car)(2) are melting temperature and homogenization temperature of the volatile part (± 0.1 °C). The Composition (3) and the Density (4) obtained from the *VX* diagram of Thiéry et al., 1994. The Pressure (5) at 32°C calculated using GERG-2004 EoS (REFPROP program) from the Composition (3) and the Density (4).

S-3 Coefficients of regression calibration equations

The relationship between the CO_2 Fermi diad splitting, composition, and pressure or calculated density are shown in Figure 2-6 and Figure 2-7, respectively.

The calibration data presented in Figure 2-6 and Figure 2-7 are then fitted by third-order polynomials (Equation 2-3, 2-4 and 2-5) for five pressure-composition (*PX*) domains: (a), (b), (c), (d) and (e) (Figure 2-9). All coefficients are listed in Table S. 2-2 (for pressure calculation, in bar) and Table S. 2-3 (for density calculation, in g·cm^{-3}).

Table S. 2-2: Coefficients of equations 3, 4, and 5 for pressure measurement (bar).

PX domains / c_{ij}	50-100 mol% CO_2		10-50 mol% CO_2	
	5-600 bar	5-160 bar	5-600 bar	5-160 bar
c00	134.85314	98.21111	164.7456	69.139111
c10	-62.13943	-31.34817	-72.9435	-26.113885
c01	95.32309	56.75174	154.8661	51.154940
c20	37.55699	10.95812	64.0668	12.433977
c11	-144.12065	-43.16425	-115.9407	-24.973630
c02	87.60480	-11.60933	35.4594	-0.610425
c30	-27.52349	-6.14760	-30.2517	-3.525410
c21	74.61282	18.06447	91.3844	12.079440
c12	-131.28751	-32.38414	-60.5821	3.668211
c03	81.04989	24.72823	21.3175	-0.998273
c31	-23.38348	-6.83208	-32.4859	-2.992345
c22	38.11773	9.44985	25.9501	-3.140110
c13	-40.14929	-16.59404	-10.2713	1.096062
c04	9.50494	5.20494	0.5895	-0.061662
h	0.79427	0.81495	0.3	0.30339
Std_h	0.17942	0.17944	0.14207	0.14138
k	103.74	103.4	103.05	102.87
Std_k	0.72596	0.6067	0.26608	0.0903082
Adjusted R^2	0.9982	0.9985	0.9990	0.9885
Uncertainty* (1σ)	± 11 bars	± 4 bars	± 8 bars	± 5 bars

* The uncertainties on calculated pressure were derived from the prediction intervals of the regression polynomial at 1σ and listed at the last row.

Table S. 2-3: Coefficients of equations 3, 4 and 5 for density measurement (g·cm^{-3}).

PX domains / c_{ij}	50-100 mol% CO_2		10-50 mol% CO_2	
	5-600 bar	5-160 bar	5-600 bar	5-160 bar
c00	0.4685489	0.2859370	0.2452815	0.0963779
c10	-0.0517038	-0.0334438	-0.0754989	-0.0275175
c01	0.3854014	0.3070979	0.2202647	0.0751329
c20	0.0082646	0.0035081	0.0328384	0.0120657
c11	-0.0225597	-0.0191686	-0.0596345	-0.0264190
c02	-0.0091876	0.0218406	0.0019097	0.0010983
c30	-0.0134169	-0.0093131	-0.0063004	-0.0028064
c21	-0.0037567	-0.0061263	0.0214861	0.0108290
c12	0.0244871	0.0106365	0.0225016	0.0065828
c03	-0.0291237	-0.0164697	-0.0051500	-0.0020218
c31	-0.0084270	-0.0110711	-0.0027620	-0.0019760
c22	-0.0076177	-0.0060320	-0.0124878	-0.0048468
c13	0.0088910	0.0016936	0.0029490	0.0019938
c04	0.0017951	0.0016010	-0.0006999	-0.0001678
h	0.79427	0.81495	0.3	0.30339
Std_h	0.17942	0.17944	0.14207	0.14138
k	103.74	103.40	103.05	102.87
Std_k	0.72596	0.6067	0.26608	0.0903082
Adjusted R^2	0.9996	0.9994	0.9996	0.9940
Uncertainty* (1σ)	± 0.008	± 0.007	± 0.006	± 0.005

* The uncertainties on calculated pressure were derived from the prediction intervals of the regression polynomial at 1σ and listed at the last row.

S-4 Uncertainty of CO_2 Fermi diad splitting

The Fermi diad splitting (Δ) is the separation between two bands of CO_2 (ν^+ and ν^+), expressed by the following equation:

$$\Delta = \nu^+ - \nu^- \ (\mathrm{cm}^{-1}) \qquad \text{S1}$$

In where the ν^+ and ν^- are the peak position of upper and lower bands of CO_2, respectively. Thus, the uncertainty of Fermi diad splitting (Δ) mainly comes from the uncertainty of peak position of the two CO_2 bands ($\pm$ 0.01 cm^{-1}) that are calculated by the following equation:

$$\sigma_\Delta = \sqrt{\left(\frac{\partial\Delta}{\partial\nu^+}\right)^2 \cdot (\sigma_{\nu^+})^2 + \left(\frac{\partial\Delta}{\partial\nu^-}\right)^2 \cdot (\sigma_{\nu^-})^2} \qquad \text{S2}$$

$$= \sqrt{(1)^2 \cdot (0.01)^2 + (1)^2 \cdot (0.01)^2} \approx 0.015 \text{ cm}^{-1}$$

S-5 Uncertainty on the determination of composition (1σ)

The composition of gas mixtures (mol% CO_2, denoted C_{CO_2}) is calculated from the sum of two CO_2 RRSCS (σ_{CO_2}), the peak area of N_2 (A_{N_2}) and the peak area of CO_2 (A_{CO_2}) by the following equation :

$$C_{CO_2} = \frac{A_{CO_2}/\sigma_{CO_2}}{A_{CO_2}/\sigma_{CO_2} + A_{N_2}} \qquad \text{S3}$$

The uncertainty of A_{N_2} and A_{CO_2} are less than ± 0.4 % of peak area values. The uncertainty of σ_{CO_2} ratio is ~ ± 0.04 (determined from a population of 160 data points recorded over a pressure range 5-600 bars and composition range 10-90 mol% CO_2). Thereby, the uncertainty on the determination of composition mainly comes from these elementary uncertainties.

For example, uncertainty calculation for fluid inclusion n° 3.4 (FI3.4):

- Peak area of N_2 = 9196 ± 37 count
- Upper peak area of CO_2 = 34723 ± 139 count
- Lower peak area of CO_2 = 20920 ± 84 count
- Total peak area of CO_2 (upper + lower) = 55643 ± 222 count
- σ_{ν^+} = 1.40 ± 0.03
- σ_{ν^-} = 0.89 ± 0.02
- Sum of two CO_2 RRSCS σ_{CO_2} = 2.29 ± 0.04

Thereby, the composition (C_{CO_2}) and its uncertainty ($\sigma_{C_{CO_2}}$) calculated by Equation S3 are:

$$C_{CO_2} = \frac{\left(\frac{55643}{2.29}\right)}{\left(\frac{55643}{2.29}\right) + 9196} = 72.5 \text{ (mol\%)}$$

$$\sigma_{C_{CO_2}} = \sqrt{\left(\frac{\partial C_{CO_2}}{\partial A_{N_2}}\right)^2 \cdot \left(\sigma_{A_{N_2}}\right)^2 + \left(\frac{\partial C_{CO_2}}{\partial A_{CO_2}}\right)^2 \cdot \left(\sigma_{A_{CO_2}}\right)^2 + \left(\frac{\partial C_{CO_2}}{\partial F}\right)^2 \cdot (\sigma_F)^2} \quad \text{S4}$$

$$\approx 0.4 \text{ mol\%}$$

Uncertainty on the composition determined from σ_{v+} (1.40 ± 0.03) or σ_{v-} (0.89 ± 0.02) can be similarly calculated using Equation S4.

S-6 Uncertainty of pressure and density measured by Raman spectroscopy

Always taking the example of FI3.4 to illustrate the determination of the uncertainty on measured pressure and density from Raman measurements.

Two main error sources contribute to the final uncertainty of measured pressure and density. The first source is directly associated with the uncertainty of the Fermi diad splitting (± 0.015 cm^{-1}) and of the measured composition of the gas mixture (as described in S-4 section). Since the regression calibration equations are not linear, the uncertainty of the first error source is not constant but vary with the composition of the gas mixture and the CO_2 Fermi diad splitting.

The composition and its uncertainty calculated from σ_{co_2} (sum of two RRSCS of CO_2) are equal to 72.5 ± 0.4 mol%. Similarly, the composition and its uncertainty calculated from σ_{v+} and σ_{v-} are 72.9 ± 0.4 mol% and 71.9 + 0.5 mol%, respectively. The final composition is the mean of these three values, so $\frac{(72.5 + 72.9 + 71.9)}{3} = 72.4$ (mol% in CO_2).

The total uncertainty of composition is

$$\sigma_{C_{CO_2}^{total}} = \sqrt{\left(\frac{1}{3}\right)^2 \cdot (0.4)^2 + \left(\frac{1}{3}\right)^2 \cdot (0.4)^2 + \left(\frac{1}{3}\right)^2 \cdot (0.5)^2} \approx \pm 0.3\ mol\%$$

The pressure and its uncertainty were then calculated from Fermi diad splitting (Δ) et composition (C_{CO2}) using regression equations with corresponding coefficients listed Table S. 2-2 and Table S. 2-3:

- Δ = 104.010 ± 0.015 cm^{-1}
- C_{CO2} = 72.4 ± 0.3 mol% in CO_2

As the composition of FI3.4 = 72.4 > 50 mol% corresponding to zone a (cf. Figure 2-9), we then used coefficients listed in column (a) of Table S. 2-2 and Table S. 2-3 for pressure and density determination, respectively. If the obtained pressure is < 150 bars, we need to recalculate one more time with coefficients listed in column (d) of Table S. 2-2 and Table S. 2-3.

In order to calculate the average pressure (and density) and its uncertainty, we need to determine every pressure and density measured from all possible cases. From the uncertainty of Δ and C_{CO2}, we have 4 following cases:

Case 1: Δ = 104.010 + 0.015 = 104.025 and C_{CO2} = 72.4 + 0.3 = 72.7 mol% CO_2.

⇨ Pressure = 280 bars, Density = 0.650 g·cm^{-3}

Case 2: Δ = 104.010 + 0.015 = 104.025 and C_{CO2} = 72.4 - 0.3 = 72.1 mol% CO_2.

⇨ Pressure = 288 bars, Density = 0.653 g·cm^{-3}

Case 3: Δ = 104.010 - 0.015 = 103.995 and C_{CO2} = 72.4 + 0.3 = 72.7 mol% CO_2.

⇨ Pressure = 266 bars, Density = 0.634 g·cm^{-3}

Case 4: Δ = 104.010 - 0.015 = 103.995 and C_{CO2} = 72.4 - 0.3 = 72.1 mol% CO_2.

⇨ Pressure = 274 bars, Density = 0.637 g·cm^{-3}

Thus:

- The pressure calculated from Δ = 104.01 ± 0.015 (cm^{-1}) and C_{CO2} = 72.5 ± 0.3 mol% in CO_2 ranges between [265; 286] bars.
  - ⇨ The average pressure $= \frac{(265 + 286)}{2} =$ 277 bars.
  - ⇨ The uncertainty$^{(*)} = \pm \frac{(max - min)}{2\sqrt{3}} = \pm \frac{(286 - 265)}{2\sqrt{3}} = \pm 6.1$ bars
- The density ranges between [0.6288; 0.6475].
  - ⇨ The average density $= \frac{(0.6470 + 0.6305)}{2} = 0.6388.$
  - ⇨ The uncertainty$^{(*)} = \pm \frac{(max - min)}{2\sqrt{3}} = \pm \frac{(0.6470 - 0.6305)}{2\sqrt{3}} = \pm 0.0054$ g.cm^{-3}.

Uncertainties$^{(*)}$ come only from the first (1) component error. The second (2) component error of the uncertainty is related to (2) how well the best-fitted equation reproduces the pressure and density values from a given Fermi diad splitting and composition. The uncertainty of each regression polynomial was derived from its prediction bounds at 1σ (corresponding 68% confident level) which are listed at last rows of Table S. 2-2 (for pressure determination) and Table S. 2-3 (for density determination). Thereby, the uncertainties of measured pressure

and density values in four cases 1, 2, 3 and 4 with coefficients in the column a are ± 12 bars and ± 0.007 g·cm^{-3}. Thus:

⇨ The uncertainty$^{(**)}$ of average pressure that comes from the best-fitted model are:

$$\text{The uncertainty}^{(**)} = \pm\sqrt{\left(\frac{1}{2}\right)^2 \cdot (12)^2 + \left(\frac{1}{2}\right)^2 \cdot (12)^2} = \pm 8.5 \text{ bars}$$

⇨ The uncertainty$^{(**)}$ of average density that comes from the best-fitted model are:

$$\text{The uncertainty}^{(**)} = \pm\sqrt{\left(\frac{1}{2}\right)^2 \cdot (0.007)^2 + \left(\frac{1}{2}\right)^2 \cdot (0.007)^2} = \pm 0.005 \text{ g. cm}^{-3}$$

The ultimate uncertainty = uncertainty$^{(*)}$ + uncertainty$^{(**)}$

⇨ **The final *PVX* properties calculated for FI3.4 are:**

- Composition = 72.4 ± 0.3 mol% CO_2
- Pressure = 277 ± (6.1 + 8.5) = 277 ± 15 bars
- Density = 0.643 ± (0.005 + 0.005) = 0.643 ± 0.010 g.cm^{-3}.

Table S. 2-4: Composition, pressure, and density of the volatile part of FIs obtained from Raman measurement at 32 °C.

FI name	mol% CO_2 [(a)]	mol% CO_2[(b)]	mol% CO_2[(c)]	Mean mol% CO_2[(d)]	Δ (cm^{-1})	Pressure[(e)] (bar)	Density[(f)] (g·cm^{-3})
1.1	73.3%	73.8%	72.4%	73.2%	104.050	285 ± 15	0.660 ± 0.010
1.2	73.0%	73.5%	72.1%	72.9%	104.050	289 ± 15	0.661 ± 0.010
1.4	72.6%	72.8%	72.2%	72.5%	103.783	189 ± 13	0.524 ± 0.010
2.1	83.3%	83.3%	83.3%	83.3%	103.787	128 ± 3	0.474 ± 0.008
2.2	84.0%	84.3%	83.6%	84.0%	103.803	126 ± 3	0.476 ± 0.010
3.1	71.4%	71.6%	71.0%	71.3%	104.000	287 ± 15	0.644 ± 0.010
3.2	72.4%	72.9%	71.6%	72.3%	104.007	276 ± 15	0.642 ± 0.010
3.3	73.5%	74.0%	72.5%	73.3%	104.077	296 ± 15	0.673 ± 0.010
3.4	72.5%	72.9%	71.9%	72.4%	104.010	277 ± 15	0.643 ± 0.010
3.5	79.9%	80.3%	79.1%	79.7%	104.210	266 ± 15	0.708 ± 0.010
3.6	79.9%	80.4%	79.2%	79.8%	104.207	263 ± 15	0.706 ± 0.010
4.2	79.4%	79.9%	78.7%	79.3%	104.153	244 ± 14	0.681 ± 0.010
4.4	80.1%	78.7%	79.6%	79.5%	104.153	244 ± 14	0.681 ± 0.010
4.5	81.5%	80.4%	81.1%	80.1%	104.180	247 ± 14	0.691 ± 0.010
4.8	81.2%	80.5%	80.9%	80.9%	104.193	242 ± 14	0.694 ± 0.010

Chemical Geology 552 (2020) 119783

Contents lists available at ScienceDirect

Chemical Geology

journal homepage: www.elsevier.com/locate/chemgeo

Chapter 3: Calibration data for simultaneous determination of *PVX* properties of binary and ternary CO_2 - CH_4 - N_2 gas mixtures by Raman spectroscopy over 5 - 600 bar: Application to natural fluid inclusions

Article soumis le 24 février 2020 et publié le 20 juillet 2020

dans Chemical Geology.

DOI : /10.1016/j.chemgeo.2020.119783

Van-Hoan Le* [a], Marie-Camille Caumon [a], Alexandre Tarantola [a], Aurélien Randi [a], Pascal Robert [a] and Josef Mullis [b]

[a] *Université de Lorraine, CNRS, GeoResssources Laboratory, BP 70239, F-54506 Vandoeuvre-lès-Nancy, France*

[b] *Department of Environmental Sciences, University of Basel, Bernoullistrasse 32, 4056, Basel, Switzerland*

Chapter 3, entitled "*Chapter 3: Calibration data for simultaneous determination of PVX properties of binary and ternary CO_2-CH_4-N_2 gas mixtures by Raman spectroscopy over 5-600 bar: Application to natural fluid inclusions*", has been published in the revue Chemical Geology on 20 July 2020.

In the previous chapter (**Chapter 2**), the experimental protocol, including the preparation of gas mixtures, the verification of composition by gas chromatography, the Raman analyses procedure and the data processing, has been successfully applied to provide high accuracy calibration data for the determination of the *PTX* properties of CO_2-N_2 mixtures of any composition at a fixed temperature (22 and 32 °C) and over a pressure range of 5-600 bars.

In **this chapter**, we further extended the analysis protocol to other binary and ternary gas mixtures. Therefore, a similar analytical procedure was performed to develop the calibration data for the CH_4-N_2 and CO_2-CH_4 mixtures at the highest accuracy. Numerous regression polynomial calibration equations fitted from the experimental data (collected at 22 and 32 °C) were specifically provided for different composition-pressure ranges. For the first time, our calibration data also gives the possibility to determine the *PVX* properties of the CO_2-CH_4-N_2 ternary mixtures at any composition directly from the CO_2 Fermi diad splitting. Applying the new calibration data to analyze a set of natural fluid inclusions always showed a good agreement with the results derived from phase transition temperatures during microthermometry experiments. Besides, we reasonably interpreted the variation of the CH_4 peak position based on the change of the intermolecular distance. A general discussion about the applicability and the reproducibility of the calibration data was also addressed by comparing the results with those published in the literature.

Abstract

The *PVX* properties of two-component fluid inclusions (FIs) are generally determined from microthermometry data using appropriate thermodynamic models (i.e., *VX* diagrams) and/or equations of state (EoS). However, some limitations can hamper the applicability of this technique such as the small size, low density or complex composition of the analyzed FI. Raman spectroscopy is known as the best-suited alternative method to microthermometry for the investigation of natural FIs because it can simultaneously provide non-destructive qualitative and possible quantitative analyses after specific calibrations. The present work aims to provide calibration data to directly determine the *PVX* properties of binary or ternary mixtures of CH_4, CO_2, and N_2. The variation of spectral features as a function of composition and pressure (or density) was investigated by using Raman spectroscopy coupled with an improved High-Pressure Optical Cell (HPOC) system and a customized heating-cooling stage. From our experimental data, the relative Raman scattering cross-section (RRSCS) of CH_4 ($\nu^*_{CH_4}$) was demonstrated to be constant at 7.73 ± 0.16 over the investigated range of pressure (5-600 bars) and for any composition. This parameter can thus be used for the determination of composition with an uncertainty of ~0.5 mol%. Several calibration equations were calculated for different *PX* domains, linking the Fermi diad splitting of CO_2 (Δ) or the relative variation of the CH_4 peak position ($\nu^*_{CH_4}$) to the pressure (or density) and composition of CO_2-CH_4, CH_4-N_2, and CO_2-N_2-CH_4 mixtures at 22 and 32 °C. The pressure and density of the fluids can henceforth be directly measured from Raman spectra with an uncertainty of ~ 20 bars and ~ 0.01 g·cm^{-3}, respectively. Our calibration equations were then validated on natural FIs by comparing the results obtained from Raman and microthermometry. We also interpreted the variation of the peak position of CH_4 based on the change of intermolecular interaction. Finally, we discussed the applicability of the obtained calibration data into another laboratory by comparing it with the data of pure CO_2 and CH_4 published in literature. A small shift between calibration curves implies a systematic error which is perhaps due to the difference in the configuration or the day-to-day deviation of the instruments. Therefore, standards of well-known *PVX* properties should be regularly measured to prevent and to correct any variation or shifting of the instrumental responses.

Keywords: *Raman spectroscopy, gas mixtures, densimeter, barometer, high-pressure optical cell system, CO_2 Fermi diad splitting, fluid inclusions.*

1. Introduction

Geological fluids containing water (± salt) and gases are the essential vectors of heat and matter within the Earth's crust and mantle (Poty, 1967; Fyfe et al., 1978; Etheridge et al., 1983; Thompson and Connolly, 1992). CO_2, CH_4, and N_2 are the most common gaseous species omnipresent in various geological environments such as sedimentary basins (Benson and Cole, 2008; Fall et al., 2012; Lammers et al., 2015; Huang et al., 2018), diagenetic, low- and high-grade metamorphic rocks (Poty et al., 1974; Hollister and Burruss, 1976; Mullis, 1979; Frey et al., 1980; Mullis, 1987; Van den Kerkhof, 1988; Mullis et al., 1994; Touret, 2001; Van den Kerkhof and Thiéry, 2001; Tarantola et al., 2007), igneous rocks (Seitz et al., 1993), hydrothermal vent fluids at near mid-ocean ridges (Kelley, 1996; Charlou et al., 2002), and hydrothermal ore deposits (Roedder, 1979b; Roedder and Bodnar, 1997; Diamond, 1990; Wilkinson, 2001; Bodnar et al., 2014). Natural fluid inclusions (FIs) are micro-volumes of geological fluids trapped within minerals during or after crystal growth. Thereby, they are assumed to preserve the *VX* conditions of paleo-fluid circulations, so, become the most reliable samples of actual ancient geologic fluids. Investigating FIs is, therefore, an unavoidable step to get that useful information for the reconstruction of *PT* history and the interpretation of different geological processes such as the source conditions, the mechanisms of mass and heat transportation involved in the precipitation and crystallization of rocks and host minerals, etc. (cf. reviews by Roedder, 1984 and Chi et al., 2003).

Microthermometry, a method based on the observation of phase transition temperatures, is currently the standard non-destructive method used for the investigation of fluid inclusions. The molar volume of one-component inclusions (i.e. pure CO_2, CH_4, or N_2) can be directly derived from the homogenization temperature using either empirical thermodynamic models or a proper equation of state (EoS) (Angus et al., 1976, 1979; Schneider, 1979; Duschek et al., 1990; Wagner and Pruss, 1993; Thiéry et al., 1994a; Bakker and Diamond, 2000; Van den Kerkhof and Thiéry, 2001; Akinfiev and Diamond, 2010).

Regarding carbonic inclusions of binary systems, the Gibb's phase rule implies that one more phase transition temperature is required for the determination of both molar fraction (*X*) and molar volume (*V)*. Several thermodynamic models were dedicatedly established for CO_2–N_2 and CH_4–CO_2 gas mixtures to directly infer the *VX* properties from the melting temperature T_m(vol) and homogenization temperature T_h(vol) of the volatile carbonic phase (Burruss, 1981; van den Kerkhof, 1990; Thiéry et al., 1994a). Refined from the previously

published models, the *VX* diagrams of Thiéry et al. (1994a) are known as the most accurate and practical ones available in literature. However, the disadvantage of these models is that Thiéry et al. (1994a) used two EoS, namely Soave (1972) to reproduce *PTX* values for liquid-vapor (LV) equilibria, and Lee and Kesler (1975) for density calculation, that may cause an incoherency of various fluid parameters (Bakker and Diamond, 2000). Using *VX* diagram of Thiéry et al. (1994), the uncertainties on measured composition and density arising from the error of T_m(vol) and T_h(vol) (~ ± 0.1 °C) could reach up to ± 5 mol% and ± 0.09 g·cm^{-3}, respectively, depending on *VX* domains (Le et al., 2019).

Otherwise, the *VX* properties of fluid inclusions could not be obtained by only using microthermometry, but must be combined with Raman spectroscopy, in the following cases:

(i) Since the temperatures of the triple points of pure CO_2, CH_4, and N_2 are – 56.6, – 182.5 and – 210 °C, respectively, mixing CO_2 with either CH_4 or N_2 will accordingly lower the T_m(vol). Thus, in the cases of CO_2-rich FIs (>80 mol% CO_2), the T_m(vol) obtained by microthermometry can be only used for checking the purity of CO_2 (Van den Kerkhof and Thiéry, 2001), and not for distinguishing between CO_2–CH_4 or CO_2–N_2 mixtures. Therefore, an additional Raman qualitative analysis is needed to confirm the actual composition of the binary system for choosing the appropriate *VX* diagram.

(ii) The binary (CH_4-N_2) and ternary (CO_2-CH_4-N_2) mixtures are rare in nature but were also recognized in different geological settings (Van den Kerkhof, 1988; Noronha et al., 1992; Mullis et al., 1994; Cathelineau et al., 2017; Caumon et al., 2019). Since the melting temperature of CH_4-N_2 mixtures is normally unreachable (under – 182.5 °C) with conventional microthermometry (cooling by liquid nitrogen), only the homogenization temperature occurring below – 82.6 °C is observable, insufficient for the direct determination of *VX* properties. Microthermometry analyses of the ternary CO_2-CH_4-N_2 mixtures are also somewhat limited due to the complex phase behavior (Van den Kerkhof, 1988; Hurai et al., 2015). To the best of our knowledge, there was no available experimental diagram for the direct determination of *PVX* properties from microthermometry measurements only. Therefore, the composition of such systems (binary CH_4-N_2 and ternary CO_2-CH_4-N_2), in many cases, must be separately determined from Raman measurement (Hurai et al., 2015, p. 97), then coupled with microthermometry data and an EoS for further determination of density and or pressure.

(iii) Gas hydrate phase can be formed during cooling-heating microthermometric experiments of high CO_2- (or CH_4-) bearing FIs and may remain above the homogenization of the volatile part of FI (T_h(vol)), or ice melting temperature (T_m(ice)) which, in turn, may affect the measured density (or salinity) deduced from T_h(vol) (or T_m(ice)) only (Mullis, 1975, 1979; Collins, 1979; Diamond, 1992; Fall et al., 2011). This problem can be solved by using T_h(vol) and the final clathrate melting temperature T_m(cla) (DENSITY computer program by Bakker, 1997) (Diamond, 1994). However, one of the prerequisites of this program is the molar fraction of CO_2 and/or CH_4 and/or N_2 in the homogeneous carbonic phase. That means, once again, an additional Raman quantitative analysis is needed to be combined with microthermometry data.

Other limitations of microthermometry also appear when analyzing FIs of small size (<~5 µm), of low density, and of even more complex composition without any observable phase transition (Rosso and Bodnar, 1995; Burke, 2001; Yamamoto et al., 2002; Kawakami et al., 2003; Yamamoto et al., 2007; Song et al., 2009).

Raman spectroscopy has been used since the 1970s for the study of natural fluid inclusions as a complementary method to microthermometry in different circumstances (as described above, and cf. review by Burke, 2001, Frezzotti et al., 2012, and Dubessy et al., 2012). It can offer fast (from a few seconds to a few minutes), high resolution (~ 1 μm^2), and simultaneous non-destructive, multi-gases qualitative and quantitative analyses.

Generally, the molar fraction of gases can be measured from their peak areas if the Raman scattering cross-sections relative to that of N_2 (RRSCS) are known accurately. The review by Schrötter and Klöckner (1979) collected the RRSCSs of the most relevant gases in geological fluids and provided a detailed discussion about the dependence of this parameter. Indeed, the temperature and wavenumber dependence of RRSCS is minimal (< 1%) and can be negligible (Schrötter and Klöckner, 1979). However, the pressure and composition dependence of RRSCS is still questionable (Wopenka and Pasteris, 1986; Dubessy et al., 1989; Chou et al., 1990; Seitz et al., 1993, 1996). Indeed, every published RRSCS values were obtained on pure gases at low pressure (1 - 5 bars) and room temperature with an uncertainty varying from 5 to 20% and never reevaluated again (Burke, 2001), whereas natural FIs contain in many cases a gas mixture at elevated pressure. Using these old data may lead to considerable errors. Le et al. (2019) reevaluated the variation of RRSCS of two CO_2 bands and concluded that there is no correlation with the variation of the composition, but the RRSCS of the upper band (and lower band)

slightly increased (and decreased) as pressure increased. Although the variation of the RRSCS of CO_2 with pressure can be negligible over 5 - 600 bars, it is still worth to check the variation of RRSCS of CH_4 over this *PT* range, especially because the RRSCS of CH_4 (~ 7.7) is much greater than that of CO_2 (≤ 1.4).

Not only providing the molar fraction, Raman spectra also reflect the interactions between the incident photons and the vibrational energy (frequency) of gaseous particles which are affected by intermolecular interactions and internal field (e.g., attractive or repulsive forces by surrounding molecules, electrostatic potential, polarization energy change, etc.). Therefore, the peak position of the Raman spectrum is literally related to the density (or pressure) of pure gases and gas mixtures. Raman spectroscopy appears then to be the best-suited technique for the study of the volatile part of natural FIs, yielding simultaneously *PVX* properties from Raman measurement only. Aiming to develop another alternative way for FI investigation, several applications of Raman spectroscopy were carried out (cf. review by Burke, 2001, and Frezzotti et al., 2012). Several calibration data were published for single-component gases that showed the variation of the peak position, and Fermi diad splitting of CO_2 as a function of pressure (density) and/or temperature: N_2 (Wang and Wright, 1973; Fabre and Oksengorn, 1992; Lamadrid et al., 2018), CH_4 (Fabre and Oksengorn, 1992; Lin et al., 2007a; Lu et al., 2007; Caumon et al., 2014; Zhang et al., 2016; Lamadrid et al., 2018), and CO_2 (Wright and Wang, 1973; Garrabos et al., 1980, 1989; Rosso and Bodnar, 1995; Kawakami et al., 2003; Yamamoto and Kagi, 2006; Wang et al., 2011; Fall et al., 2011; Yuan et al., 2017; Lamadrid et al., 2017; Wang et al., 2019). It is to note that these calibrations were made only for the cases of a pure component.

The effect of composition on the variation of the spectral features of CO_2, CH_4, and N_2 was reported very early by analyzing a binary (Fabre and Oksengorn, 1992; Hacura, 1997) or a ternary mixture (Lamadrid et al., 2018). However, there is a paucity of accurate experimental data covering a full composition-range of binary CO_2-CH_4-N_2 subsystems. For instance, the relationship between the Raman spectral features (peak shape, width, peak area/intensity ratio, peak position, etc.), the pressure (or density), and the composition of CO_2-CH_4 and CH_4-N_2 binary mixtures were revealed by Seitz et al. (1993, 1996). However, the results were somewhat scattered due to the use of low spectral resolution (~ 5 cm^{-1}). Besides, although Fermi diad splitting (Δ) is much more reliable with good reproducibility, Seitz et al. (1996) did not study the variation of Δ but study that of a single peak of CO_2 (ν^+ and ν^-) with the variation of the composition of CO_2-CH_4 mixtures. Consequently, no robust calibration with uncertainty

analysis was given. Otherwise, the calibration data of CH_4-H_2 and CO_2-N_2 mixtures were recently provided by Fang et al. (2018) and Le et al. (2019), respectively, showing the capability of Raman spectroscopy to provide high-accurate quantitative analyses applicable for FI investigations. Furthermore, no calibration data for the CO_2-CH_4-N_2 ternary system by Raman spectroscopy is available yet in literature.

The present study aims (1) to redefine the RRSCS of the ν_1 band of CH_4 with considering the effect of composition and pressure, and (2) to establish Raman calibration data for binary and ternary mixtures of CO_2, CH_4, and N_2. For these purposes, Raman in-situ analyses of gas mixtures of known composition were performed at 22 and 32 °C (above the critical temperature of CO_2) over a pressure range from 5 to 600 bars thanks to an improved High-Pressure Optical Cell (HPOC) system coupled with a heating-cooling stage and a fused silica micro-capillary. The variations as a function of pressure and composition of the most reliable spectral parameters of each gas (Δ for CO_2, and peak position of the ν_1 band for CH_4) were thereby studied to provide the best-fitted regression calibration equations for the direct determination of *PVX* properties from Raman spectra. The latter were then applied to natural fluid inclusions hosted in quartz from the Central Alps, Switzerland (Mullis et al., 1994) and then compared with results from microthermometry for validation. Uncertainty analyses and applicability of our calibration were then discussed through a comparison with calibration data recently published in literature.

2. Material and Methods

The experimental protocol of the present study is similar to the one developed in our previous works (Le et al., 2019). It consists of three main steps (gas mixtures preparation, pressurization, in-situ Raman analyses and data processing – Figure A. 3-1 in Appendix A) that are detailed in the following subsections.

2.1. Preparation of binary and ternary gas mixtures

Binary and ternary gas mixtures of desired compositions were prepared from high-purity CO_2, CH_4, and N_2 (99.99 % purity, Air Liquide™) using a gas mixer (GasMix AlyTech™). They were subsequently compressed up to ~ 130 bars and stored in a stainless-steel cylinder by a home-made compressor system. After the pressurization step, a gas chromatograph previously calibrated with different commercially standard mixtures of known compositions (purchased from Air Liquide™) was used to double-check the actual composition of the

prepared gas mixtures. The final composition of the gas mixtures is given with uncertainty of ~ ± 0.3 mol% (1σ). In this study, the CH_4-N_2 and CO_2-CH_4 binary mixtures were constituted by ~ 10, 20, 30, 50, 60, 70, 80 and 90 mol% CH_4; the CO_2-CH_4-N_2 ternary mixtures were composed by ~ 90, 80, 50 and 33.3 mol% CO_2 with equal proportions of N_2 and CH_4, i.e., ~ 5, 10, 25 and 33.3 mol%, respectively.

2.2. Improved pressurization system

The HPOC system consists of a manual screw pressure-generator, a pump, two pressure-transducers (± 1 bar), and stainless steel microtubes connected by several valves (Chou et al., 2005, 2008; Garcia-Baonza et al., 2012; Caumon et al., 2014). A transparent fused silica micro-capillary (FSC) of 200 µm internal diameter was sealed at one end by a hydrogen flame (Caumon et al., 2013, 2014) and coupled to the HPOC system by the other end. Then it was set on a customized heating-cooling stage (Linkam CAP500). The temperature of the stage was previously calibrated against the triple point of distilled water (0.0 °C) and of pure CO_2 (– 56.6 °C). The system was purged under vacuum for about 30 minutes to remove any other gas before loading the gas mixture into the system. The advantage of our home-made system is that it requires neither mercury nor water for pressurization (Fang et al., 2018; Wang et al., 2019). Indeed, the total effective internal volume of the system is about some dozen µL (included the volume of the FSC, stainless steel microtubes, and valves), while that of the manual pressure generator is 20 mL. The pressure could be adjusted step-by-step from 5 to 600 bars by turning the manual pressure-generator. Thereby, the gas mixtures were analyzed by Raman spectroscopy through the transparent microcapillary at controlled *PTX* conditions.

2.3. In-situ Raman measurement and data processing

Raman analyses were carried out by a LabRAM HR spectrometer (Horiba Jobin-Yvon®) equipped with an 1800 groove·mm^{-1} grating and a liquid nitrogen-cooled CCD detector. The apertures of the confocal hole and of the slit width were respectively set at 1000 and 200 µm giving a spectral resolution of about 1.6 cm^{-1}. The excitation radiation was provided by an Ar^+ laser (Stabilite 2017, Spectra-Physics) at 514.532 nm with a power of 200 mW, focused in the transparent FSC through a ×20 objective (Olympus, NA = 0.4), or in natural FIs (of sizes <15 µm) through a ×50 Olympus (Olympus, NA = 0.5). Acquisition time was between 1 - 30 seconds per accumulation depending on the nature of the analyzed sample (FCS or natural IFs, the size, shape, and depth of natural FIs) for the optimization of the S/N ratio within a minimum measurement time. Each measurement was repeated successively six times (with ten

accumulations per measurement) at the same *PTX* conditions for statistical purposes. A spectrum was recorded before loading any gas mixture into the microcapillary for the subtraction of the signal of atmospheric N_2.

The Raman spectrum of N_2 exhibits a single band corresponding to the stretching vibration mode at ~ 2331 cm^{-1}, denoted by ν_1. The variation of the N_2 band as a function of pressure (5-600 bars) and composition (within CO_2-N_2 gas mixtures) was studied in our previous work (Le et al., 2019). This study demonstrated the modest reproducibility of the variation of the position of the N_2 band even after a wavelength calibration by a neon band at 2348.43 cm^{-1} (cf. Figure 5 in Le et al., 2019). Similar modest reproducibility of N_2 band within CH_4-N_2 mixtures was also observed in the experiments conducted in the present study (see Figure A. 3-3 in Appendix A). Indeed, although the same tanker containing the CH_4-N_2 mixture was used to repeat the analyses over several days, the obtained position of the N_2 band presented a noticeable difference (leading thus to non-systematic variation as the composition changes), whereas the variation of the peak position of associated CH_4 remained consistent (see section 3.2 below). Moreover, the magnitude of the variation is quite small (< ~ 3 cm^{-1} at 600 bars) compared to that of CH_4 (~ 7 cm^{-1} at 600 bars, see below). Thus, the following sections exclusively report the most reliable spectral parameters, i.e., the variation of the peak position of the ν_1 band of CH_4 (ν_{CH_4}) and the Fermi diad splitting of CO_2 (Δ) as a function of pressure (or density) and composition of gas mixtures.

The Raman spectrum of CH_4 is characterized by a major band corresponding to the symmetric stretching mode (ν_1) at ~ 2917 cm^{-1}. The Raman spectrum of CO_2 is characterized by two strong bands (denoted ν^+ at ~ 1385 cm^{-1} and ν^- at ~ 1288 cm^{-1}) arising from the so-called Fermi resonance effect occurring between the symmetric stretching vibration mode (ν_1) and the first overtone of bending vibration mode ($2\nu_2$) (Fermi, 1931). Besides, there are two weak bands at the outer sides of both main bands of CO_2 (at ~ 1409 cm^{-1} and 1265 cm^{-1}, assigned to hot bands) and a weak band at 1370 cm^{-1} assigned to the signal $^{13}CO_2$. Extended interpretation of the spectral features of CO_2 can be found in literature (Placzek, 1934; Amat and Pimbert, 1965; Howard-Lock and Stoicheff, 1971; Bertrán, 1983). Since the intensities of the hot bands are too small, there are not of clear interest for our quantitative calibration purpose. In the present work, the interesting spectral parameters include the ν_1 band of CH_4, and the two main bands ν^+ and ν^- of CO_2.

The spectra of CO_2, N_2 and CH_4 were recorded over three different spectral windows from 1100 to 1580 cm^{-1}, from 2100 to 2525 cm^{-1} and from 2675 to 3050 cm^{-1}, respectively. They were processed, after baseline subtraction, by an asymmetrical Gaussian-Lorentzian function from the peak fitting tool of LabSpec 6 software (HORIBA). The fitted peak position of the CH_4 band (ν_{CH_4}) was then corrected ($\nu_{CH_4}^{corrected}$) against two closely well-known emission lines of neon (ν_{Ne}^{1} at 2851.38 cm^{-1} and ν_{Ne}^{2} at 2972.44 cm^{-1}) using Equation 1 of Lin et al. (2007a). The reference value of ν_{Ne}^{1} and ν_{Ne}^{2} are cited from NIST Chemistry webbook (Kramida et al., 2018). Because the two main bands of CO_2 were recorded by a single measurement and that only the variation of CO_2 Fermi diad splitting (the difference between the two bands) was studied, no peak position correction was required for the case of CO_2 (Fall et al., 2011). The uncertainties of spectral features were determined from six consecutive measurements, yielding an uncertainty of about ± 0.4 % in peak area values, ± 0.01 cm^{-1} in the fitted peak position of a single band of CH_4 and CO_2, and ± 0.015 cm^{-1} in Fermi diad splitting value of CO_2 (1σ).

2.4. Microthermometry analyses of natural fluid inclusions

Microthermometry measurements of natural fluid inclusions were performed using a THMS600 heating-cooling stage coupled with an Olympus BX50 microscope. The calibration of temperature was carried out with standard inclusions of pure CO_2 (– 56.6 °C) and pure H_2O (0.0 °C), yielding an uncertainty of about ±0.1 °C. Natural prismatic quartz crystals (Ta15, Mu618 and Mu1381) were collected in the CH_4-zone in the late Alpine tension gashes from the Central Alps, Switzerland (Mullis et al., 1994; Tarantola et al., 2007). They contain one- and two-phase < ~ 25 µm pseudo-secondary CH_4-dominated FIs mixed with CO_2 or N_2. Two-phase aqueous-dominated fluid inclusions hosted in a quartz sample from the W-Cu-Sn deposit of Panasqueira (Portugal) (denoted PAN-V3) were also selected for the analysis of their vapour, which contains a ternary CO_2-CH_4-N_2 mixture (Figure 3-1) (Noronha et al., 1992; Cathelineau et al., 2017; Carocci et al., 2019; Caumon et al., 2019).

Both homogenization (T_h(vol)) and melting (T_m(vol)) temperatures of the volatile phase could be observed in the FIs of sample Ta15. Therefore the *VX* properties could be directly obtained from the *VX* diagrams for CH_4-CO_2 gas mixtures of Thiéry et al. (1994a). In reason of the very low triple points of CH_4 and N_2 (– 182 and –210 °C, respectively), measuring the melting temperature of the CH_4-N_2 mixture in the volatile phase of the FIs of sample Mu1381 was not possible with our heating-cooling stage instrument, which operates in the range – 180

to 600 °C. Also, the melting temperature of CO_2-CH_4 phases within the FIs of selected Mu618 samples could not be observed due to the small size and the low density of the fluids. Therefore, only the homogenization temperature could be accurately determined, and so the composition of these FIs could only be fully determined from Raman analyses. The molar volume (density) and pressure were obtained from the homogenization temperature and composition of the volatile phases using an appropriate EoS. In the case of the fluid inclusions hosted in sample PAN-V3, no phase transitions were observed in the carbonic phase. Only the existence of clathrate pointed out the presence of low-density gas in these FIs.

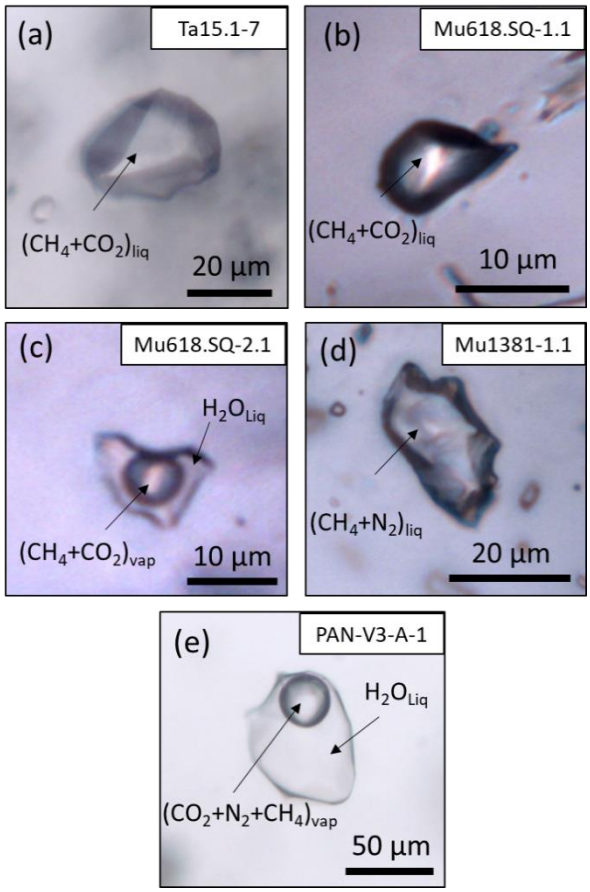

Figure 3-1: Microphotographs of selected FIs at room temperature trapped within the sample Ta15.1, Mu168.SQ, Mu1381 and PAN-V3. Monophasic FIs containing a liquid composed of CH_4-CO_2 (a, b) or of CH_4-N_2 (d); Biphasic FI containing H_2O liquid and a bubble of CO_2-CH_4 vapor (c) and of CO_2-N_2-CH_4 vapor (e).

In the present work, the GERG-2004 EoS, integrated into REFPROP software (Lemmon et al., 2013), was chosen because it is known as the most accurate available EoS. Concerning the binary and ternary mixtures of CH_4, CO_2, and N_2, the GERG-2004 EoS were fitted from more than 3300 experimental data points, and cover large pressure and temperature ranges, up

to 5000 bars and over – 53 to 400 °C (Kunz, 2007). The uncertainties in density were claimed less than 0.5%.

3. Experimental results

3.1. Reevaluation of the RRSCS of CH_4 for molar fraction determination

Based on the polarizability theory of Raman scattering by Placzek (1934), the RRSCS of the ν_1 band of CH_4 (σ_{CH_4}) is calculated from the peak area of CH_4 and N_2 bands (A_{CH_4} and A_{N_2}), their molar fraction (C_{CH_4} and C_{N_2}) and instrumental efficiency at their respective position (ζ_{CH_4} and ζ_{N_2}) using Equation 3.1 (Pasteris et al., 1988). Since our Raman spectrometer was calibrated using a white lamp of known emission (Raman Calibration Accessory, Kaiser Optical System, Inc) and all Raman spectra were corrected by an ICS function (Intensity Correction System) integrated into Labspec 6 software (HORIBA), the instrumental efficiencies at the wavelength of CH_4 (ζ_{CH_4}) and N_2 (ζ_{N_2}) bands are thereby identical (Dubessy et al., 2012).

$$\sigma_{CH_4} = \frac{A_{CH_4} \cdot C_{N_2} \cdot \zeta_{N_2}}{C_{CH_4} \cdot A_{N_2} \cdot \zeta_{CH_4}} \qquad 3.1$$

σ_{CH_4} was plotted as a function of pressure and composition of CH_4-N_2 mixtures (Figure 3-2). In general, σ_{CH_4} remains constant as pressure increases. The latter result agrees well with the study of Fabre and Oksengorn (1992) where the authors reported the constancy of the peak area ratio up to 3000 bars. A shift between the curves of different concentrations is not significant as this can be due to small errors in the measured composition of gas mixtures. Otherwise, the irregular deviation of the σ_{CH_4} values were observed exclusively at a low-pressure range (< ~70 bars). A similar deviation of the variation of A_{CH_4}/A_{N_2} ratio at low pressure was also observed by Fabre and Oksengorn (1992) and Seitz et al. (1993). This deviation could be explained by two reasons:

(1) The error in the fitted N_2 peak area and the subtraction of the atmospheric N_2 peak area. Indeed, the peak of N_2 is asymmetric at low density and becomes more and more symmetric with increasing density (Musso et al., 2002, 2004). Measuring the peak area of an asymmetric band may cause a higher error than for symmetric one. Especially at low pressure, the peak of N_2 in microcapillary (> 5 bars) and in the atmosphere (1 bar) are quite interfered. Besides, the intensity (or area) of the N_2 band at low pressure (or

density) is much smaller than that of CH_4. Thus, a small fluctuation of N_2 intensity (or area) value can result in an important variation of the A_{CH_4}/A_{N_2} ratio.

(2) The variation of the peak area ratio also reflects the change of the effective scattering efficiency of each individual gas that are sensitive to the change of internal field (which is quantified by the refraction index) with increasing density (Eckhardt and Wagner, 1966; Schrötter and Klöckner, 1979; Dubessy et al., 1989). Otherwise, the effect of intermolecular interaction change is rather small at low pressure range, and so negligible (see in the subsection 3.2). According to the experimental data of Fabre and Oksengorn (1992) and Seitz et al. (1993), the internal field increases with density and might reach its maximum at around 50 - 75 bars, then do not change up to 3 kbar.

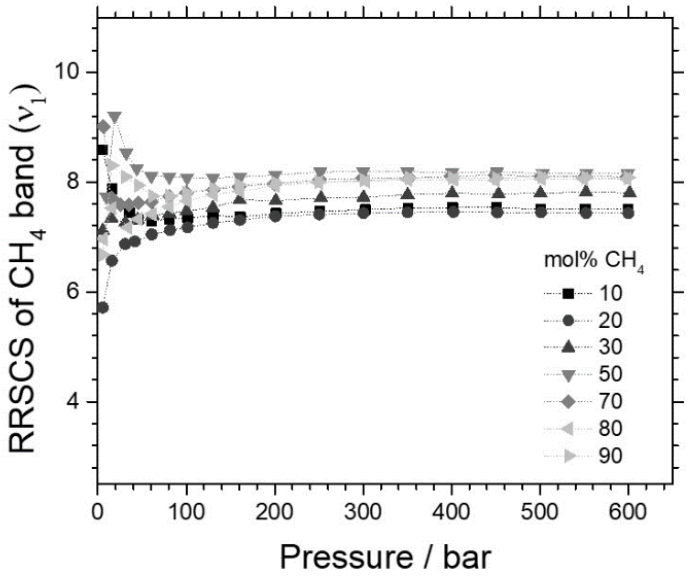

Figure 3-2: Pressure and composition dependence of the RRSCS of the CH_4 band (ν_1) in CH_4-N_2 binary mixtures.

Overall, we can now confirm the independence of σ_{CH_4} on pressure (or density) and composition. The average value of the σ_{CH_4} measured from 127 experimental data points over all the studied pressure range is 7.73 ± 0.16 (1σ) corresponding to an error of about ± 0.5 mol%. In the low-pressure range, the uncertainty of the average values of σ_{CH_4} is slightly higher (± 0.3), that in turn, can cause an error of up to ± 2 mol%. However, the latter error can be negligible upon the determination of pressure or density of gas mixture because the effect of the composition on density is not appreciable at < 50 bars (see the following sections). Table 3-1 shows a comparison of our results to values published in literature. There is a slight

difference, but our experiments provide better accuracy. Note that RRSCS of CH_4 was evaluated using an excitation wavelength of 514.5 nm. RRSCS value for other excitation wavelengths can be calculated from result obtained herein using Equation 11 in Garcia-Baonza et al. (2012).

Table 3-1: Comparison of RRSCSs of CH_4 band (ν_1) at 514.5 nm.

	This study	Fouche and Chang (1971b)	Penney et al. (1972)	Dubessy et al. (1989)	Seitz et al. (1993)
Pressure (bar)	5-600	2.35	-	≤ 1	7-700
σ_{CH_4}	7.73 ± 0.16	8.0	7.7 ± 0.4	7.57	7.39 ± 0.2

3.2. Evolution of Raman spectral features as a function of composition, pressure, and density

3.2.1. Variation of the CH_4 peak position

Figure 3-3a and b represent the variation of the corrected peak position of methane ($\nu_{CH_4}^{corrected}$) as a function of pressure and composition in CH_4-N_2 and CO_2-CH_4 gas mixtures, respectively. In general, $\nu_{CH_4}^{corrected}$ decreases as pressure increases in both cases. However, the effect of the composition on the variation of $\nu_{CH_4}^{corrected}$ is completely different. More discernible composition effects were observed for CH_4-N_2 mixtures than for CO_2-CH_4 ones. Indeed, while pressure increases from 5 to 600 bars the downshift of $\nu_{CH_4}^{corrected}$ reduced from ~ 6.76 cm^{-1} (pure CH_4) to ~ 1.86 cm^{-1} for the CH_4-N_2 mixture of 10 mol% CH_4, but reduced only to 5.90 cm^{-1} for the CO_2-CH_4 mixture of 10 mol% CH_4. Otherwise, with the diminution of the CH_4 content, the downshift of $\nu_{CH_4}^{corrected}$ within CH_4-N_2 mixtures gradually decreases over the entire studied pressure range (Figure 3-3a), whereas the downshift of $\nu_{CH_4}^{corrected}$ within CH_4-CO_2 mixtures increases between 80 and ~ 300 - 400 bars then decreases as pressure increases further (Figure 3-3b). The difference between these variation trends of CH_4 peak position in mixtures with N_2 and CO_2 is further interpreted based on intermolecular interaction changes in the discussion section.

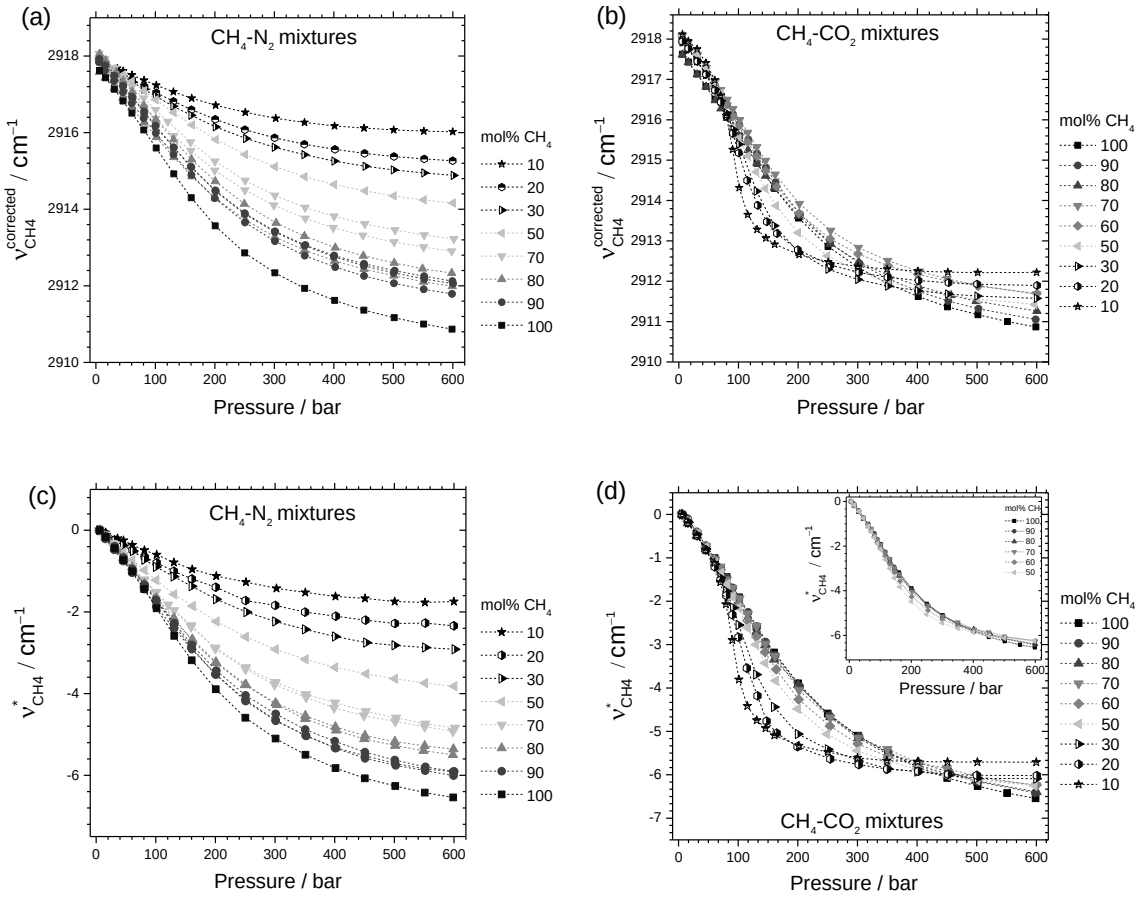

Figure 3-3. (a) Variation of the corrected peak position of the ν1 band of CH_4 ($\nu_{CH_4}^{corrected}$) within CH_4-N_2 gas mixtures as a function of pressure and composition. Reproducibility tests were performed by analyzing two times the mixtures of 70 and 80 mol% CH_4 and three times the mixtures of 90 mol% CH_4. Calibration curves of the same concentration obtained in different days are parallel indicating a day-to-day-systematic error (see text). (b) Variation of $\nu_{CH_4}^{corrected}$ within CH_4-CO_2 gas mixtures as a function of pressure and composition. (c) Relative variation of the fitted CH_4 peak position ($\nu_{CH_4}^{*}$) as a function of pressure and composition of CH_4-N_2 and (d) CH_4-CO_2 gas mixtures. The insert in figure (d) is plotted only for calibration data for the mixtures of ≥ 50 mol% CH_4.

Reproducibility tests were performed by analyzing two or three times the mixtures of 70, 80 and 90 mol% CH_4. The calibration curves of the same concentrations (represented in Figure 3-3a) obtained at different days are parallel, indicating a systematic day-to-day error. The latter error can be explained by the fact that our neon lamp was not permanently fixed in the optical path of the Raman spectrometer, resulting in the variation of the shape and so, of the fitted peak position of the neon lines. That, in turn, leads to a variation upon the peak position correction using Equation (1) in Lin et al. (2007a). As a result, the whole data set collected within the same day was shifted by an identical error. This problem was also reported in our previous

study of the N_2 peak position within the CO_2-N_2 mixtures (Le et al., 2019). Therefore, a higher-accurate method of wavelength correction is needed for any quantitative measurements based on the absolute corrected peak position value. To avoid the day-to-day systematic error, we studied the relative variation (or the variation of the downshift) of the fitted CH_4 peak position ($\nu^*_{CH_4}$) calculated by Equation 3.2, where $\nu^{i}_{CH_4}$ is the fitted peak position of CH_4 measured at i bar (i ranges from 5 to 600 bars), $\nu^{5\ bar}_{CH_4}$ is the fitted peak position of CH_4 at ~5 bars of a standard (cf. Appendix A).

$$\nu^*_{CH_4} = \nu^{i}_{CH_4} - \nu^{5\ bars}_{CH_4} \qquad 3.2$$

Figure 3-3c represents the variation of $\nu^*_{CH_4}$ as a function of pressure and composition of CH_4-N_2 gas mixtures. The curves of 70 and 90 mol% CH_4 are now nearly superimposed and can be clearly distinguished from the curve of 80 mol% CH_4, indicating the excellent reproducibility of $\nu^*_{CH_4}$ all over the studied pressure-composition range (Figure 3-3c). The reproducibility of $\nu^*_{CH_4}$ was also improved for the case of CH_4-CO_2 mixtures (Figure 3-3d). Compared with Figure 3-3b, the evolution of the calibration curves represented in Figure 3-3d shows a better correlation with the variation of mixture compositions.

The total pressure of the gas mixtures of known composition at a given temperature was converted to density using GERG-2004 EoS. Figure 3-4a and b represent the relationships between $\nu^*_{CH_4}$, the calculated density and the composition of CH_4-N_2 and CO_2-CH_4 gas mixtures, respectively, which can be used as densimeters for direct density determination.

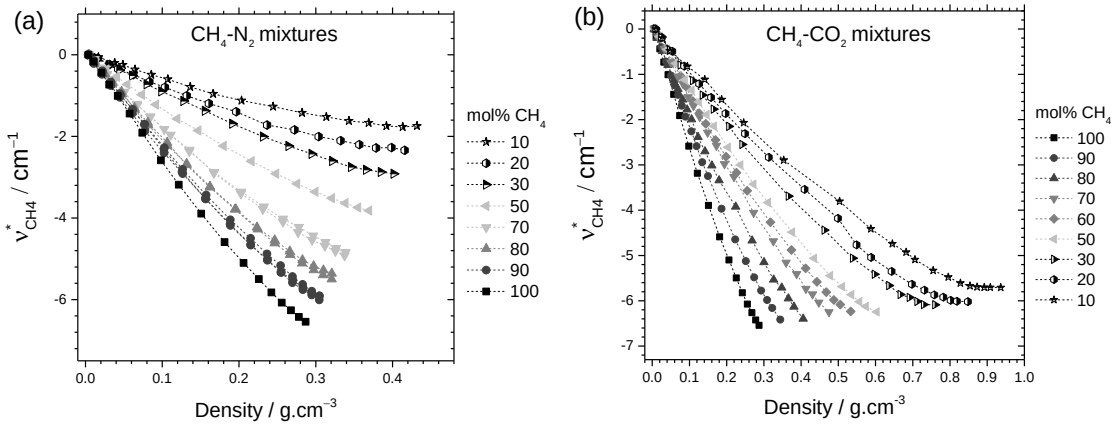

Figure 3-4. Relative variation of the fitted CH_4 peak position ($\nu^*_{CH_4}$) as a function of density and composition of (a) CH_4-N_2 and (b) CH_4-CO_2 gas mixtures. The density was calculated from a given pressure and composition using GERG-2004 EoS.

3.2.2. Variation of the CO_2 Fermi diad splitting

The relationship between the Fermi diad splitting of CO_2 (Δ), pressure, and composition of the CO_2-CH_4 gas mixture plotted in Figure 3-5 shows similar behavior with that observed for CO_2-N_2 gas mixtures (cf. Fig. 6 in Le et al. (2019)). In general, Δ increases with increasing pressure. The effect of composition on the variation of Δ is rather small at low-pressure but more pronounced at high-pressure. For instance, the magnitude of the total Δ variation of pure CO_2 is about ~2.583 cm^{-1} (increased from 102.765 cm^{-1} at 5 bars to 105.348 cm^{-1} at 600 bars) and gradually diminishes with the increase of the CH_4 content, down to ~0.5 cm^{-1} for the CO_2-CH_4 of 90 mol% CH_4 (Figure 3-5).

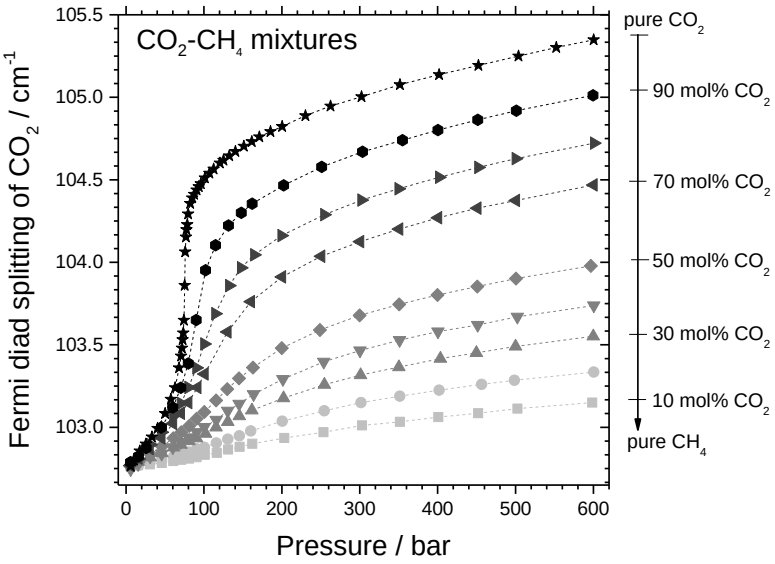

Figure 3-5. Variation of CO_2 Fermi diad splitting (Δ) at 32 °C as a function of pressure and composition of CO_2-CH_4 gas mixtures.

The variation of Δ as a function of density (calculated from a given pressure, temperature and composition using GERG-2004 EoS) and composition of the CO_2-CH_4 gas mixture is plotted in Figure 3-6. Δ increases with increasing CO_2 content and density of the gas mixture. Otherwise, a drastic increase of Δ value was observed for the pure CO_2 at ~ 74 bars (Figure 3-5). It is because all Raman analyses were made at ~ 32 °C, very close to the critical point of CO_2. At that *PT* point, a small fluctuation of either pressure or temperature can result in a significant variation of density. Besides, we noted that the Δ-density calibration curve of pure CO_2 is nearly superimposed with that of the mixture with 10 mol% CH_4 which agrees well with the statement of Wang et al. (2011) "*The calibration data of pure CO_2 can be applied for CO_2-*

CH_4 mixtures of less than 10 mol% CH_4". For instance, at $\Delta = 105$ cm^{-1}, the calculated pressure for pure CO_2 and for the CO_2-CH_4 mixture of 10 mol% CH_4 is 293 and 561 bars, respectively (268 bars of difference), but the calculated densities are very close, i.e., 0.940 g·cm^{-3} for pure CO_2 and 0.925 g·cm^{-3} for the mixture (0.015 g·cm^{-3} of difference).

Overall, the experimental results indicate that Δ is a reliable parameter for monitoring pressure (or density) of CO_2-CH_4 mixtures. Notably, it presents a good reproducibility without any wavelength correction, making it a robust and practical spectral parameter for quantitative analysis.

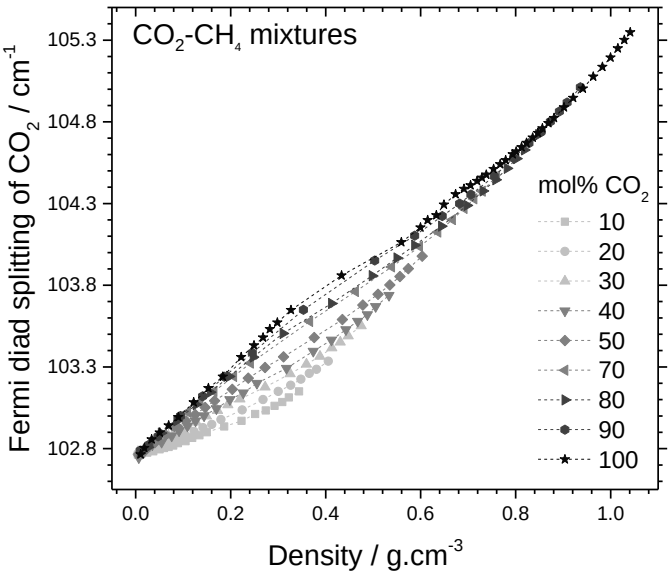

Figure 3-6. Variation of CO_2 Fermi diad splitting (Δ) as a function of density and composition of CO_2-CH_4 gas mixtures. The density was calculated by GERG-2004 EoS at a given temperature, pressure, and composition.

3.2.3. Effect of temperature on the variation of Raman spectral parameters

All calibration data presented above were performed at 32 °C (above the critical temperature of pure CO_2) to avoid the biphasic L-V domain of any gas mixtures, and to combine with the calibration data set of Le et al. (2019) for ternary mixtures analyses. The calibration of CO_2-CH_4 mixtures was also performed at 22 °C to examine the effect of temperature on the variation of Δ and $\nu^*_{CH_4}$ with pressure (or density) and composition. All calibration data obtained at 22 °C can be found in Appendix B (Figure B. 3-1 and Figure B. 3-3) and in Supplementary Material.

The effect of temperature on the variation of Δ for CO_2-CH_4 mixtures is very similar to that observed for CO_2-N_2 mixtures (Le et al., 2019) (Figure B. 3-2 in Appendix B). Indeed, at the same pressure and composition, Δ is shifted toward higher wavenumbers at 22 °C compared to 32 °C (Figure B. 3-2-a). However, the Δ-density relationships obtained at 22 et 32 °C are almost superimposed (Figure B. 3-2-b). Slight differences, of up to 0.02 g·cm^{-3}, are noticed for some concentration ranges in good agreement with the observation of Wang et al. (2011) and Wang et al. (2019).

Also, the effect of temperature was observed for the variation of $\nu^*_{CH_4}$ as a function of pressure and composition with a downshift toward lower wavenumbers as temperature decreases (Figure 3-7a). Figure 3-7b presents the variation of $\nu^*_{CH_4}$ as a function of density, composition, and temperature. Overall, the difference between the two calibration data sets obtained at 22 and 32 °C is discernible but rather small, less than about 0.015 g.cm^{-3}. The latter observations confirm that the calibration should be dedicatedly provided for each temperature to minimize the error due to the effect of temperature on the variation of spectral parameters.

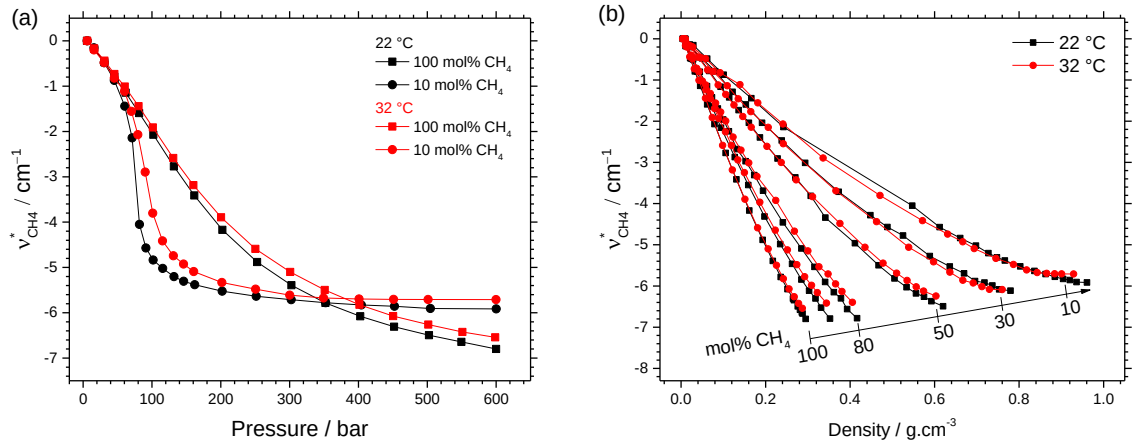

Figure 3-7. Effect of temperature on the variation of $\nu^*_{CH_4}$ as a function of (a) pressure and (b) density of CO_2-CH_4 mixtures.

3.3. Calibration polynomial equations for pressure and density determination

3.3.1. Determination of pressure and density of CH_4-N_2 and CO_2-CH_4 binary gas mixtures

Both Δ and $\nu^*_{CH_4}$ can be used as a parameter sensitive to the variation of pressure (or density) and composition for the determination of pressure and density of gas mixtures. Note that Δ can be directly measured from any CO_2 Raman spectrum whereas $\nu^*_{CH_4}$ requires a reference value of the peak position of pure CH_4 (or mixtures of CH_4) at 5 bars ($\nu^{5\,bar}_{CH_4}$)

according to Equation 3.2. A sealed transparent microcapillary containing ~ 5 bars (± 1) of pure CH_4 were made for the wavelength correction (called CH_4 standard, Figure A. 3-2 – Appendix A). The CH_4 standard should be analyzed before and/or after analyzing the actual sample to evaluate any spectrometer calibration deviation.

In the CH_4-N_2 gas mixtures, only $\nu^*_{CH_4}$ could be used for pressure and density measurement. The variation of the N_2 peak position should not be used because of its moderate reproducibility (see Figure A. 3-3 – Appendix A, and Figure 5 in Le et al. (2019)). The experimental data plotted in Figure 3-3c, and Figure 3-4a were fitted by the polynomial Equation 3.3, linking pressure (P) or density (ρ) to CH_4 concentration (C_{CH_4}) and $\nu^*_{CH_4}$, where a_{ij} (with $i + j \leq 4$) are the coefficients of the best-fitting regression models. To decrease the uncertainty on the measurement of pressure and density, experimental data were independently fitted for two different composition domains (≥ and ≤ 50 mol% CH_4). The coefficients a_{ij} fitted for each domain are listed in Table 3-2. The uncertainties reported in the last row of Table 3-2 were derived from the prediction bounds of the fitting model at 1σ.

$$P \text{ (or } \rho) = \sum_{i=0}^{3}\sum_{j=0}^{4} a_{ij} \cdot \left(C_{CH_4}\right)^i \cdot \left(\nu^*_{CH_4}\right)^j \qquad 3.3$$

Table 3-2: Fitted coefficients (a_{ij}) of Equation 3.3 for the determination of pressure (P) and density (ρ) of CH_4-N_2 gas mixtures. Calibration equations were given for two mixture composition domains (≥ and ≤ 50 mol% CH_4). The uncertainties on calculated pressure and density were derived from the prediction intervals of the regression polynomial at 1σ

Coefficients	Pressure determination (bar)		Density determination (g·cm^{-3})	
	≥ 50 mol% CH_4	≤ 50 mol% CH_4	≥ 50 mol% CH_4	≤ 50 mol% CH_4
a_{00}	-172.82	-37.14	-0.06753	0.01993
a_{10}	862.35	746.68	0.3112	-0.08883
a_{01}	-188.59	-197.31	-0.2024	-0.1465
a_{20}	-1346.66	-3310.32	-0.4362	0.02792
a_{11}	644.02	1388.21	0.5052	0.1963
a_{02}	68.58	97.16	0.02588	0.06475
a_{30}	678.52	4097.22	0.1984	0.2052
a_{21}	-1217.18	-6921.35	-0.5917	-0.7082

a_{12}	-272.09	-1024.40	-0.06615	-0.5293
a_{03}	-16.01	-48.88	-0.00212	-0.01924
a_{31}	767.45	10121.08	0.2576	1.559
a_{22}	248.60	2221.96	0.04373	0.9825
a_{13}	29.09	223.16	0.00294	0.07004
a_{04}	1.279	10.04	8.673e-05	0.002134
Adjusted R^2	0.9976	0.9946	0.9995	0.9988
Uncertainty (1σ)	± 11	± 18	± 0.003	± 0.006

Regarding the CO_2-CH_4 mixtures, since the $\nu^*_{CH_4}$ of the mixtures of <50 mol% CH_4 becomes less sensitive to the variation of pressure above ~200 bars, in the following we consider only calibration data of the mixtures dominated by CH_4 (≥50 mol% CH_4) for regression analysis (insert of Figure 3-3d and Figure 3-4b). Experimental data of $\nu^*_{CH_4}$ in CH_4-dominated mixtures were therefore fitted by polynomial Equation 3.4. Every coefficient b_{ij} (with $i + j \leq 4$) and uncertainty of the best-fitting equations were listed in Table 3-3.

$$P \text{ (or } \rho) = \sum_{i=0}^{3}\sum_{j=0}^{4} b_{ij} \cdot \left(C_{CH_4}\right)^i \cdot \left(\nu^*_{CH_4}\right)^j \qquad 3.4$$

Table 3-3: Fitted coefficients (b_{ij}) of Equation 3.4 for determination of pressure (P) and density (ρ) of CO_2-CH_4 gas mixtures. Calibration equations were only given for the mixtures of ≥ 50 mol% CH_4. The uncertainties on the calculated pressure were derived from the prediction interval of the regression polynomial at 1σ.

	Pressure determination (bar)	Density determination ($g \cdot cm^{-3}$)
	≥ 50 mol% CH_4	≥ 50 mol% CH_4
b_{00}	16.99349	- 0.003751
b_{10}	-75.74656	0.07936
b_{01}	-35.59074	-0.060703
b_{20}	139.47675	-0.155453
b_{11}	-150.71132	-0.106032
b_{02}	-20.60863	0.003617

b_{30}	-63.05569	0.08733
b_{21}	359.92530	0.217043
b_{12}	83.88300	-0.005841
b_{03}	6.20787	-0.000248
b_{31}	-175.56035	0.07916
b_{22}	-20.17127	0.006827
b_{13}	6.95781	0.001283
b_{04}	1.31372	0.0001002
Adjusted R^2	0.9963	0.9996
Uncertainty (1σ)	± 15	± 0.004

Pressure and density of CO_2-CH_4 gas mixtures can also be determined from Δ, especially for the CO_2-dominated mixtures (<50 mol% CH_4). The experimental data of Δ reported in Figure 3-5 and Figure 3-6 were fitted by a fourth-order polynomial. The general formula of the best-fitting regression model is expressed by Equation 3.5, where $\bar{C}_{CO2}$ and $\overline{\Delta}$ are respectively defined by Equation 3.1, 3.6, and 3.7, C_{CO_2} is the concentration of CO_2 in CO_2-CH_4 gas mixtures, c_{ij} (with $i + j \leq 4$), h, k Std_h and Std_k are coefficients of the best-fitting regression models. In order to minimize the uncertainty on pressure and density from best-fitting models, the calibration data were divided into four smaller pressure-composition (*PX*) domains. The obtained coefficients and uncertainties of the best-fitting equations of every *PX* domains were listed in Table 3-4 for pressure determination (bar) and Table 3-5 for density determination ($g \cdot cm^{-3}$).

$$P \text{ (or } \rho) = \sum_{i=0}^{3} \sum_{j=0}^{4} c_{ij} \cdot (\bar{C}_{CO2})^i \cdot \overline{\Delta}^j \qquad 3.5$$

where:

$$\bar{C}_{CO2} = \frac{C_{CO_2} - h}{Std\_h} \qquad 3.6$$

$$\overline{\Delta} = \frac{\Delta - k}{Std\_k} \qquad 3.7$$

Table 3-4: Fitted coefficients of Equation 3.5 for the determination of pressure of CO_2-CH_4 gas mixtures. Experimental data were fitted over four different *PX* domains in order to minimize uncertainty. The uncertainties on the calculated pressure of each best-fitting equation were derived from the prediction intervals of the regression polynomial at 1σ.

PX domains / Coefficients	50-100 mol% CO_2		10-50 mol% CO_2	
	5-600 bars	5-160 bars	5-600 bars	5-160 bars
c_{00}	117.48157	94.656228	160.30964	86.45553
c_{10}	-64.00435	-29.90432	-70.7304	-36.98006
c_{01}	75.902022	31.9463	143.1939	63.38251
c_{20}	33.79624	11.05019	61.43567	16.24622
c_{11}	-153.2075	-41.39264	-118.0653	-18.99735
c_{02}	110.19830	-5.575568	44.22433	-9.01309
c_{30}	-17.72552	-2.412150	-30.10597	-3.58623
c_{21}	81.79481	21.269723	94.64936	5.9654
c_{12}	-148.3062	-39.40095	-88.33662	11.75184
c_{03}	93.93866	33.513762	40.28167	0.85861
c_{31}	-13.57701	-1.313218	-35.52924	-2.43154
c_{22}	43.93126	10.23037	39.00078	-5.96449
c_{13}	-49.64265	-22.26971	-20.5409	-1.512
c_{04}	10.75316	7.070998	0.75141	-1.51232
h	0.82613	0.83997	0.3022	0.3022
Std_h	0.1781	0.17804	0.1414	0.14182
k	103.86	103.53	103.09	102.92
Std_k	0.74857	0.63658	0.30473	0.13981
Adjusted R^2	0.9982	0.9980	0.9987	0.9885
Uncertainty (1σ)	± 10	± 3	± 8	± 6

Table 3-5: Fitted coefficients of Equation 3.5 for the determination of density of CO_2-CH_4 gas mixtures. Experimental data were fitted over four different *PX* domains in order to minimize the uncertainty of measurements. The uncertainties on the calculated pressure of each best-fitting equation were derived from the prediction intervals of the regression polynomial at 1σ.

PX domains / Coefficients	50-100 mol% CO_2		10-50 mol% CO_2	
	5-600 bars	5-160 bars	5-600 bars	5-160 bars
c_{00}	0.486313	0.318294	0.22219	0.10363
c_{10}	-0.041249	-0.03372	-0.05087	-0.02684
c_{01}	0.369020	0.295141	0.20111	0.09192
c_{20}	-0.001314	0.003835	0.009753	0.01111
c_{11}	-0.003488	-0.03453	-0.02361	-0.01222
c_{02}	-0.00996	0.03615	-0.008584	-0.002226
c_{30}	-0.0002312	-0.001593	-0.0004959	-0.002867
c_{21}	-0.0135392	0.004029	-0.008539	0.001242
c_{12}	0.037468	0.006008	0.02996	0.01194
c_{03}	-0.030967	-0.005571	-0.009055	-0.003394
c_{31}	0.001645	0.0004832	0.00217	-0.002554
c_{22}	-0.0102471	-0.0008909	-0.01292	-0.006362
c_{13}	0.0124289	0.008034	0.005291	0.0005239
c_{04}	-0.002157	-0.008589	-0.0007252	0.0007116
h	0.82613	0.83997	0.3022	0.3022
Std_h	0.1781	0.17804	0.1414	0.14182
k	103.86	103.53	103.09	102.92
Std_k	0.74857	0.63658	0.30473	0.13981
Adjusted R^2	0.9997	0.9994	0.9992	0.9940
Uncertainty (1σ)	± 0.008	± 0.008	± 0.006	± 0.006

3.3.2. Determination of pressure and density of CO_2-CH_4-N_2 ternary mixtures

Figure 3-8 shows a comparison between the variation of Δ as a function of pressure and composition of CO_2 within CO_2-CH_4, CO_2-N_2 and CO_2-CH_4-N_2 mixtures. The experimental data of CO_2-CH_4 and CO_2-CH_4-N_2 mixtures are from this study, whereas that of CO_2–N_2 mixtures are from the study of Le et al. (2019). Overall, the variations of Δ within binary and ternary mixtures as a function of pressure and composition are very similar, indicating that Δ could be used as a quantitative parameter not only to determine pressure and density of binary (as described in section 3.2.2), but also of CO_2-CH_4-N_2 ternary mixtures. The pressure of CO_2-N_2 mixture (P_2) is systematically higher than that of CO_2-CH_4 mixtures (P_1) at the same value of Δ and molar proportion of CO_2 (insert in Figure 3-8). The difference between the measured pressure P_2 and P_1 can be negligible at low pressure-range (<100 bars) but becomes more appreciable at elevated pressures. The most significant difference between the two calibration data sets was noticed for the curves of 50 mol% CO_2 (up to 150 bars at $\Delta = 102.85$ cm^{-1}). Most importantly, for a given CO_2 concentration, the experimental calibration curves of ternary mixtures are always in the middle of the two curves of CO_2-CH_4 and CO_2-N_2 binary mixtures (Figure 3-8). For instance, the curve 80-10-10 ($X$$CO_2$-$X$$CH_4$-$X$$N_2$) is in the middle of the 80-20 $X$$CO_2$-$X$$CH_4$ and $X$$CO_2$-$X$$N_2$. Note that the molar proportion of CH_4 and N_2 within our ternary mixtures are equal, and the pressure P of the CO_2-CH_4-N_2 ternary mixtures (at a given value of Δ and mol% CO_2) is approximately the mean of (P_1+P_2) (cf. the insert in Figure 3-8). According to our analytical analyses (Appendix C), the a/b ratio varies somewhat by a linear function of the molar fraction of CH_4 and N_2 (with a and b the difference between P_1 or P_2 and P, cf. insert in Figure 3-8). Thereby, the pressure (P) of ternary mixtures can be deduced from the "nominated" pressures P_1 and P_2 (which are calculated from calibration equations of the binary mixtures described above) using Equation 3.8, where a and b are now the molar proportions of N_2 and CH_4 in the ternary mixture, respectively.

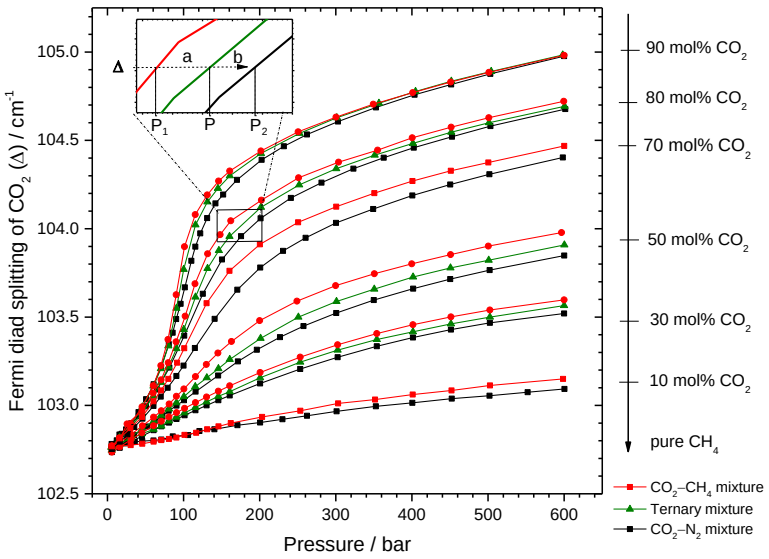

Figure 3-8. Variation of CO_2 Fermi diad splitting (Δ) as a function of pressure and composition. The experimental data of CO_2-CH_4 binary mixture, of CO_2-N_2 binary mixture, and of CO_2-CH_4-N_2 ternary mixture are represented by red, black and green points, respectively. The solid lines are a guide for the eye. The concentration of CO_2 within binary and ternary gas mixtures is indicated in the figure. The molar proportion of N_2 and CO_2 within the ternary mixtures is equal. Overall, the calibration curves of the ternary mixtures are always in the middle of the two calibration curves of the binary mixtures at a given CO_2 concentration (see insert).

$$P = \frac{aP_2 + bP_1}{a + b} \qquad 3.8$$

Once the composition and the pressure of the ternary mixture are determined, the density can be calculated by using an appropriate EoS, or similarly deduced from the corresponding calibration equations dedicated to density determination of binary systems provided above.

3.3.3. Uncertainty analyses

The uncertainty of the final composition, pressure, and density calculated from Raman measurements is contributed by two main sources of error. The first one, denoted u1, arises from the best-fitting models obtained by the least-square regression analysis of the experimental data. It reflects how well the calibration equations reproduce the pressure (or density) of the mixture from a given concentration (C_{CH_4} or C_{CO_2}) and Δ or $\nu^*_{CH_4}$. This uncertainty was derived from the prediction intervals (at 1σ) of each best-fit regression equation and reported in the last row in Table 3-2, Table 3-3, Table 3-4 and Table 3-5.

However, concentration (C_{CH_4} or C_{CO_2}) and spectral features (Δ or $\nu^*_{CH_4}$) were measured with a certain uncertainty. In the present study, the uncertainty of each spectral feature was calculated from six Raman spectra recorded at the same *PTX* conditions (see method section above). Thereby, the uncertainty of a single fitted peak position of CH_4 and CO_2 (ν_{CH_4}, ν^+, ν^-) is about ±0.01 cm^{-1}, and so the uncertainty of $\nu^*_{CH_4}$ and Δ is about ±0.015 cm^{-1} (denoted i1). Besides, the uncertainties of the RRSCS of CH_4 (±0.16, this study) and of CO_2 (±0.04, Le et al., 2019) result in uncertainty of ~ ± 0.5 mol% on the measured composition (denoted i2). Thus, the second source of uncertainty (denoted "u2") is the one that relates to the uncertainty i1 and i2. Since the regression calibration equations are not linear (up to fourth-order polynomial), the uncertainties i1 and i2 can cause either significant error or less, depending on the mixture composition and pressure (or density) range. Indeed, the uncertainty calculated for a gas mixture of <50 mol% CH_4 is expected to be higher than that of a mixture of >50 mol% CH_4 because the sensitivity of $\nu^*_{CH_4}$ to the variation of pressure decreases with the decrease of the CH_4 content (e.g., the curve of 10 mol% CH_4 is much less steep than the curve of pure CH_4) (Figure 3-3a). For example, the $\nu^*_{CH_4}$ value = – 1.800 ± 0.015 cm^{-1} can cause a fluctuation of 22 bars for the CH_4-N_2 mixture of 10 mol% CH_4 (~558 bars at $\nu^*_{CH_4}$ = – 1.815 cm^{-1}, and ~ 536 bars at $\nu^*_{CH_4}$ = – 1.785 cm^{-1}) but only 2 bars for pure CH_4. Similarly, the Δ = 103.300 ± 0.015 cm^{-1} causes a fluctuation of 44 bars for the CO_2-CH_4 mixture of 10 mol% CO_2 but only 2 bars for pure CO_2. Thus, the uncertainty u2 arising from uncertainties i1 and i2 should be individually estimated for each measurement. More details in the calculation procedure of uncertainty propagation can be found in Supporting Information of Le et al. (2019).

The ultimate uncertainty on the calculated pressure and density can be estimated by the sum of these two error components (u1 and u2) (Fall et al., 2011; Wang et al., 2011). Overall, the uncertainty of our calibration data is comparable or even better than those of the calibration for pure components published in literature. For example, the calibration data established for pure CO_2 by Wang et al. (2011) yields the uncertainty of ~33 bars and less than about 0.025 $g{\cdot}cm^{-3}$ over a pressure range from 22 to 357 bars at room temperature. Regarding the peak position of CH_4, the pure CH_4 calibration data proposed by Lin et al. (2007) cover a pressure range of up to 600 bars with an uncertainty similar to the one in the present study (~ ± 10 bars). Our calibration equations, however, can be applied to any relevant mixture composition.

4. Discussion

4.1. Interpretation of the CH_4 peak position variation with pressure (density) and composition

As the peak position shift is due to the fundamental changes in intermolecular interactions at the molecular scale (Ben-Amotz et al., 1992; Zhang et al., 2016), the difference between the variation trend of the CH_4 peak position in the mixtures with N_2 or CO_2 (Figure 3-3) could be partially explained by the change of the intermolecular separation r (Å). According to the Lennard-Jones 6-12 potential approximation, the intermolecular potential consists of a contribution of attractive (dispersion) and repulsive forces which vary as a function of the intermolecular separation r (Jones and Chapman, 1924). At very low pressure (low density), the intermolecular distance r is large enough as such gaseous molecules are completely independent (no interactions between molecules). As pressure increases, the distance between molecules is reduced, and so molecules begin to interact with one another with more frequent collisions and steric restrictions, which impact the vibration mode of gaseous molecules (i.e., lengthening or shortening of C-H bond length of CH_4, perturbing electron cloud distribution, and so resulting to a small change in polarizability, etc.). Firstly, the attractive forces appear and dominate, whereas the repulsive forces are negligible (cf. Figure D. 3-1 – Appendix D). With further increase of pressure (decrease of the intermolecular distance r), the attractive force increases and reaches its maximum value at a distance r_0, and the repulsive force also increases and completely compensates the attractive force at $r = \sigma$ (with $r_0 = 1.1224\sigma$). In general, the attractive forces cause a redshift (shifts toward lower wavenumbers) whereas the repulsive ones cause a blueshift (shifts toward to higher wavenumbers) (Zakin and Herschbach, 1986; Lin et al., 2007).

Regarding CH_4-N_2 mixtures, the total number of gaseous molecules per volume unit steadily increases as pressure increases (Figure 3-9), leading to a decrease in the distance r between molecules. However, the intermolecular distance r is in the range such that the attractive forces between them always dominate and the repulsive forces are insignificant (cf. Figure D. 3-1– Appendix D). Over the studied pressure range (5–600 bars), the attractive forces become more and more important with increasing pressure, resulting in the continuous downshift of the CH_4 peak position (Figure 3-3c). In addition, the total number of molecules per volume unit also decreases (so, r increases) as the CH_4 proportion decreases (Figure 3-9),

leading to the decrease of the peak shift magnitude with decreasing CH_4 content (Figure 3-3a and c).

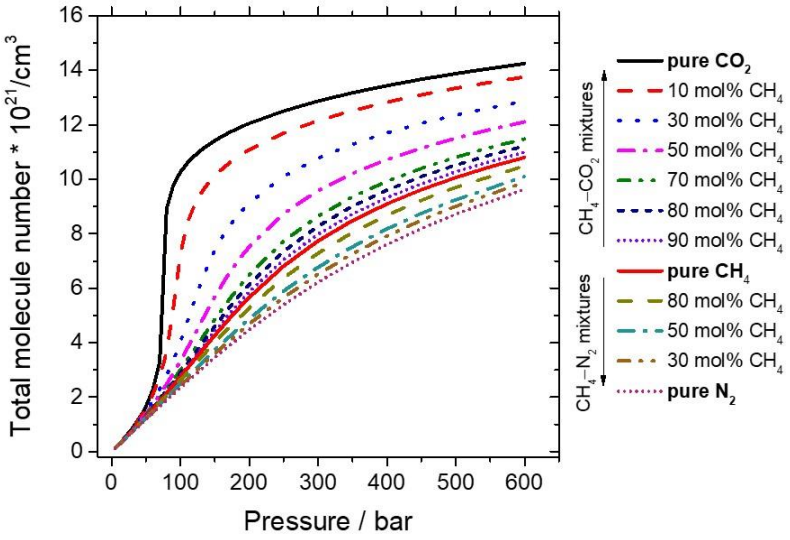

Figure 3-9. Evolution of density (molecule number.cm^{-3}) of CO_2-CH_4 and CH_4-N_2 mixtures as a function of pressure (bar) and composition at 32 °C.

On the contrary to CH_4-N_2 mixtures, the total number of molecules per volume unit within CH_4-CO_2 mixtures increases (corresponding to a decrease of r) as the CH_4 content decreases (Figure 3-9). The relationship between the CH_4 peak position and pressure is nearly unchanged for the mixtures of ≥ 70 mol% CH_4 (insert of Figure 3-3d), indicating that there is no (or little) change in the sum of attractive and repulsive forces, even when the intermolecular distance r slightly decreases. This suggests that intermolecular distance r reaches the vicinity of the r_0 value and the repulsive forces now become more important. Indeed, at that density range (~ $11 \cdot 10^{21}$ molecules·cm^{-3}), when decreasing the distance between molecules, the repulsive forces become more important and partly compensate the attractive forces. For the CH_4-CO_2 mixtures dominated by CO_2 (< 30 mol% CH_4), the total molecule number drastically increases from 70 bars and quickly reaches ~ $11 \cdot 10^{21}$ molecules·cm^{-3} at around 200 - 300 bars (Figure 3-9), resulting in a noticeable downshift in CH_4 peak position. Then, the density slowly increases as the pressure further increases from 200 to 600 bars, explaining the stepwise behavior of the calibration curve of the CO_2 dominated mixtures. With a further increase of pressure, the repulsive forces would certainly dominate, leading to a peak shift to higher wavenumber, from over ~ 1300 bars as shown by Fabre and Oksengorn (1992) and Zhang et al. (2016) (cf. Figure D. 3-1 – Appendix D).

4.2. Validation of the calibration data with natural fluid inclusions

The selected natural FIs containing CO_2-CH_4 (samples Ta15 and Mu618), CH_4-N_2 (sample Mu1381), and CO_2-CH_4-N_2 (sample PAN-V3) mixtures were first analyzed by microthermometry in order to observe significative phase transitions for the determination of composition and density. Quartz samples were cooled to temperatures down to –160 °C in order to permit the appearance of a vapor bubble and of a solid phase. The homogenization temperature of the volatile phase T_h(vol), determined by observing the disappearance of the vapor bubble, ranged from – 105 to – 110 °C for CO_2-CH_4 FIs within sample Ta15, from – 74.9 to – 89.0 °C for CO_2–CH_4 FIs within sample Mu618 and from – 101.2 to – 103.7 °C for CH_4-N_2 FIs within sample Mu1381. Melting temperatures of the volatile phase were only accurately determined within FIs of sample Ta15 between – 95 and – 103 °C. Thereby, the density of FIs of sample Ta15 were directly obtained from the *VX* diagram of Thiéry et al. (1994a), whereas that of FIs of samples Mu618 and Mu1381 could be only calculated using GERG-2004 EoS from the combination of T_h(vol) and the composition obtained from Raman measurement.

Because of the low density of the gas bubble in FI Mu618.SQ-2.1, no phase transition was observed. Also, no phase transition within the volatile part of FIs of sample PAN-V3 could be observed due to their low density and complex composition (ternary mixture). Only T_m(ice) and T_m(cla) were measured, ranging between – 3.8 and – 6.2 °C and between 7.9 and 11.3 °C, respectively. The latter microthermometry data imply that (i) the salinity is not equal to zero and (ii) there is a volatile component either made of pure CH_4 or of a gas mixture with unknown other component(s). In order to reconstruct the composition of the fluid inclusions with a complex gas mixture and where clathrate is present, the values of T_m(cla) and of the density of the volatile phase are required (Bakker, 1997). The two latter cases are typical examples illustrating some limitations of microthermometry analyses.

The selected natural FIs were also analyzed by Raman spectroscopy. Since all Raman calibration data were carried out at 22-32 °C, the *PVX* properties of the volatile part of FIs could be determined without the impact of the clathrate nucleation and dissociation, except a few particular cases where CH_4 clathrates could dissociate at up to 27 °C (Mullis, 1979; Sloan et al., 2007). Measurements were performed three times by focusing the laser on different places inside the FIs. For measuring $\nu^*_{CH_4}$ of CH_4 bearing FIs, a fused silica microcapillary (FSC) containing about 5 - 6 bars of CH_4 was analyzed before and after analyzing each FI

(Figure A. 3-2 – Appendix D). The average values of the peak areas of gases were then used for the determination of composition using Equation 1 in Pasteris et al., (1988), with RRSCS of N_2 = 1 (by convention), RRSCS of CH_4 = 7.73 ± 0.16 (this study) and RRSCS of CO_2 = 2.29 ± 0.04 (Le et al., 2019). Once the composition of the fluid inclusion is determined, the relative variation of the peak positions of CH_4 ($v^*_{CH_4}$) and/or the CO_2 Fermi diad splitting (Δ) is used for the determination of pressure and density, using the appropriate calibration equation (from Equation 3 to 8). The uncertainty of the Raman results is the ultimate one calculated as described in section 3.3.3, whereas the uncertainty of microthermometry was determined from the uncertainty of the homogenization temperature (± 0.1 °C) and the graphic reading error (up to ± 1 °C) while using the *VX* diagrams of Thiéry et al. (1994a).

Table 3-6 presents the comparison between the results obtained by Raman and microthermometry. Regarding sample Ta15, the composition of FIs determined from microthermometry data (93.8 - 96.5 mol% CH_4) is similar to that measured by Raman analyses (94.0 - 95.5 mol% CH_4). However, a noticeable difference in the measured pressure and density is observed (e.g., 899 - 942 bars and 0.353 - 0.366 g·cm^{-3} for microthermometry measurements, compared to 736 - 784 bars and 0.338 - 0.347 g·cm^{-3} for Raman measurements. The latter significant difference can be partially explained by the fact that the *PV* properties of FIs of sample Ta15 greatly exceed the calibrated pressure (density)-range of our study (5 - 600 bars) (Table 3-6).

Regarding sample Mu618, the pressure and density determined by microthermometry and the composition (determined from Raman) using GERG-2004 EoS (319 - 632 bars and 0.242 - 0.370 g·cm^{-3}, respectively) are very close to the ones directly determined by Raman measurements. The difference in measured pressure and density are always less than 13 bars and 0.005 g·cm^{-3}, respectively. The low density (0.098 g·cm^{-3}) of the bubble within FI Mu618.SQ-2.1 (Figure 3-1c) made it impossible to be characterized by microthermometry but it can be measured out by Raman analysis.

Regarding sample Mu1381, Raman and microthermometry results are overall in very good agreement. The most significant difference in pressure and density noticed for FI Mu1381-2.2 are 35 bars (~ 8%) and 0.014 g·cm^{-3} (~ 5 %), respectively (Table 3-6).

According to the study of Mullis et al. (1994), the trapping temperature of fluids within CH_4-zone was obtained from the homogenization of H_2O-rich FIs that is up to 270 °C. The

trapping pressure is calculated within CH_4-rich FIs at 270 °C from the measured density. Here, we also used the GERG-2004 EoS to calculate the trapping pressure and reported in Figure 3-10 for comparison. With a small difference of 0.005 $g \cdot cm^{-3}$ between the density obtained by Raman and microthermometry (IF Mu618-2.1), the two relevant isochores are nearly identical. However, with a larger difference in density (e.g., a difference of 0.017 $g \cdot cm^{-3}$ for FI Ta15.1-2, and of 0.014 $g \cdot cm^{-3}$ for FI Mu1381-2.2), the isochores slightly deviate by a difference of ~ 100 - 200 bars (around 10%) at 270 °C (trapping temperature), which however does not significantly change the geological interpretation (Table 3-6 and Figure 3-10). The *PVX* properties of the volatile part of FIs within PAN-V3 sample were determined from Raman measurements only because of the complex composition and low density (Table 3-6). Thus, new calibration data can provide *PVX* properties much faster than microthermometry measurements and with a larger field of applicability.

Table 3-6: Comparison between Raman and microthermometry results. P_{Raman} and $P_{Microth}$ are pressure (bar) measured at 32°C. ρ_{Raman} is the density (g·cm^{-3}) directly determined from Raman measurement and $\rho_{Microth}$ is the density calculated from microthermometry data using GERG-2004 EoS. $\Delta(P) = P_{Raman} - P_{Microth}$. $\Delta(\rho) = \rho_{Raman} - \rho_{Microth}$. The uncertainty was provided for 1σ.

N° IFs	Raman results						Microthermometry results		Difference	
	%CO_2	%CH_4	%N_2	P_{Raman}	ρ_{Raman}		$P_{Microth}$	$\rho_{Microth}$	$\Delta(P)$	$\Delta(\rho)$
	(mol%)			bar	g·cm^{-3}		bar	g·cm^{-3}		
Ta15.1-2	6.0	94.0		740	0.349		899 ± 8	0.366 ± 0.001	159	0.017
Ta15.1-6	4.5	95.5		736	0.338		927 ± 9	0.353 ± 0.001	191	0.015
Ta15.1-7	4.5	95.5		784	0.347		942 ± 8	0.354 ± 0.002	158	0.007
Mu618.SQ-1.1	13.4	86.6		365 ± 8	0.296 ± 0.003		375 ± 11	0.300 ± 0.004	10	0.005
Mu618.SQ-2.1	16.7	83.3		102 ± 7	0.098 ± 0.002		-	-	-	-
Mu618-2.1	13.5	86.5		636 ± 10	0.371 ± 0.004		632 ± 11	0.370 ± 0.002	-4	-0.001
Mu618-2.2	9.8	90.2		374 ± 8	0.281 ± 0.003		387 ± 12	0.286 ± 0.004	13	0.005
Mu1381-1.1		69.1	30.9	344 ± 12	0.253 ± 0.004		319 ± 14	0.242 ± 0.005	-25	-0.011
Mu1381-1.2		69.3	30.7	344 ± 12	0.252 ± 0.004		333 ± 14	0.248 ± 0.005	-11	-0.004
Mu1381-1.3		69.1	30.9	342 ± 12	0.252 ± 0.004		348 ± 14	0.256 ± 0.005	6	0.004

Mu1381-2.2		73.1	26.9	409 ± 13	0.275 ± 0.004		444 ± 13	0.289 ± 0.003	35	0.014
Mu1381-3.3		72.7	27.3	458 ± 11	0.292 ± 0.004		449 ± 13	0.291 ± 0.003	-9	-0.001
PAN V3 A-1	40.6	22.6	36.8	103 ± 6	0.157 ± 0.003		-	-	-	-
PAN V3 A-3	54.7	11.8	33.5	124 ± 7	0.232 ± 0.004		-	-	-	-
PAN V3 D-1	63.0	13.5	23.5	102 ± 6	0.207 ± 0.003		-	-	-	-

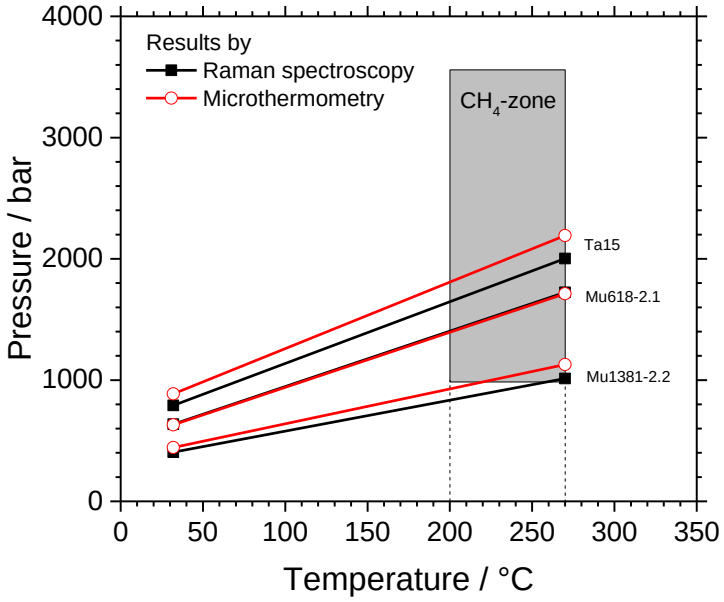

Figure 3-10. Isochores of FIs Mu618-2.1, Mu1381-2.2 and Ta15 calculated by GERG-2004 EoS. The grey area represents the *PT* conditions of fluid entrapment within the CH_4-zone (Mullis, 1979; Mullis et al., 1994).

4.3. Comparison with calibration data published in the literature

The spectral features of CO_2 and CH_4 within the mixture of CO_2-CH_4 and CH_4-N_2 reported here show similar behaviors as a function of pressure (density) and composition of gas mixtures, compared to the results published by Seitz et al. (1993, 1996). However, Seitz and co-workers used a different spectrometer with relatively low spectral resolution resulting in the scattering of their results. Also, they did not study the variation of the Fermi diad splitting and did not specify the temperature of the analyses (stated room temperature). Therefore, we represent only the comparison with the most recent published calibration data using similar instruments (LabRAM HR, Horiba Jobin-Yvon) and configurations (Table 3-7).

Table 3-7: Instrument and configurations of recent work for establishing calibration data for pure CO_2.

	Laser (nm)	Grattings (grooves/mm)	Slit/hole	*T* (°C)	*P* (bar)	Peak position correction
This study	514	1800	200/1000	22 & 32	5-600	No
Wang et al. (2019)	532 & 514	1800	100/500	25 & 40	5-500	Yes
Sublett et a. (2019)	514	1800	150/400	–160 to 450	10-500	-
Lamadrid et al. (2017)	514	1800	150/400	22-23	< 60	Yes

Fall et al. (2011)	514	600/1800/2400	150/400	–10 to 35	10-300	No
Wang at al. (2011)	532	1800	-	21	22-357	Yes
Lin et al. (2007b)	514	1800	150/-	22	1-600	Yes

Figure 3-11: Comparison of the relationship between Δ and (a) pressure or (b) density established at different temperatures and from different laboratories.a represents the comparison of the relationship between Δ and pressure of pure CO_2 obtained in this work with previous studies. Since each published calibration data was made at a different temperature, we observed a good agreement in the variation trend of Δ and the effect of temperature. Indeed, the calibration curve was reasonably shifted to lower Fermi diad splitting with increasing temperature, as noticed by Wang et al. (2011), Fall et al. (2011), Le et al. (2019), and Sublett et al. (2019). We noticed that the departure of the calibration curve of Fall et al. (2011), Lamadrid et al. (2017) and Sublett et al. (2019) differ from that of the calibration curves of Wang et al. (2011), Wang et al. (2019), Le et al. (2019) and this study. That may indicate that there was a systematic error causing a Δ-shift of about – 0.1 cm^{-1} to the whole curves.

Figure 3-11b represents the relationship between Δ and the density of pure CO_2 of this study, along with those of earlier studies. Our calibration is in excellent agreement with the whole experimental data by Wang et al. (2011) and Wang et al. (2019), and slightly different from those of Fall et al. (2011), Lamadrid et al. (2017) and Sublett et al. (2019) over high- (above ~ 0.76 $g{\cdot}cm^{-3}$) and low-density-range (under ~ 0.2 $g{\cdot}cm^{-3}$). The difference is always less than about 0.04 $g{\cdot}cm^{-3}$. The more pronounced discrepancy was observed over the middle density-range (~ 0.20 - 0.75 $g{\cdot}cm^{-3}$) with the difference of up to 0.1 $g{\cdot}cm^{-3}$. According to the study of Lamadrid et al. (2017), these discrepancies of calibration data may be due to the inconsistent procedure of the calibration of the Raman instruments, the wavelength correction method and also the systematic day-to-day errors (as seen in Figure 3-11a, b). The significant difference in the middle density-range that was obtained at near critical point of CO_2 could be caused by small fluctuation of pressure and temperature, different instrumentation, and/or by error in the use of different EoS in calculating density from pressure.

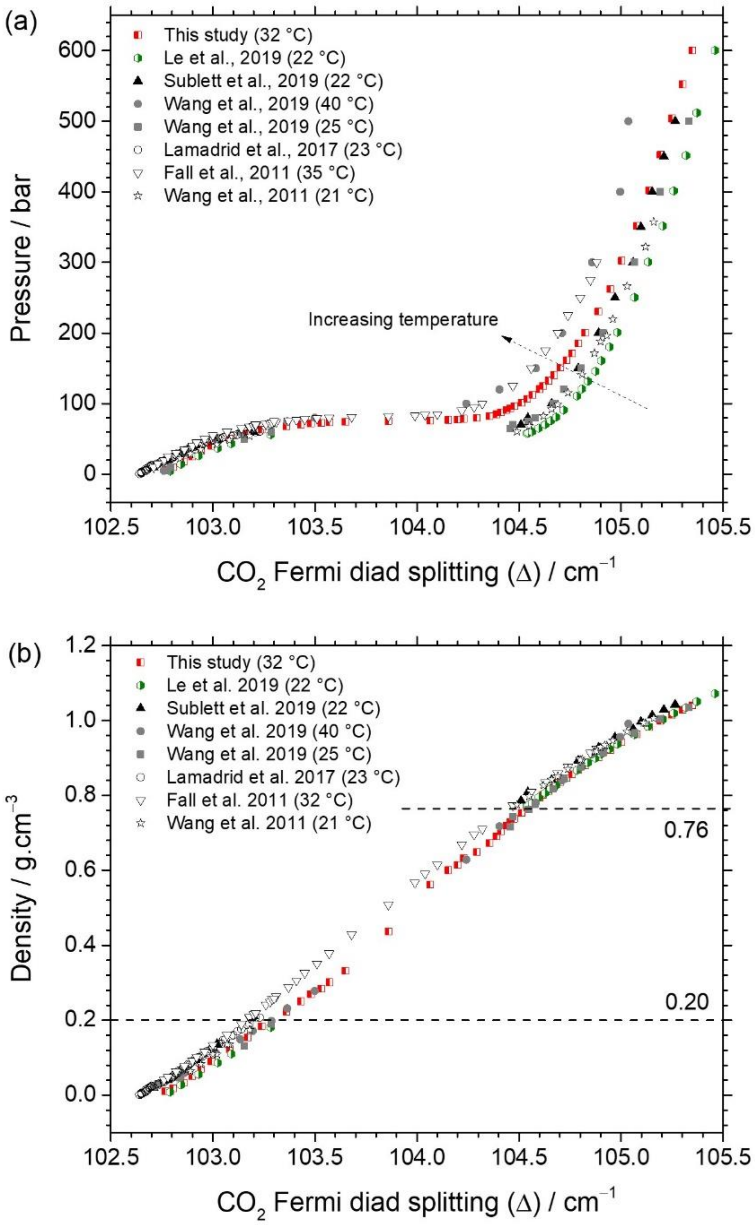

Figure 3-11: Comparison of the relationship between Δ and (a) pressure or (b) density established at different temperatures and from different laboratories.

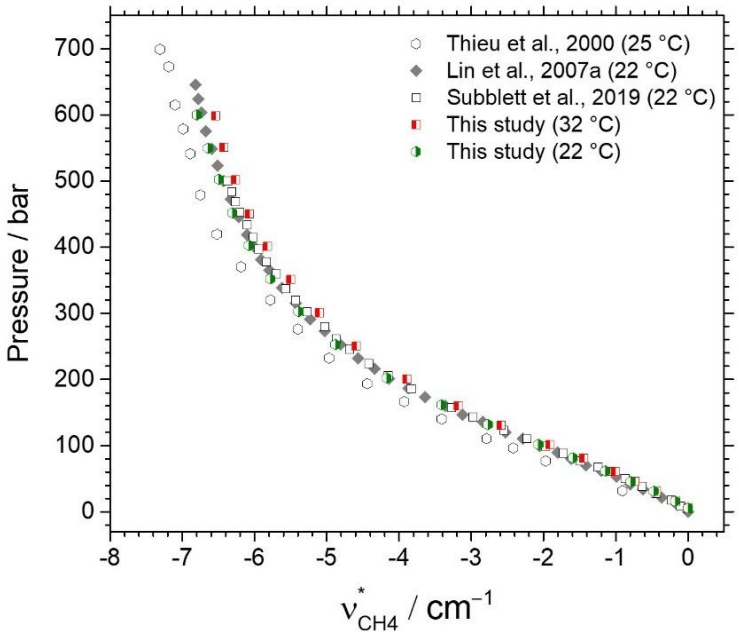

Figure 3-12: Comparison of the variation of the downshift of the CH_4 peak position as a function of pressure and temperatures.

Figure 3-12 shows a similar variation trend of $\nu^*_{CH_4}$ with pressure. With the consideration of temperature effect, our calibration curves obtained at 32 and 22 °C agree well with the published data obtained by Thieu et al. (2000) (at 25 °C), Lin et al. (2007) and Sublett et al. (2019) (at 22 °C). This proves the good reproducibility of the variation of the CH_4 band position for quantitative measurements. Overall, the applicability of the calibration data should be examined and corrected for each Raman instrument within different laboratories before being applied to the study of natural FIs. Even in the same laboratory, standards (natural/synthetic FIs or FSC) of known *PVX* properties should be regularly measured to prevent any variation or shifting of the instrumental responses.

5. Conclusions

Thanks to the use of an improved HPOC system, a system to prepare many gas mixtures at any composition at ~ 130 bars, and Raman spectroscopy, the relative Raman scattering cross-section of CH_4 (σ_{CH_4}) could be reevaluated within CH_4–N_2 mixtures of different compositions. It can be considered constant (7.73 ± 0.16) with the variation of pressure (density) and composition and so, used for the determination of the molar fraction with an uncertainty of about ~ 0.5 mol%. Also, the Fermi diad splitting of CO_2 (Δ) and the relative variation of the

peak position of CH_4 ($\nu^*_{CH_4}$) were demonstrated to be the most reliable spectral parameters with a satisfactory reproducibility for the monitoring of pressure and density (*PV*) of CO_2-CH_4 and CH_4-N_2 mixtures. We also provided an interpretation of CH_4 peak position variation based on intermolecular interaction change using the Lennard-Jones 6-12 potential approximation. Several calibration polynomials fitted from our experimental results were dedicatedly provided for each *PX* range, linking pressure or density to the spectral parameters and the composition of the mixtures. Henceforth, the *PVX* properties of fluids containing binary or even ternary mixtures of CO_2, CH_4 and N_2 gases (coupled with calibration data of Le et al. (2019)) can be directly determined from Raman spectra without any other complementary microthermometry analyses, making it a productive and accurate technique to quickly analyze FIs. Testing these calibration equations to natural FIs showed a good agreement with microthermometry data. It was noted that applying the calibration data reported in the present study may cause a higher uncertainty depending on the sensitivity of each Raman instrument, the instrumental calibration, and data processing protocol from one laboratory to another. Therefore, an examination and correction by analyzing standard samples are imperatively required before using any calibration data published in literature.

6. Acknowledgements

This paper is a part of the thesis of Van-Hoan Le (Université de Lorraine) who acknowledges the French Ministry of Education and Research and the ICEEL Institut Carnot. The work benefited financial support from CNRS-INSU CESSUR program. The authors are grateful to Dr. Alfons van den Kerkhof and an anonymous reviewer for their thorough review and constructive comments.

Appendix A. Experimental protocol

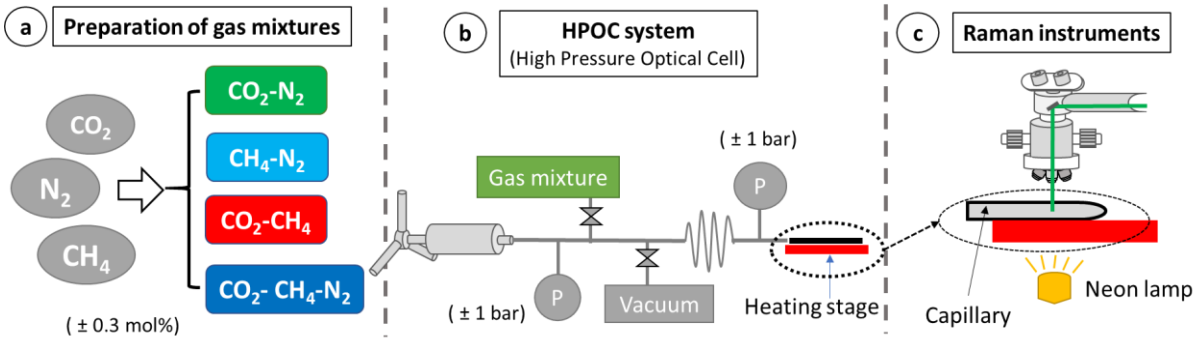

Figure A. 3-1: Scheme of the calibration strategy: (a) gas mixtures were prepared by a gas mixer and compressed (up to 130 bars) by a home-made pressurization system. It was then connected to (b) an HPOC system coupled with a transparent fused silica capillary (FSC) set on a Linkam CAP500 heating-cooling stage (± 0.1 °C). The HPOC system is composed of a manual pressure generator, two pressure transducers (± 1 bar), several valves, microtubes, and a pump to purge the system. (c) Raman in-situ analyzed of gas mixtures of known composition at controlled *PT* conditions. A neon lamp was set under the whole capillary and heating-cooling stage for wavelength correction.

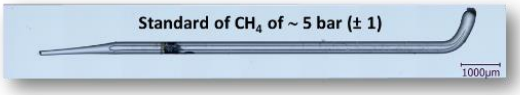

Figure A. 3-2: Photography of a sealed transparent microcapillary (called CH_4-standard) containing ~ 5 ± 1 bars of CH_4 at room temperature. This standard was used for measuring $\nu^*_{CH_4}$ of CH_4 bearing within natural fluid inclusions (FIs). It was analyzed before and after analyzing every natural FIs for wavelength calibration of the spectrometer.

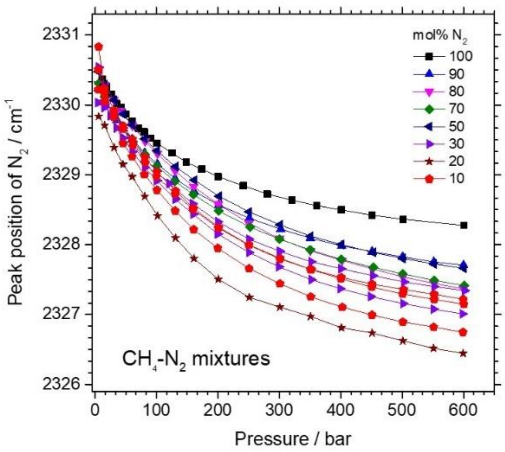

Figure A. 3-3: Variation of the fitted peak position of N_2 (corrected by a Ne line at ~ 2348.43 cm^{-1}) as a function of pressure and composition of CH_4-N_2 mixtures at 32 °C.

Appendix B. Calibration data of CO_2–CH_4 mixtures at 22 °C

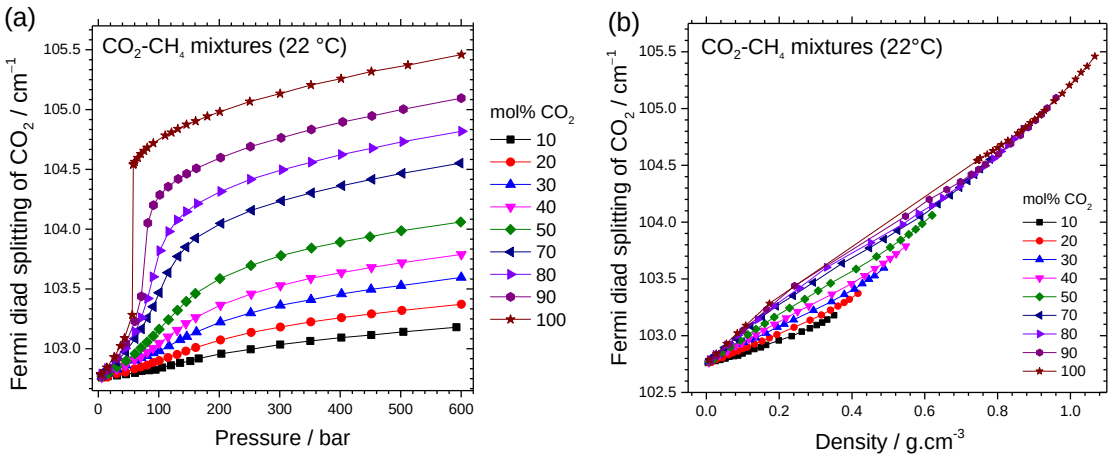

Figure B. 3-1: Variation of the Fermi diad splitting of CO_2 (Δ) as a function of pressure (a) or density (b) and composition of CO_2-CH_4 mixtures at 22 °C.

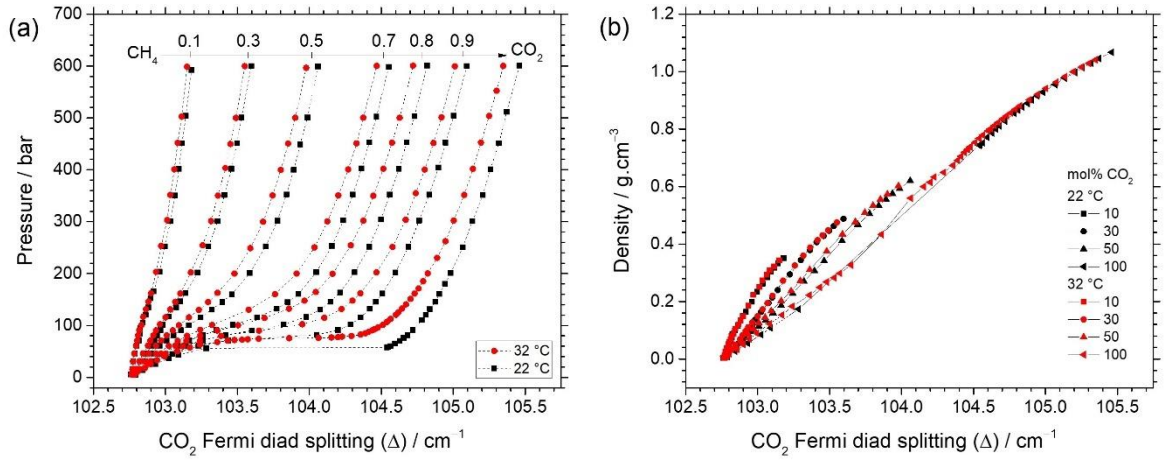

Figure B. 3-2: Comparison between the variation of the Fermi diad splitting of CO_2 as a function pressure (a) or density (b) and composition of CO_2-CH_4 mixtures obtained at 22 and 32 °C.

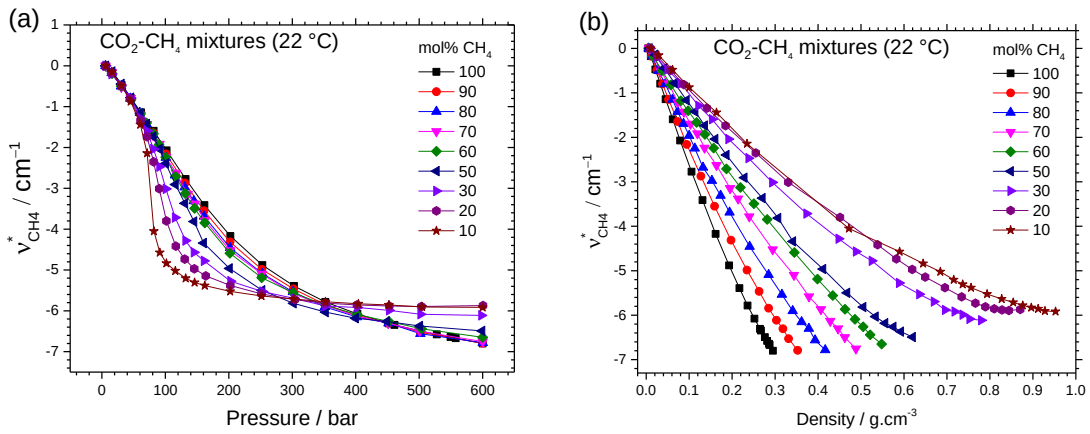

Figure B. 3-3: Relative variation of the fitted CH_4 peak position ($\nu^*_{CH_4}$) within CO_2-CH_4 mixtures as a function of composition (a) pressure or (b) density at 22 °C.

Appendix C. Statistical analyses for Raman calibration data of ternary gas mixtures

P_1 and P_2 is the "nominated" pressure determined from a given Δ value and molar proportion of CO_2 using the calibration equation of CO_2-CH_4 and CO_2-N_2 mixtures, respectively. Figure C. 3-1 represents the variation of the difference between P_2 and P_1 as a function of Δ and mixture composition. As shown in the insert in Figure 3-8 and described in the section 3.3.2, the pressure (P) of the CO_2-CH_4-N_2 ternary mixtures can be deduced from the two "nominated" pressures P_1 and P_2 which are calculated from Δ and molar proportion of CO_2 using the calibration data set of two binary mixtures (CO_2-CH_4 and CO_2-N_2) if the *a/b* ratio is accurately known (*a* and *b* are described in the insert of Figure 3-8). The a/b ratio is calculated from experimental data by Eq. C.1 and reported in Figure C. 3-2. We assumed that the *a/b* ratio varies by a linear function of the molar fraction of CH_4 and N_2.

$$\frac{a}{b} = \frac{P - P_1}{P_2 - P} \qquad \text{(Eq. C.1)}$$

Because the uncertainty of the polynomial calibration equations of the binary gas mixtures ranges from ± 5 to ~ 20 bars (reported in section 3.3.1), we thus considered only the data points where the pressure difference ($P_2 - P_1$) is more than 20 bars (that were surrounded by the red frame in Figure C. 3-1). The pressure difference ($P_2 - P_1$) of the points outside the red frame (< 20 bars) is therefore negligible. Statistical analyses give the average value of the *a/b* ratio = 0.98 ± 0.06 ≈ 1 that validated our assumption of the linear correlation between the molar fraction of N_2 and CH_4 (within ternary mixtures) in the determination of pressure P from P_1

and P_2 (Figure C. 3-2). Therefore, *a* and *b* are reasonably the molar proportion of CH_4 and N_2 in ternary mixtures, respectively. The pressure and the density of ternary mixtures of any concentration can be henceforth determined from the molar concentration and the Fermi diad splitting of CO_2 using the calibration equations of CO_2-CH_4 (this study) and CO_2-N_2 (Le et al., 2019) mixtures (3.8).

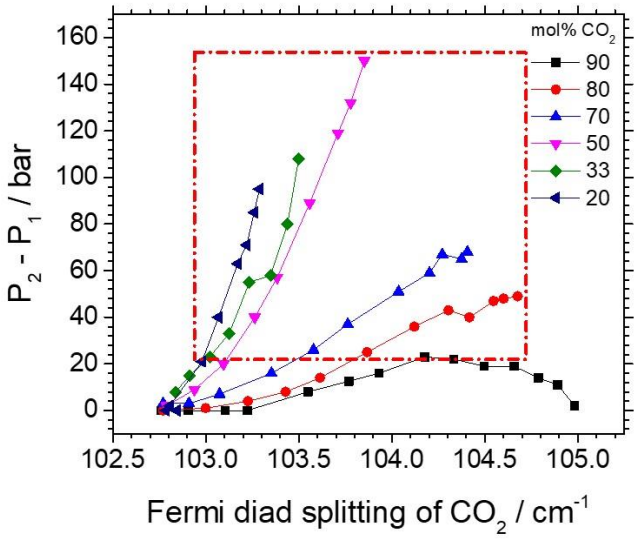

Figure C. 3-1: Difference between the "nominated" pressure of CO_2-CH_4 and CO_2-N_2 mixtures ($P_2 - P_1$) at given Δ value and CO_2 concentration. According to the uncertainty reported for regression polynomial calibration equation, the difference of ($P_2 - P_1$) that is less than about 20 bars is negligible.

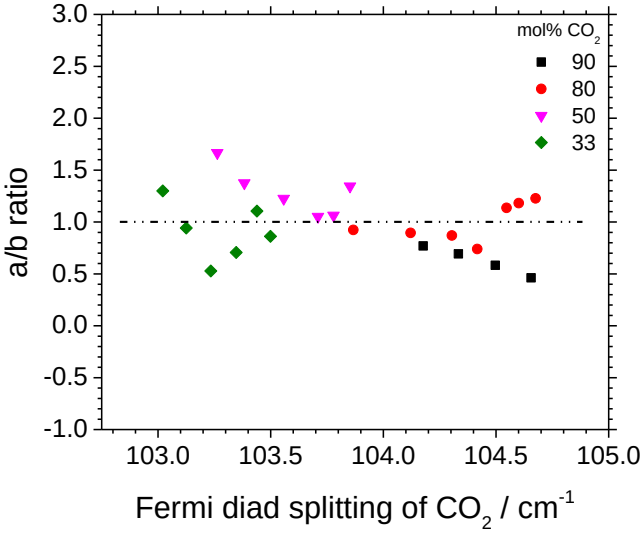

Figure C. 3-2: Variation of the *a/b* ratios as a function of Δ and composition of gas mixtures. Statistical analyses give the averaged value of the *a/b* ratio = 0.98 ~ 1 while the molar proportions of CH_4 and N_2 in the ternary mixture are equal.

Appendix D. Interpretation of the peak shift as a function of intermolecular interaction

Table D. 3-1: Density ($g \cdot cm^{-3}$ or molecular number.cm^{-3}) and intermolecular separation r (Å) of CH_4 molecules calculated for a given pressure (bar). The intermolecular separation r at a given pressure (or given density) is calculated by assuming that every molecule is separated by the same distance.

Pressure	Density	Density	Intermolecular distance (r)
(bar)	($g \cdot cm^{-3}$)	(Molecule number$\cdot cm^{-3}$) $\cdot 10^{21}$	Å
15	0.010	0.37	14.0
30	0.020	0.75	11.0
90	0.065	2.45	7.4
130	0.097	3.67	6.5
200	0.150	5.66	5.6
300	0.206	7.74	5.1
400	0.242	9.10	4.8
500	0.267	10.06	4.6
600	0.287	10.80	4.5
1200	0.355	13.37	4.2
1400	0.370	13.92	4.2
1600	0.382	14.39	4.1

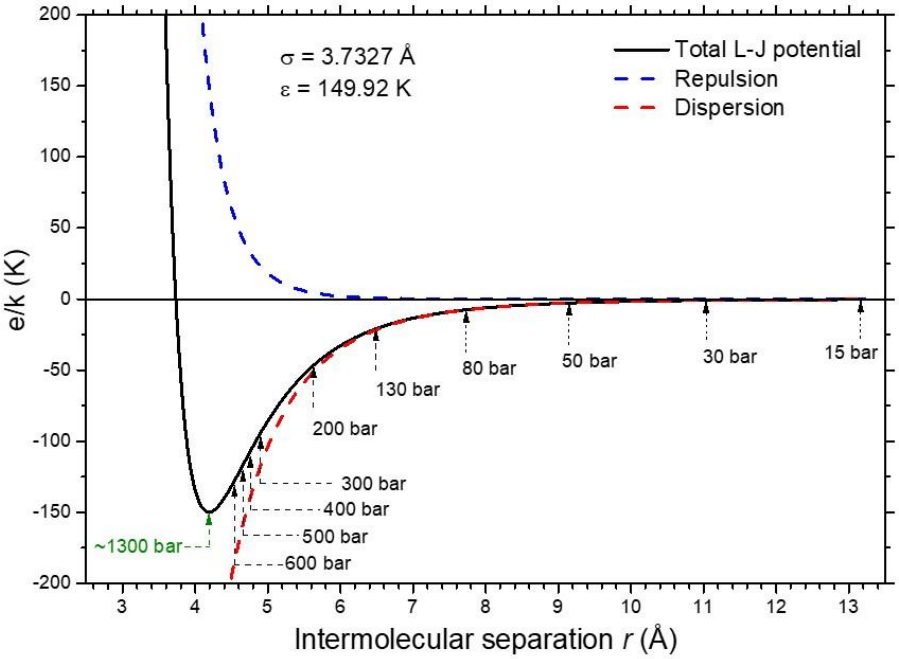

Figure D. 3-1: Black-solid line: the variation of Lennard-Jones 6-12 potential of pure CH_4 as a function of intermolecular separation r. The total potential energy (solid-black line) is the sum of energy coming from repulsive (blue-dashed line) and attractive forces (red-dashed line) experienced between molecules. Lennard-Jones parameters (σ, ε) of CH_4 are from Möller et al. (1992).

Chapter 4: Interpretation of the pressure-induced frequency shift of the ν_1 stretching bands of CH_4 and N_2: effect of solvation repulsive and attractive contribution within CH_4-CO_2, N_2-CO_2 and CH_4-N_2 binary mixtures

In previous chapters, the effect of composition, pressure, and density on the variation of Raman spectral features (i.e., peak area ratio, peak position) of CO_2, CH_4, and N_2 gases were revealed by an experimental approach, i.e. *in-situ* Raman analyses of pure, binary, and ternary mixtures at controlled *PVTX* conditions. The relationship between the relative frequency shift of the stretching modes of gas species (e.g., the CH_4 ν_1 band and/or the CO_2 Fermi diad splitting) has been described and fitted in order to develop high-accurate empirical barometers and densimeters for the direct determination of *PVX* properties of gas mixtures encountered in various geological systems, over a wide composition- and pressure-range. The latter results have been successfully applied, as an alternative way to microthermometry measurements, to the investigation of natural fluid inclusions. This chapter is devoted to the interpretation of the origin of the pressure-induced vibrational frequency shifts of the ν_1 stretching bands of CH_4 and N_2 in mixtures at the molecular scale. The frequency shift of the ν_1 stretching band of CO_2, however, could not be separately observed in Raman spectra, but only the Fermi diad split that consists of two bands (ν^+ and ν^-) arising from the Fermi resonance effect (see text in section 2.3, Chapter 3). Thus, the variation of the CO_2 bands is not discussed herein. Two different theoretical models, i.e., the Lennard-Jones 6-12 potential energy approximation (LJ) and the generalized perturbed hard-sphere fluid (PHF) model, are used to intuitively and qualitatively assess the variation trend as well as the magnitude of the frequency shift of CH_4 and N_2 ν_1 bands. Thereby, the contribution of the attractive and repulsive forces to the variation of the frequency shift as a function of pressure and composition is evaluated for an in-depth understanding. A predictive model of the frequency shift of the CH_4 ν_1 band as a function of pressure (density) and composition of CH_4-N_2 and CH_4-CO_2 binary mixtures is then provided. That of the N_2 ν_1 band is not provided herein because of the modest reproducibility in its measured peak positions (cf. Le et al., 2019, 2020). The solvation induced mean-forces experienced along the vibrational bond and the relative change of the bond length are also determined. The results and discussion presented in this chapter are intended to be submitted as an article in the journal Physical Chemistry.

1. Introduction

Raman spectroscopy is a straightforward developed analytical tool to quickly identify the chemical nature of substances. Based on the basic of Raman effect (Raman, 1929), the peak position reported on Raman spectra results from the difference between the wavenumber of the incident beam and the inelastically diffused photons issued from the laser-matter interaction, and known as "Raman shift". Thus, the "original" peak position recorded at low pressure (low density) characterizes the nature of the analyzed gases, i.e., the "*normal*" intramolecular vibration mode of "*likely-isolated*" gaseous molecules with nearly no interaction with its surrounding molecules. Upon qualitative analyses, the value of the Raman peak position is used as a "fingerprint" to identify the nature matter. Nevertheless, the vibration mode can be slightly perturbed by the interaction with its medium under the effect of pressure, density, temperature, and composition (Placzek, 1934). Consequently, the Raman band undergoes a small, yet measurable and reproducible shift from its original position. Thus, interpretation and determination of the Raman frequency shifts may provide a direct proxy for investigating dynamical behaviors, physicochemical and thermodynamic properties of different fluids at molecular level, including solute-solvent coupling mechanisms and intermolecular interaction forces (Buckingham, 1960; Schweizer and Chandler, 1982). With continuous technical progress in the fabrication of high-pressure and micro-instruments, Raman spectroscopy nowadays could provide more and more accurate and consistent analyses even at extreme conditions (microvolumes, elevated pressure, wide range-temperature), after an adequate calibration process. This makes Raman spectroscopy to become a very useful and practical technique for several scientific disciplines, ranging from physicochemical and/or electrical properties of materials (Goubert et al., 2018; Le Van-Jodin et al., 2019), biological (Jochum et al., 2016; Sieburg et al., 2018), geological (Dubessy et al., 1989, 1999; Chou, 2012; Chou et al., 2005; Caumon et al., 2014; Wang et al., 2019), environnemental (Taquet et al., 2013), medical sciences (Hand et al., 2014; Bögözi et al., 2015), etc.

CH_4, N_2 and CO_2 are among the most common volatile species ubiquitous in various geological fluids (Mullis, 1979; Roedder, 1984; Mullis et al., 1994; Tarantola et al., 2007). Their pressure-induced Raman frequency shift has been intensively studied since the 1970s to develop barometers and densimeters, which could be used for identification and quantification of a minor amount of CH_4 and N_2 contained in natural fluid inclusions (microvolume trapped in mineral or rock) with other geological fluids (Wang and Wright, 1973; Fabre and Oksengorn, 1992; Thieu et al., 2000; Lin et al., 2007a). However, most of the works published in the

literature could only be done for pure components without fully considering the effect of composition in the variation of the peak position of CH_4 and N_2 bands, whereas the latter depends strongly on composition. Indeed, the effect of composition in Raman peak position of CH_4 and N_2 bands was demonstrated by the works of Seitz et al. (1993, 1996), although the accuracy of their calibration data is not good enough for accurate quantitative analyses. Recently, Le et al. (2019, 2020) presented a protocol for quantitative analyses by measuring the relative variation of the peak position (shifted wavelengths) of the CH_4 ν_1 band, not only as a pure gas phase but also in CH_4, N_2, and CO_2 binary and ternary mixtures, with good reproducibility and high accuracy ($\sim \pm 0.02$ cm^{-1}). The wavelength shift of CH_4 band was then used for the accurate determination of pressure ($\pm$ 20 bars) and density ($\pm$ 0.02 $g{\cdot}cm^{-3}$) of the volatile part of natural fluid inclusions. Besides, the peak position measurement of the N_2 band was demonstrated to be less reproducible than that of the CH_4 band due to its asymmetric shape at low pressure (density) and the overlapping with the signal of atmospheric nitrogen (Le et al., 2019, 2020). Therefore, the frequency shift of the N_2 band was not used for accurate quantitative measurements, even though a variation trend as a function of pressure (density) and composition was observed in good agreement with Seitz et al. (1993, 1996).

However, the above-mentioned works were dedicated to providing accurate experimental calibration data of a Raman signal (based on the variation of peak area- or peak intensity ratio and/or frequency shift) for a direct application in the quantitative measurement of the composition of natural fluid inclusions. Thus, the pressure-induced vibrational frequency shift of CH_4 and N_2 ν_1 band was principally described rather than interpreted from a chemical-physical point of view. Therefore, the present study aims to interpret the fundamental mechanisms hidden behind the observed Raman frequency shift of the CH_4 and N_2 ν_1 bands and their variation trends as a function of pressure (or density) and composition (mol%, and the nature of the mixture, i.e., binary mixtures of CH_4 with N_2 or CO_2), which emphasizes the relationship between the variation of intermolecular interaction forces (composed of repulsion and attraction parts). In this study, interpretations and discussions are based on two different theoretical models, i.e. Lennard-Jones 6-12 potential energy approximation (LJ) (Jones and Chapman, 1924) and the generalized perturbed hard-sphere fluid model (PHF) (Schweizer and Chandler, 1982; Ben-Amotz and Herschbach, 1993). Both LJ and PHF models describe the evolution of the repulsive and attractive intermolecular interaction forces experienced between molecules that contribute to the resulting Raman frequency shift as a function of density and/or intermolecular distance.

The PHF model was successfully tested for studying the frequency shift of the ν_1 band of pure N_2 and CH_4 as a function of density and temperature (Ben-Amotz et al., 1992). The results showed a good correlation between the theoretically predicted and experimentally measured frequency shifts. It is to note that Ben-Amotz et al. (1992) treated the frequency shift part of the CH_4 ν_1 band, that is induced by the attractive mean-force, as a linear density-dependent one according to the mean-field approximation of the van der Wall's equation of state (Schweizer and Chandler, 1982). However, more recent experimental results suggested that the attractive force-induced frequency shift of the vibrational modes involving hydrogen bonds (e.g., O–H or C–H bonds) varies nonlinearly as a function of density rather than linearly, especially at high density or pressure (Ben-Amotz and Herschbach, 1993; Hutchinson and Ben-Amotz, 1998). Besides, Le et al. (2020) highlighted a gradual change of the ν_1 band of CH_4 as a function of pressure (bar) and composition (mol%), and also a noticeable difference between the variation trends of the ν_1 band of CH_4 in CH_4-N_2 and CH_4-CO_2 mixtures. Thus, more studies like the present one are still needed to firmly confirm the applicability of the PHF model and to interpret the aforementioned observations. It is therefore interesting and beneficial to test the PHF model in these systems at varying composition over a wider range of density (or pressure) (i) to evaluate the nonlinearity of the attractive force-induced frequency shift and (ii) to interpret from a molecular point of view the observed frequency shift of the CH_4 ν_1 band as a function of pressure (density) and composition.

The present chapter is organized as follows. In section 2, the theoretical background of the LJ approximation and the PHF model is recalled to better understand the results and discussion which will be presented in the next sections. Also, we explain why the LJ approximation could be used to intuitively and practically interpret the global variation trend of the pressure-induced frequency shift of the CH_4 and N_2 bands without any complex molecular dynamic simulation or *ab-initio* calculations. Section 3 is the description of the experimental protocol conducted in this study for the *in-situ* measurement of the pressure-induced frequency shift of the CH_4 and N_2 bands within CH_4-N_2 and CH_4-CO_2 mixtures of varying composition, as well as the processing of Raman spectra. The experimental results and the discussion will be presented in section 4. First, we interpret the pressure-induced vibrational frequency shift of the CH_4 and N_2 bands using the LJ approximation, by attributing them to the contribution of the repulsive and attractive intermolecular potential energy as a function of density (or intermolecular separation) and pressure. Second, since the LJ approximation cannot fully interpret the effect of composition (mol%) on the variation trend of the frequency shift, the PHF model is then

used to decompose the net frequency shift of the ν_1 band of CH_4 into the repulsive and attractive components for evaluating the contribution of repulsive and attractive solvation mean-forces, respectively, both as a function of composition (mol%) and of the chemical nature of the solution (pure CH_4, and mixtures of CH_4-N_2 or CH_4-CO_2). For that, the non-linearity of the attractive force-induced frequency shift of the CH_4 ν_1 band is firstly evaluated. Then, new attractive coefficient parameters (C_a, B_a) used for the PHF model are provided by fitting our experimental data. Afterwards, the predictive model of the frequency shift of the ν_1 band of CH_4 within any CH_4-N_2 and CH_4-CO_2 mixtures over 5-3000 bars is provided. Also, the intermolecular solvation-mean forces and the bond length change could be inferred from Raman spectroscopy data using the PHF model. The chapter end with a conclusion highlighting the significance of our findings.

2. Background theory

2.1. The Lennard-Jones (LJ) potential approximation

The Lennard-Jones 6-12 potential energy (U_{LJ}) approximation is the most widespread semi-empirical model, thanks to the simplicity of its mathematical expression and its accuracy, describing the evolution of the repulsive and attractive potentials experienced between two molecules as a function of their intermolecular separation *r* (Jones and Chapman, 1924). The general mathematic form of the LJ 6-12 approximation is expressed by Equation 4.1.

$$U_{LJ} = 4\varepsilon\left(\left(\frac{\sigma}{r}\right)^{12} - \left(\frac{\sigma}{r}\right)^{6}\right) \qquad 4.1$$

where U_{LJ} is the potential interaction energy given in Kelvin (K), the parameters σ have the dimension of a length (Å) and ε has also the dimension of an energy (K). The parameter ε represents the maximum attraction energy between two molecules that interacts at a distance of $r_0 = 1.1224\sigma$. The LJ parameters σ and ε can be empirically calibrated from experimental data, such as critical temperature, density, viscosity or virial coefficient (Hirschfelder et al., 1964; Möller et al., 1992; Bouanich, 1992; Cuadros et al., 1996) or from quantum-mechanical calculation (Poling et al., 2001). Figure 4-1 represents the variation of the net LJ potential of CH_4 as a function of the distance *r* between two CH_4 molecules. Note that the LJ energy potential experienced between two different molecules can also be estimated from parameters σ_{ij} and ε_{ij} determined using Lorentz-Berthelot combining rules (Equations 4.2 and 4.3). Herein,

LJ parameters (σ, ε) of CH_4, N_2 and CO_2 are cited from Möler et al. (1992) and Hirschfelder et al. (1964) and listed in Table 4-1.

$$\sigma_{ij} = \frac{\sigma_i + \sigma_j}{2} \quad 4.2$$

$$\varepsilon_{ij} = \sqrt{\varepsilon_i \varepsilon_j} \quad 4.3$$

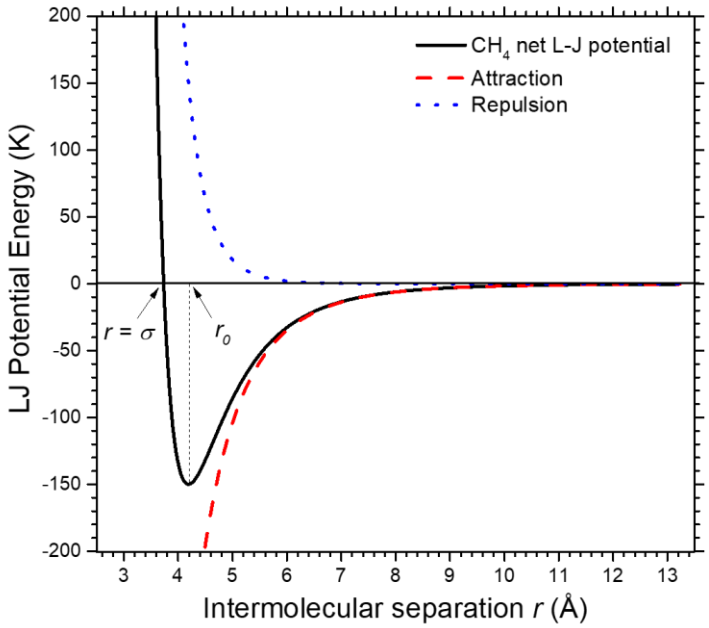

Figure 4-1: Lennard-Jones 6-12 potential energy of CH_4 as a function of intermolecular distance *r*. The LJ potential of CH_4 is also decomposed into repulsive (dashed line) and attractive (dot-line) contributions.

Table 4-1: Lennard-Jones parameters between two identical or non-identical molecules of CH_4, N_2 and CO_2

Molecular pair	σ (Å)	ε (K)
CH_4-CH_4	3.733	149.9
N_2-N_2	3.745	95.2
CO_2-CO_2	3.713	257.8
CH_4-N_2	3.739	119.5
CH_4-CO_2	3.723	196.6

In general, at very low pressure (low density) where the intermolecular distance (r) is large enough, gaseous molecules are entirely independent. Therefore, there is no interaction between molecules. As pressure increases, the distance between molecules is reduced, and so molecules begin to interact with each another with more frequent collisions and steric restrictions. This may impact the vibration mode of gaseous molecules by different phenomena such as lengthening or shortening of C-H bond length of CH_4 or perturbing electron cloud distribution, and so resulting in polarizability changes. The net LJ potential energy of CH_4 is decomposed into repulsive and attractive contributions and plotted along in Figure 4-1. At long distance-range, the attractive force dominates and produces a significant effect, whereas the repulsive forces are negligible (i.e., up to 200 bars corresponding to the separation range of ~ 5Å, Figure 4-1). As pressure increases (or intermolecular distance r decreases), the attractive force increases and reaches its maximum value at a separation r_0, and the repulsive force also increases and completely compensates the attractive force at $r = \sigma$, where the net potential energy equals zero (Figure 4-1).

Overall, the attractive forces tend to expand the geometry (and so the bond length) of a molecule, implying that less energy is required to stretch the bond (Buckingham, 1960; Zakin and Herschbach, 1986; Lin et al., 2007b). On the contrary, the repulsive forces, which produce a more significant effect at short distance range, tend to contract the geometry of molecules, and so, the bond length. The observed vibration mode requires therefore more energy, which, in turn, leads to a shift toward higher wavenumbers (blueshift). Since CH_4, N_2 and CO_2 are all non-polar molecules, the effects of the electrostatic potential energy (which occurred between permanent-dipole molecules) and polarization potential energy (which occurred between permanent- and induced-dipole molecules) potential energies within these systems may be negligible (Coulomb's law). In other words, the intermolecular interactions experienced between these molecules chiefly consist of repulsive and attractive (dispersion) forces. Therefore, it is reasonable to consider that the use of LJ potential energy approximation could accurately interpret the overall fashion of the variation of the pressure-induced frequency shifts of the above-mentioned gaseous systems.

2.2. Perturbed hard-sphere fluid model

2.2.1. Implication of pair distribution function in perturbed hard-sphere fluid model

According to the original treatment of Schweizer and Chandler (1982) and its extension developed by Ben-Amotz et al. (1992, 1993), the hard-sphere pair distribution function

$y_{12}^{HS}(r_{12})$ is related to the excess chemical potential $\Delta\mu^{HS}(r_{12})$ by the following expression (Equation 4.4):

$$\Delta\mu^{HS}(r_{12}) = -k_B \cdot T \cdot \ln y_{12}^{HS}(r_{12}) \quad 4.4$$

where:

$y_{12}^{HS}(r_{12})$ describes the distribution of objects within a medium, i.e., the probability of finding two cavities (denoted 1 and 2) at a given separation (r_{12}), that dissolved in a hard-sphere fluid. Ben-Amotz et al. (1993) reviewed numerous theories and semi-empirical models for the determination of $y_{12}^{HS}(r_{12})$ by evaluating their prediction accuracy and practical utility. The authors proposed that $y_{12}^{HS}(r_{12})$ can be expressed by Equation 4.5, where A, B, C and D are coefficients depending on solute diameters and solvent density, which can be accurately determined from an adequate equation of state (Mansoori et al., 1971; Grundke and Henderson, 1972). The detailed calculation process of these coefficients can be found in the works of Ben-Amotz and coworkers (1992; 1993).

$$y_{12}^{HS}(r_{12}) = A_{12} + B_{12} r_{12} + C_{12} r_{12}^3 + D_{12}\left(\frac{1}{r_{12}}\right) \quad 4.5$$

$\Delta\mu^{HS}(r_{12})$ is the chemical potential change associated with the formation of a hard-sphere diatomic solute of bond length r_{12} (having a chemical potential μ_{12}^{HS}) from two hard-spheres of diameters σ_1 and σ_2 at infinite distance (having a chemical potential μ_1^{HS} and μ_2^{HS}, respectively) dissolved in a solution composed of hard-sphere solvents of diameter σ_s and bulk density ρ. Thereby, $\Delta\mu^{HS}(r_{12})$ can be accordingly calculated using Equations 4.6 to 4.8.

$$\Delta\mu^{HS}(r_{12}) = \mu_{12}^{HS} - (\mu_1^{HS} + \mu_2^{HS}) \quad 4.6$$

$$\mu_{12}^{HS} = -k_B \cdot T \cdot \ln\left[\frac{y_{12}^{HS}(r_{12})}{y_{11}^{HS}(0) \cdot y_{22}^{HS}(0)}\right] \quad 4.7$$

$$\mu_{i\ (i=1\ or\ 2)}^{HS} = k_B \cdot T \cdot \ln y_{ii}^{HS}(0) \quad 4.8$$

Note that both $y_{12}^{HS}(r_{12})$ and $\Delta\mu^{HS}(r_{12})$ depend on σ_1, σ_2, σ_s, r_{12}, and ρ. Since the $\Delta\mu^{HS}(r_{12})$ arises from the formation of a hard diatomic solute from two separate atoms (Equation 4.6), it reflects the repulsive contribution to the interaction (perturbation) potential energy of the mean-force ($V_{mean-force}^{HS}$) exerted by the solvent on the solute molecules (Equation 4.9) (Schweizer and Chandler, 1982; Zakin and Herschbach, 1986).

$$V^{HS}_{mean-force}(r_{12}) = \Delta\mu^{HS}(r_{12}) \quad 4.9$$

Combining Equations 4.4 and 4.9, the solvation-induced mean repulsive force (F_R) experienced along the bond r_{12} of a hard diatomic (or pseudo-diatomic) solute can be determined from the first derivative of $\Delta\mu^{HS}(r_{12})$ respectively to r_{12}, with r_{12} equals to the equilibrium bond distance r_e ($r_{12} > |(\sigma_1 - \sigma_2)/2|$, otherwise $F_R = 0$) (Equation 4.10).

$$F_R = \left[\frac{\partial\Delta\mu^{HS}(r_{12})}{\partial r_{12}}\right]_{r_e} = -k_B{\cdot}T.\left[B_{12} + 3C_{12}r_{12}^2 - D_{12}\left(\frac{1}{r_{12}^2}\right)\right] \quad 4.10$$

G_R represents the mean-field approximation of the quadratic repulsive solvation force that can be approximately determined from the second derivative of the excess chemical potential $\Delta\mu^{HS}(r_{12})$:

$$G_R = \frac{1}{2}\left[\frac{\partial^2\Delta\mu^{HS}(r_{12})}{\partial r_{12}^2}\right]_{r_e} = -(k_B{\cdot}T)\left[3C_{12}r_{12} + D_{12}\left(\frac{1}{r_{12}^3}\right)\right] \quad 4.11$$

2.2.2. Determination of density- or solvent-induced vibration frequency shift

Based on the theoretical model developed by Buckingham (1960), the relationship between vibrational frequency shifts ($\Delta\nu$) and medium-induced intermolecular forces experienced along the bond is represented by Equation 4.12 (Zakin and Herschbach, 1986; Ben-Amotz et al., 1992), where ν_0 is the unperturbed vibrational frequency measured at low density; *f* and *g* are the harmonic and anharmonic force constants of an isolated diatomic solute (Equation 4.13) that can be obtained from vibrational frequencies and bond lengths (measured in the gas phase at low density) using extended Barger's rule correlation (Herschbach and Laurie, 1961); *F* and *G* are the linear and quadratic coefficients in an expansion of the solvent potential of mean-force as a function of solute bond length (Equation 4.14), respectively; and $f_1(\kappa)$ and $f_2(\kappa)$ are the modified Morse coefficients for anharmonic vibration (Dijkman and van der Maas, 1977; Zakin and Herschbach, 1988; Ben-Amotz et al., 1992).

$$\Delta\nu \approx \nu_0\frac{F}{f}\left[-\left(\frac{3g}{2f}\right)f_1(\kappa) + \left(\frac{G}{F}\right)f_2(\kappa)\right] \quad 4.12$$

$$U_0(r_{12}) = \frac{1}{2}f(r_{12} - r_e)^2 + \frac{1}{2}g(r_{12} - r_e)^3 + \cdots \quad 4.13$$

$$V_{mean-force} = F(r_{12} - r_e) + G(r_{12} - r_e)^2 + \cdots \quad 4.14$$

The change in bond length Δr corresponding to the resulting frequency shift $\Delta\nu$ can be simply determined from average solvation mean-force (F) and harmonic force constant (f) using Equation 4.15:

$$\Delta r = \frac{F}{f} \qquad 4.15$$

The net frequency shift $\Delta\nu$ can be decomposed into the repulsive ($\Delta\nu_R$) and attractive ($\Delta\nu_A$) components, which is induced by repulsive and attractive solvation-mean force, respectively, (Equation 4.16):

$$\Delta\nu = \Delta\nu_R + \Delta\nu_A \qquad 4.16$$

The repulsive contribution ($\Delta\nu_R$) to the net frequency shift can be accurately calculated from F_R and G_R parameters using the perturbed hard-fluid model as described above (Equations 4.10 - 4.12 with $F = F_R$ and $G = G_R$). All required hard-sphere parameters of solute CH_4 and solvent (CH_4, N_2 and CH_4) are reported in Table 4-2 (Ben-Amotz et al., 1992). To our best knowledge, the attractive contribution ($\Delta\nu_A$), however, could not be theoretically described yet. According to Schweizer and Chandler (1982), within diatomic (e.g., N_2) or pseudoatomic (e.g., CH_4) molecules, the $\Delta\nu_A$ is proportional to the attractive force (F_A) acting along the vibrational bond. Since F_A relatively slowly varies, Chandler and coworkers assumed that, based on the van der Walls' equation of state, the attractive contribution ($\Delta\nu_A$) varies linearly with the solvent density, i.e., $\Delta\nu_A = C_a \cdot \rho$ (where C_a is an empirical coefficient fitted from a few experimental data). This assumption had shown a good agreement in various solvent-solute systems by fitting experimental data (Schweizer and Chandler, 1982; Zakin and Herschbach, 1986; Ben-Amotz et al., 1992).

However, recently published experimental data showed a systematical deviation from the theoretical prediction (linear density dependence) and that $\Delta\nu_A$ may rather vary as a nearly quadric function of the solvent density, i.e., $\Delta\nu_A = B_a \cdot \rho^2 + C_a \cdot \rho$, (Zakin and Herschbach, 1988; Ben-Amotz and Herschbach, 1993; Lee and Ben-Amotz, 1993; Meléndez-Pagán and Ben-Amotz, 2000; Saitow et al., 2004; Kajiya and Saitow, 2013), especially for hydrogen stretching vibrations (e.g., C–H, O–H). The parameters C_a and B_a can also be empirically fitted from experimental data. Once these parameters are determined, the repulsive frequency shift $\Delta\nu_A$ can be thus calculated for any arbitrary density. It should be kept in mind that the frequency shift of the CH_4 ν_1 band changes not only with different solvents but also gradually changes as

a function of the molar fraction (composition) (Le et al., 2019, 2020). Thus, C_a and B_a are expected to be composition-dependent. In the present study, both assumptions (linear and quadric density-dependence of $\Delta\nu_A$) will be evaluated for the case of CH_4 (ν_1 stretching band) dissolved in different solvents (pure CH_4, CH_4-N_2 and CH_4-CO_2 mixtures). The adjustable parameters C_a and B_a are then provided by fitting from our experimental data.

Table 4-2: Hard sphere fluid parameters of solute (CH_4) and solvent (CH_4, N_2, and CO_2) (Ben-Amotz et al., 1992).

bond	ν_0 (cm^{-1})	r_e (Å)	σ_1 (Å)	σ_2 (Å)	$\sigma_s^{CH_4}$ (Å)	$\sigma_s^{N_2}$ (Å)	$\sigma_s^{CO_2}$ (Å)	f (dyne/Å)	g (dyne/Å^2)
C-H	2917	1.091	2.22	3.53	3.58	3.45	4.00	0.005049	-0.01047

ν_0 : Raman peak position of CH_4 ν_1 band at near zero density.

r_e : bond length of CH_4 ν_1 band at equilibria.

σ_1 and σ_2 : pseudo-diatomic hard-sphere diameters of CH_4 solute.

σ_s : hard-sphere diameters of solvent.

f, g : harmonic and anharmonic force constants of isolated CH_4 solute molecule, respectively.

3. Experimental pressure-induced frequency shift measurements

The Raman in-situ measurements of gas mixtures are performed over 5 - 600 bars using the same experimental apparatus and protocol described in our previous works (Le et al. 2019, 2020, i.e., Chapter 3 and 4 of the present dissertation). Briefly, binary gas mixtures of any desired composition are prepared from high-purity CH_4, CO_2 and N_2 gases (99.99% Air Liquid^{TM}) using a commercial mixer (GasMix Alytech^{TM}), then compressed by a home-made pressurization system and stored in a 300 cm^3 stainless steel tanker (Swagelok 316L-50DF4-300) at ~ 130 bars. The composition of the obtained mixtures, before being loaded in an improved High-Pressure Optical Cell (HPOC) system (Chou et al., 2005; Caumon et al., 2014), is double-checked by gas chromatography which was previously calibrated by standard gases with an uncertainty of about ± 0.3 mol%. The HPOC system serves as a chamber sample, whose one end is equipped with a manual screw pump for pressure adjustment, and the other end is connected to a sealed transparent microcapillary placed on a Linkam CAP500 heating-cooling stage for temperature control. In this study, the temperature is maintained at 22 ± 0.1 °C. Once the prepared gas mixture is loaded into the system, the internal pressure can be adjusted by

turning the manual screw and monitored by two different pressure-transducers (±1 bar). Thereby, Raman *in-situ* measurement of gas mixtures within the transparent microcapillary can be performed at controlled *PTX* conditions. Pressure-to-density conversion is done using the GERG-2004 equation of state (Kunz, 2007; Kunz and Wagner, 2012) integrated in REFPROP software (Lemmon et al., 2013).

Raman spectra are collected with a LabRAM HR spectrometer (Horiba Jobin-Yvon®) equipped with a liquid-nitrogen cooling CCD detector, a 514.532 nm Ar^+ laser (Stabilite 2017, Spectra-Physics), a ×20 Olympus objective (NA = 0.4) and an 1800 groove·mm^{-1} grating. The confocal hole and the slit are set at 1000 and 200 µm, respectively, giving a spectral resolution of about 1.6 cm^{-1}. At any given *PTX* condition, each Raman measurement (average of 10 accumulations) is repeated at least six times for statistical purposes. Thereby, depending on the pressure range and the composition of the analyzed gases, the total acquisition time varies from ~100 to 600 seconds in order to optimize the S/N ratio and measurement time. The Raman spectra are then fitted with Labspec6 software (Horiba), after baseline correction, using asymmetry Gaussian-Lorentzian function (for N_2) and symmetry Gaussian-Lorentzian function (for CH_4 and CO_2). Herein, we are interested in the relative variation of the fitted peak position of the ν_1 stretching band of CH_4 and N_2 ($\Delta\nu$) within different mixtures, which is the difference between the fitted peak position recorded at a given pressure and near-zero pressure (~ 5 bars). To minimize the day-to-day deviation arising from the instrumental response, the whole analysis series (from 5 to 600 bars) of a specific mixture must be continuously performed and done within one experimental section of the same day. According to our analytical analyses the uncertainty on the $\Delta\nu$ value is about 0.02 cm^{-1}.

4. Results and discussion

4.1. Interpretation of the frequency shift based on the Lennard-Jones potential energy approximation: effect of density (pressure) change

The relative variation of the peak position of the ν_1 stretching band of N_2 (within the CH_4-N_2 and CO_2-N_2 mixtures) and CH_4 (within the CH_4-N_2 and CH_4-CO_2 mixtures) as a function of pressure and composition are presented in Figure 4-2 and Figure 4-3, respectively. The experimental data are from this study (binary mixtures over 5-600 bars) and from Fabre and Oksengorn (1992) (pure CH_4 and N_2, up to 3000 bars). Note that "relative variation" means the difference between the peak position measured at a given pressure and near-zero pressure (e.g.,

~ 5 bars in this study), so-called hereafter as "frequency shift". Overall, both N_2 and CH_4 bands shift toward lower wavenumbers as pressure (density) increases or intermolecular separation (*r*) decreases. The magnitude of the frequency shift also varies as a function of the composition of the mixture. The composition effect is quite small at the low pressure and becomes more pronounced at high pressure (cf. Figure 4-2 and Figure 4-3). As evidence, the curves converge to a point at near-zero pressure (low density) and tend to span out as pressure increased, except in the pressure range between 300 - 400 bars in the case of CH_4-CO_2 mixtures (Figure 4-2 and Figure 4-3). Besides, the magnitude of the frequency shift of N_2 in CH_4-N_2 and CO_2-N_2 mixtures gradually increases with decreasing N_2 concentration, whereas that of CH_4 band in the CH_4-N_2 mixtures shows an inversion, i.e., the frequency shift magnitude decreases with decreasing CH_4 concentration. The difference between the propensity of the frequency shift of CH_4 in CH_4-N_2 mixtures and that in CH_4-CO_2 mixtures are also observed in Figure 4-3 and described in section 3.2.1. Indeed, the magnitude of the frequency shift of CH_4 within CH_4-CO_2 mixtures may increase or decrease as CH_4 concentration decreases, depending on the pressure-range (Figure 4-3b).

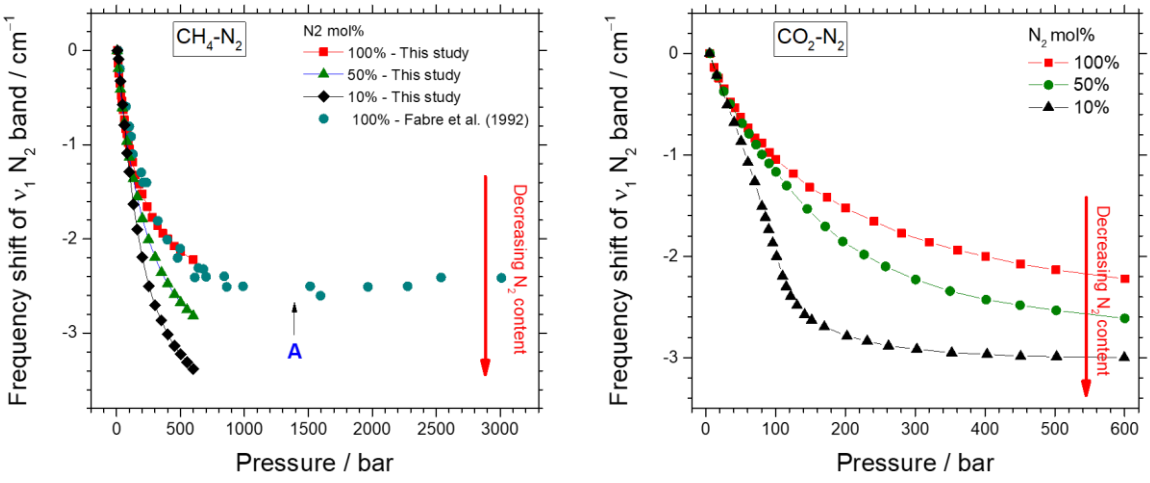

Figure 4-2: Frequency shift of the ν_1 stretching band of N_2 as a function of pressure and composition in (a) CH_4-N_2 or (b) CO_2-N_2 mixtures. Experimental data are from this study (up to 600 bars) and Fabre et Oksengorn (1992) (up to 3000 bars). The frequency shift of the ν_1 band of pure N_2 reaches the minimal value within the pressure range A, i.e., ~ 1200 - 1600 bars.

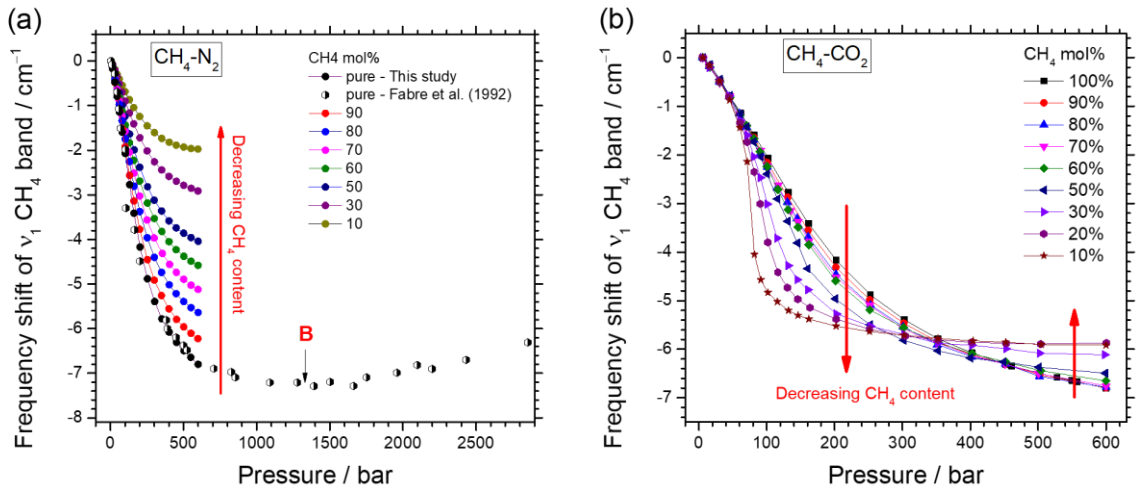

Figure 4-3: Frequency shift of the ν_1 stretching band of CH_4 as a function and pressure and composition in (a) CH_4-N_2 or (b) CH_4-CO_2 mixtures. Experimental data are from this study (up to 600 bars) and Fabre et Oksengorn (1992) (up to 3000 bars). The frequency shift of the ν_1 band of pure CH_4 reaches the minimal value within the pressure range B, i.e., ~ 1200 - 1700 bars.

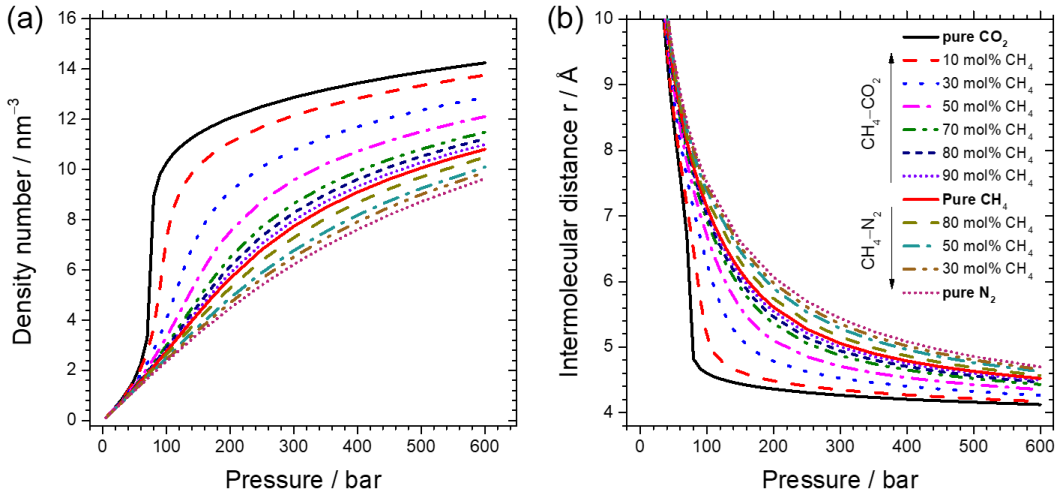

Figure 4-4: Variation of (a) density number (nm^{-3}) or (b) intermolecular distance *r* (Å) as a function of pressure of pure CH_4 and of the mixtures with CO_2 and N_2. The intermolecular separation *r* between CH_4 and/or N_2 molecules was estimated from the density ($g \cdot cm^{-3}$) by assuming that all gaseous molecules are separated by the same distance.

Figures 4-4a and 4-4b present the variation of density number or intermolecular separation *r* as a function of the pressure of pure CH_4 and different mixtures with N_2 and CO_2. Overall, the curves plotted in Figure 4-4 show a close affinity with the relative order and the shape change as a function of composition of the frequency shift-pressure curves plotted in Figure 4-2 and Figure 4-3. More concretely, the intermolecular distance at any pressure decreases

from pure N_2 to pure CH_4 then pure CO_2 (Figure 4-4b), which is in good agreement with the overall variation trends of the frequency shift magnitude of the N_2 and CH_4 bands as composition varies, i.e., the magnitude of the N_2 band frequency shift always decreases when it is mixed with either CH_4 or CO_2 (Figure 4-2), whereas that of the CH_4 band decreases when it is mixed with N_2 or increases when it is mixed with CO_2 (over ~ 1 - 400 bars) (Figure 4-3). Moreover, the curvature of the frequency shift calibration curves of CH_4 and N_2 bands within CH_4-N_2 mixtures progressively changes with the change of CH_4 or N_2 content (Figure 4-2a and Figure 4-3a). Regarding CO_2-N_2 and CH_4-CO_2 mixtures dominated by CO_2 (e.g., CO_2 mol% > ~ 70%), the curvature undergoes a remarkable change with increasing CO_2 content. For instance, the intermolecular separation *r* of CH_4-CO_2 mixture of 10 mol% CH_4 (90 mol% of CO_2) is drastically decreased at around 80-110 bars then continues slowly decreasing as pressure increases up to 600 bars (Figure 4-4b). These variation trends correspondingly mirror the significant decrease, then followed by a stepwise-like behavior of the curve of the CH_4-CO_2 mixture of 10 mol% CH_4 (Figure 4-3b). Similar variation is observed for the curve of the CO_2-N_2 mixture of 90 mol% CO_2 (Figure 4-2b). The similarity described above is thus an evidence of the intrinsic correlation between the observed Raman frequency shifts and the intermolecular distance change, as well as the variation of intermolecular interactions between molecules. The LJ potential approximation can therefore be used to practically interpret the pressure-induced Raman frequency shift.

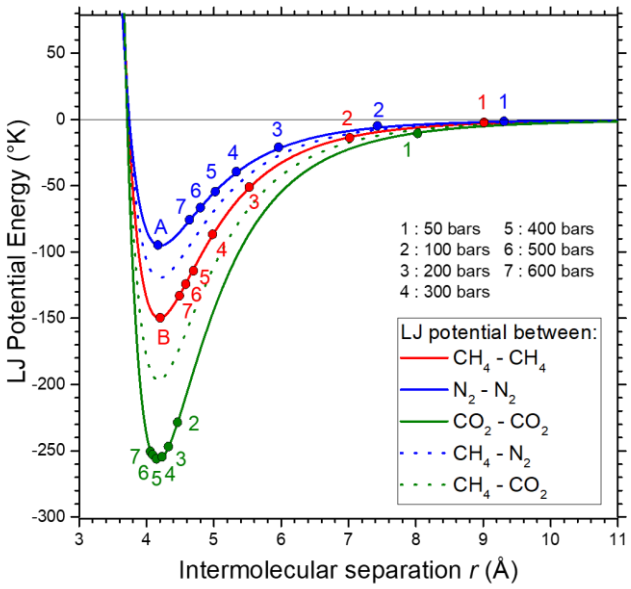

Figure 4-5: Variation of the Lennard-Jones 6-12 potential energy experienced between (solid lines) a pair of identical molecules of CH_4, N_2 and CO_2, or (dotted-lines) a pair of non-identical molecules

(CH_4-N_2 or CH_4-CO_2). The points A (~ 1400 bars) and B (~ 1300 bars) correspond to the points where the intermolecular interaction reaches the minimal value.

Figure 4-5 shows, according to the Lennard-Jones 6-12 approximation, how the interaction between a pair of two (identical or non-identical) molecules of CH_4, N_2, and CO_2 varies as a function of intermolecular separation *r* and pressure. The pressure variation is also represented by solid points denoted 1 to 7 in Figure 4-5. Over the studied pressure-range (5-600 bars), the LJ repulsive potentials of pure or binary mixtures of CH_4, N_2, and CO_2 are quite small (Figure 4-1). In contrast, the attractive potential is much more important and always dominates, resulting in a negative value of the net LJ potential (Figure 4-5). Also, the net LJ potential becomes more and more negative with increasing pressure. As a consequence, the bands of N_2 and CH_4 continuously shift toward lower wavenumbers as pressure (density) increases. As a further increase of pressure, the molecules come closer to each other and reach the separation value $r = r_0$, where the net LJ potentials of N_2 and CH_4 are minimal (marked respectively by points A, B and 5 in Figure 4-5). At these points, the repulsive potential balances the attractive one and begins to dominate the net intermolecular potential. Thereby, the CH_4 and N_2 bands are expected to undergo a blueshift afterwards because of the onset of the important contribution of repulsive potential. The experimental data of Fabre et Oksengorn (1992) show a good agreement with the above interpretation, i.e., an inflection is observed on the frequency shift-pressure curve at around ~ 1400 bars for pure N_2 and ~ 1300 bars for pure CH_4 (Figure 4-2 and Figure 4-3a) corresponding to point A and B marked in Figure 4-5, respectively.

Besides, the downshift magnitude of the CH_4 band is more significant than that of N_2 at any pressure (Figure 4-2 and Figure 4-3). It can be directly explained by the fact that the derivative of the polarizability corresponding to the vibrational coordinate ($d\alpha/dQ$) for the C–H bond within CH_4 molecules is much larger than that of the N–N bond within N_2 molecules (e.g., 2.08 in CH_4 > 0.66 in N_2; Murphy et al. 1969). The LJ potential energy also well reflects the relative difference between the downshift magnitude of CH_4 and N_2 bands. Indeed, at a given pressure (cf. points 1-7 in Figure 4-5), the difference of the intermolecular separation *r* in pure N_2 and pure CH_4 is rather small. Also, the LJ potential energy experienced inside N_2-N_2 molecular pairs is always less than that experienced inside CH_4-CH_4 pairs (Figure 4-4 and Figure 4-5), leading systematically to a smaller downshift of the N_2 band compared to that of the CH_4 band. Besides, the LJ potential energy experienced inside CH_4-N_2 pairs is expected to be smaller than that between CH_4-CH_4 pairs and larger than that between N_2-N_2 pairs at any pressure (Figure 4-5). Thus, this can reasonably interpret the progressive decrease (or increase)

of the downshift magnitude of the CH_4 band (or the N_2 band) as CH_4 (or N_2) content in CH_4-N_2 mixtures decreases.

However, the LJ 6-12 potential energy could not interpret quantitatively the downshift magnitude of the CH_4 band in CH_4–CO_2 mixtures as the CH_4 content decrease. For instance, over 350 - 600 bars, the intermolecular separation between CH_4 molecules (in pure CH_4) is much larger than that between CO_2 molecules (in pure CO_2) at the same pressure (cf. points 5, 6, and 7 in Figure 4-5), which may partially be due to a noticeable difference between the respective diameters of the molecules (3.8 and 3.3 Å for CH_4 and CO_2, respectively). Moreover, the LJ intermolecular potential energy inside CH_4-CO_2 pairs is expected to be discernibly greater than that between CH_4-CH_4 pair (Figure 4-5). Notwithstanding, the CH_4 band in CH_4-CO_2 mixtures with < 30 mol% CH_4 is less shifted than the CH_4 band in pure CH_4 or CH_4-CO_2 mixtures with > 50 mol% CH_4 (Figure 4-3b). One may imply a complex interaction between molecules when they are in the near-critical state (the critical temperature of pure CH_4 and CO_2 are – 82.6 and 31.05 °C, respectively). It is noteworthy that the LJ potential approximation only describes the variation between two molecules (identical or non-identical), not between the analyzed molecules and its medium (e.g., all surrounding molecules). Therefore, the effect of the composition change could not fully be taken into account by the LJ potential approximation as well as the above interpretations, whereas the Raman frequency shift of the observed vibration mode chiefly arises from the perturbation caused by its medium. Moreover, the effect of the perturbation strongly depends on the geometrical configuration between molecules (Hellmann et al., 2014), and so on the composition of mixtures (Figure 4-2 and Figure 4-3). Thus, to quantitatively appraise the pressure-induced frequency shift with composition change, the solvation mean-forces acting along the vibration bond of the analyzed molecules must be considered using an appropriate model such as the perturbed hard-fluid model (PHF). In the following, the PHF model is therefore used to determine the contribution of repulsive and attractive mean-forces to the observed frequency shift of the CH_4 ν_1 band, and also to evaluate the bond length change as a function of pressure and composition. A predictive model is also provided to predict the pressure-induced frequency shift of the CH_4 band in pure and/or binary mixtures with CO_2, and N_2, up to 3000 bars.

4.2. Decomposition of the observed pressure-induced frequency shift into attractive and repulsive components: evaluation of composition variation

Figure 4-6 represents the repulsive and attractive force induced-frequency shifts ($\Delta\nu_R$ and $\Delta\nu_A$, respectively) and the net predicted frequency shift ($\Delta\nu = \Delta\nu_R + \Delta\nu_A$) of the CH_4 ν_1 band as a function of density within a pure CH_4 gas system. $\Delta\nu_R$ (blue solid line) was determined using the PHF model, as described in section 2.2. $\Delta\nu_A$ was fitted from experimental data by the two assumptions described in section 2.2.2 for accuracy evaluation, which is a linear (green solid line, $\Delta\nu_A^1$) or a quadric (red solid line, $\Delta\nu_A^2$) function of density. The intercept of the regression equation (linear or quadric) was equal to 0 at the near-zero density value (corresponding to ~5 bars in the present study). Thereby, the net predicted frequency shift $\Delta\nu^1$ and $\Delta\nu^2$ are correspondingly the product of $\Delta\nu_R$ and $\Delta\nu_A^1$ or $\Delta\nu_A^2$, presented in Figure 4-6 by black solid-curve or dashed solid-curve, respectively. The experimental data ($\Delta\nu^{exp}$) of the net frequency shift over 5 - 3000 bars, which are from this study and Fabre and Oksengorn (1992), are also represented by points in Figure 4-6.

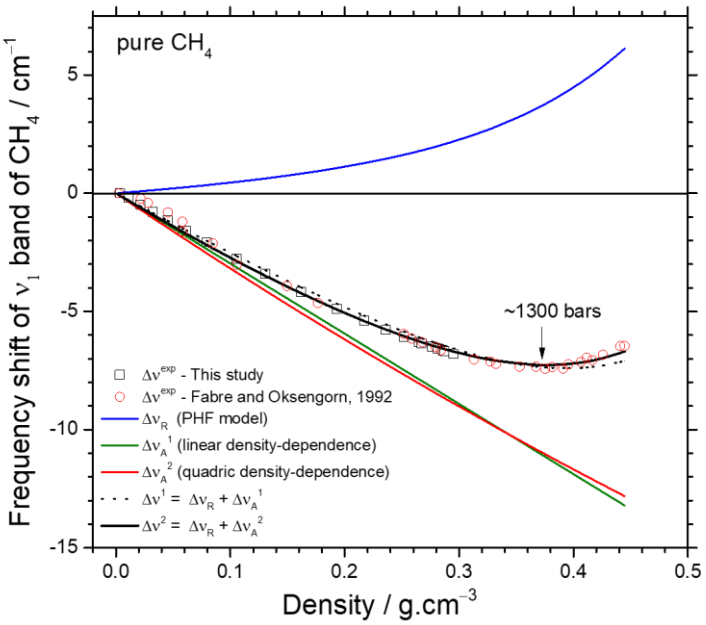

Figure 4-6: Variation of the frequency shift of the ν_1 band of CH_4 as a function of density. Experimental data ($\Delta\nu^{exp}$) performed at 5-3000 bars are from this study and Fabre and Oksengorn, (1992). The repulsive force-induced frequency shift ($\Delta\nu_R$) was calculated using the PHF model. The attractive force-induced frequency shift ($\Delta\nu_A^1$ and $\Delta\nu_A^2$) were fitted from experimental data ($\Delta\nu_A = \Delta\nu^{exp} - \Delta\nu_R$) by a linear or quadric function, respectively (read the text in section 2.2.2). The net

predicted frequency shift ($\Delta\nu^1$ and $\Delta\nu^2$) is the sum of the $\Delta\nu_R$ component and the attractive component ($\Delta\nu_A^1$ or $\Delta\nu_A^2$).

Overall, the contribution proportion of the attractive and repulsive force-induced frequency shift ($\Delta\nu_R$ and $\Delta\nu_A$) are in good agreement with the interpretation based on the LJ potential energy approximation above (section 4.1, Figure 4-1 and Figure 4-5), that is the repulsive component is rather insignificant at low density (pressure), and become more and more balanced by the attractive component above 1300 bars, resulting in an inversion of the frequency shift direction of the CH_4 ν_1 band. Comparing between the linear and quadric regressions, the net predicted frequency shift curves ($\Delta\nu^1$ and $\Delta\nu^2$) are in good agreement at low-density range (e.g., < ~ 0.4 g·cm^{-3}), then it starts to slightly deviate at higher density range (Figure 4-6), although the difference between the curves of the two attractive components ($\Delta\nu_A^1$ and $\Delta\nu_A^2$) are rather small. Comparing the net predicted curves with the experimental data ($\Delta\nu^{exp}$) confirmed that the quadric function could describe a little bit more accurately the density-dependence of $\Delta\nu_A$ than the linear one over the studied density-range. The quadric function is therefore used to fit our experimental data of CH_4-N_2 and CH_4-CO_2 binary mixtures. All resulting parameters C_a and B_a of the regression by the quadric function are listed in Table 4-3. The correlation coefficient (adjusted-R^2) obtained from the least-square analysis is always higher than 0.997.

Table 4-3: Density-dependence parameters of $\Delta\nu_A$ of the CH_4 ν_1 band within CH_4-N_2 and CH_4-CO_2 binary mixtures, with $\Delta\nu_A = B_a \cdot \rho^2 + C_a \cdot \rho$.

mol% CH_4	CH_4-N_2 mixtures		CH_4-CO_2 mixtures	
	B_a	C_a	B_a	C_a
100	8.633	-32.660	8.633	-32.660
90	6.824	-28.686	1.945	-26.473
80	5.257	-24.946	1.928	-23.019
70	4.856	-22.106	-0.904	-18.888
60	4.335	-19.413	-1.420	-16.637
50	3.873	-16.987	-1.136	-15.100
40	2.828	-14.468	-0.662	-13.739
30	1.793	-12.904	-1.361	-11.944
20	2.121	-10.645	-2.147	-10.254
10	2.337	-9.275	-3.370	-8.405

The variation of the repulsive ($\Delta\nu_R$) and attractive ($\Delta\nu_A$) components of the net frequency shift ($\Delta\nu$) of the CH_4 ν_1 band as a function of density and composition of CH_4-N_2 and CH_4-CO_2 mixtures are presented in Figure 4-7a and b. In general, both repulsive ($\Delta\nu_R$) and attractive ($\Delta\nu_A$) components change gradually with the variation of density and composition. The value of the attractive component ($\Delta\nu_A$) is always greater than $\Delta\nu_R$ value at any given density-composition condition, which is in good agreement with the variation of the resulting redshift (with respect to that at near-atmospheric pressure, c.f., Figure 4-3) observed for the ν_1 band of CH_4. Over the studied density-range (up to 3000 bars), the highest value of the repulsive component $\Delta\nu_R$ within CH_4-N_2 mixture only shows a subtle change (from + 6.2 to + 5.8 cm^{-1}), whereas that in CH_4-CO_2 mixtures steadily increases from + 6.2 to + 13.3 cm^{-1} as the content of CH_4 decreases. Also, an inverse variation trend is observed for the absolute value of the attractive component $|\Delta\nu_A|$, with a progressive decrease in the CH_4-N_2 mixtures (from about – 12.9 to – 5.8 cm^{-1}) but a slight increase in the CH_4-CO_2 mixtures (from about – 12.9 to – 15.1 cm^{-1}) as the CH_4 content decreases.

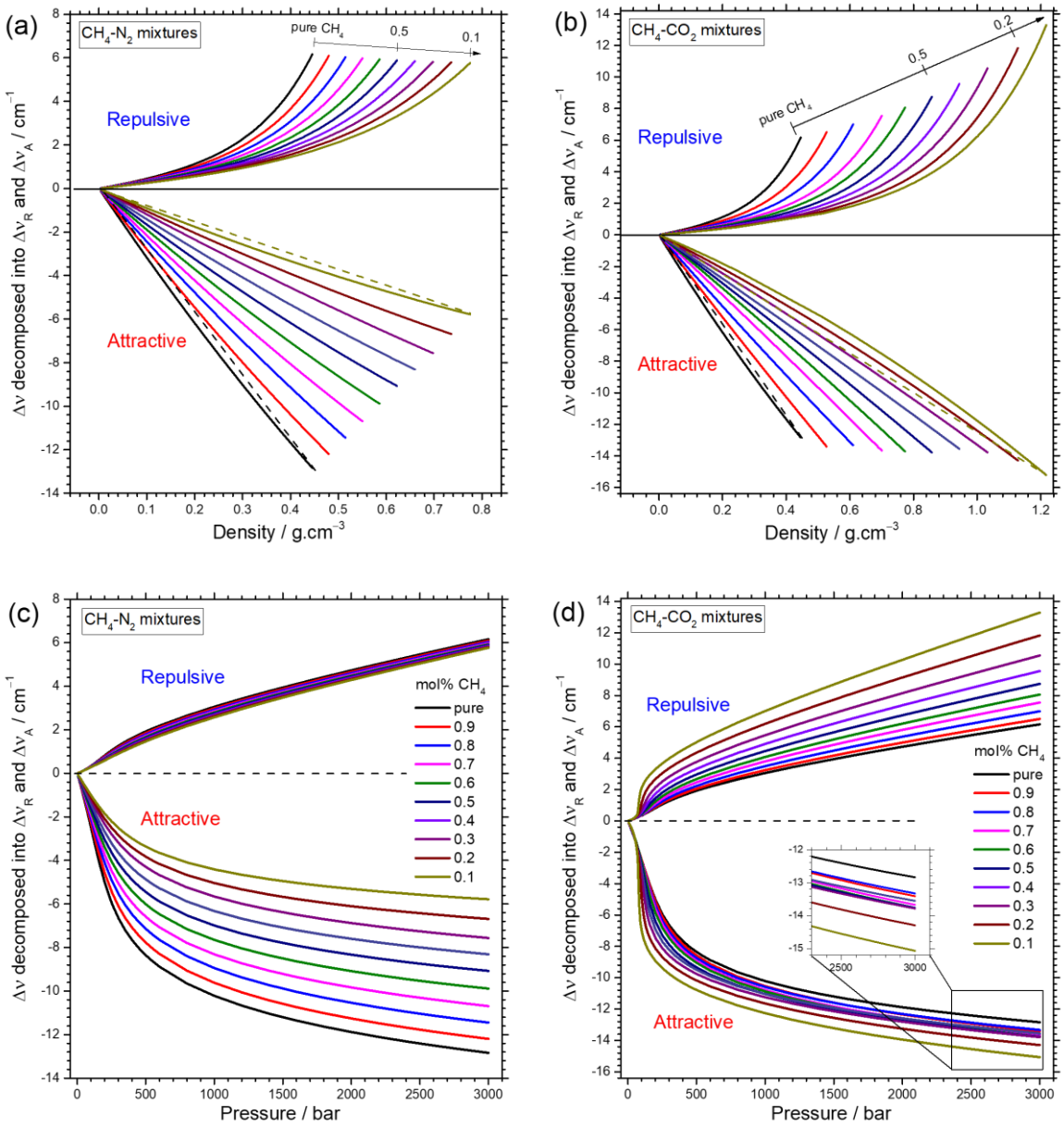

Figure 4-7: Variation of repulsive and attractive components ($\Delta\nu_R$ and $\Delta\nu_A$) of the net frequency shift of the ν_1 band of CH_4 as a function of composition of CH_4-N_2 and CH_4-CO_2 binary mixtures and density (a, b) or pressure (c, d). Pointed-straight-lines in Figure a and b are guides for eye for curvature evaluation.

The curvature of the attractive component $\Delta\nu_A$-density curves systematically changes from positive (for CH_4-N_2 mixtures dominated by N_2) to negative (for CH_4-CO_2 mixtures dominated by CO_2) fashion (cf. guiding pointed straight lines in Figure 4-7a and b, and B_a coefficient values in Table 4-3). Thus, the degree of the nonlinear density dependence of $\Delta\nu_A$ likely depends on the T_c of the analyzed mixtures. The critical temperatures (T_c) of pure N_2, CH_4 and CO_2 are – 146.5, – 82.6 and 31.05 °C, respectively (cited form NIST Chemistry webbook,

Kramida et al. 2018). Consequently, the T_c of CH_4-N_2 mixtures, which vary between – 146.5 and – 82.6 °C depending on mixture composition, is far lower than room temperature. Thereby, CH_4-N_2 mixtures are always in supercritical state upon the analyses performed at controlled 22 °C. On the other hand, the T_c of CH_4-CO_2 mixtures, which ranges from – 82.6 to 31.05 °C as a function of composition, can be closer to the analyzed temperature of 22 °C. For instance, the CH_4-CO_2 mixture of 90 mol% of CO_2 has a critical point at ~ 23.4 °C (calculated by REFPROP program), and so the analyses has been performed (at 22 °C) outside the supercritical region.

The nonlinearity of the density-dependence of the attractive component $\Delta\nu_A$ can also be explained by an enhancement of local density around the solute molecules, especially for supercritical fluids (Rice et al., 1995; Song et al., 2000; Saitow et al., 2004; Cabaço et al., 2007). Furthermore, the deviation of the density-dependence of the attractive component $\Delta\nu_A$ from the linear variation trend could also be ascribed to the aggregation of "non-identical" molecules. Indeed, the uniform molecular distribution may cause less attractive force than the non-uniform one (Saitow et al., 2004). Comparing with the diameter of a CH_4 molecule (3.8 Å), the diameter of a N_2 molecule (3.65 Å) is rather comparable, whereas that of CO_2 molecule is clearly smaller (3.3 Å). As a result, the nonlinearity of the density-dependence of the attractive component $\Delta\nu_A$ in CH_4-N_2 mixtures is less noticeable than that observed for CH_4-CO_2 mixtures (Figure 4-7a and b).

Another reason that could be attributed to the nonlinear density-dependence of the attractive frequency shift component $\Delta\nu_A$ is the formation of the short-range hydrogen bonds between solute and solvent molecules whose strength increases nonlinearly with density. Although the latter mechanism mostly takes place within a system composed of polar molecules, resulting in a significant effect on density dependence of attractive components (Zakin and Herschbach, 1988; Lee and Ben-Amotz, 1993; Meléndez-Pagán and Ben-Amotz, 2000; Raveendran and Wallen, 2002), a slight effect could still be found in non-polar systems at high pressure (density) (Meléndez-Pagán and Ben-Amotz, 2000) (e.g., pure solution of ethane (Lee and Ben-Amotz, 1993)) and perhaps in this study (pure or binary mixtures of CH_4 with CO_2 and N_2). Indeed, Figure 4-5 clearly shows that the length scale of the net interaction forces (whose attractive component prevails) experienced within CH_4-CH_4 or CH_4-N_2 pairs is rather shorter than that within CO_2-CO_2 or CO_2-CH_4 pairs at any given pressure, suggesting a shorter-range cohesive interaction between CH_4 and CO_2 molecules than between CH_4 and N_2

or CH_4 and CH_4. This may favor local interactions, i.e., the formation of hydrogen bonds that partially contribute to the slight non-linear density dependence of CH_4 ν_1 bonds (Figure 4-7a and b).

Various types of bond (C–C, C=C, N–H, C–H, O–H, etc.,) within different molecules dissolved in different solvents (methanol, dichloromethane, tetrahydrofuran, octene, etc.) have been investigated in earlier published works (Hutchinson and Ben-Amotz, 1998; Meléndez-Pagán and Ben-Amotz, 2000). The authors noticed that the bonds of the same type tend to experience similar solvent forces, and the solvation force (and so, the induced frequency shift) weakly depends on the location of the bond within the molecules and the nature (molecular structure) of the solvent (i.e., solute-solvent coupling mechanisms). However, the experimental results presented here (the C–H stretching vibration mode of CH_4) indicate that the induced frequency shift depends not only on bond type but also strongly depends on the composition of the solution as well as the nature of the solvent (i.e., solvent parameters).

The origin of the difference on the variation trend of the frequency shift of CH_4 ν_1 band reported in Figure 4-3a and b can be better understood by decomposing the net frequency shift into $\Delta\nu_R$ and $\Delta\nu_A$ components, and represented in frequency shift-pressure-composition space (Figure 4-7c and d). Regarding CH_4-N_2 mixtures, the repulsive component $\Delta\nu_R$ is likely "unchanged", whereas the attractive component $\Delta\nu_A$ significantly and progressively changes with the change of composition. This indicates that the attractive solvation mean-forces is the predominant contribution to the variation trend of the position of the CH_4 ν_1 band as a function of pressure and composition within CH_4-N_2 mixtures (Figure 4-7c). On the contrary, the change of the attractive component $\Delta\nu_A$ as a function of pressure and composition is quite small in the case of CH_4-CO_2 mixtures compared to that of the repulsive one (except at low-pressure range, i.e., < ~200 bars) (Figure 4-7d). Thus, the variation of CH_4 band ν_1 position is chiefly governed by the change of repulsive component $\Delta\nu_R$ as well as of the repulsive solvation mean-force. Inversely to the variation trend of the repulsive component $\Delta\nu_R$ observed in CH_4-N_2 mixtures, the repulsive component $\Delta\nu_R$ in CH_4-CO_2 mixtures increases drastically as CH_4 content decreases, indicating that at near-critical temperature, the contribution of the solvation mean-force becomes somewhat significant.

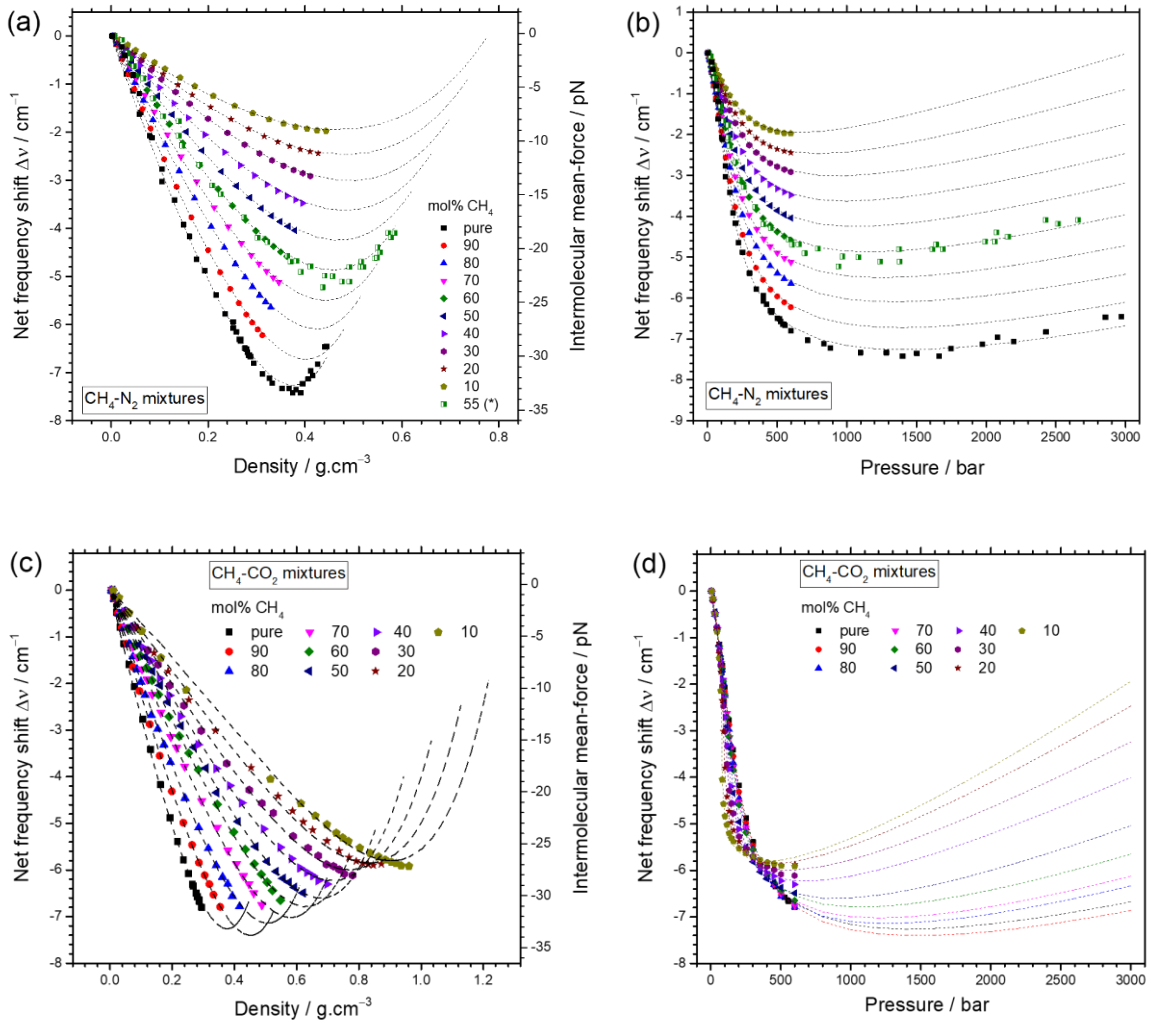

Figure 4-8: (a, c) Variation of the net predicted frequency shift (Δν) of the CH_4 ν_1 band as a function of density (left y-axis) or intermolecular mean-force acting along with the H–CH_3 bond of CH_4 solute molecules (right y-axis) and composition within CH_4-N_2 and CH_4-CO_2 mixtures. (b, d) Variation of the net predicted frequency shift (Δν) of the CH_4 ν_1 band as a function of pressure and composition within CH_4-N_2 and CH_4-CO_2 mixtures. The predicted frequency shift is represented by dashed lines. The experimental data from this study and Fabre et Oksengorn (1992) are represented by points.

The net predicted frequency shift $\Delta\nu = \Delta\nu_R + \Delta\nu_A$ (where $\Delta\nu_R$ and $\Delta\nu_A$ are reported in Figure 4-7) is calculated over 5-3000 bars for every CH_4-N_2 and CH_4-CO_2 mixtures. They are plotted in Figure 4-8 as a function of composition and density or pressure, along with experimental data from this study and Fabre et Oksengorn (1992). Regarding the CH_4-N_2 mixture, the predicted frequency shift curves show a good agreement with experimental data (Figure 4-8a and b). A slight dispersion is observed when comparing the experimental data of CH_4-N_2 mixture of 55 mol% CH_4 from Fabre et Oksengorn (1992). Indeed, the latter seems to be superimposed to the experimental data of the CH_4-N_2 mixture of 60 mol% CH_4 of the present

study (Figure 4-8a). This could be partially explained by the uncertainty of the mixture composition (55 ± 3 and 60 ± 0.5 mol% CH_4) and the error of the measured frequency shift (± 0.3 and ± 0.02 cm^{-1} reported in the two studies, respectively).

Regarding the CH_4-CO_2 mixtures, the predicted frequency shift also shows a good agreement with most experimental data (Figure 4-8c and d). However, a deviation becomes more appreciable for the mixture dominated by CO_2. The experimental data of the mixtures containing ≤ 40 mol% CH_4 start to deviate from the associated predicted curve at high-density range, i.e., near the inflection point of the predicted curves (Figure 4-8c). In particular, a significant discrepancy between experimental data points and the predicted curve is observed for CH_4-CO_2 mixtures of 10 mol% CH_4 at low (~ 0.1 - 0.4 $g{\cdot}cm^{-3}$) and high (> ~ 0.9 $g{\cdot}cm^{-3}$) density ranges, which can be ascribed to the error arising from the quadratic regression due to the blank region corresponding to the phase transition of CH_4-CO_2 mixtures (upon analyses performed at controlled temperature of 22 °C). Focusing on the relative order of the fitted curves of the attractive component $\Delta\nu_A$ (insert in Figure 4-7d), we noticed an irregular order and separation between the fitted curves as a function of composition. Also, the anomalous order is observed in Figure 4-8d. Namely, the order of the curves of pure CH_4 and the mixture of 90 mol% CH_4 seems to be inverse. Latter observations indicate that the predictive model of CH_4-CO_2 mixtures contains an appreciable error, which should not be negligible upon accurate quantitative measurements.

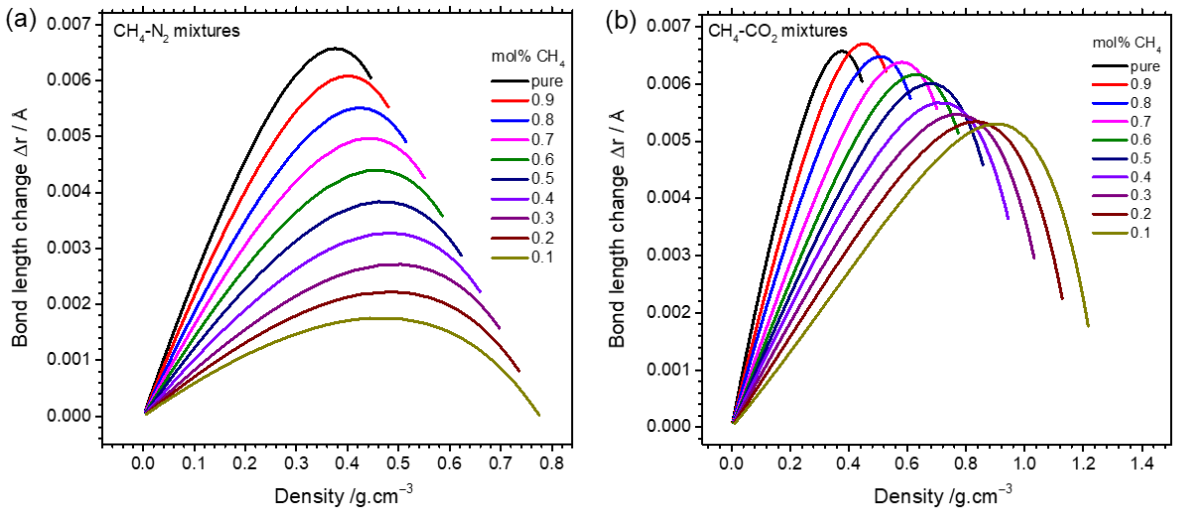

Figure 4-9: Pressure-induced bond length change of the CH_4 molecule within (a) CH_4-N_2 or (b) CH_4-CO_2 mixtures over 5-3000 bars at 22 °C.

Talking about the uncertainty of the predictive model, the attractive component $\Delta\nu_A$ were fitted from experimental data by a quadratic density-dependence, but not a linear one. Most of the experimental data used herein were obtained at ≤ 600 bars. Thus, extrapolation to 3000 bars from the best-fitted quadratic function could obviously cause more or less deviation in the predicted curves, depending on its curvature. Thereby, the predicted model of CH_4-CO_2 mixtures is expected to have a larger error than that of CH_4-N_2 mixtures because the non-linearity of the $\Delta\nu_A$-density dependence within CH_4-CO_2 mixtures is more important than the one within CH_4-N_2 mixtures (see text above and Figure 4-7a and b). Therefore, in order to obtain a higher accurate predictive model of the frequency shift of the CH_4 ν_1 band, further experimental data at a higher pressure/density range are needed, especially for the CH_4-CO_2 mixtures dominated by CO_2, where the $\Delta\nu_A$ remarkably deviates from the linear density-dependence function. Fortunately, the change of the frequency shift of the CH_4 ν_1 band within CH_4-CO_2 mixtures is chiefly governed by the change of the repulsive component $\Delta\nu_R$ as described above (Figure 4-7d). Thus, the predicted model of the frequency shift presented in this study can still hold and could be used to reasonably predict and/or interpret the variation trend of the CH_4 ν_1 band, as well as of the relative variation of the pressure-induced solvation mean-forces with respect to a reference state (at ~ 5 bars in this study).

The relative change of the solvation mean-force and the bond length of C–H bond can be readily calculated using Equation 4.12 and 4.15 (Meléndez-Pagán and Ben-Amotz, 2000), and respectively represented in Figure 4-8 (a, c - right y-axis) and Figure 4-9. Overall, the variation trends of the solvation mean-force F and the bond length are analogue to the variation trend of the net frequency shift, except the opposite sign of the bond length variation. They also strongly depend on the solvent parameters and mixture compositions, even for the same type of vibration bond. The bond length change reported in Figure 4-9 is in good agreement with the one derived from *ab-initio* calculations performed by Lin et al. (2007b) and discussions in section 4.1: attractive solvation-induced mean-force lead to an elongation of the bond, and so the resulting redshift of the observed vibration mode. The accuracy and the detection limit of solvation forces mainly come from the accuracy of the measured vibrational band position. According to the evaluation of Hutchinson et al. (1998), the relative accuracy of force measurement that arises from the uncertainty of ± 0.5 cm^{-1} in measured band position is about ± 10 pN. Since the uncertainty in the relative frequency shift measured herein is about ± 0.02 cm^{-1}, the relative accuracy of the force measurement is thereby expected to be far less than ±

10 pN within the studied pressure (density) range, e.g., 5 - 600 bars. Concerning the extrapolated range (up to 3000 bars), more experimental data points are still needed to properly calibrated the variation trends of the attractive component ($\Delta\nu_A$) in order to ensure a accuracy good enough for any interpretation and observation of the global change of intermolecular forces and the relative bond length change.

5. Conclusion

The variation of the peak position of the ν_1 stretching band of CH_4 and N_2 within different non-polar solutions (i.e., pure CH_4, pure N_2, and binary mixtures with CO_2 or N_2), where attractions and repulsions are the major intermolecular interaction forces, has been intuitively interpreted based on the basic of the Lennard-Jones 6-12 potential energy approximation, without any complex *ab-initio* calculations or molecular dynamics simulations. Thereby, the redshift and blueshift of the CH_4 ν_1 band as varying pressure (density) have been reasonably attributed to the contribution of the attractive and repulsive forces, simply as a function of intermolecular separation *r* derived from the bulk density. The experimental results reported in this study surprisingly showed a very close affinity between the variation trend of the Raman peak position and the variation of the net LJ potential energy, especially the superposition of inflection points A and B observed on Raman frequency shifts curves and LJ potential curves (Figure 4-5 and Figure E. 4-1) upon an isotherm increase of pressure or density. This proved the intrinsic correlation of the Raman spectral feature (peak position) and the intermolecular interaction. The LJ potential approximation could also point out the difference in the length scale of the intermolecular interaction forces exercising within CH_4-N_2 and CH_4-CO_2 gas mixtures, e.g., the molecules within CH_4-N_2 mixtures experience longer distance-range forces than that within CH_4-CO_2 mixtures at a given pressure at room temperature, even though in both cases the attractive forces always dominate the net intermolecular forces, resulting in a redshift over the studied pressure/density range (Figure 4-5).

The shortcoming of the LJ 6-12 potential approximation in the interpretation of Raman frequency shift of the CH_4 ν_1 band as a function of composition (i.e., the molar proportion of solute and solvent) is completed by using the generalized PHF model. It has been successfully applied to CH_4-N_2 and CH_4-CO_2 binary mixtures of any molar fraction to investigate quantitatively the interaction between solute and solvent molecules. The observed frequency shift of the CH_4 ν_1 band could be therefore decomposed into the attractive and repulsive components, which are induced by the attractive and repulsive solvation mean-forces,

respectively. The predictive frequency shift of the CH_4 ν_1 band within CH_4-N_2 and CH_4-CO_2 mixtures could also be provided over 5 - 3000 bars, instead of being empirically measured over the whole interesting pressure (density) range. Moreover, the experimental and predicted data over a wide composition-range also revealed some interesting information. The change in the solvation-induced attractive component is responsible for the change of frequency shift of the CH_4 ν_1 band in CH_4-N_2 mixtures (Figure 4-7c), whereas that in CH_4-CO_2 mixtures is governed by the change of the solvation-induced repulsive component (Figure 4-7d). Also, the slight non-linear density dependence of the frequency shift of the C-H bond of CH_4 has been evaluated and confirmed. It was clearly shown that the frequency shift of the same type of bond (herein C–H in CH_4 molecules) strongly depends on solvent parameters as well as the composition of the solution.

Overall, the study conducted herein illustrates the practicality and reliability of Raman spectroscopy for investigating thermodynamic and intermolecular behavior of gaseous molecule systems at molecular scale, yielding an alternative way to directly and quickly determine or estimate intermolecular forces, relative bond length change, and physical properties of gas mixtures with good accuracy (after a specific calibration of Raman signal) such as *PVTX* properties (Le et al., 2019, 2020), fugacity and fugacity coefficients (Lamadrid et al. (2018) and cf. Appendix F).

Acknowledgements

This paper is a part of the thesis of Van-Hoan Le (Université de Lorraine) who acknowledges the French Ministry of Education and Research and the ICEEL Institut Carnot. The work benefited of financial support from CNRS-INSU CESSUR program.

Appendix E: Comparison between the variation of Lennard-Jones potential energy and pressure-induced frequency shift determined by the PHF model

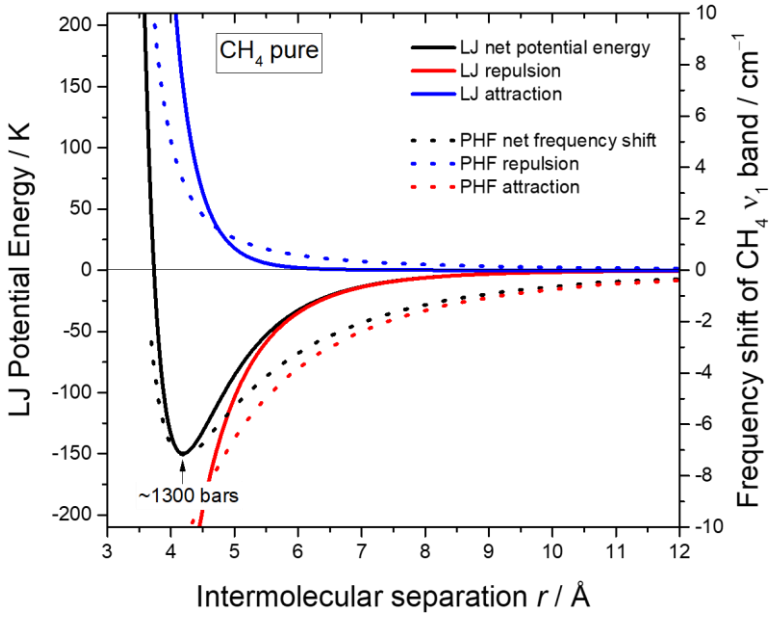

Figure E. 4-1: Comparison between the variation of the Lennard-Jones 6-12 (LJ) potential energy (K) and the frequency shift (cm^{-1}) of the ν_1 CH_4 band as a function of intermolecular interaction *r*. The values of the LJ potential and the frequency shift are referred to the left and right y-axis, respectively. The net-LJ potential is decomposed into the repulsive and attractive interaction forces, denoted LJ repulsion and LJ attraction, respectively. The frequency shift of the ν_1 band of pure CH_4 is also decomposed into the repulsive and attractive components using the Perturbed Hard-Sphere Fluid model (PHF). Overall, the trend and the variation of the magnitude of the net, attractive and repulsive frequency shift are very similar to the variation of the estimated LJ potential energy, implying an intrinsic correlation between the frequency shift and the LJ potential energy.

Appendix F: Determination of fugacity of gas species from Raman spectra

a. Revision of the predictive model of fugacity of Lamadrid et al. (2018)

Lamadrid et al. (2018) proposed a predictive model for the direct determination of the fugacity of gases within gas mixtures of CH_4, CO_2 and N_2 from Raman spectra (i.e., the frequency shift of peak position) using the following equation:

$$f_{\mathrm{Eq3}} = P_{\mathrm{i}}\varphi_{\mathrm{i}} = P_{\mathrm{i}}\frac{f_{\mathrm{v}}}{P_{\mathrm{v}}} \qquad \text{(Eq. F.1)}$$

where:

- f_{Eq3} is the fugacity predicted by the model of Lamadrid et al. (2018).
- P_{i} is the partial pressure of gas species calculated from the total pressure (P_{total}) and the known molar faction (X_i), i.e., $P_i = X_i P_{total}$.
- $\varphi_{\mathrm{i}} = \frac{f_{\mathrm{i}}}{P_{\mathrm{i}}}$ is the fugacity coefficient of the gas species *i* in the mixture, calculated from P_{i} and f_{i}, with f_i is determined using an equation of state.
- P_{v} is the partial pressure determined from the experimental calibration curve of the pressure-induced frequency shift of gas species within the mixture. Note that Lamadrid et al. (2018) used herein the calibration curves of pure components, e.g., pure N_2, CH_4 and CO_2, which do not consider the effect of composition (mixtures) on the variation of peak positions.
- f_{v} is the fugacity of gas species calculated from P_v using the Redlich-Kwong equation of state.

Figure F. 4-1 represents the comparison between the theoretical fugacity (f_{i}) and the predictive fugacity (f_{Eq3}). The experimental data (point) are from the study of Lamadrid et al. (2018) et Le et al. (2020). Due to the lack of experimental data over a wider composition- and pressure-range, Lamadrid et al. (2018) noted a good correlation between f_{i} and f_{Eq3}. However, according to the experimental data represented in Figure F. 4-1, their model only holds true at the low-pressure range and for some compositions. Indeed, a significant deviation between the theoretical and predictive fugacity is observed for every gas, e.g., N_2, CH_4, and CO_2.

Otherwise, the applicability (and the significance) of the predictive model of Lamadrid et al. (2018) is still questionable for the direct determination of fugacity from Raman spectra because:

(1) For the gas mixture of unknown composition and unknown total pressure (or bulk density):

The chemical composition (and the molar proportion) of the gas mixture can be readily determined using the peak area ratio and the Raman scattering cross-sections available in literature. However, the total pressure P_{total} is still needed upon the determination of the partial pressure P_{i} of gas species within the mixtures, i.e., $P_{\mathrm{i}} = X_{\mathrm{i}} P_{\mathrm{total}}$ (cf. Eq. F.1), whereas the authors did not provide any mean to estimate or to measure P_{total} of an unknown mixture trapped within fluid inclusions. Note that the pressure-induced frequency shifts of the CH_4 and CO_2 bands are strongly composition-dependent and the

accurate calibration data for the direct determination of P_{total} of gas mixtures (of CH_4, CO_2, and N_2) based on frequency shifts were not available at that moment. They were only provided recently by Le et al. (2019, 2020).

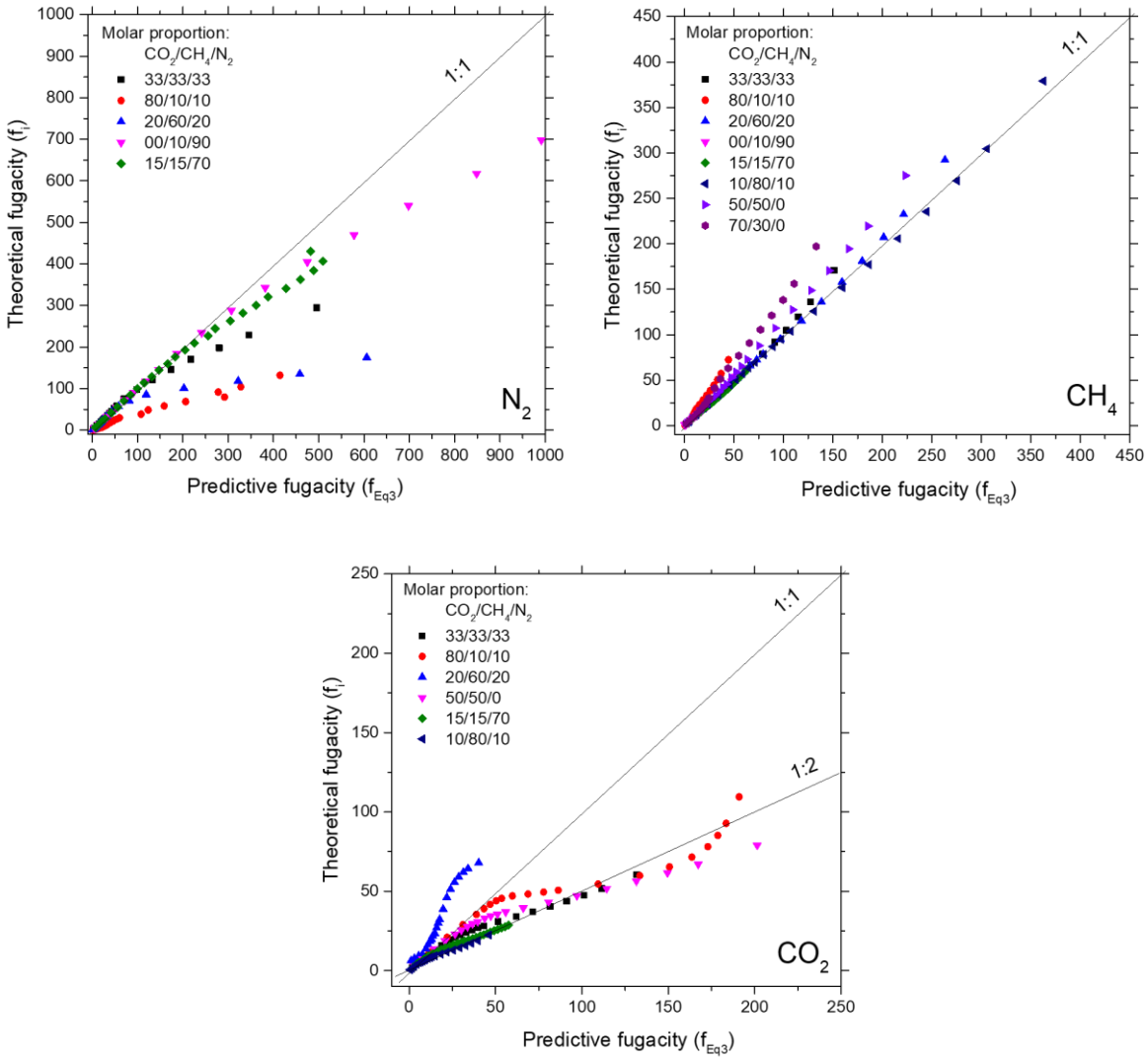

Figure F. 4-1: Relationships between the fugacity of N_2, CH_4 and CO_2 predicted by the model of Lamadrid et al. (2018), denoted f_{Eq3}, and the theoretical fugacity (f_i) measured from the partial pressure (P_i) using GERG-2008 EoS for difference CO_2-CH_4-N_2 gas mixtures.

(2) For the gas mixture of unknown composition and of known total pressure:

In this case, the chemical composition (and the molar proportion) of the gas mixture can be readily determined from Raman spectra as described above. The partial pressure P_i can also be calculated from the known total pressure P_{total}. However, once we have the (i) chemical composition and (ii) the total pressure of the mixture, the use of the predictive

model of Lamadrid et al. (2018) is unnecessary because the fugacity can be already calculated through an equation of state.

b. Calibration data for direct determination of the fugacity of gas within CH_4-CO_2-N_2 mixtures from Raman measurement.

The variation of the CH_4 ν_1 band peak position and the CO_2 Fermi diad splitting as a function of pressure (density) and composition are provided and described in Le et al. (2019, 2020). The latter calibration data is used to directly determine the *PVX* properties of CH_4-CO_2-N_2 binary or ternary mixtures from Raman spectra.

Herein, the fugacity and the fugacity coefficient of CH_4, CO_2 and N_2 gases within CH_4-CO_2-N_2 binary or ternary mixtures are calculated at 22 °C for given pressures and compositions using GERG-2008 equation of state. The calculated fugacity and fugacity coefficient are then plotted versus the variation of the peak position of ν_1 band of CH_4 or the Fermi diad slitting of CO_2 and as a function of composition. The final calibration data are respectively presented in Figure F. 4-2, Figure F. 4-3 and Figure F. 4-4.

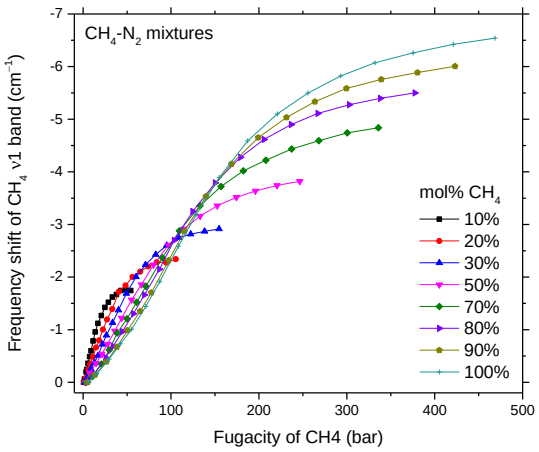

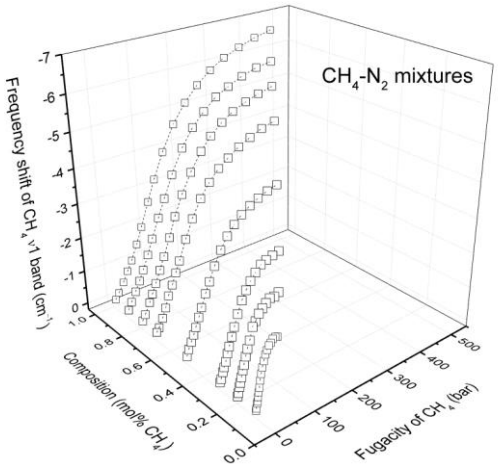

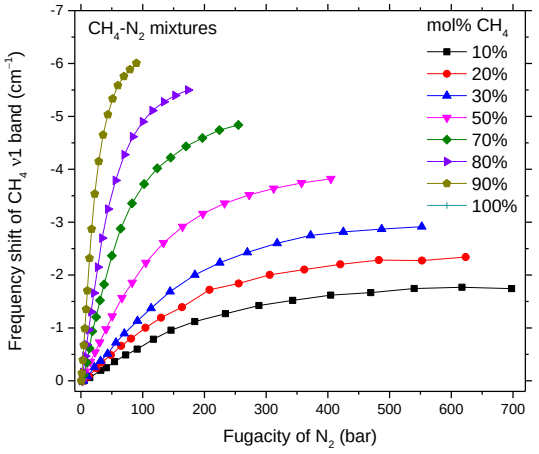

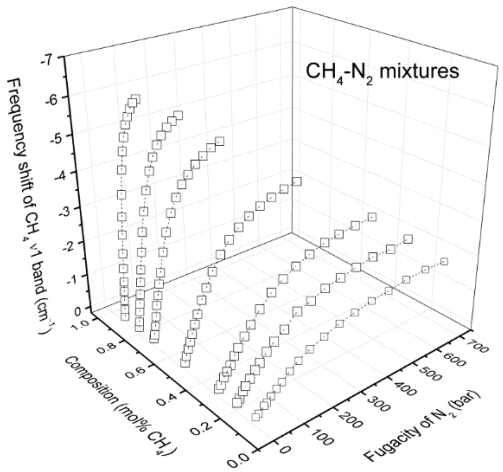

Figure F. 4-2: Relationship between the relative frequency shift of the CH_4 ν_1 band and the fugacity of CH_4 (a, b) and of N_2 (c, d) within CH_4-N_2 mixtures.

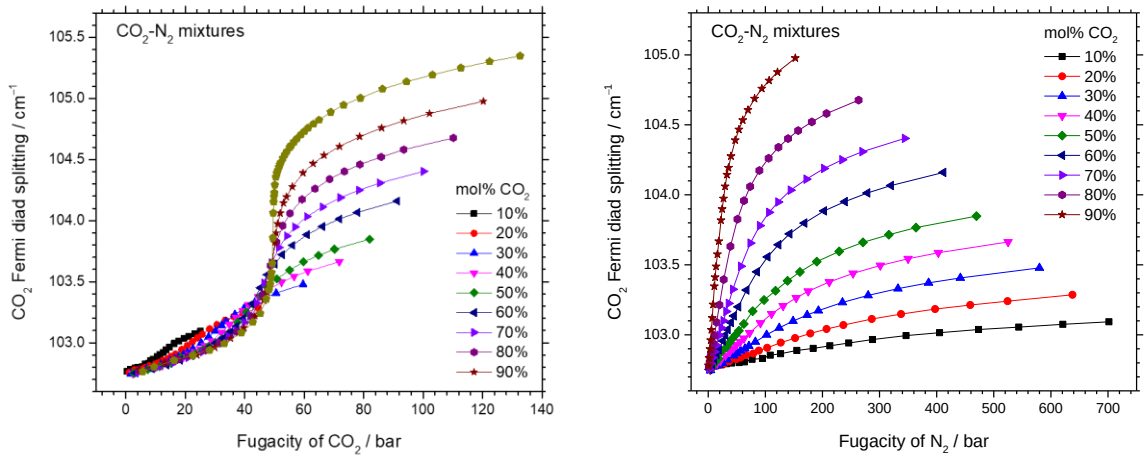

Figure F. 4-3: Relationship between the CO_2 Fermi diad splitting and the fugacity of CO_2 (a) and of N_2 (b) within CO_2-N_2 mixtures.

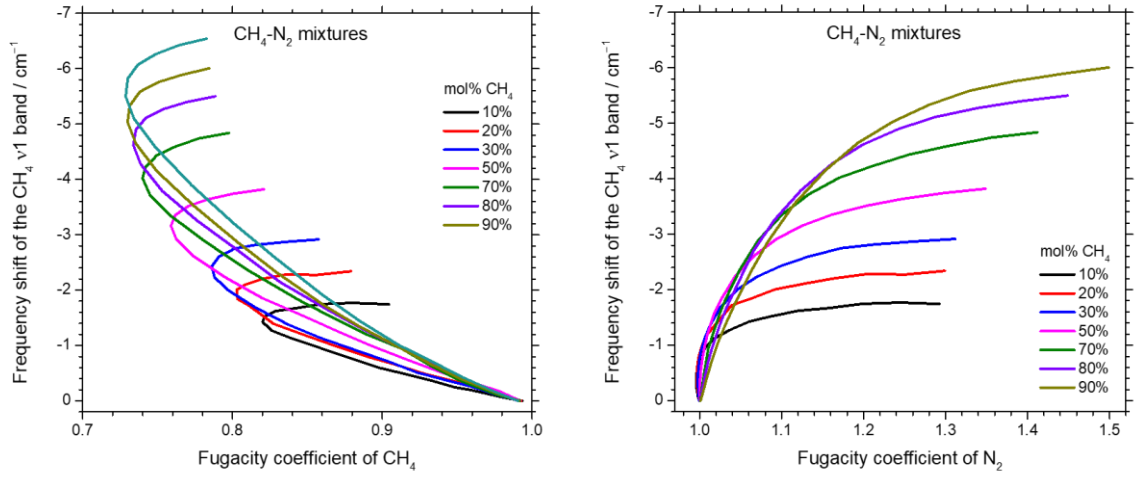

Figure F. 4-4: Variation of the fugacity coefficient of CH_4 (left) and N_2 (right) as a function of the frequency shift of CH_4 ν_1 band and the composition of CH_4-N_2 mixtures.

Chapter 5: General discussion about the applicability of the calibration data in different laboratories and within other gas systems. Development of a user-friendly program for the calculation of *PVX* properties of the CO_2-CH_4-N_2 and CH_4-H_2O systems from Raman spectra (FRAnCIs)

In this chapter, we collect the experimental calibration data (i.e., densimeters or barometers) of pure CH_4 and N_2 previously published in literature and compare with ours. The reproducibility and the applicability of the calibration data within different laboratories, (i.e. using different Raman apparatus) can thereby be examined. New calibration data based on the relative variation of the quantitative spectral parameters, which are applicable in any other laboratories with satisfactory uncertainty are then provided.

The calculation program **FRAnCIs** (**F**luids: **R**aman **An**alysis **C**omposition of **I**nclusion**s**) integrating all regression polynomial calibration equations is developed to facilitate the application of our calibration data via a user-friendly interface. This program also allows to calculate the global uncertainty associated with the final *PVX* results, which arises from two different error sources, i.e., from (i) the uncertainty of the best-fitting regression calibration equation, and (ii) the uncertainty of the measured of Raman spectral parameters.

Finally, we discuss about the possible extrapolation of the calibration data to other gas system containing additional gaseous species which are also commonly found within geological fluid such as H_2, H_2S, O_2, etc. Since the calibration data of the H_2-CH_4 mixtures was recently published in the literature by Fang et al. (2018), the composition effect of H_2 on the variation of the CH_4 ν_1 band position is further discussed to see if the calibration data can be extended to the ternary mixtures of CH_4-N_2-H_2.

1. Introduction

The experimental results presented in the previous chapters (i.e., chapter 2 and 3) demonstrated that the frequency shift of the ν_1 stretching band of CH_4 and the Fermi diad splitting of CO_2 are the most reliable spectral parameters for monitoring the variation of pressure (*P*), density (ρ), and composition (*X*) (and possibly temperature, *T*). In general, the calibration data are based on the variation of these spectral parameters as a function of *P*, ρ and *X* at a fixed temperature (22 and 32 °C). Accurate densimeters and barometers in the form of regression polynomial equations linking the spectral parameters (i.e., the relative variation of the CH_4 peak position ($\nu^*_{CH_4}$) or the CO_2 Fermi diad splitting (Δ)) with pressure (or density) and composition were thereby provided for various binary and ternary mixtures of CH_4, CO_2, and N_2, over different pressure-(density)-composition ranges. Calibration data were also successfully tested on natural fluid inclusions and validated by comparing the obtained results to those derived from microthermometry data. Overall, the *PVX* properties of the volatile part of natural fluid inclusions can be determined from our calibration data with reasonable uncertainty for any geological interpretations (i.e., ~ 0.5 mol%, 20 bars, and 0.02 g·cm^{-3} for composition, pressure and density determination, respectively). Furthermore, the variation of the peak area ratio of CH_4 and H_2O (A/I) was calibrated as a function of pressure, salinity, temperature for the determination of CH_4 concentration in CH_4-H_2O system (e.g., the CH_4 dissolved or non-dissolved in H_2O) (Caumon et al., 2014). The latter calibration data was also successfully validated with natural fluid inclusions.

However, it is important to note that these aforementioned calibration data were only tested and validated using the Raman apparatus at GeoRessouces laboratory, whereas the measured values of spectral parameters such as the frequency shift were demonstrated to fluctuate as a function of instruments (Lamadrid et al., 2017). Numerous densimeters and barometers have been previously published in literature for pure CH_4 and CO_2. However, there is a noticeable discrepancy between these calibration data, which can lead to a significant difference in the estimated pressure or density depending on which densimeters or barometers are used (Lu et al., 2007; Zhang et al., 2016; Lamadrid et al., 2017). Therefore, the applicability of the published calibration data into other laboratories (other Raman apparatus) is still questionable. Lamadrid et al. (2017) recommended that researchers should develop their own calibration data that is applicable and specific to their instruments and data collection protocol.

The first aim of this chapter is to evaluate the applicability of the calibration data obtained in the present study by comparing to other calibration data published by different research groups, i.e., using different Raman apparatus. New universal regression polynomial calibration equations are then provided, ensuring the applicability in other laboratories with satisfactory uncertainty. The validity ranges and conditions of use of each calibration data set will also be discussed and defined. Since a large number of the regression calibration equations (76 equations in total) have been specifically provided for different pressure-composition ranges and different measurement temperatures (22 and 32 °C), it is thus not convenient and practical to select the adequate calibration equations for a specific analysis. Also, the calculation of *PVX* properties of gas mixtures from the Raman spectroscopic data involves an uncertainty estimation step. The latter is quite complicated and a time-consuming task because the error propagation must consider several error sources, i.e., the uncertainty in the measurement of various spectral parameters (peak area, peak position) and the uncertainty of the regression polynomial equations themselves.

The second aim of this chapter is, therefore, to develop a user-friendly interface to make our calibration data more accessible. Thus, the so-called FRAnCIs calculation program was developed to (i) automatically select the adequate calibration equation based on the measured composition-pressure range of the sample calculated from the Raman spectroscopic input data, and (ii) to simultaneous provide the final *PVX* properties of the CH_4-CO_2-N_2-H_2O systems with the estimated global uncertainty. Thereby, the FRAnCIs program can facilitate the use of our calibration data upon daily analyses procedure. Finally, we disused about the possibility of extending the calibration data obtained in the present study to other systems containing other gaseous species such as H_2, H_2S, O_2, etc.

2. Applicability of the calibration data for determination of pressure and density in other laboratories

2.1. Calibration data based on the variation of the CH_4 peak position

In this section, the applicability to various Raman apparatus and laboratories of the calibration data based on the variation of the peak position of the CH_4 ν_1 band (ν_{CH_4}) as a function of pressure and composition is evaluated by comparing a set of densimeters developed by different research groups. The instrumental configurations (i.e., laser, slit, hole, grating and objectives) and the temperature used upon the experimental analyses are all listed in Table 5-1. These references are chosen for the comparison study because they were established over a long period of time (since 1992 to 2020) with very assorted collection parameters and configurations (settings), e.g., at near room temperature (22 - 32 °C), by an excitation laser of 488, 514 and 532 nm, and various spectral resolutions (from 0.2 to 4.4 cm^{-1}). In the following, the reproducibility of the calibration data based on the variation of ν_{CH_4}, and their validity range will be successively addressed.

Table 5-1: Comparison of the instrumental configurations and the temperature used upon the establishment of the calibration data of CH_4.

Reference	λ (nm)	*T* (°C)	Grating (grooves/mm)	Slit/hole (µm)	Res. (cm^{-1})	Obj. (Mag./N.A.)
Fabre et al., 1992(*)	488	22	nr	nr/nr	0.8	nr
Seitz et al., 1993(*)	514	23	1800	500/nr	4.4	50×/ 0.55
Thieu et al., 2000	514	25	2400	nr/nr	nr	20×/ nr
Lin et al., 2007a	514	22	1800	150/400	1.37	3.5×/ 0.1
Lu et al., 2007	532	22	1800	nr/nr	1	40×/ 0.25
Zhang et al., 2016	532	25	1800	50/-	0.65	50×/ 0.50
Fang et al., 2018	532	22	1800	nr/nr	0.2	50×/ 0.35
Sublett et al., 2019	514	22	1800	150/400	nr	40×/ 0.55
This study (**)	514	22, 32	1800	200/1000	1.7	20×/ 0.40

Calibration data were also provided for (*) binary (**) and/or ternary mixture(s).
Res. - Spectral resolution, Obj. - Objective, Mag. - Magnification, N.A. - Numerical aperture
nr : not reported

2.1.1. Reproducibility on the measurement of the density-induced wavenumber of the CH_4 ν_1 band.

First, let us talk about the calibration data for pure CH_4. Experimental data indicated that the peak position of the CH_4 ν_1 band (ν_{CH_4}) is very sensitive to the variation of pressure and density. For instance, a downshift of about 7 cm^{-1} (from ~ 2918 to 2911 cm^{-1}) was recorded for pure CH_4 when pressure increases from 5 to 600 bars (Figure 3-3, Chapter 3). Therefore, most of densimeters (barometers) available in literature were developed by establishing the relationship between the variation of ν_{CH_4} and density (pressure). Figure 5-1a presents ten densimeters for pure CH_4 based on the variation of ν_{CH_4}, which were developed by different research teams. Temperature and spectral configurations used in these works are listed in Table 5-1. The peak position of ν_{CH_4} is corrected by one or more nearby well-defined emission lines (i.e., neon emission).

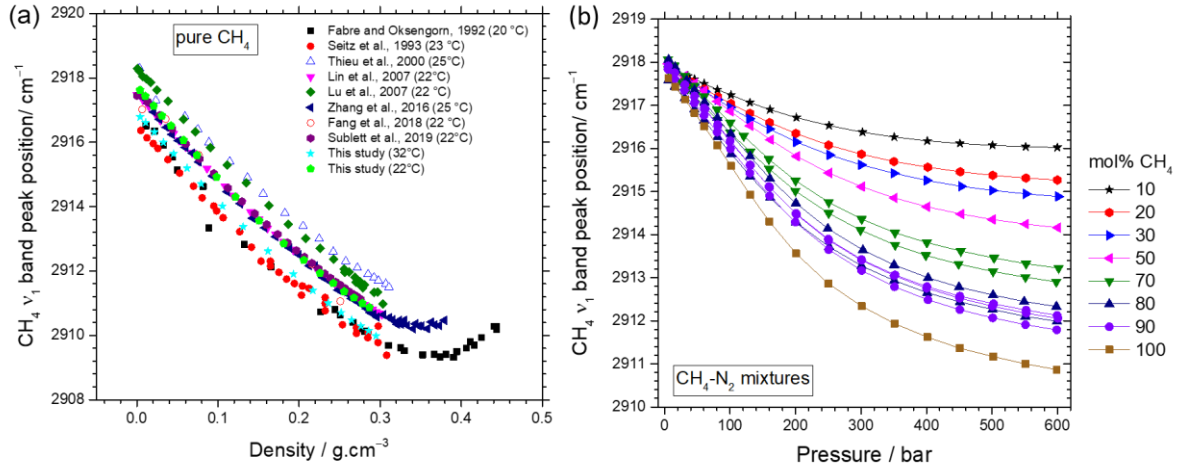

Figure 5-1: (a) Comparison of densimeters of pure CH_4 developed by different laboratories. The densimeter is based on the variation of the CH_4 band position (ν_{CH_4}) as a function of density. (b) Barometers based on the variation of the ν_{CH_4} as a function of pressure and composition of CH_4-N_2 mixtures (cited from Chapter 3). The calibration data of CH_4-CO_2 mixtures are not presented here but can also be found in Chapter 3.

In general, the variation trends of these calibration curves are in very good agreement, e.g., ν_{CH_4} shifts to lower wavenumbers with increasing density (pressure). However, a noticeable separation between these curves is observed, implying the modest reproducibility in the determination of the *absolute* value of the peak position of the CH_4 band (ν_{CH_4}). The maximum difference of the intercepts at near zero density of these curves is about 2 cm^{-1} (Figure 5-1a),

which can lead to a significant error upon the determination of density (up to ~ 0.1 g·cm^{-3}) when using a calibration curve published in literature by others. This thus leads to consider ν_{CH_4} as a poor reliable spectral parameter for developing accurate densimeters and barometers, and so restrict the applicability of the calibration data available in the literature. Consequently, each laboratory has to build their own calibration data.

The variation of ν_{CH_4} has also been evaluated as a function of pressure (density) and composition within CH_4-N_2 (Figure 5-1b) and CH_4-CO_2 mixtures (see Chapter 3 for more detail). Indeed, the magnitude of the downshift of the ν_{CH_4} changes gradually with the change of composition (Figure 3-3a and b). This was reasonably interpreted by the variation of the intermolecular interaction forces (including attraction and repulsion) as the pressure and the composition changes (cf. Chapter 4). The important point that we want to emphasize here is that even when the calibration curves are established in the same laboratory with exactly the same instruments and configurations (performed over different periods of time), they still present a discernible discrepancy (Figure 5-1b).

For instance, the calibration curves based on the variation of the ν_{CH_4} within CH_4-N_2 mixtures of 70, 80 or 90 mol% CH_4 were repeated several times over a period of ~ 1 - 4 months to test their reproducibility. The CH_4 peak position ν_{CH_4} was also corrected by two neon emission lines (at ~2851.38 and ~2972.44 cm^{-1}) following the procedure described in Lin et al. (2007). Nevertheless, the obtained curves are not superimposed, but are parallel with a separation of up to 0.3 cm^{-1} (Figure 5-1b). The latter variation may be attributed to a day-to-day systematic error. Moreover, the calibration curves of the mixtures of 80 and 90 mol% CH_4 are indistinguishable (Figure 5-1b), indicating even more significant spontaneous deviations in the response of the spectrometer with time. The maximum fluctuation of these repeated calibration curves is therefore estimated at up to ~ 0.6 cm^{-1}. The fluctuation between the calibration curves performed repeatedly in the same laboratory (curves of 70, 80 and 90 mol% CH_4, Figure 5-1b) are nonetheless smaller than the separation observed for the calibration curves performed within different laboratories (Figure 5-1a), e.g., 0.6 << 2 cm^{-1}. However, the resulting errors are still important, i.e., up to 150 bars for the pressure determination over the range 5 - 600 bars (corresponding a relative error of > 25%) and are expected to be even higher for a wider pressure (density) range.

Although the discrepancy between the densimeters based on the variation of ν_{CH_4} has been reported in Lu et al. (2007), this spectral parameter was still recently being used to provide "new" calibration curves, e.g., for pure CH_4 (Sublett et al., 2019) or CH_4-H_2 mixtures (Fang et al., 2018). It has been demonstrated in Chapter 3 that, instead of using the *absolute* values of the peak position of the CH_4 ν_1 band (ν_{CH_4}), the calibration curves should be established from the relationship between the density (pressure) and the *relative* variation of the CH_4 ν_1 band position, denoted as $\nu^*_{CH_4}$ and calculated by Equation 5.1.

$$\nu^*_{CH_4} = \nu_{CH_4} - \nu^0_{CH_4} \qquad 5.1$$

where: ν_{CH_4} is the peak position measured at a given density (pressure), and $\nu^0_{CH_4}$ is the peak position measured at near-zero density (pressure). We recalculated thus the values of $\nu^0_{CH_4}$ are for every experimental calibration data set published in literature, and then listed in Table 5-2. Thereby, the systematic error and/or the day-to-day deviation of the spectrometer (observed in Figure 5-1) could be eliminated because the calibration curves are generally performed within one working day.

Table 5-2: Values of the peak position of the CH_4 ν_1 band measured at near-zero density ($\nu^0_{CH_4}$). These values of $\nu^0_{CH_4}$ derived from the experimental data published are used to determine the relative variation of the CH_4 band ($\nu^*_{CH_4}$).

Ref.	Fabre and Oskengorn, 1992	Seitz et al., 1993	Thieu et al., 2000	Lin et al., 2007	Lu et al., 2007
T (°C)	22	23	25	22	22
$\nu^0_{CH_4}$ (cm^{-1})	2916.51	2916.37	2918.60	2917.47	2918.20
Ref.	Zhang et al., 2016	Fang et al., 2018	Sublett et al., 2019	This study	
T (°C)	25	22	22	22 and 32	
$\nu^0_{CH_4}$ (cm^{-1})	2917.50	2917.02	2917.45	2916.78 - 2917.63	

The experimental data points based on the variation of ν_{CH_4} presented in Figure 5-1 were thereby converted to $\nu^*_{CH_4}$, and plotted in Figure 5-2. Overall, all calibration curves of pure CH_4 are now in good agreement, except the data of Fang et al. (2018) (for unknown reasons) and some data points of Seitz et al. (1993) (perhaps due to the use of high spectral resolution, e.g.,

4.4 cm^{-1} (Table 5-1), their experimental data are very scattered). Also, the separation between calibration curves developed by different laboratories is almost eliminated (Figure 5-2a) and the curves of 80 and 90 mol% CH_4 are now clearly distinguishable (Figure 5-2b). At a given $\nu^*_{CH_4}$, the fluctuation of the density derived from these calibration curves of pure CH_4 is less than ~ 0.015 $g{\cdot}cm^{-3}$ for a density range between ~ 0.0 to 0.2 $g{\cdot}cm^{-3}$, and less than ~ 0.02 $g{\cdot}cm^{-3}$ for density range from ~ 0.2 to 0.3 $g{\cdot}cm^{-3}$ (visual inspection of Figure 5-2a). Regarding the repeated calibration curves developed in the same laboratory (cf. Figure 5-2b and Figure 3-4a in Chapter 3), the fluctuation of the derived densities (or pressures) is smaller than that observed in Figure 5-2a, e.g., less than 0.01 $g{\cdot}cm^{-3}$ upon the whole studied density range from ~ 0 to 0.3 $g{\cdot}cm^{-3}$.

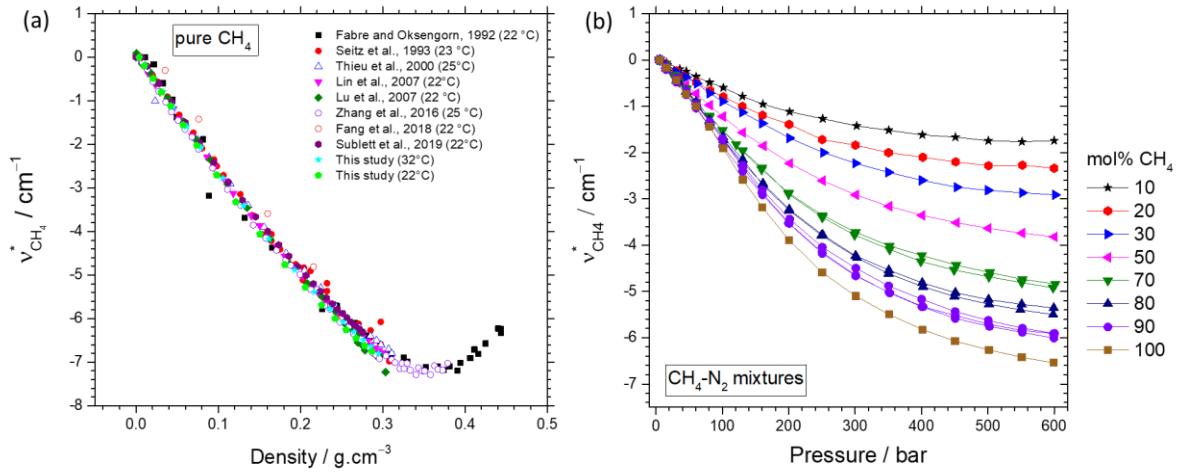

Figure 5-2: Relative variation of the peak position of the CH_4 ν_1 band ($\nu^*_{CH_4}$) within (a) pure CH_4 (provided by several research teams), and (b) CH_4-N_2 mixtures (experimental results of this study).

It should be kept in mind that there is an important temperature effect on the variation of the CH_4 peak position as a function of pressure (Figure 3-7a in Chapter 3 or cf. Lin e al., 2007a, Lu et al., 2007). However, the temperature effects on the variation of $\nu^*_{CH_4}$ as a function of density are very subtle and can be negligible over the range 22 to 32 °C (cf. Figure 5-2 and Figure 3-7b). At elevated temperature, the exact effect of temperature is still unclear. Indeed, the experimental data of Zhang et al. (2016) recorded over temperature range 25 - 200 °C shown a significant effect of temperature, whereas that of Lu et al., (2007) recorded over 22 - 200 °C did not show any effect.

We can now firmly confirm the good reproducibility of the densimeters based on the variation of $\nu^*_{CH_4}$, at least over a small temperature range from 22 to 32 °C. Therefore, our

calibration data (developed at 22 and 32 °C) reported in Chapter 3 can be applied to other laboratories with reasonable uncertainties (see below).

More attention should be paid to the analysis temperature, i.e., if the temperature of experimental analyses and that used upon developing of the calibration data are the same, both barometer and densimeter can be used for directly determination of pressure and density of fluid inclusions. Otherwise, only densimeters can be used to determine the density (due to the temperature effect on the variation of $\nu^*_{CH_4}$ as a function of pressure). The pressure can be then calculated from density for any given temperature using an appropriate equation of state. Also, the calibration data reported herein must not be applied for analyses at elevated temperatures.

2.1.2. Validity range of the calibration data of pure and mixtures of CH_4

In this study, the relative variation of the CH_4 peak position ($\nu^*_{CH_4}$) was properly calibrated over a pressure range from 5 to 600 bars (at 22 and 32 °C) for pure CH_4 (corresponding to a density of less than ~ 0.29 g·cm^{-3}) and every binary mixtures of CH_4-N_2 and CH_4-CO_2 (corresponding to a density of less than ~ 1.0 g·cm^{-3}, cf. Chapter 3). These calibration data were then validated by successfully applying them to natural fluid inclusions. Moreover, experimental calibration data of pure CH_4 were also provided in literature by numerous research teams up to 3000 bars (corresponding ~ 0.44 g·cm^{-3}) (Figure 5-2a). Overall, all these calibration data are in good agreement as described above. In the following, we will evaluate and define the validity range of the regression calibration equations, which can provide results with satisfactory uncertainty.

The change of the intermolecular interaction with increasing density leads to the change of the behavior of the $\nu^*_{CH_4}$ variation. Indeed, as can be seen in Figure 5-2a, $\nu^*_{CH_4}$ within the pure CH_4 system, measured at a temperature between 22 and 32 °C, decreases monotonically as the density increases until ~ 0.35 - 0.37 g·cm^{-3} (corresponding to a pressure of ~1300 - 1400 bars), then increases as further increasing of density (see Chapter 4 for more detail). This behavior of $\nu^*_{CH_4}$ is translated by the inflection point of the regression calibration curve (Figure 5-2a). Consequently, two values of density are possible for any given $\nu^*_{CH_4}$ when $\nu^*_{CH_4}$ is between ~ – 6.2 and – 7.3 cm^{-1}, corresponding to a density range of ~ 0.27 to 0.45 g·cm^{-3} (or a pressure range of 500 to 3000 bars). Another spectral parameter is therefore required to constrain the actual density of the regression calibration equation.

The full width at half maximum (FWHM) of the CH_4 ν_1 band is, among the other studied spectral parameters, the only one which continuously increases with increasing density (or pressure), from near-zero density to (at least) 0.45 g·cm^{-3} (corresponding to 3000 bars at ~ room temperature). This parameter can therefore be potentially used to point out the correct density value between the two possibilities (before and after the inflection point of the calibration curves). Figure 5-3a plots the variation of the FWHM the ν_1 band of CH_4 pure as a function of density. Experimental data of the FWHM are from five different research groups (already listed in Table 5-1). The discrepancy between these experimental data set is very similar to that observed for the densimeters plotted in Figure 5-1a. The separation between the data sets are huge, e.g., up to 2.5 cm^{-1}.

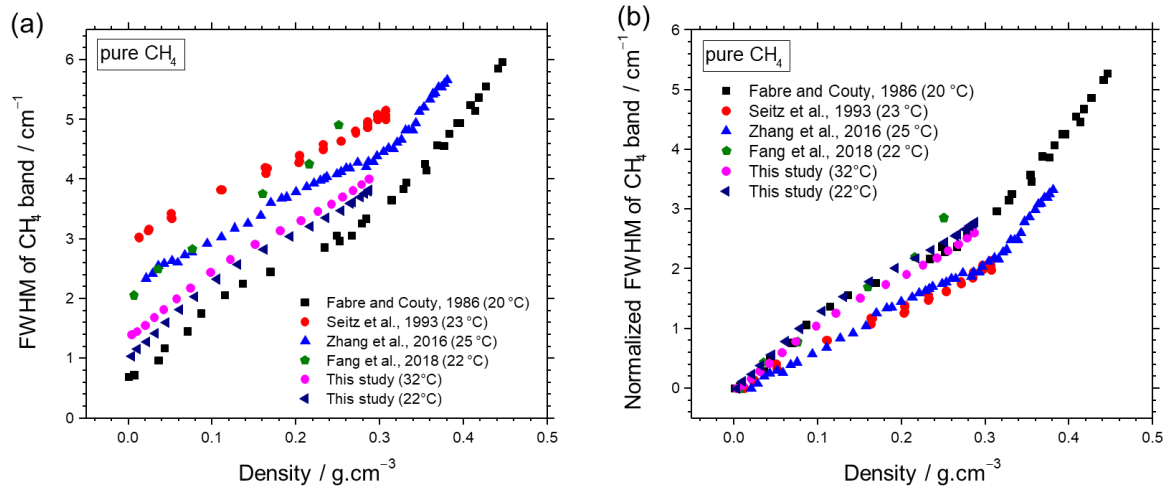

Figure 5-3: (a) Variation of the measured FWHM (full width at half maximum) or (b) the relative normalized of the FWHM of the ν_1 band of pure CH_4 as a function of density.

The *relative* variation of the FWHM of these five data sets was then considered by normalizing the *absolute* values of the FWHM measured at a given density to the value of the FWHM measured at near-zero density, i.e., same to what we have done for determination of $\nu^*_{CH_4}$ in previous subsection 2.1.1. Nevertheless, the obtained results are still in disagreement (Figure 5-3b). One indicates that this spectral parameter is very sensitive not only to the density (and pressure), but also to the measurement configurations (i.e., spectral resolution) and to the response of each instruments (Table 5-1). In addition, two data sets of the present study measured at 22 and 32 °C (using the same spectrometer and configurations) also points to the temperature dependence of the FWHM parameter (Figure 5-3b). Therefore, the determination of the *absolute* or *relative* variation of the FWHM is clearly less reproducible than that of the

$\nu^*_{CH_4}$ (Figure 5-2a and b). Consequently, the FWHM should neither be used as a quantitative parameter, nor as an additional factor to point out the actual density derived from a given $\nu^*_{CH_4}$ values between ~ -6.2 and -7.3 cm^{-1}.

Otherwise, the value of $\nu^*_{CH_4}$ is nearly unchanged as the density varies from ~ 0.35 to 0.40 $g{\cdot}cm^{-3}$, e.g. corresponding to a pressure of ~1070 to 1840 bars at 22 °C (Figure 5-2a or Figure 4-8a and b). Fortunately, most of natural fluid inclusions containing pure CH_4 have a density lower than ~ 0.35 $g{\cdot}cm^{-3}$. The experimental calibration data are therefore fitted only for the density range from 0 to ~ 0.35 $g{\cdot}cm^{-3}$, i.e., just before the inflection point to ensure the reliability of the calibration curve.

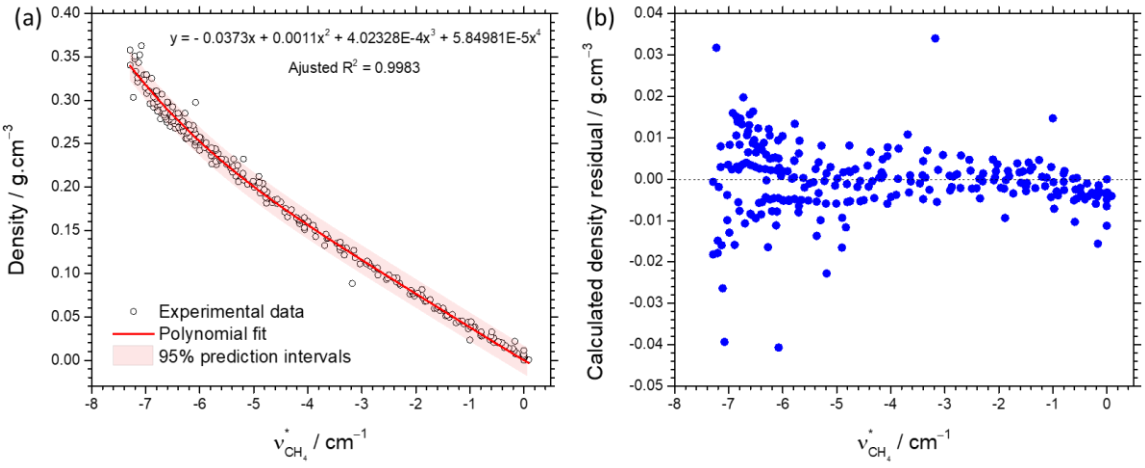

Figure 5-4: (a) Regression polynomial fit of the variation of $\nu^*_{CH_4}$ as a function of the density and (b) variation of the residual of the calculated density as a function of $\nu^*_{CH_4}$. This regression equation was fitted from experimental data points of nine different research teams and can thus be used in other laboratory with good accuracy.

Figure 5-4a presents the regression polynomial equation of the density-$\nu^*_{CH_4}$ relationship, which is fitted from all experimental data points measured over the density range from 0 to ~ 0.35 $g{\cdot}cm^{-3}$, corresponding to a maximal pressure of 1065 bars at 22 °C (or 1140 bars at 32 °C). The mathematical formula of the regression equation is expressed by Equation 5.2. The residual of the density calculated by the regression equation is less than ~ 0.01 $g{\cdot}cm^{-3}$ for density range < ~ 0.22 $g{\cdot}cm^{-3}$, and less than ~ 0.02 for density between 0.02 and ~ 0.35 $g{\cdot}cm^{-3}$ (Figure 5-4b). The uncertainty of the predicted density is always less than 0.008 $g{\cdot}cm^{-3}$ (derived from the confidence intervals of 1σ). Fitting for a wider density range does not help increasing the applicability of the pure CH_4 densimeters, but significantly decrease the overall

accuracy of the density measurements. The regression calibration Equation 5.2 (cf. Figure 5-4) is thus the final validity range for pure CH_4 that will be integrated into the FRAnCIs calculation program (see below).

$$\rho = -0.0373\nu^*_{CH_4} + 0.0011\left(\nu^*_{CH_4}\right)^2 + 4.02328 * 10^{-4}\left(\nu^*_{CH_4}\right)^3 + 5.84981 * 10^{-5}\left(\nu^*_{CH_4}\right)^4 \qquad 5.2$$

Regarding the validity range of the calibration data of the CH_4-N_2 and CH_4-CO_2 **binary mixtures,** the theoretical model presented in Chapter 4 gives the possibility to predict the variation trend of the CH_4 ν_1 band position as varying of the N_2 or CO_2 concentration and as a function of pressure (density) up to 3000 bars. However, it should be kept in mind that these predictive models are semi-empirical ones because the attractive component of the wavelength shift of the CH_4 band (i.e., $\Delta\nu_R$ which is induced by attractive intermolecular interaction forces) was fitted from few experimental data points over 5-600 bars (cf. section 4.2 in Chapter 4). An extrapolation of the variation trend of the $\Delta\nu_R$ to conditions that exceed the experimental data range (e.g., up to 3000 bars) may cause additional uncertainty. Indeed, there was a noticeable difference between the predictive curve and the experimental data points of the CH_4-N_2 mixture of 55/45 mol% (Fabre and Oksengorn, 1992) (cf. Figure 4-8a, Chapter 4). Therefore, for accurate quantitative measurement of density and pressure from the $\nu^*_{CH_4}$, these predictive models are still needed to be validated and confirmed with more experimental points over a higher pressure (density) range. Anyway, the inflection points of the predictive curves also hamper the applicability of the whole density range (or pressure range from 0 - 3000 bars).

Thus, to ensure the best accuracy of the quantitative measurement, the regression calibration equations for binary and ternary mixtures based on the variation of the $\nu^*_{CH_4}$ are only fitted from experimental data measured in this study, e.g., over a pressure range of 5 to 600 bars for any binary mixtures containing CH_4 (as reported in Chapter 3). The application of these calibration data for pressure and density determination beyond the studied pressure range (e.g., wider than 5 - 600 bars) may still be possible. For instance, the application of the obtained calibration data to the fluid inclusions with an internal pressure of ~ 700 - 900 bars (at 32 °C) within the sample Ta15 (section 4.2 in Chapter 3) still shows a good agreement compared to microthermometry results, e.g., the difference is less than 0.02 $g{\cdot}cm^{-3}$.

2.1.3. Remark on experimental analyses procedure

As shown in Table 5-2, significant fluctuation (~ 0.85 cm^{-1}) of the values of $\nu^0_{CH_4}$ is still observed even though the measurements were performed using same instruments and configurations. Therefore, it is important to keep in mind that the accuracy of the determination of pressure or density using the regression calibration equations based on the $\nu^*_{CH_4}$ can only be assured if the value of $\nu^0_{CH_4}$ (e.g., measured near-zero density) is accurately and properly determined.

From our experience, the fluctuation of $\nu^*_{CH_4}$ is due to the spontaneous day-to-day deviation of the Raman spectrometer (including all optical instruments). The value of $\nu^0_{CH_4}$ must be therefore calibrated at least at the beginning and at the end of the analyses section (e.g., one working day). It is highly recommended that the exact value of $\nu^0_{CH_4}$ should also be measured again every 3-5 fluid inclusions analyses to prevent and correct if necessary any minimal deviation of the response of the spectrometer (Figure 5-5). In this study, the value of $\nu^0_{CH_4}$ is measured using a silica microcapillary containing less than 5 bars of pure CH_4 (Figure A. 3 2, Appendix A in Chapter 3). As such, the uncertainty on the determination of the $\nu^*_{CH_4}$ in our experiments is assured to be less than ± 0.02 cm^{-1}.

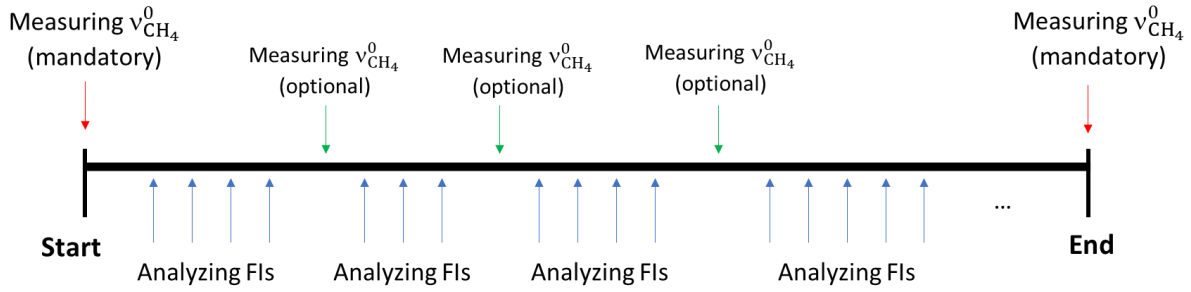

Figure 5-5: Recommended experimental analysis procedure.

2.2. Calibration data based on the variation of the CO_2 Fermi diad splitting

2.2.1. Evaluation of the reproducibility of the calibration data

Numerous densimeters or barometers based on the variation of the CO_2 Fermi diad splitting (Δ_{CO_2}) can be found in literature for the direct estimation of the density or pressure of pure CO_2 (Wright and Wang, 1973; Garrabos et al., 1989; Rosso and Bodnar, 1995; Yamamoto and Kagi, 2006; Song et al., 2009; Wang et al., 2011; Fall et al., 2011; Lamadrid et al., 2018; Wang et al., 2019). However, there is a discernible discrepancy between these calibration data

sets (cf. Figure 3-11, Lamadrid et al., 2017, Wang et al., 2019), which is very similar to that observed between the densimeters of pure CH_4 (as reported in Figure 5-1). In general, the calibration curves provided by various laboratories always present a similar variation trend (i.e., the curves are almost parallel). However, they are separated by a distance of up to 0.1 cm^{-1} (cf. Figure 3-11 in Chapter 3, and Lamadrid et al., 2017). Consequently, the density (or pressure) estimated from a given Δ_{CO_2} presents a substantial variation of up to 0.2 $g{\cdot}cm^{-3}$, depending on which densimeter (or barometer) is used.

Lamadrid et al. (2017) have carefully reassessed the difference between the several densimeters of **pure CO_2** available in the literature. Various potential causes were examined, e.g., (i) the variety of instrumentation, (ii) the difference in the data collection and the data processing (cf. Table 3-7 in Chapter 3), and (iii) the temporal variations (e.g., the spontaneous deviation in the response of the spectrometers with time). Experimental analyses were thus conducted in different laboratories at low-density range (< 0.2 $g{\cdot}cm^{-3}$, corresponding to the pressure from 0.6 to 60 bars at room temperature), using different Raman spectrometers, different excitation lasers (514, 532, 632 or 785 nm), different gratings (600, 800 or 2400 grooves/mm) and different spectral resolutions (from 1.4 to 8 cm^{-1}) (Lamadrid et al., 2017). Thereby, the reproducibility in the measurement of Δ_{CO_2} performed over a long period (up to 4 years), as well as the applicability of the published densimeters of pure CO_2 were examined. The authors addressed thereby some crucial remarks and conclusions:

(i) *First, to minimize the error in the determination of the fitted peak position of the two main bands of CO_2 (ν^+ and ν^- at 1388 and 1285 cm^{-1}, respectively), it should be corrected by one or more well-known Raman emission lines (such as Ne emissions). In addition, the ν^+ and ν^- bands and Ne emission lines must be simultaneously recorded by a single spectral window collection.*

(ii) *Second, the long-term reproducibility of the densimeters based on the variation of Δ_{CO_2} was confirmed by comparing the Δ_{CO_2} values (measured at a fixed pressure) as well as the densimeters developed over different periods (~ 2 - 4 years) using the same instruments and configurations (in the same laboratory). That means the effect of the temporal deviation of the Raman spectrometers upon the determination of the Δ_{CO_2} is minimal. Indeed, a variation of only ~ ± 0.02 cm^{-1} in the measurement of Δ_{CO_2} was observed.*

Nevertheless, the densimeter of Fall et al. (2011) established without wavelength correction do not present any anomalous variation trend when comparing to the others (cf. Table 3-7, Chapter 3). Also, according to our experimental data recorded during more than two years and using the same instruments and configurations, we also noticed that the wavelength calibration for the fitted position of the CO_2 bands (ν^+ and ν^-) is not required because the parameter of interest herein is Δ_{CO_2}, not the individual band positions of ν^+ and ν^-. Indeed, there was a variation of only ± 0.02 cm^{-1} in the Δ_{CO_2} value measured in our study at near-zero density (see Table 5-1 below) even though the position of the ν^+ and ν^- bands of CO_2 have been processed without any wavelength correction. This is because these two bands of CO_2 were simultaneously recorded by a single collection over a small spectral window. Therefore, all external errors (including the spectral deviation), which can potentially affect these two fitted band positions, must be identical. All external errors can therefore be subtracted upon the measurement of Δ_{CO_2}. That is why the variation observed in our study over two years of the Δ_{CO_2} (~ 0.02 cm^{-1}) is much smaller than the variation of the individual band position of CH_4, ν_{CH_4}, (up to ~ 0.85 cm^{-1}, cf. Table 5-2).

(iii) *Finally, Lamadrid et al. (2017) stated that the use of different equations of state upon the development of densimeters (for the calculation of density from a given pressure and temperature) only lead to a relative difference of density of less than 1%, and so can be negligible. Moreover, the authors concluded that the discrepancy between the densimeters published in the literature arises mainly from the use of different instruments and different collection parameters. The authors also recommended that researchers should not use any calibration data in the literature for accurate density or pressure measurements, and that each laboratory should develop their own calibration data.*

Notwithstanding, in previous section 2.1, we demonstrated that instead of using the ***absolute*** variation of the CH_4 ν_1 band position (ν_{CH_4}), the use of the ***relative*** band position variation ($\nu^*_{CH_4}$) significantly increased the reproducibility and the applicability of the obtained densimeters or barometers into another laboratory (other Raman spectrometers). Universal polynomial regression equations for pure CH_4 and binary mixtures of CO_2-CH_4 and CH_4-N_2 based on the variation of $\nu^*_{CH_4}$, which is applicable in other laboratories with satisfactory uncertainty, were thereby provided. Thus, we believe that this can also be performed for the whole calibration data of CO_2. Therefore, in the following, we conduct a similar procedure to convert all calibration data based on the ***absolute*** variation of the CO_2 Fermi diad splitting

(Δ_{CO_2}) (which were already reported in Chapter 2 and 3) into the ones based on the ***relative*** variation of the CO_2 Fermi diad splitting ($\Delta^*_{CO_2}$) using Equation 5.3:

$$\Delta^*_{CO_2} = \Delta_{CO_2} - \Delta^0_{CO_2} \quad 5.3$$

where Δ_{CO_2} and $\Delta^0_{CO_2}$ are the CO_2 Fermi diad splitting measured at a given density and at near-zero density, respectively. New calibration regression equations applicable to another laboratory were thereby provided. It is to note that these new calibration data can only be used if the reference value of the CO_2 Fermi diad splitting at near-zero density ($\Delta^0_{CO_2}$) is determined accurately for each specific instrument used for performing the analytical experiments and upon the development of calibration data (cf. Figure 5-5 in section 2.1.3 above).

2.2.2. Universal regression equations applicable to other laboratories

To examine the reproducibility of the developed densimeters and barometers within different laboratories, seven experimental calibration data sets of pure CO_2 were selected for comparison. The instruments and measurement configurations used in these studies are listed in Table 3-7 in Chapter 3. The values of $\Delta^0_{CO_2}$ at near-zero density of these studies was individually determined from the intercept of each calibration curves at zero density, then listed in Table 5-3. The $\Delta^0_{CO_2}$ measured in our laboratory during two years present a variation of only ~ 0.02 cm^{-1} whereas that measured within various laboratories present a fluctuation up to ~ 0.1 cm^{-1} (Table 5-3). This indicates a significant impact of the instrumental factor on the reproducibility and the applicability of the experimental calibration data.

Table 5-3: CO_2 Fermi diad splitting at zero density (Δ_0) calculated from different published experimental calibration curves.

Ref.	This study	Wang et a. (2011)	Fall et al. (2011)
T (°C)	22 & 32	21	35
Δ_0 (cm^{-1})	102.75 ± 0.02	102.710	102.651
Ref.	Lamadrid et al. (2017)	Wang et al. (2019)	Wang et al. (2019)	Sublett et al. (2019)
T (°C)	23	25	40	22
Δ_0 (cm^{-1})	102.630	102.734	102.719	102.667

The *relative* variation of the CO_2 Fermi diad splitting $\Delta^*_{CO_2}$ at a given pressure (and temperature) is then determined from the *absolute* variation of the CO_2 Fermi diad splitting (Δ_{CO_2}) subtracted by the associated value of $\Delta^0_{CO_2}$, that is measured using the same instrument as described above (cf. Equation 5.3 and Table 5-3). The variation of the $\Delta^*_{CO_2}$ as a function of density or pressure were then plotted in Figure 5-6a and Figure 5-7a, respectively.

Overall, a significant improvement of the reproducibility is observed when comparing the densimeters based on the Δ_{CO_2} (Figure 3-11b, Chapter 3) with those based on the $\Delta^*_{CO_2}$ (Figure 5-6a). These densimeters, which were developed in different laboratories and with different configurations (cf. Table 3-7 in Chapter 3), are now nearly superimposed, meaning that the variation of the $\Delta^*_{CO_2}$ do not depend on the laser nor other instrumental settings (such as the slit and/or the confocal aperture size). The effect of temperature on the $\Delta^*_{CO_2}$-density relationship is also subtle and can be negligible, at least for temperatures between 21 and 40 °C.

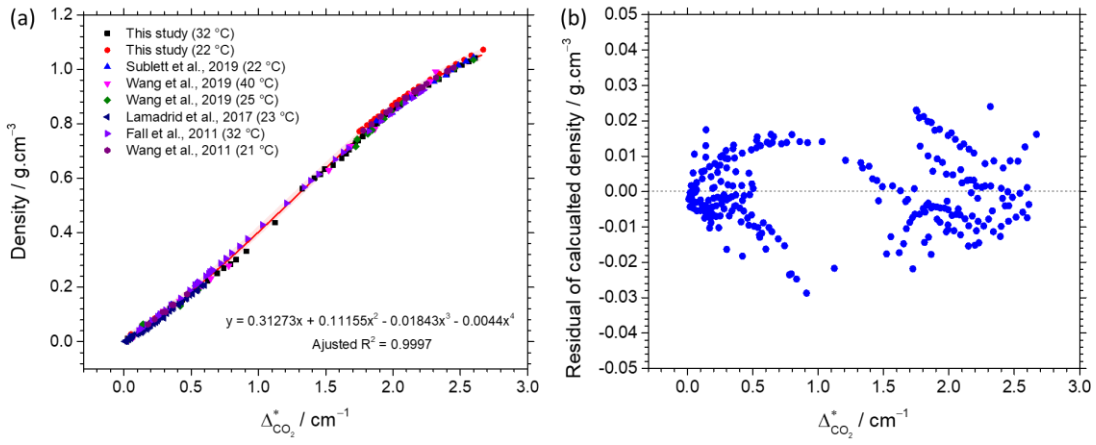

Figure 5-6: (a) Relative variation of the CO_2 Fermi diad splitting ($\Delta^*_{CO_2}$) as a function of density. Experimental data are from seven research teams measured at different temperatures (from 21 to 40 °C). Overall, all densimeters based on the variation of $\Delta^*_{CO_2}$ are in good agreement, indicating the good applicability to other laboratories. The temperature effect on the variation of $\Delta^*_{CO_2}$ is subtle and can be considered as negligible. The red-solid line is the regression polynomial which was fitted from all experimental data points (Equation 5.4). (b) Variation of the residual of the calculated density. The uncertainty of the density predicted from the regression equation is about ± 0.01 g·cm^{-3} (1σ).

The difference of the density derived from different calibration data sets is now less than ~ 0.04 g·cm^{-3} for the density region of 0.22 - 0.5 g·cm^{-3}, or less than 0.025 g·cm^{-3} for other regions. Thus, a unique calibration equation can be fitted from all these experimental data points. The regression polynomial fit is presented by the red-solid line in Figure 5-6a and

expressed by Equation 5.4. The residual of the density calculated from the regression equation is always less than 0.03 g·cm^{-3} (Figure 5-6b). The uncertainty of the predicted density is about ~ ± 0.01 g·cm^{-3} (estimated from the 1σ confidence interval).

$$\rho = 0.31273\Delta^*_{CO_2} + 0.11155\left(\Delta^*_{CO_2}\right)^2 - 0.01843\left(\Delta^*_{CO_2}\right)^3 - 0.0044\left(\Delta^*_{CO_2}\right)^4 \qquad 5.4$$

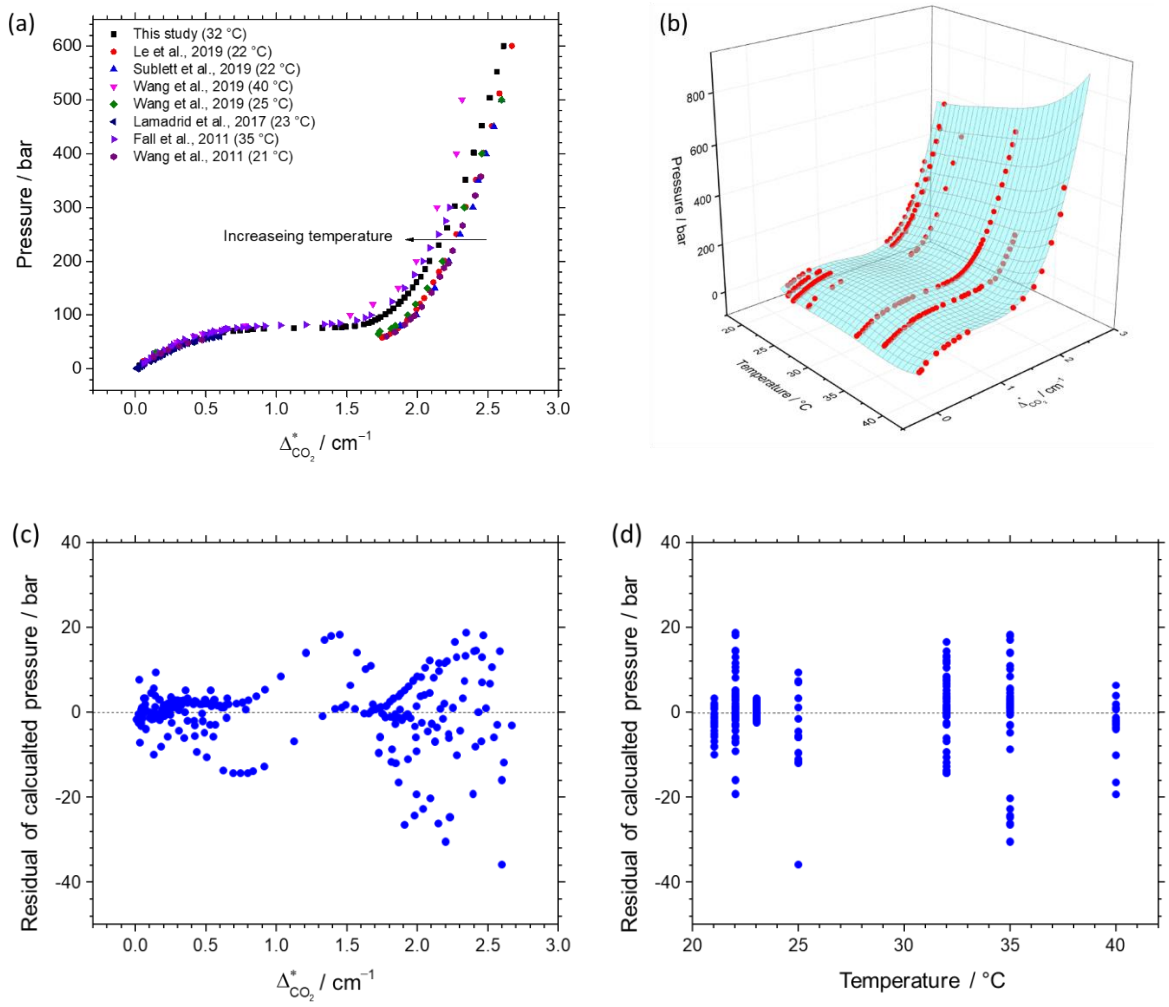

Figure 5-7: (a) Relative variation of the CO_2 Fermi diad splitting ($\Delta^*_{CO_2}$) as a function of pressure and temperature. The experimental data, measured over 5-600 bars and 21-40 °C, are from seven different research teams and in good agreement. This also indicates a good applicability of these calibration data to other laboratories. (b) Regression polynomial equation linking the variation of the $\Delta^*_{CO_2}$ as a function of pressure and temperature (Equation 5.5). (c, d) Residual of the pressure calculated from the regression polynomial equation.

The effect of temperature on the variation of $\Delta^*_{CO_2}$ as a function of pressure is, however, discernible and cannot be negligible (Figure 5-7a). At the same pressure, the $\Delta^*_{CO_2}$

systematically decreases with increasing temperature. The experimental data were therefore fitted by a unique regression polynomial equation linking the pressure to $\Delta^*_{CO_2}$ and temperature (Equation 5.5 and Figure 5-7b).

$$P = \sum_{i=0}^{4}\sum_{j=0}^{4} a_{ij} \cdot (T)^i \cdot \left(\Delta^*_{CO_2}\right)^j \qquad 5.5$$

Where P is the pressure (bar) calculated from temperature T (°C) and $\Delta^*_{CO_2}$ (cm^{-1}), a_{ij} are the coefficients of the regression polynomial equation, listed in Table 5-4. The residual of the pressure calculated from the obtained regression equation varies from 10 to 40 bar depending on the pressure ranges (Figure 5-7c and d). The uncertainty of the pressure predicted by the regression Equation 5.5 is about ± 10 bars (1σ).

Table 5-4: Coefficients of the regression polynomial equation 5.5. This calibration equation can be used for the determination of pressure of pure CO_2 over a temperature range from 21 to 40 °C. It can also be used in other laboratories (with other spectrometers) as long as the CO_2 fermi diad splitting at near zero $\Delta^0_{CO_2}$ is accurately measured by using the same instruments.

a_{00}	5238.71	a_{12}	-29.84
a_{10}	-717.60	a_{03}	-111.65
a_{01}	-1297.02	a_{40}	0.01
a_{20}	36.48	a_{31}	0.02
a_{11}	118.59	a_{22}	0.41
a_{02}	401.87	a_{13}	1.90
a_{30}	-0.82	a_{04}	38.69
a_{21}	-2.94		
Adjusted-R^2	0.9946	Uncertainty (1σ)	± 10 bars

Regarding universal calibration data for gas mixtures based on the variation of $\Delta^*_{CO_2}$, Figure 5-8 presents the relationship between the $\Delta^*_{CO_2}$ (cm^{-1}), pressure (bar) and composition (mol% CO_2) of binary and ternary mixtures of CO_2, CH_4 and N_2 over a pressure range of 5-600 bars at 32 °C. Also, Figure 5-9 represents the variation of the $\Delta^*_{CO_2}$ as a function of density ($g \cdot cm^{-3}$) and composition (mol%) within CO_2-CH_4 and CO_2-N_2 binary mixtures, over the same

pressure range and temperature. The experimental data measured at 22 °C are very similar, hence not shown here.

Overall, the variation trends of $\Delta^*_{CO_2}$ shown in Figure 5-8 and Figure 5-9 are identical to those reported in Chapter 2 and Chapter 3. The only difference is that the calibration data herein are normalized to the CO_2 Fermi diad splitting at near-zero density ($\Delta^0_{CO_2}$) and can therefore be applied in other laboratories if the value of $\Delta^0_{CO_2}$ is accurately measured using the same instruments.

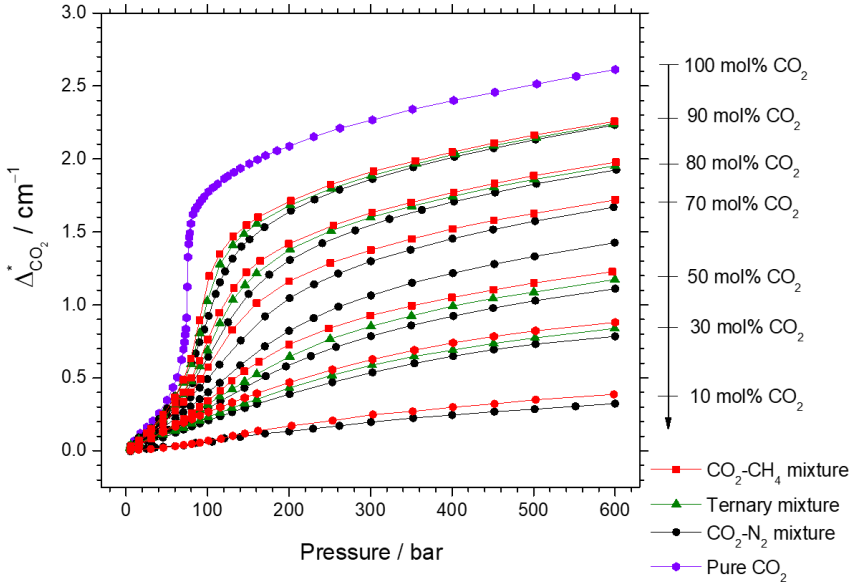

Figure 5-8: Relative variation of the CO_2 Fermi diad splitting ($\Delta^*_{CO_2}$) as a function of pressure and composition within binary and ternary mixtures of CO_2-CH_4-N_2 measured in this study at 32 °C. The concentration of CO_2 within mixtures is directly indicated in the figure. The concentrations of CH_4 and N_2 within the ternary mixture are equal. The calibration data obtained at 22 °C are similar and so not presented here.

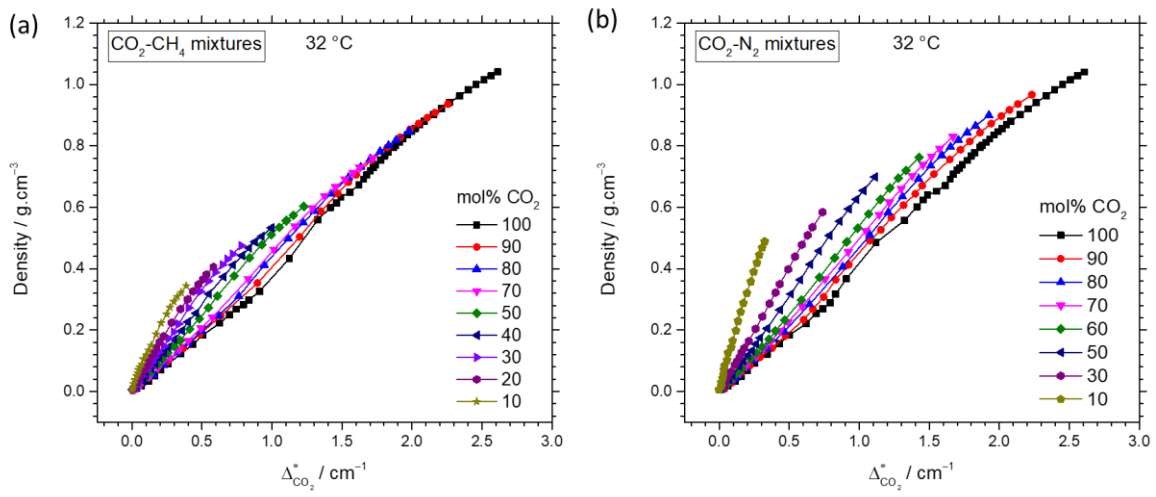

Figure 5-9: Relative variation of the CO_2 Fermi diad splitting ($\Delta^*_{CO_2}$) as a function of density and composition within (a) CO_2-CH_4 mixtures and (b) CO_2-N_2 mixtures (at 32 °C). The calibration data obtained at 22 °C are similar and so not presented here.

All these new calibration data were then fitted to provide universal calibration equations for the direct determination of the pressure and density of the CO_2-N_2 and CO_2-CH_4 binary and CO_2-CH_4-N_2 ternary gas mixtures at a fixed temperature (22 and 32 °C). The mathematical formula of the polynomial regression fit is expressed by Equation 5.6, where $\Delta^*_{CO_2}$ is the relative variation of the CO_2 Fermi diad splitting. P and ρ are respectively the pressure (bar) and density ($g{\cdot}cm^{-3}$) calculated from a given composition (mol% CO_2) and $\Delta^*_{CO_2}$ (cm^{-1}). b_{ij} (with $i + j \leq 4$) are fitting coefficients of the regression polynomial equations.

$$P \text{ (or } \rho) = \sum_{i=0}^{3}\sum_{j=0}^{4} b_{ij} \cdot \left(X_{CO_2}\right)^i \cdot \left(\Delta^*_{CO_2}\right)^j \qquad 5.6$$

To minimize the uncertainty of the regression calibration equations, the experimental data were separately fitted for different concentration-pressure (or density) ranges (cf. section 3.3 in Chapter 3 for more detail). Thus, the coefficients b_{ij} in the regression Equation 5.6 were correspondingly listed for each composition-pressure range within different tables, i.e., Table 5-5, Table 5-6, Table 5-7 and Table 5-8 for the determination of pressure or density of the CO_2-CH_4 mixtures at 32 and 22 °C, and in Table 5-9 Table 5-10, Table 5-11, and Table 5-12 for the determination of pressure or density of the CO_2-N_2 mixtures at 32 and 22 °C, respectively. The uncertainty (1σ) of the predicted pressure or density is also reported in the last row of every tables.

Table 5-5: Fitted coefficients of Equation 5.6 for the determination of pressure (at 32 °C) of CO_2-CH_4 gas mixtures. The uncertainty (1σ) of the calibration polynomial equation of each range is listed in the last row.

PX domains / c_{ij}	50-100 mol% CO_2		10-50 mol% CO_2	
	5-600 bar	5-160 bar	5-600 bar	5-160 bar
c00	-105.913	141.952	20.141	54.201
c10	631.841	-579.239	119.317	-579.442
c01	1192.786	614.574	1735.798	2003.442
c20	-1078.549	760.306	-1063.462	1889.818
c11	-4347.619	-598.096	-10364.644	-5145.786
c02	758.153	-207.733	1503.426	-4786.568
c30	554.031	-322.119	1503.573	-1886.673
c21	6980.102	255.994	33241.615	456.077
c12	-3305.090	-483.570	-14970.863	19020.925
c03	631.878	401.280	3045.567	1651.598
c31	-3652.934	-109.853	-35823.587	6424.637
c22	2458.432	637.310	22248.061	-18744.547
c13	679.754	-475.666	-5471.870	-5277.348
c04	34.686	40.255	80.945	1174.052
Adjusted R^2	0.9993	0.9988	0.9989	0.9951
Uncertainty (1σ)	± 5 bars	± 3 bars	± 10 bars	± 4 bars

Table 5-6: Fitted coefficients of Equation 5.6 for the determination of density (at 32 °C) of CO_2-CH_4 gas mixtures. The uncertainty (1σ) of the calibration polynomial equation of each range is listed in the last row.

PX domains / c_{ij}	50-100 mol% CO_2		10-50 mol% CO_2	
	5-600 bar	5-160 bar	5-600 bar	5-160 bar
c00	0.267075	0.254772	0.062867	0.047241
c10	-1.169842	-1.082592	-0.683745	-0.543798
c01	0.816076	0.762897	1.281116	1.582450
c20	1.651565	1.481580	2.274286	1.857576
c11	-0.872643	-0.893355	-1.634755	-2.644046
c02	-0.055892	0.113777	-0.901265	-3.137805
c30	-0.745041	-0.658874	-2.317295	-1.907131
c21	0.1121156	0.673482	-4.154535	-5.118171
c12	0.7575122	-0.138406	5.889787	18.341107
c03	-0.1854704	0.027368	-0.595327	-1.806949
c31	0.2196812	-0.161483	8.311497	11.389876
c22	-0.5740299	-0.100446	-7.983288	-21.602594
c13	0.1726441	0.156471	1.397482	0.245593
c04	-0.0071123	-0.055429	-0.102337	1.535738
Adjusted R^2	0.9997	0.9996	0.9996	0.9980
Uncertainty (1σ)	± 0.006	± 0.005	± 0.003	± 0.004

Table 5-7: Fitted coefficients of Equation 5.6 for the determination of pressure (at 22 °C) of CO_2-CH_4 gas mixtures. The uncertainty (1σ) of the calibration polynomial equation of each range is listed in the last row.

PX domains / c_{ij}	50-100 mol% CO_2		10-50 mol% CO_2	
	5-600 bar	5-160 bar	5-600 bar	5-160 bar
c00	178.110	63.138	45.382	-18.197
c10	-493.276	-229.832	-437.060	291.460
c01	174.125	409.524	-13.891	853.921
c20	320.292	268.950	1379.635	-1096.748
c11	-580.958	-52.822	9096.755	413.727
c02	773.463	-154.154	-385.162	-1397.053
c30	-1.111	-101.463	-1398.590	1181.763
c21	2655.985	-352.855	-33996.147	-7348.360
c12	-3584.041	-417.642	-2105.436	5112.146
c03	654.829	307.936	2163.473	249.588
c31	-2100.462	147.065	35077.079	9121.890
c22	2686.202	525.599	3647.292	-6356.070
c13	-669.269	-400.575	-3723.511	208.556
c04	26.174	45.434	95.283	-35.643
Adjusted R^2	0.9989	0.9987	0.9944	0.9987
Uncertainty (1σ)	±8 bars	±3 bars	±12 bars	±3 bars

Table 5-8: Fitted coefficients of Equation 5.6 for the determination of density (at 22 °C) of CO_2-CH_4 gas mixtures. The uncertainty (1σ) of the calibration polynomial equation of each range is listed in the last row.

PX domains / c_{ij}	50-100 mol% CO_2		10-50 mol% CO_2	
	5-600 bar	5-160 bar	5-600 bar	5-160 bar
c00	-0.095144	0.042391	-0.028497	-0.015283
c10	0.388100	-0.163524	0.446167	0.250370
c01	0.627318	0.311039	0.823317	0.817400
c20	-0.479419	0.220851	-1.795601	-0.924644
c11	-0.314993	0.814068	-0.498819	-0.526408
c02	-0.019846	0.041350	0.067829	0.290467
c30	0.189601	-0.105147	2.075280	0.972751
c21	-0.723497	-1.843815	-0.668362	-3.491540
c12	0.873300	0.609623	0.985340	5.508150
c03	-0.216237	-0.199379	-0.587449	-3.529910
c31	0.683057	1.115065	-0.193511	6.275225
c22	-0.744117	-0.894715	-1.604829	-12.943609
c13	0.216532	0.467502	1.174957	8.131834
c04	-0.009033	-0.069460	-0.054438	-0.328421
Adjusted R^2	0.9998	0.9999	0.9994	0.9953
Uncertainty (1σ)	±0.006	±0.004	±0.006	±0.005

Table 5-9: Fitted coefficients of Equation 5.6 for the determination of pressure (at 32°C) of CO_2-N_2 gas mixtures. The uncertainty (1σ) of the calibration polynomial equation of each range is listed in the last row.

PX domains / c_{ij}	50-100 mol% CO_2		10-50 mol% CO_2	
	5-600 bar	5-160 bar	5-600 bar	5-160 bar
c00	-141.222	44.653	-7.980	27.879
c10	682.710	-178.218	269.903	-309.341
c01	2377.959	1317.024	2587.526	2420.432
c20	-1033.802	228.764	-1224.785	1080.882
c11	-8587.547	-3376.477	-17336.257	-11059.840
c02	782.696	63.581	2115.167	-1531.374
c30	492.546	-94.070	1435.628	-1154.706
c21	11797.178	3759.578	49648.794	18759.022
c12	-2971.818	-848.445	-14261.990	11079.420
c03	533.510	348.836	2095.490	-2896.324
c31	-5410.457	-1534.820	-47522.157	-9353.915
c22	2092.099	721.810	18998.615	-17517.273
c13	-576.573	-415.550	-3716.869	7020.022
c04	33.948	38.401	110.044	-346.217
Adjusted R^2	0.9980	0.9983	0.9990	0.9924
Uncertainty (1σ)	± 10 bars	± 3 bars	± 10 bars	± 4 bars

Table 5-10: Fitted coefficients of Equation 5.6 for the determination of density (at 32 °C) of CO_2-N_2 gas mixtures. The uncertainty (1σ) of the calibration polynomial equation of each range is listed in the last row.

PX domains / c_{ij}	50-100 mol% CO_2		10-50 mol% CO_2	
	5-600 bar	5-160 bar	5-600 bar	5-160 bar
c00	0.322557	0.014508	0.052969	0.032500
c10	-1.373203	-0.086464	-0.591457	-0.361537
c01	1.982120	2.409656	2.418676	2.738940
c20	1.901505	0.152268	2.021816	1.267886
c11	-5.113733	-6.734110	-8.676565	-11.352661
c02	0.073184	-0.116314	-0.998621	-1.873395
c30	-0.848128	-0.074937	-2.112004	-1.359611
c21	5.307588	7.477710	11.215350	17.034457
c12	0.589915	0.807514	6.539504	16.500441
c03	-0.209968	-0.136942	-0.392779	-5.356779
c31	-1.909427	-2.902051	-2.564151	-5.818552
c22	-0.462021	-0.460642	-8.685633	-26.584920
c13	0.135753	0.040956	1.017467	13.567035
c04	0.006276	0.011606	-0.138500	-1.565370
Adjusted R^2	0.9996	0.9996	0.9996	0.9950
Uncertainty (1σ)	± 0.006	± 0.006	± 0.005	± 0.005

Table 5-11: Fitted coefficients of Equation 5.6 for the determination of pressure (at 22 °C) of CO_2-N_2 gas mixtures. The uncertainty (1σ) of the calibration polynomial equation of each range is listed in the last row.

PX domains / c_{ij}	50-100 mol% CO_2		10-50 mol% CO_2	
	5-600 bar	5-160 bar	5-600 bar	5-160 bar
c00	-137.742	88.967	1.955	8.931
c10	683.702	-377.311	147.811	-50.301
c01	1930.147	1118.943	1682.405	1814.667
c20	-1089.503	522.272	-844.985	29.398
c11	-6950.342	-2680.493	-9024.047	-7550.765
c02	865.542	121.155	1402.170	-406.409
c30	547.846	-233.627	1091.816	70.929
c21	10147.692	2796.365	26032.684	17082.171
c12	-3537.190	-757.074	-11773.206	-6973.173
c03	600.002	204.249	2319.004	5905.099
c31	-4980.751	-1072.487	-26651.658	-15617.520
c22	2557.165	552.456	17438.386	15041.744
c13	-624.148	-267.490	-4651.095	-11712.853
c04	28.644	38.666	205.721	44.608
Adjusted R^2	0.9990	0.9986	0.9994	0.9955
Uncertainty (1σ)	±7 bars	±3 bars	±8 bars	±3 bars

Table 5-12: Fitted coefficients of Equation 5.6 for the determination of density (at 22 °C) of CO_2-N_2 gas mixtures. The uncertainty (1σ) of the calibration polynomial equation of each range is listed in the last row.

PX domains / c_{ij}	50-100 mol% CO_2		10-50 mol% CO_2	
	5-600 bar	5-160 bar	5-600 bar	5-160 bar
c00	0.376216	0.010280	0.035844	0.011260
c10	-1.740868	-0.064068	-0.397086	-0.070292
c01	1.490436	2.626929	1.877266	2.107761
c20	2.561821	0.127033	1.398697	0.065704
c11	-2.248784	-8.142853	-4.921546	-7.480476
c02	-0.234697	0.523089	-0.713235	-0.621856
c30	-1.200926	-0.074232	-1.505246	0.061639
c21	0.665529	9.839291	2.879115	15.938249
c12	1.201509	-0.367180	5.144878	-6.107679
c03	-0.169712	-0.348974	-0.405858	6.501687
c31	0.405396	-3.991261	3.153925	-14.697989
c22	-0.884667	-0.209187	-6.276756	16.066299
c13	0.171749	0.469233	0.431299	-13.570084
c04	-0.007822	-0.035452	0.005927	0.072953
Adjusted R^2	0.9999	0.9999	0.9997	0.9953
Uncertainty (1σ	±0.004	±0.003	±0.004	±0.004

3. FRAnCIs calculation program

3.1. Summary of the validity range of all regression calibration data

Table 5-13 outlines the validity range of all experimental calibration data (i.e., the regression polynomial calibration equations) reported in this study and the associated uncertainty (1σ) of the pressure and density predicted from each equation.

Regarding the calibration data of CH_4, only one set of regression calibration equations based on the *relative* variation of the CH_4 ν_1 band position ($\nu^*_{CH_4}$) was provided. These equations can apply to analyses performed with any Raman spectrometer, even in other laboratories. The measurement of the $\nu^0_{CH_4}$ value (using a standard sample, e.g., a sealed microcapillary) is therefore mandatory in order to calculate accurately the $\nu^*_{CH_4}$ from the *absolute* value of the fitted CH_4 band position ν_{CH_4}.

Regarding the calibration data of CO_2, two sets of calibration equations were provided. The first one (reported in Chapters 2 and 3) is based on the *absolute* variation of the CO_2 Fermi diad splitting (Δ_{CO_2}), hence is validated only for the Raman spectrometer LabRAM HR ("Dassin") available at GeoRessources laboratory, which was used to develop the calibration data. The use of these calibration equations does not require any reference value of the CO_2 Fermi diad splitting at near-zero density ($\Delta^0_{CO_2}$). The second calibration equations set (reported in the present chapter) is based on the *relative* variation of the CO_2 Fermi diad splitting ($\Delta^*_{CO_2}$), which can apply for measurements performed with any other Raman spectrometers. The use of these calibration equations requires, however, the measurement of $\Delta^0_{CO_2}$, i.e., similar to the experimental analysis procedure of CH_4.

Table 5-13: Recapitulation of the validity range (*PVT* conditions), the uncertainties, and the required spectral parameters of the regression calibration equations in the CO_2-CH_4-N_2 systems.

	T (°C)	Spectral parameters involved	*P* (bars)	ρ (g·cm^{-3})	Nb of Eq. [a]	Uncert.[a] (1σ) (bars)	Uncert. [a] (1σ) (g·cm^{-3})
CO_2	21 - 40	Δ_{CO_2}, $\Delta^*_{CO_2}$	600	1.06	2	< 11	< 0.010
CH_4	22 - 35	$\nu^*_{CH_4}$	1140	0.35	2	-	< 0.010
CO_2-N_2	22, 32	Δ_{CO_2}, $\Delta^*_{CO_2}$	600	1.06	32	< 10	< 0.006
CO_2-CH_4	22, 32	Δ_{CO_2}, $\Delta^*_{CO_2}$, $\nu^*_{CH_4}$	600	1.06	24	< 12	< 0.008
CH_4-N_2	22, 32	$\nu^*_{CH_4}$	600	1.06	16	< 18	< 0.006
CH_4-CO_2-N_2	22, 32	Δ_{CO_2}, $\Delta^*_{CO_2}$	600	1.06	-	< 20	< 0.010

[a] : Nb of Eq.: the total number of calibration equations. Uncert.: uncertainty

All these regression calibration equations are integrated into the FRAnCIs program for the determination of *PVX* properties and the estimation of the corresponding uncertainty directly from Raman spectroscopy data.

3.2. General introduction of the calculation program – FRAnCIs

Overall, 76 regression polynomial calibration equations were fitted from our experimental data for the determination of *PV* and/or *X* properties of pure and binary gas mixtures over different composition-pressure ranges at different temperatures (22 and 32 °C). Thus, the selection of an appropriate calibration equation for a specific analysis is somewhat unwieldy. Also, the complexity of the calculation procedure of *PVX* properties in the CO_2-CH_4-N_2 ternary mixture, which requires the combination of at least four calibration equations of the CO_2-N_2 and CO_2-CH_4 systems (as described further below), makes the use of the calibration data even more onerous. Otherwise, estimating the ultimate uncertainty of the final results is also complex and cannot be done within a simple spreadsheet. Therefore, a calculation program is necessary to handle all these aforementioned tiresome processes.

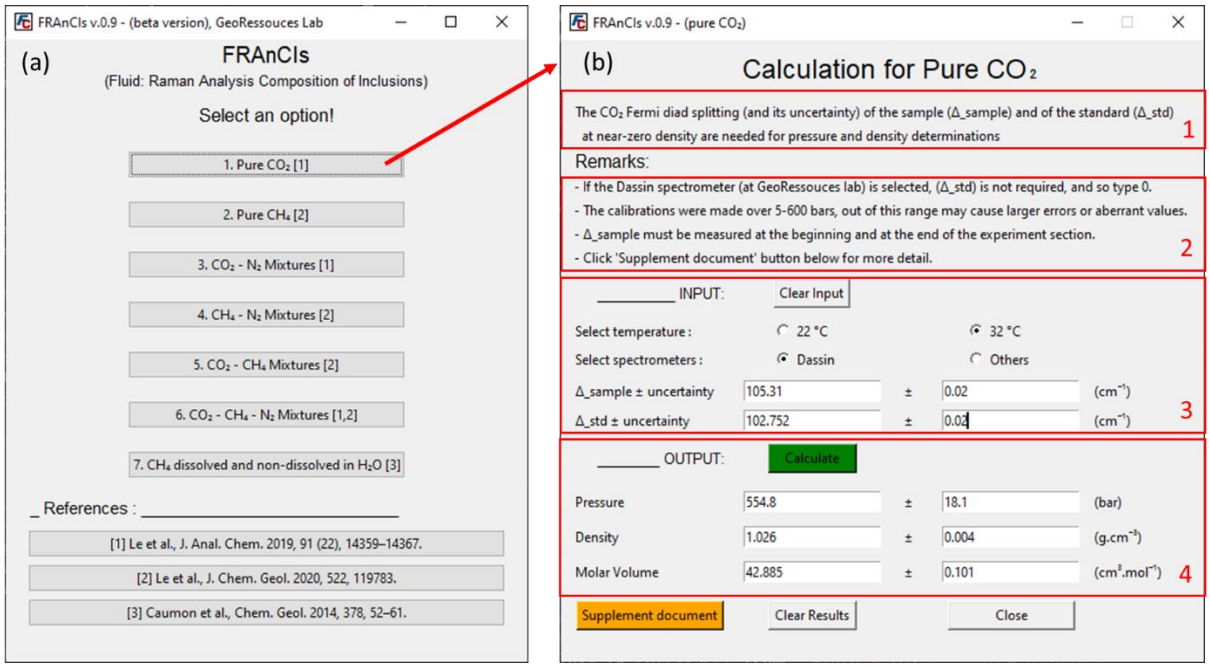

Figure 5-10: User interface of the FRAnCIs program. (a) The starting window shows different options corresponding to different calculation modules developed specifically for each gas system, e.g., from pure to binary or ternary mixtures. The references for the corresponding calibration data are listed at the bottom of the first window. (b) The interface of each module includes four main sections: (1) recall of all required spectral parameters, (2) some remarks that must be taken into account before performing the calculation, (3) the "INPUT field" to enter the required parameters for calculation, and (4) the "OUTPUT field" to display the results and uncertainties. The calculation module shows an example of the calculation of *PVX* properties of pure CO_2 from spectroscopic data recorded at 32 °C.

FRAnCIs (**F**luids: **R**aman **An**alysis **C**omposition of **I**nclusion**s**) is such a program developed to make the application of our calibration data as convenient as possible via an easy-to-use user interface. The program comprises seven independent calculation modules, which can be selected from the first window (Figure 5-10a). Each module was dedicatedly developed for a specific gas system (e.g., pure CO_2, pure CH_4, binary mixtures of CO_2-N_2, CO_2-CH_4, CH_4-N_2, ternary mixtures of CO_2-CH_4-N_2, and CH_4-H_2O system), where all corresponding calibration equations are integrated. The relevant references are also listed at the bottom of the first window.

The corresponding calculation module is opened as a new window by selecting an option available in the first window (Figure 5-10b). The interface of each module is slightly different, but in general contains four main sections: (1) a short precaution recalling all required spectral parameters, (2) a list of some important remarks must be taken into account upon performing the calculation, (3) the "INPUT field" to enter the measured spectral parameters, and (4) the "OUTPUT" field" to display the final results, i.e., composition (mol%), pressure (bar), density ($g{\cdot}cm^{-3}$ and $cm^3{\cdot}mol^{-1}$), and the associated uncertainties. A detailed notice was explicitly written for each module and can be opened using the pushbutton "Supplement document". In this document, all information relevant to the selected system can be found, including the Raman spectral features of gases, the instrumental configurations, the step-by-step spectra collection and data processing, all figures of calibration data and all tables containing the relevant regression calibration equations, etc.

3.3. Procedures of the *PVX* properties calculation and uncertainty estimation

The calculation procedure and the estimation of uncertainty are somehow different, depending on the selected gas system. All regression calibrations integrated into each module are automatically selected corresponding to the composition-pressure ranges calculated from the input spectroscopic data (see sections below).

Regarding the estimation of the global uncertainty of the final results, we considered herein two main error sources:

- The first error source, denoted as "**i**", arises from the uncertainty of the measured spectral parameters itself. Thus, this uncertainty component is mainly related to the efficiency of the instruments. In the present study, the uncertainty on the determination of the spectral parameters was estimated from six Raman spectra recorded at the same *PTX* conditions (and with the same instrumental configurations). According to the statistical analysis, the

uncertainty (1σ) of the measured peak area is about ± 0.4% of the absolute value of the fitted peak area. The uncertainty (1σ) of the RRSCS of CO_2 (i_{CO_2}) and CH_4 (i_{CH_4}) are 0.04 and 0.16, respectively (cf. the results reported in Chapters 2 and 3).

For example, the composition of CO_2 (X_{CO_2}) within CO_2-CH_4 mixtures can be calculated by Equation 5.7 from the CO_2 and CH_4 peak area (A_{CO_2} and A_{CH_4}) and RRSCS (σ_{CO_2} and σ_{CO_2}). Thus, the standard uncertainty of the measured X_{CO_2} ($i_{C_{CO_2}}$) combining the uncertainty of every variable in Equation 5.7, e.g., $i_{A_{CH_4}}$, $i_{A_{CO_2}}$, $i_{\sigma_{CH_4}}$, and $i_{\sigma_{CO_2}}$ is calculated by Equation 5.8. The calculation of the composition of other binary mixtures or ternary mixtures and the associated uncertainties can be done using a similar equation to the Equation 5.7 and 5.8.

$$X_{CO_2} = \frac{\frac{A_{CO_2}}{\sigma_{CO_2}}}{\frac{A_{CO_2}}{\sigma_{CO_2}} + \frac{A_{CH_4}}{\sigma_{CH_4}}} \qquad 5.7$$

$$i_{C_{CO_2}} = \sqrt{\left(\frac{\partial X_{CO_2}}{\partial A_{CH_4}}\right)^2 \cdot (i_{A_{CH_4}})^2 + \left(\frac{\partial X_{CO_2}}{\partial A_{CO_2}}\right)^2 \cdot (i_{A_{CO_2}})^2 + \left(\frac{\partial X_{CO_2}}{\partial \sigma_{CH_4}}\right)^2 \cdot (i_{\sigma_{CH_4}})^2 + \left(\frac{\partial X_{CO_2}}{\partial \sigma_{CO_2}}\right)^2 \cdot (i_{\sigma_{CO_2}})^2} \qquad 5.8$$

The calculation from our experimental data shows that the global uncertainty of the measured composition is always less than ± 0.5 mol% (1σ). For any further calculation involving the concentration of the gas mixtures, 0.5 mol% is therefore used as the standard deviation of the measured composition ($i_{C_{CO_2}}$).

On the other hand, the uncertainty of an individual fitted peak position measured in our study is about ~ ± 0.01 cm^{-1}, resulting in the uncertainty of the measured CO_2 Fermi diad splitting ($i_{\Delta_{CO_2}}$) and the variation of the CH_4 peak position ($i_{\nu_{CH_4}}$) of about ± 0.015 - 0.020 cm^{-1}.

- The second error source, denoted as "**u**", is related to how well the best-fitted regression equation reproduces the pressure or the density from the measured composition and the CO_2 Fermi diad splitting (with uncertainty ± $i_{\Delta_{CO_2}}$) or the variation of the CH_4 peak position (with an uncertainty ± $i_{\nu_{CH_4}}$). The uncertainty component "**u**" was specifically derived from the 1σ prediction interval of each regression polynomial equation fitted from the experimental

calibration data. The uncertainty **u** is listed in the last row in the same table than with the fitted coefficients of each regression equation.

The global uncertainty of the final measured density or pressure is, therefore, the **sum** of these two error sources, e.g., (u + i). Since the regression calibration equations reported in this study are nonlinear, the uncertainty component i can cause either significant error or not, depending on the "slope" of the fit curve or surface at the considered composition-density region. The calculation procedure, including the uncertainty estimation of each system, will be further detailed in the following.

3.3.1. Pure systems of CO_2 and CH_4

The calculation procedure of pure systems (CO_2 and CH_4) is relatively simple because it involves only one regression polynomial calibration equation for the entire density or pressure range at a fixed temperature. Figure 5-10b and Figure 5-11 present the user interface of the calculation module of the pure CO_2 and CH_4 systems, respectively. The temperature used in the experiments must be selected (22 or 32 °C) before entering the other spectroscopic data in the INPUT fields of the calculation module. Namely, the required spectral parameters of the pure CH_4 calculation module are "ν_1_sample", "ν_1_std" and "uncertainty", which are respectively the *relative* variation of the CH_4 ν_1 band ($\nu^*_{CH_4}$) of the sample and of the standard at near-zero density ($\nu^0_{CH_4}$), and the associated uncertainty (e.g., ~ ±0.02 cm^{-1} for the measurements performed in this study).

Regarding the module of pure CO_2, the calculation is based on the CO_2 Fermi diad splitting and its uncertainty (Figure 5-10b). It is to note that only the absolute value of the CO_2 Fermi diad splitting (Δ_{CO_2}) is needed for the pressure and density determination when the analysis is performed using the LabRAM HR ("Dassin") spectrometer at GeoRessouces laboratory. When using other spectrometers, the calculation is based on the relative variation of the CO_2 Fermi diad splitting ($\Delta^*_{CO_2}$). A standard sample containing less than ~ 5 bars of CO_2 is therefore needed to measure the value of the CO_2 Fermi diad splitting at near-zero density ($\Delta^0_{CO_2}$) (Figure 5-10b).

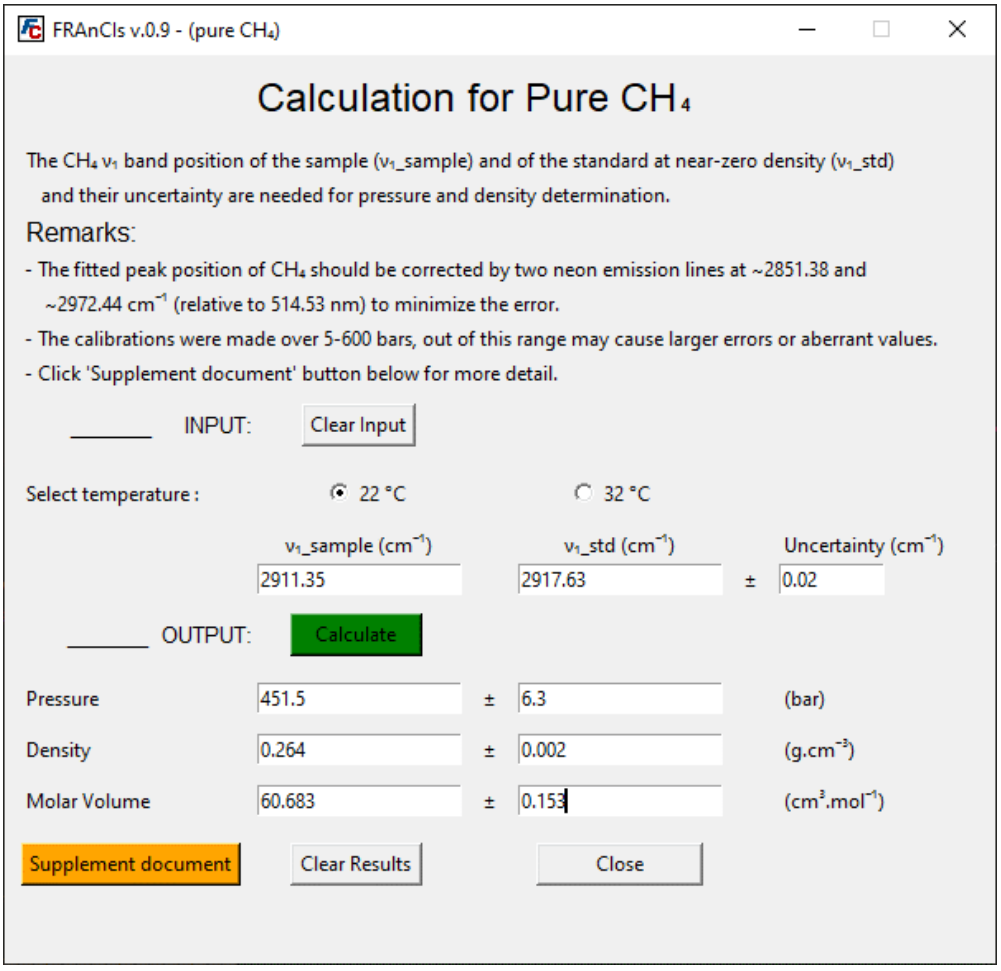

Figure 5-11: User interface of the calculation module of pure CH_4 with an example of the calculation of *PVX* properties from spectroscopic data recorded at 22 °C.

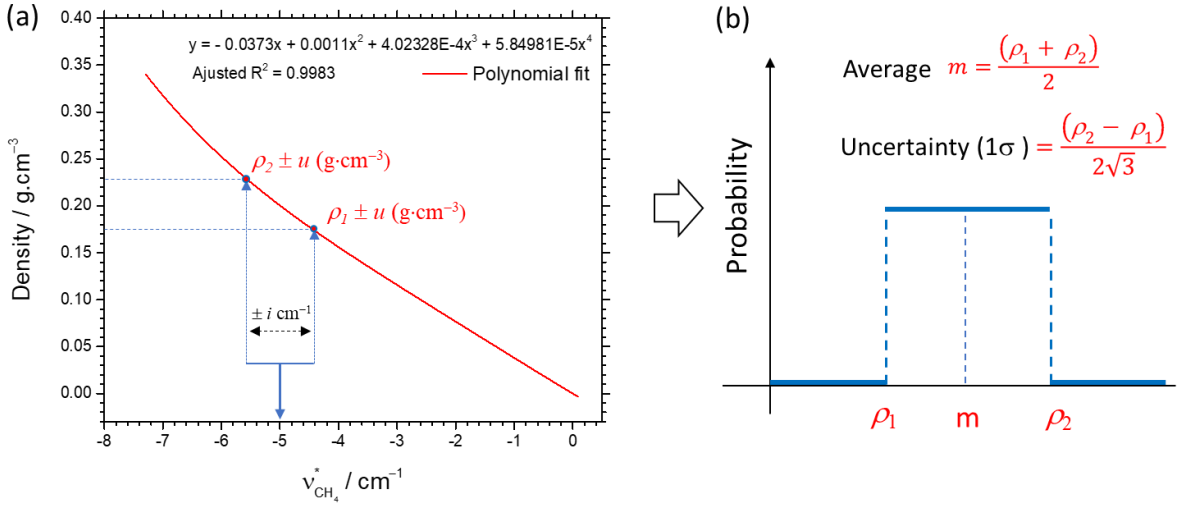

Figure 5-12: Calculation procedure of pure CH_4 module (a) Error propagation arising from the uncertainty of a given band position of CH_4 (± i) and of the regression calibration equation (± u). The red-solid line is the regression equation fitted from experimental data (cf. Figure 5-4a). (b) Probability

function of the rectangular distribution. Indeed, the probability of the density calculated from a given $\nu^*_{CH_4} \pm i$ (cm^{-1}) falls between ρ_1 and ρ_2 ($g \cdot cm^{-3}$) is always the same. Otherwise, the probability is equal to zero.

Figure 5-12a presents the schema of the error propagation upon the calculation procedure of the density of pure CH_4 system from $\nu^*_{CH_4}$. Indeed, for a given $\nu^*_{CH_4}$ measured with an uncertainty of ± i (1σ), the calculated density is expected to fall between ρ_1 and ρ_2, where ρ_1 and ρ_2 are the densities derived respectively from $(\nu^*_{CH_4} + i)$ and $(\nu^*_{CH_4} - i)$ using the regression equation. Herein, the rectangular distribution is used because of its simplicity, and it gives the largest standard deviation (compared to others, e.g., the normal or triangular distributions). The distribution function of the expected densities is described in Figure 5-12b. Thereby, the average density (m) and the uncertainty (i^*) arising from the first error source i (i.e., the uncertainty of the measured spectral parameter $\nu^*_{CH_4}$) can be calculated using Equation 5.9 and 5.10, respectively.

$$m = \frac{\rho_1 + \rho_2}{2} \qquad 5.9$$

$$i^* = \frac{\rho_2 - \rho_1}{2\sqrt{3}} \qquad 5.10$$

Furthermore, both densities ρ_1 and ρ_2 that were derived from the regression polynomial equation contain already an uncertainty ± u (1σ), e.g., the second error source. Thus, there is additional uncertainty (u^*) of the average density (m). The uncertainty u^* can be calculated using Equation 5.11. Finally, the final uncertainty is the sum of two error sources, e.g., $i^* + u^*$ (Fall et al., 2011; Wang et al., 2011). The calculation procedure for pure CO_2 is identical to that of CH_4.

$$u^* = \sqrt{\left(\frac{\partial m}{\partial \rho_1}\right)^2 \cdot (u)^2 + \left(\frac{\partial m}{\partial \rho_2}\right)^2 \cdot (u)^2} \qquad 5.11$$

3.3.2. Binary systems: CO_2-N_2, CH_4-N_2, and CO_2-CH_4 mixtures

The calculation procedure and the uncertainty estimation for the binary mixtures are a little bit more complicated because there are two variables in the regression calibration (e.g., the measured composition and the CO_2 Fermi diad splitting or the variation of the CH_4 band position). To minimize the uncertainty associated with the second error source (u), different

regression equations were individually fitted from experimental data over a specific composition-pressure range. Overall, the regression equations of binary mixtures were fitted for four different ranges, i.e., > 50 mol% or < 50 mol%, and over 5-600 bars or over 5-160 bars (cf. Figure 2-9 in Chapter 2). The spectral parameters required for the quantitative measurements of each binary system are also different. For instance, due to the modest reproducibility of the spectral parameters of N_2, only the CO_2 Fermi diad splitting (Δ_{CO_2} or $\Delta^*_{CO_2}$) can be used as a reliable parameter for the quantitative measurement of the CO_2-N_2 mixtures. Similarly, only the variation of the CH_4 ν_1 band position ($\nu^*_{CH_4}$) can accurately be used for the CH_4-N_2 mixtures.

Regarding the CO_2-CH_4 mixtures, both Δ_{CO_2} (or $\Delta^*_{CO_2}$) and $\nu^*_{CH_4}$ can be used as reliable spectral parameters for quantitative measurement of pressure and density. However, it is to note that the sensibility (as varying of pressure or density) of the Δ_{CO_2} (or $\Delta^*_{CO_2}$) and the $\nu^*_{CH_4}$ decreases with decreasing CO_2 or CH_4 concentration. Therefore, Δ_{CO_2} (or $\Delta^*_{CO_2}$) is used when the concentration of CO_2 > 50 mol%, whereas $\nu^*_{CH_4}$ is used when the concentration of CO_2 < 50 mol% (i.e., > 50 mol% CH_4).

Figure 5-13 presents the user interface of the module of the CO_2-CH_4 mixtures with an example of a calculation from the spectroscopic data recorded at 32 °C. The spectral parameters required in the CO_2-CH_4 module are the peak areas (A_{CO_2} and A_{CH_4}), $\nu^*_{CH_4}$, Δ_{CO_2} (or $\Delta^*_{CO_2}$) and their uncertainties $i_{\nu^*_{CH_4}}$ and $i_{\Delta_{CO_2}}$. The uncertainty of the fitted peak area is not required because we already assumed, from our statistical analyses, that the uncertainty of the measured composition is always less than ±0.5 mol% (Equation 5.8).

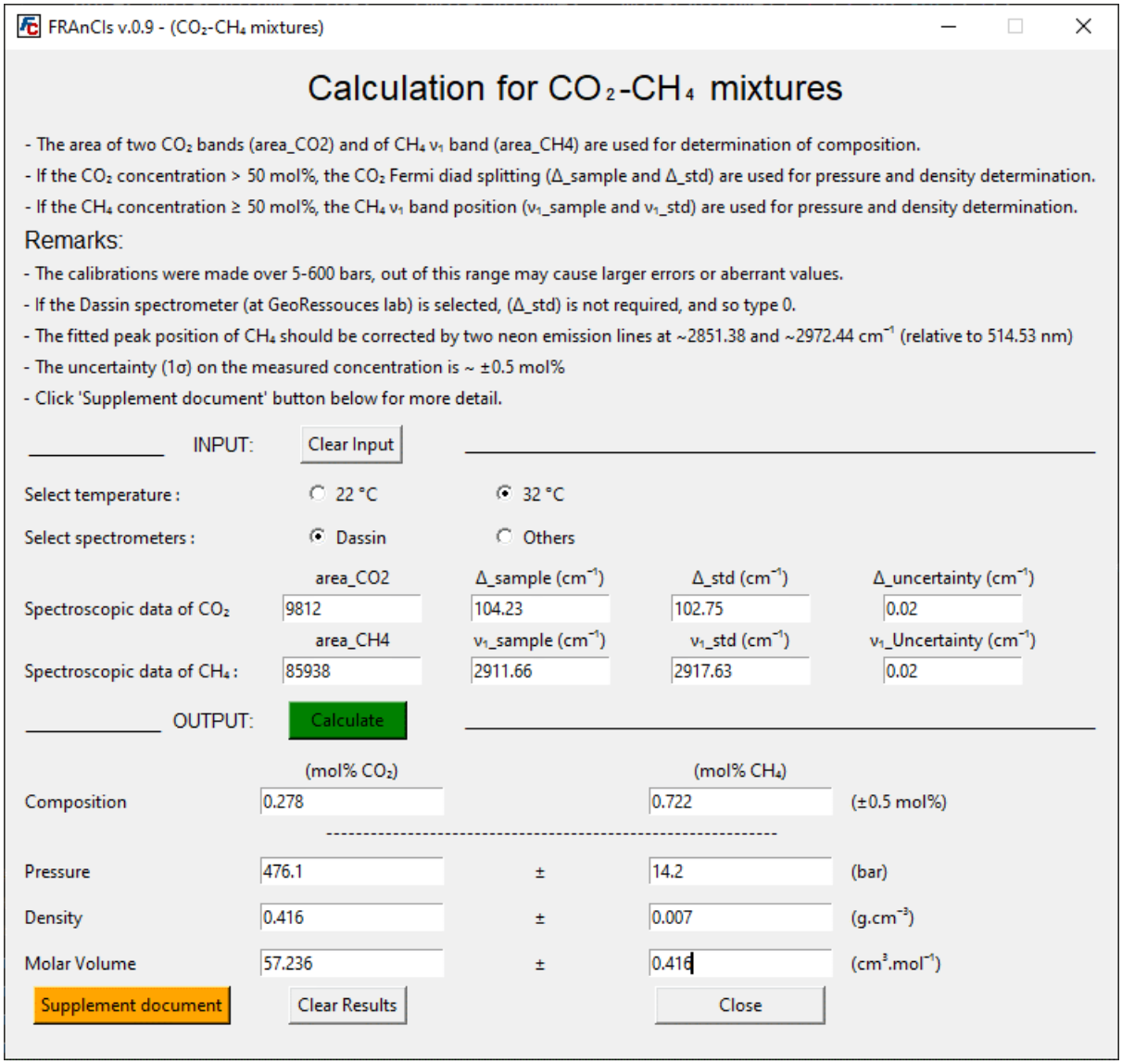

Figure 5-13: User interface of the calculation module for CH_4-CO_2 mixtures with an example of measurements and of *PVX* calculation at 32 °C.

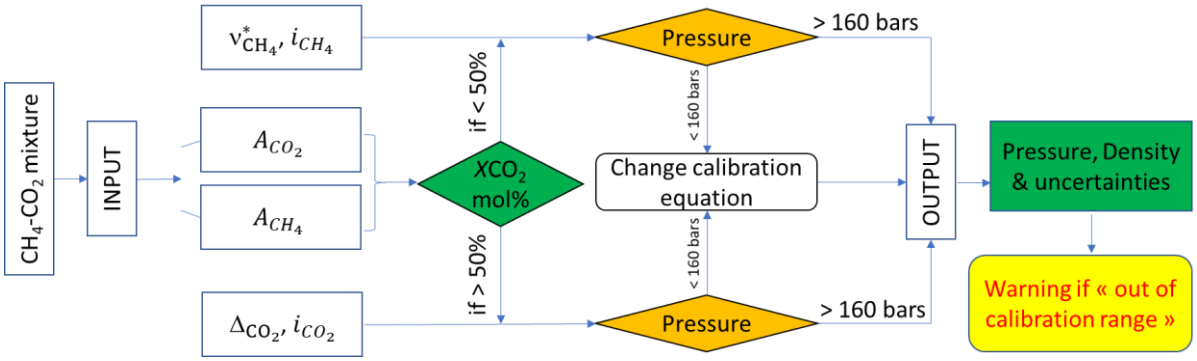

Figure 5-14: Schema of the procedure of the *PVX* properties calculation within the module of CO_2-CH_4 mixtures (read text for more detail).

Figure 5-14 describes the calculation procedure of the module for CO_2-CH_4 mixtures. Indeed, the composition of CO_2-CH_4 mixtures is firstly calculated from the peak areas and RRSCS of CO_2 and CH_4 (e.g., 2.29 ± 0.02 and 7.73 ± 0.15, respectively, reported in Chapters 2 and 3). If the CO_2 concentration is more than 50 mol%, only Δ_{CO_2} and its uncertainty $i_{\Delta_{CO_2}}$ (combined with the obtained concentration) are used for further calculation of pressure, density, and associated uncertainties. In the other cases (< 50 mol% CO_2), $\nu^*_{CH_4}$ and its uncertainty $i_{\nu^*_{CH_4}}$ are then used (Figure 5-14).

Then, the appropriate regression calibration equation fitted over the entire studied pressure range (5-600 bars) is automatically selected for the calculation of pressure. If the obtained pressure is > 160 bars, the calculated *PVX* properties and all associated uncertainties are then displayed in the OUTPUT fields. If the calculated pressure is < 160 bars, the *PVX* properties are then re-calculated using another regression equation, which was fitted over a lower pressure range (5-160 bars) to minimize the uncertainty of the measurement further.

The final results are then displayed in the OUTPUT fields. If the final results are out of the calibration range (cf. Table 5-13), a pop-up will appear to warn and suggest the user to refer to the "Supplement document" for more information.

The calculation procedures of the other binary mixtures (CH_4-N_2 and CO_2-N_2) are similar and can be deduced from the schema presented in Figure 5-14. The only difference is that only Δ_{CO_2} (or $\Delta^*_{CO_2}$) is required for the calculation within the CO_2-N_2 mixtures, and only $\nu^*_{CH_4}$ is required for the calculation within the CH_4-N_2 mixtures.

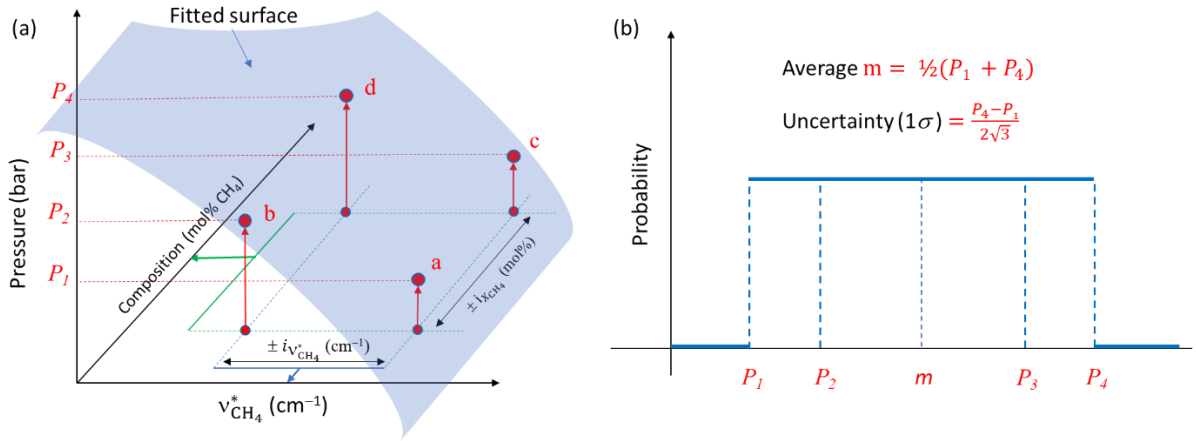

Figure 5-15: (a) Illustration of the error propagation arising from the uncertainty ± $i_{\nu^*_{CH_4}}$ (of the $\nu^*_{CH_4}$) and the uncertainty ± $i_{C_{CH_4}}$ (of the measured composition X_{CH_4}). (b) Probability of the expected

pressure (or density) according to the rectangular distribution. The pressure (or density) is calculated from a given ($\nu^*_{CH_4} \pm i_{\nu^*_{CH_4}}$) and ($X_{CH_4} \pm i_{C_{CH_4}}$), and is expected to fall between P_1 (min) and P_4 (max) with the same probability. Otherwise, the probability is equal to zero.

Figure 5-15a illustrates the error propagation upon the pressure calculation of the CH_4-N_2 binary mixtures. Indeed, the pressure calculated from a given composition ($X_{CH_4} \pm i_{C_{CH_4}}$) and a given peak position ($\nu^*_{CH_4} \pm i_{\nu^*_{CH_4}}$) using the regression polynomial calibration equation is expected to fall within a "*rectangular*" limited by four extremes (a, b, c and d) on the fitting surface Figure 5-15a. This means that the calculated pressure ranges from P_1 to P_4, where P_1 and P_4 are respectively the maximal and minimal possible values. Similarly, the rectangular distribution is also used herein to calculate the average value of the final pressure and to estimate the global uncertainty (Figure 5-15b). According to the rectangular distribution function, the average pressure (or density) and the associated uncertainty can be calculated using Equation 5.12 and 5.13, respectively. The calculation of density and its uncertainty within the binary mixtures are similar to that of pressure and so not described herein.

$$P = \frac{P_1 + P_4}{2} \quad 5.12$$

$$i^* = \frac{P_4 - P_1}{2\sqrt{3}} \quad 5.13$$

$$u^* = \sqrt{\left(\frac{\partial P}{\partial P_1}\right)^2 \cdot (u)^2 + \left(\frac{\partial P}{\partial P_4}\right)^2 \cdot (u)^2} \quad 5.14$$

It is to note that all pressure or density of the binary mixtures derived from a given composition and $\nu^*_{CH_4}$ using the regression calibration data also contains a certain uncertainty "u" (e.g., the second error source as described above). Therefore, the average pressure (or density) calculated from Equation 5.12 must have an additional uncertainty (u^*) calculated using Equation 5.14. The global uncertainty in the final pressure or density is thereby the sum of two error sources, i.e., ($i^* + u^*$).

3.3.3. Ternary system: CO_2-CH_4-N_2

Figure 5-16 presents the user interface of the calculation module of CO_2-CH_4-N_2 ternary mixtures with an example of calculation at 32 °C. All required spectral parameters are the peak areas of CO_2, CH_4 and N_2 bands and the CO_2 Fermi diad splitting (and its uncertainty). Since

the variation of the CH_4 ν_1 band position ($\nu^*_{CH_4}$) cannot be used for the determination of the pressure and density of the ternary mixtures (cf. Chapter 3), only the CO_2 Fermi diad splitting (Δ_{CO_2} for the Dassin spectrometer or $\Delta^*_{CO_2}$ for other spectrometers) is thus used for the entire composition range, even when the concentration of CO_2 is less than 50 mol%.

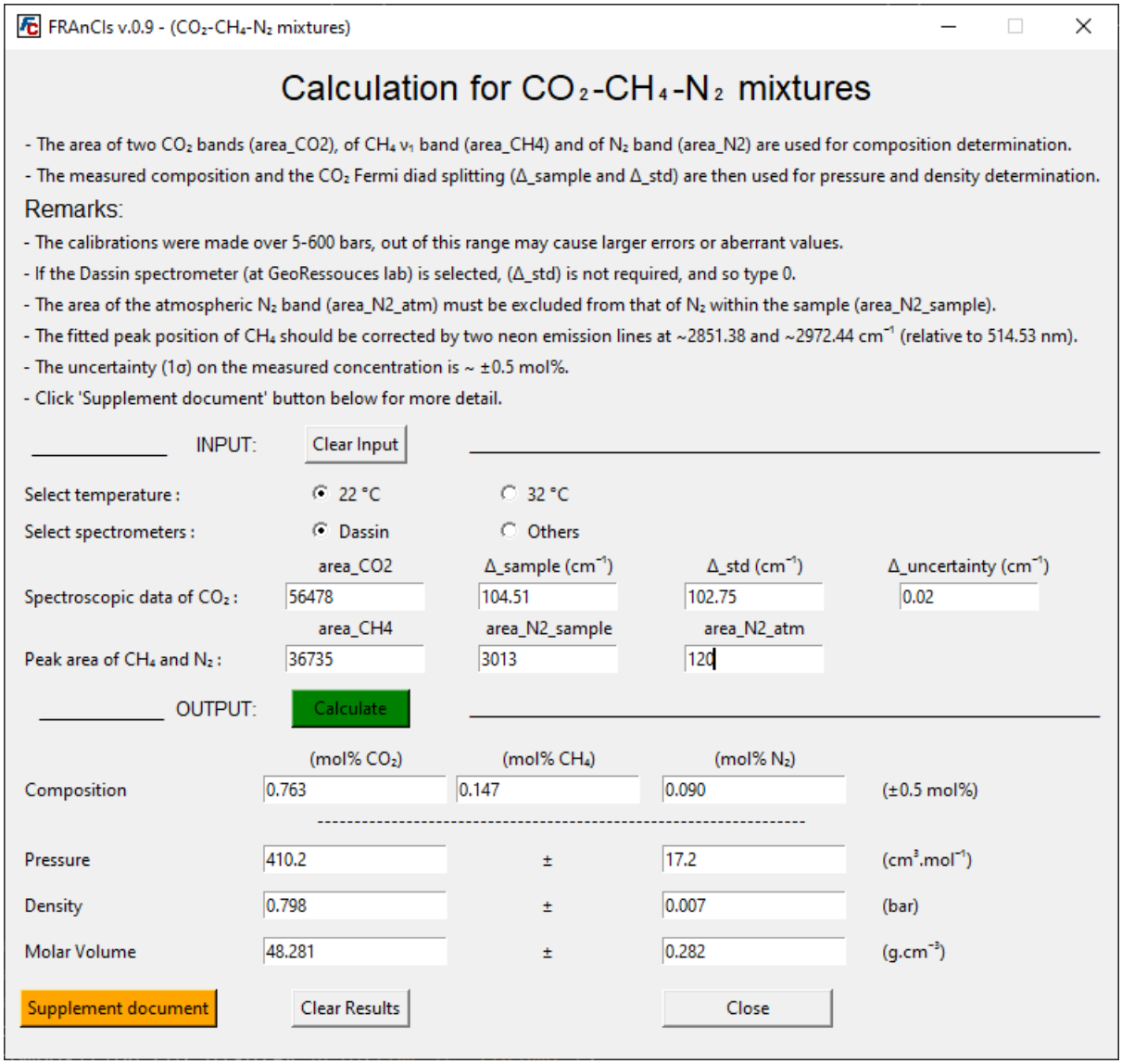

Figure 5-16: User interface of the calculation module for ternary CH_4-CO_2-N_2 mixtures with an example of measurements and of *PVX* calculation at 32 °C.

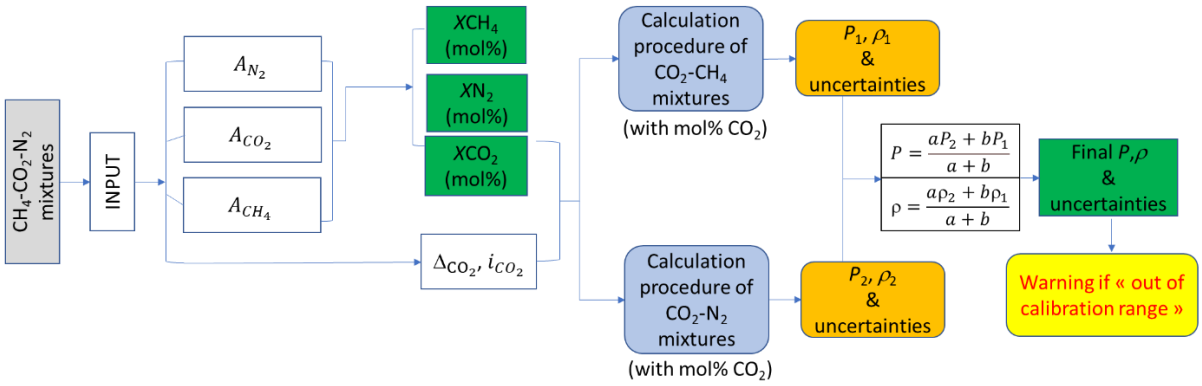

Figure 5-17: Calculation procedure for the *PVX* properties determination within the module of CO_2-CH_4-N_2 ternary mixtures.

Figure 5-17 presents the scheme of the calculation procedure within the module developed for the CO_2-CH_4-N_2 ternary mixtures. The composition of the ternary mixtures (XCO_2, XCH_4 and XN_2) is firstly calculated from the peak area of CO_2, CH_4, and N_2 (A_{CO_2}, A_{CH_4} and A_{N_2}) and their RRSCSs (e.g., 2.29 ± 0.02, 7.73 ± 0.15, and 1, respectively). The pressure and the density of the ternary mixtures (P and ρ) are then calculated from the CO_2 composition (XCO_2) and the CO_2 Fermi diad splitting (Δ_{CO_2} or $\Delta^*_{CO_2}$ depending on the used Raman spectrometer).

Pressure P (or density ρ) of the ternary mixtures was demonstrated to be always between pressure P_1 and P_2 (or density ρ_1 and ρ_2) of the CO_2-CH_4 and CO_2-N_2 binary mixtures, respectively, with P, P_1 and P_2 (or ρ, ρ_1 and ρ_2) all measured from a given XCO_2 and Δ_{CO_2} (or $\Delta^*_{CO_2}$) (cf. Figure 5-8, and section 3.3.2 in Chapter 3). Therefore, the calculation procedure of the pressure P (or density ρ) of the ternary mixtures involves two individual calculations of P_1 (or ρ_1) and P_2 (or ρ_2) (Figure 5-17).

For instance, considering here the determination of pressure P (or density ρ) of the ternary mixture of 80-a-b mol% (XCO_2-XCH_4-XN_2) with $a + b = 20$ mol%, the program will process two calculation procedures for the determination of the pressure P_1 and P_2 (or density ρ_1 and ρ_2) of the binary mixtures of 80 mol% CO_2 (, i.e., CO_2-CH_4 (80-20) and CO_2-N_2 (80-20), respectively) from the measured value of Δ_{CO_2} (or $\Delta^*_{CO_2}$) within the analyzed ternary mixture. Once the pressure P_1, P_2 are calculated, the pressure P of the ternary mixtures is then deduced from the molar proportion of CH_4 and N_2 within the ternary mixture (e.g., a and b mol%, respectively) using Equation 5.15 (see section 3.3.2 in Chapter 3 for more detail). Similarly,

the density ρ of the ternary mixtures can be calculated from ρ_1 and ρ_2 and the molar proportions a and b using Equation 5.16.

The global uncertainty of P, P_1 and P_2 (or of ρ, ρ_1 and ρ_2) can be calculated by following the calculation procedure described for the binary mixtures in the previous subsection (cf. Equations 5.10, 5.11, 5.13 and 5.14).

$$P = \frac{aP_2 + bP_1}{a + b} \quad 5.15$$

$$\rho = \frac{a\rho_2 + b\rho_1}{a + b} \quad 5.16$$

4. Discussion about the applicability of the calibration data to other gas systems

4.1. Effect of the presence of other gases

Beyond the pure, binary, and ternary systems of CO_2, CH_4, and N_2, many other gaseous species such as H_2, H_2S, SO_2, CO, O_2, and higher hydrocarbons (e.g., C_2H_6, C_3H_8) were detected in geological fluids (cf. reviews of Dubessy et al. (1989), Burke (2001), Frezzotti et al. (2012)). For instance, CO_2-rich fluid inclusions with a small amount of CO were found in magmatic rocks or mantle fluids (Bergman and Dubessy, 1984; Huraiova et al., 1991). A small amount of H_2S, SO_2 and/or COS was also recognized in CO_2-rich fluid inclusions within basaltic rocks from Arizona, Hawaii, and Germany (Murck et al., 1978) or in rubies from marble-hosted deposits in the Luc Yen mining strict, Vietnam (Giuliani et al., 2003), for example. CH_4-rich inclusions with a small quantity of H_2 and/or O_2 is rare but also have been found in various geological environments, such as high-grade metamorphic rock (Dubessy et al., 1988; Tsunogae and Dubessy, 2009; Ferrando et al., 2010), granitic rocks (Dubessy et al., 1988), igneous rock (Potter and Konnerup-Madsen, 2003; Li and Chou, 2015), etc. In the following, we discuss about the possibility of extrapolating the calibration data obtained in this study for the binary or ternary mixtures of CO_2-CH_4-N_2 to mixtures containing other gaseous species.

Indeed, the minor admixture of additional gaseous species in fluids containing CO_2, CH_4, or N_2, even with a small quantity, cannot be ignored because it may cause a significant change in the thermodynamic properties. Consequently, the composition of the fluids becomes more complex, and so the determination of the *PVTX* properties of the fluids from microthermometry data (i.e., phase transition temperatures) is very difficult, even impossible. For instance, the

presence of H_2 cannot be recognized by the microthermometry technique, which usually uses liquid N_2 for cooling (the T_{vap} of N_2 = – 196.15 °C), due to its very low critical temperature (T_{vap} of H_2 = – 252.79 °C). The CH_4-N_2-rich fluid inclusions may also contain a small quantity of H_2 or H_2S (T_c = – 87.5 °C) or CO_2 (T_c = – 56.6 °C) that leads to somewhat difficulty upon the interpretation of the observed phase transitions. Consequently, the presence of a small amount of these gaseous species within CH_4-N_2-rich fluid inclusions cannot be straightforwardly confirmed by only microthermometry data. Also, the possibility of diffusion of H_2 through the host crystal at high temperature has been reported in some works (Hollister and Burruss, 1976; Mavrogenes and Bodnar, 1994; Morgan Vi et al., 1993), that may also cause an alteration of the original composition of the fluid.

For all these aforementioned reasons, Raman spectroscopy seems to be a better-suited method that can overcome the inherent limitations of the microthermometry technique. All gaseous species such as H_2S, H_2, O_2, SO_2, CO… can be easily detected by a Raman analysis even at low density and/or low concentration. However, the accurate calibration data of the mixture containing these gases are not available yet or poorly documented in the literature. This is due to the high sensibility of the Raman signal of each gaseous species as well as the complexity of the calibration procedure. It is also to note that modification of the thermodynamic properties which is due to the change of the chemical composition of gaseous mixtures, reflects the change of the intermolecular interactions at the molecular levels. Thus, the Raman spectra of gaseous species obviously change as a function of the chemical composition. This was already shown via the experimental data reported in Chapters 2 and 3. Namely, the variation trend of the CH_4 ν_1 band position as a function of pressure (or density) and composition within the CH_4-N_2 mixtures are entirely different from those observed for the CH_4-CO_2 mixtures (cf. Figure 3-3 in Chapter 3). On the other hand, the variation trend of the CO_2 Fermi diad splitting within CO_2-CH_4 or CH_4-N_2 mixtures is similar, but the magnitude of the variation is slightly different (cf. Figure 5-8). That is why we developed the calibration data of the CO_2-CH_4-N_2 ternary mixtures based on the variation of the CO_2 Fermi diad splitting (cf. section 3.3.2 in Chapter 3).

The complexity and the variety of the composition effect of gases to the variation of spectral features (e.g., peak position shift) were also early reported in Seitz et al. (1993). Figure 5-18 presents the variation of the ν_1 band position of CH_4 mixed at 1:1 mol% ratio with four different gases, i.e., CO_2, N_2, H_2, and Ar. In general, the composition effect is relatively small

at low pressure (< ~ 50 bars), then becomes more discernible at higher pressures. This is because the gaseous molecules are far apart from each other, and so the intermolecular interactions are insignificant at very low pressure (or low density). Thus, they can be considered as an isolated molecule. With increasing pressure, the intermolecular distance decreases, and so the intermolecular interaction increases. This leads to the significant change of the Raman spectral features, i.e., the Raman band position, and a more discernible effect of the chemical composition (Figure 5-18).

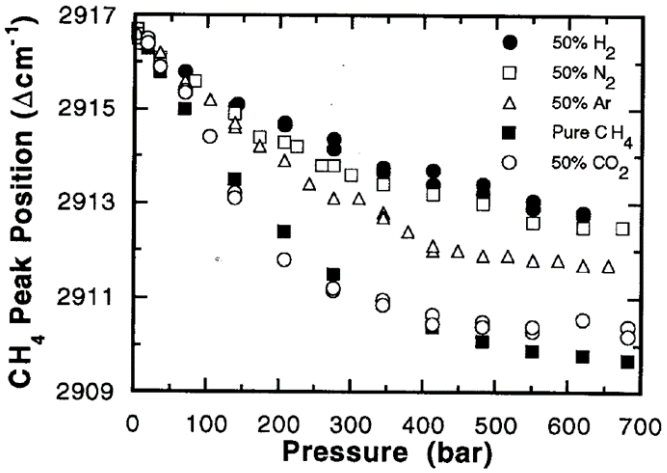

Figure 5-18: Variation of the peak position of the CH_4 ν_1 band as a function of pressure and chemical composition within different binary mixtures. The figure is cited from Seitz et al. (1993).

Moreover, the change of intermolecular forces as a function of pressure (density) depends not only on the intermolecular distance *r*, but also on several other factors, e.g., the size, the geometrical configuration, and the polarization of each gaseous molecule, etc. The latter molecular characteristics are specific to each molecule. That means, once again, the effect of composition to the sensitive variation of the Raman band position (and other Raman spectral parameters) of gases cannot theoretically be identical. Consequently, each gaseous system must be individually studied to dedicatedly provide the accurate Raman calibration data for the quantitative analyses of pressure and density, which requires high accuracy as for the analyses of natural fluid inclusions, for example.

4.2. Effect of the presence of H_2

The Raman spectrum of H_2 shows four vibrational bands $Q_1(0)$, $Q_1(1)$, $Q_1(2)$ and $Q_1(3)$ at ~ 4163, 4156, 4145, and 4128 cm^{-1}, respectively, with the band $Q_1(1)$ the most intense one

(Veirs and Rosenblatt, 1987). The latter is therefore used in preference for the quantitative analyses.

The variation of the spectral parameters of CH_4 and H_2 (e.g., peak position, peak height, peak area, and FWHM) within the CH_4-H_2 mixtures were recently established by Fang et al. (2018). Five mixtures of CH_4-N_2 of different molar ratios (1:10, 1:5, 1:1, 5:1, 10:1) were analyzed at ambient temperature and for a pressure range of 10 to 400 bars. Over the studied pressure range, the H_2 $Q_1(1)$ band position decreases (from ~4155.49 cm^{-1}) as increasing pressure and reaches a minimum value (4156.92 cm^{-1}) at about 300 bars (i.e., a magnitude of 1.43 cm^{-1}), then increases as pressure further increases. The magnitude shift of the H_2 $Q_1(1)$ (~ 1.43 cm^{-1}) is much smaller than that of the CH_4 ν_1 band (~ 6.16 cm^{-1}) for the same pressure range.

Figure 5-19a shows the variation of the CH_4 ν_1 band position as a function of pressure and composition within the CH_4-H_2 mixtures. The experimental data are from Fang et al. (2018). In general, the variation trend of the CH_4 ν_1 band position within the CH_4-H_2 mixtures is very similar to that observed in the CH_4-N_2 mixtures. Indeed, the CH_4 band position decreases as increasing of pressures, and also decreases as the H_2 concentration decreases at any constant pressure (Figure 5-19a).

Figure 5-19b shows the variation of the distance between molecules *r* within the CH_4-H_2 mixtures as a function of pressure and composition. The intermolecular distance *r* (Å) was derived from the density calculated by the GERG-2004 equation of state using the REFPROP software (Lemmon et al., 2013). Indeed, the variation trend of the intermolecular distance *r* is quite similar to that observed for CH_4-N_2 mixtures (cf. Figure 4-4b in Chapter 4). Therefore, the calibration data of the CH_4-H_2 and CH_4-N_2 binary mixtures can probably be combined to generate the calibration data for the ternary mixtures of CH_4-N_2-H_2 based on the relative variation of the CH_4 ν_1 band position (as we did for the ternary mixtures of CO_2-CH_4-N_2).

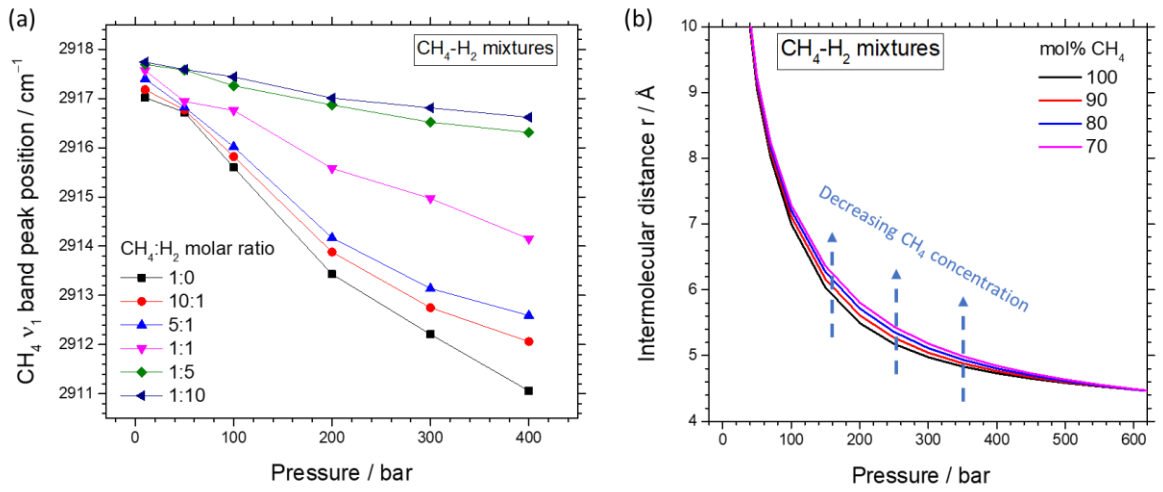

Figure 5-19: (a) Variation of the CH_4 ν_1 band position (cm^{-1}) as a function of pressure (bar) and composition (molar ratio) within CH_4-H_2 binary mixtures at ambient temperature. The experimental data cited from Fang et al. (2018). (b) Evolution of the intermolecular distance *r* (Å) as a function of pressure (bar) and composition (mol% CH_4) of CH_4-H_2 mixtures.

Overall, the calibration data of Fang et al. (2018) revealed the general variation trend of the peak position of CH_4 as a function of pressure and composition within CH_4-N_2 mixtures. However, we noticed that the peak position of the CH_4 ν_1 band within different mixtures at the lowest pressure (10 bars) are very scattered with a significant fluctuation of about 0.75 cm^{-1} (Figure 5-19a), whereas they should converge to (nearly) the same value because the effect of the composition at such a low pressure (density) is minimal and can be negligible (as explained above). This indicated that there was a significant fluctuation (error) in the experimental calibration data points reported in Fang et al. (2018) (Figure 5-19), which may arise from the deviation of their Raman apparatus. Indeed, the comparison of 9 different densimeters of pure CH_4 developed by different research teams also confirms the discrepancy of the calibration data of Fang et al. (2018) (Figure 5-2a). Besides, the calibration data is relatively sparse, i.e., only 6 data points for each mixture composition over the entire studied pressure range (10-400 bars). Therefore, more experimental data of CH_4-H_2 with higher accuracy are still needed in order to develop the most accurate calibration data for the ternary mixtures of CH_4-N_2-H_2.

5. Conclusion

In this study, numerous experimental densimeters and barometers previously published in the literature were collected and compared together to examine the applicability of the calibration data obtained herein to other Raman apparatus (i.e., within other laboratories). The

discrepancy of the several densimeters (barometers) was mainly attributed to the systematic day-to-day deviation of the instrumental factor. The relative variation is therefore used to establishing the universal regression calibration equations which are applicable in any other laboratories. The latter calibration equations are based on the relative variation of the CO_2 Fermi diad splitting ($\Delta^*_{CO_2}$) and the CH_4 ν_1 band position ($\nu^*_{CH_4}$). The standard value of the CO_2 Fermi splitting and the CH_4 ν_1 band position at near-zero density (denoted $\Delta^0_{CO_2}$ and $\nu^0_{CH_4}$ respectively) must be accurately determined for each specific Raman apparatus. Due to the deviation day-to-day of the Raman spectrometer, these values of $\Delta^0_{CO_2}$ and $\nu^0_{CH_4}$ must be daily measured at least two times, i.e., at the beginning and the end of the experiment section where the samples are analyzed. More checks are also recommended during the analytical section (e.g., after every measurement of about 3 to 5 samples, in order to be able to prevent as soon as possible any minimal deviation of the response of the spectrometers, and so to ensure the highest accuracy of the measurements. A sealed silica microcapillary containing pure CH_4 or CO_2 at less than ~ 5 bars are highly recommended to be used as standards for the routine calibration.

FRAnCIs calculation program was also developed to facilitate the application of our calibration data. Thereby, the final *PVX* properties of the sample and the associated global uncertainty can be conveniently calculated from Raman spectroscopic data via a user-friendly interface.

Finally, a discussion about the extrapolation of the calibration data obtained in this study to the mixture containing additional gaseous species was addressed. Since the highly sensitivity of Raman spectral parameters to the *PVTX* conditions, the calibration data must be dedicatedly developed for each specific gas mixtures to ensure a satisfactory uncertainty of the quantitative measurement of density and pressure. The effect of the presence of H_2 on the variation of the CH_4 ν_1 band position is further described thanks to the new calibration data recently published in the literature by Fang et al. (2018). In general, the variation trend of the CH_4 ν_1 band position within CH_4-N_2 and CH_4-H_2 binary mixtures is very similar. The calibration data of the CH_4-N_2-H_2 ternary mixtures can, therefore, potentially be obtained by combining the calibration data of these two binary mixtures. However, the calibration data reported in Fang et al. (2018) is somewhat less accurate, according to our analyses and comparison. More accurate calibration data are thus still needed.

General conclusions and Perspectives

General conclusions and perspectives

The present work aimed to develop Raman analysis-based technique for the direct determination of the *PVX* properties of pure gases (CH_4 and CO_2) and of any binary and ternary mixtures of CO_2, CH_4 and N_2 at the highest accuracy. Nowadays, the microthermometry is still used as a standard technique for almost every fluid inclusion analysis. However, this technique has some inherent limitations. For instance, microthermometry analyses cannot be performed for samples of small size (< 5 µm) or of low density because no phase transition could accurately be observed. Besides, the lack of adequate thermodynamic models for the mixtures of complex composition (e.g., containing more than two salts or volatile species) and/or the impact of the formation of the CO_2 and CH_4 hydrates to the observed phase transition temperatures are also notable drawbacks which restrict the applicability of the microthermometry method in certain practical cases.

Otherwise, the microthermometry method is usually (obligatory) used in combination with Raman spectroscopy to fully determine the *PVX* properties of fluid inclusions when the actual composition cannot be defined from the observed phase transition(s). On the other hand, only Raman analyses can literally be able to provide simultaneously qualitative and quantitative information, e.g., *PVX* properties (after accurately establishing calibration data) without needing any complementary microthermometry analyses. However, Raman spectral features (e.g., peak area, peak intensity, peak position) are highly sensitive to numerous instrumental parameters and analytical conditions (pressure, density, composition and/or temperature). This makes the development of accurate calibration data a very delicate and complicated procedure. Therefore, Raman calibration data of gas mixtures was poorly documented and/or at very low accuracy.

Moreover, most calibration data published in literature was provided only for pure gases at low pressure (density). Using these published data may lead to non-quantified errors, especially when applied to geological fluids containing more than one substance at elevated pressure (density). The objective herein is to make Raman spectroscopy become a practical and accurate technique that can alternatively be used when the microthermometry approach is impossible, and even further, to completely replace microthermometry in most practical cases.

1. Providing accurate calibration data for the direct determination of *PVX* properties from Raman spectroscopic data.

In this study, a complete experimental protocol was developed and validated with excellent reproducibility, from the preparation of the desired gas mixtures of CO_2, CH_4 and N_2 and the verification of the composition of the obtained mixtures by gas chromatography (giving an accuracy of about ± 0.3 mol% in the composition of the prepared mixtures), to the *in situ* Raman analyses of gases and gas mixtures and the Raman data processing. The *in-situ* Raman analyses were precisely performed under controlled *PVTX* conditions thanks to the combination of the HPOC (High-Pressure Optical Cell) system, and the heating-cooling stage (Linkam CAP500®) coupled with a Raman spectrometer.

Through an experimental approach, the responses for numerous questionable problems concerning the quantitative measurements of the *PVX* properties of gas mixtures were thus addressed:

(i) **The effect of composition and pressure (or density) on the relative Raman scattering cross-section (RRSCS)**, i.e., a physical parameter characterizing the Raman scattering efficiency of each vibrational mode, was demonstrated. In general, the RRSCS of the CH_4 ν_1 symmetric stretching vibration mode remains constant (~ 7.73 ± 0.16) as pressure and composition changed. Regarding CO_2, the effect of composition on the variation of RRSCSs of CO_2 was not observed, i.e., it is similar to that observed for the RRSCS of CH_4. However, the RRSCS of the upper band of the CO_2 Fermi diad splitting (i.e., ν^+ at ~ 1388 cm^{-1}) slightly increases, whereas that of the lower band of CO_2 (i.e., ν^- at ~ 1285 cm^{-1}) slightly decreases as increasing of pressure (or density). This small increase (or decrease) of $\sigma_{\nu+}$ (or $\sigma_{\nu-}$) leads to only a minor error on the measured composition (less than about 0.2 mol%). According to the statistical analyses, the RRSCSs of two CO_2 bands can still be considered as constant over the studied pressure range (5 - 600 bars), with values of 1.40 ± 0.03 and 0.89 ± 0.02 for $\sigma_{\nu+}$ and $\sigma_{\nu-}$, respectively. The latter error may become more discernible at elevated pressure (for example, at several kilobars, i.e., far away from the studied pressure range herein). Besides, our experimental results allowed us to revise the statement of Seitz et al. (1996) that "*only the RRSCS of the upper band of CO_2 should be used for the determination of the composition*". Indeed, the sum of the two RRSCS of CO_2 is almost constant at ~ 2.29 ± 0.04 over the entire studied pressure range. Therefore, it is recommended to use the sum of the two RRSCS of CO_2 ($\sigma_{\nu+} + \sigma_{\nu-}$) instead of using individual RRSCS ($\sigma_{\nu+}$ or $\sigma_{\nu-}$) to determine the

composition of gas mixtures when possible. In other words, the Fermi diad of CO_2 should be treated as one Raman band for the highest accuracy possible (cf. Chapter 2). Overall, with our new data of the RRSCS of CO_2 and CH_4, the uncertainty of the measured composition is about ± 0.5 mol% (1σ).

(ii) **Calibration data for pure CO_2 and CH_4, and any binary and ternary mixtures of CO_2, CH_4 and N_2**: The CO_2 Fermi diad splitting and the variation of the CH_4 ν_1 band position were demonstrated to be the most reliable spectral parameters for quantitative measurements of pressure or density with the best reproducibility compared to that of other spectral parameters (the peak area/intensity ratio, the FWHM…). However, the peak position of the N_2 ν_1 band is not recommended to be used as a quantitative parameter due to (i) the small downshift magnitude (e.g., a downshift of about 2.2 cm^{-1} is observed for the ν_1 band of pure N_2 as pressure increased from 5 to 600 bars), and especially (ii) the modest reproducibility. The latter was firmly confirmed by several repeated tests over different periods. Different reasons were attributed to explain the modest reproducibility in the measurement of the N_2 ν_1 band. Namely, the N_2 ν_1 band is asymmetric at low pressure, with a low cross section (= 1), and is easily perturbed by the superimposition of the Raman signal of atmospheric N_2. This leads to a noticeable error in the actual fitted band position even after a wavelength correction by two nearby neon emission lines.

For the first time, the calibration data of the CO_2-N_2 mixtures based on the variation of the CO_2 Fermi diad splitting (Δ) were accurately provided for the direct determination of the *PVX* properties for any composition. The experimental protocol was then successfully extended to other binary mixtures to provide the calibration data for CH_4-N_2 (based on the relative variation of the CH_4 ν_1 band position, $\nu^*_{CH_4}$) and for CO_2-CH_4 systems (based on the variation of Δ and $\nu^*_{CH_4}$, depending on the concentration range e.g., > or < 50 mol% CO_2). Overall, the uncertainty of the pressure and density derived from our calibration data (estimated from the 1σ confidence interval of the regression polynomial calibration) was always less than ± 20 bars and ± 0.02 $g{\cdot}cm^{-3}$, respectively. The calibration data of the CO_2-CH_4-N_2 ternary mixtures were basically the combination of two calibration data sets of the CO_2-N_2 and CO_2-CH_4 binary mixtures. In this study, our calibration data were experimentally established over 5 - 600 bars at 22 and 32 °C (higher than the critical temperature of CO_2). The validation of our calibration was made by applying to a different set of natural fluid inclusions containing various composition, pressure, and density range (collected from the Alpine fissures of the external part of the

Central Alps (Switzerland) or W-Cu-Sn deposit of Panasqueira (Portugal). The obtained Raman results were in good agreement with those derived from microthermometry data.

2. In-depth interpretation of the pressure-induced frequency shifts of the CH_4 and N_2 ν_1 bands at the molecular level.

Indeed, the effect of chemical composition on the variation of the peak position was distinctly demonstrated through experimental calibration data. Namely, the variation behavior of the peak position of N_2 (in pure N_2 or binary mixtures with CO_2 or CH_4) and CH_4 (in pure CH_4 or binary mixtures CO_2 or N_2) are very different.

First, **by a theoretical approach,** the global variation trends of these bands of **pure** N_2 and CH_4 were intuitively interpreted based on the basic of the Lennard-Jones 6-12 potential energy approximation (cf. Chapter 4). The pressure-induced redshift and blueshift were reasonably attributed to the contribution of the attractive and repulsive forces, respectively, which vary as a function of the intermolecular separation *r* (derived from the density). Overall, the redshift of the CH_4 and N_2 bands (in the pure systems) observed throughout the studied pressure range (i.e., from 5 to 600 bars) is due to the domination of the attractive intermolecular forces. Indeed, the intrinsic correlation between the Raman band position variation and the intermolecular interaction change was demonstrated by (i) the close affinity between the variation trend as a function of intermolecular distance *r* of the Raman peak position and the net LJ potential energy (cf. Figure E. 4-1), and especially (ii) the superposition of the inflection points observed on the calibration curves and the LJ potential approximation curves (Figure 4-5). Besides, the application of the LJ potential energy herein also pointed out the difference of the length scale of the interaction forces between molecules exercising within CH_4-N_2 and CH_4-CO_2 mixtures, e.g., the molecules within CH_4-N_2 mixtures experience longer distance-range forces than that within CH_4-CO_2 mixtures at a given pressure.

Second, **for a more in-depth understanding**, the contribution of the attractive and repulsive solvation mean-forces to the corresponding attractive and repulsive components ($\Delta\nu_R$ and $\Delta\nu_A$, respectively) decomposed from the net frequency shift of the CH_4 band ($\Delta\nu$) was quantitatively assessed as a function of pressure (density) and composition, using the perturbed hard-phere fluid (PHF) model. Interesting information could thereby be revealed, i.e., the variation change (as a function of the composition) of the frequency shift of the CH_4 ν_1 band within CH_4-N_2 mixtures is responsible by the solvation induced attractive component $\Delta\nu_A$ (i.e.,

mainly by the attractive solvation mean-forces), whereas that in the CH_4-CO_2 mixtures is governed by the change of the repulsive component $\Delta\nu_R$ (i.e., arising from the change of the repulsive solvation mean-forces) (cf. Figure 4-7c and d in Chapter 4). A predictive model was also provided to predict the variation trends of the CH_4 ν_1 band position within CH_4-N_2 and CH_4-CO_2 mixtures for a pressure range of up to 3000 bars.

3. Reassessment of the applicability of calibration data to other Raman apparatus (other laboratories). Development of the FRAnCIs calculation program for universal use.

The applicability of the calibration data obtained in this study to other Raman apparatus as well as other laboratories was examined by revising and comparing with numerous calibration data of pure CH_4 and CO_2 published in the literature (cf. Chapter 5). The main reason causing the discrepancy between different published densimeters and barometers was assigned to the systematic deviation of different Raman spectrometers. Consequently, the relative variation of the selected quantitative spectral parameters, i.e., the CH_4 ν_1 band position ($\nu^*_{CH_4}$) and the CO_2 Fermi diad splitting ($\Delta^*_{CO_2}$), not the absolute values (ν_{CH_4} and Δ_{CO_2}), must be used for establishing the universal regression calibration equations.

By combining with previously published calibration data, the validity range of the calibration equation of the pure CH_4 was extended to ~ 0.35 g·cm^{-3} (corresponding to 1140 bars at 32 °C). For other gaseous systems (including pure CO_2, CO_2-N_2, CH_4-N_2, CO_2-CH_4 and CO_2-CH_4-N_2 mixtures), the validity range was less than 1.06 g·cm^{-3} (i.e., the studied density range of this study, corresponding to pressure from 5 to 600 bars). Overall, 76 regression polynomial calibration equations were individually provided for different composition-pressure ranges at a fixed temperature (22 and 32 °C). Indeed, every calibration equations of CH_4 were based on $\nu^*_{CH_4}$, so-called universal calibration equations. The latter is, therefore, applicable to any laboratories (any Raman apparatus). On the other side, the calibration equations of CO_2 were divided into two types. The first one is based on the variation of the absolute variation of the CO_2 Fermi diad splitting (Δ_{CO_2}) and applicable only for Raman spectrometer LabRAM HR (the one used upon developing the calibration data) available at GeoRessouces laboratory. The second one is based on the relative variation of the CO_2 Fermi diad splitting ($\Delta^*_{CO_2}$), and so-called universal calibration equation as well. The latter is thus applicable to any other Raman apparatus. Since the universal calibration equations are based on the relative variation of the selected quantitative parameters ($\nu^*_{CH_4}$ and $\Delta^*_{CO_2}$), the value of

the corresponding spectral parameter at near-zero density ($\nu^0_{CH_4}$ and $\Delta^0_{CO_2}$) are imperatively required. It is important to note that value $\nu^0_{CH_4}$ and $\Delta^0_{CO_2}$ are specific for each Raman spectrometer. Also, they must be measured and verified several times in the same experimental section of the sample analyses (i.e., on the same working day) to ensure the best accuracy of the measurements.

The calculation program FRAnCIs with a user-friendly interface was developed to facilitate the application of our calibration data upon the daily laboratory analyses. All regression calibration equations aforementioned were therefore integrated into the program. Thereby, they can be automatically selected depending on the composition-pressure range calculated from the input spectroscopic parameters (i.e., spectroscopic data) (cf. Chapter 5). The global uncertainty of the measured pressure and density (arising from the uncertainty of the measured spectroscopic data and of the regression calibration calibrations) is also calculated and simultaneously provided with the final results (cf. section 3 of Chapter 5).

Overall, we demonstrated the feasibility of Raman spectroscopy for a specific application of the quantitative analyses of microvolumes of gaseous systems at elevated pressure (i.e., natural fluid inclusions) with satisfactory accuracy. This was done at multiple scales and by multiple approaches: from experimental *in-situ* Raman analyses to the interpretation and modeling of the variation trend of the Raman band position from the theoretical chemical-physical point of view.

Our calibration data is the most complete and accurate one compared with the previously published in the literature. This can be used not only for the accurate quantitative measurement of *PVX* properties of gaseous systems but also have the potential application with an easy adaptation to multidisciplinary approach, e.g., for investigating thermodynamic and intermolecular behavior of gaseous at molecule scale, etc. For instance, from our calibration data, new relationships between Raman spectral features and several physical parameters of interest, such as the intermolecular interaction forces, the relative variation of the bond length, or some physical properties of gases such as fugacity, fugacity coefficients, etc., can be readily established using more elaborated modelling approaches (Monte-Carlo, ab-initio methods, etc.). The experimental protocol used in this study can also be extended and applied entirely or partially in different research fields concerning gas analyses such as environmental gas sensing, monitoring of geological storage, monitoring of polluted air, diagnosis of disease states by human breath analysis, etc.

It should be kept in mind that the experimental calibration data obtained in this study was developed at a fixed temperature (e.g., 22 and 32 °C), thus cannot be accurately extended to higher temperature. Besides, the discussion about the extrapolation of the calibration data to other gas systems (i.e., containing additional gaseous species usually founded within geological fluids such as H_2, H_2S, O_2…) pointed out that the calibration data must be dedicatedly developed for each specific gas mixtures to ensure a satisfactory uncertainty due to the high sensitivity of the spectral parameters to the variation of pressure, density, temperature, and especially of the mixture chemical composition. Therefore, to further increase the applicability of the Raman analysis-based quantitative method developed herein to a wider *PVTX* range, more experimental calibration data are still needed.

Références bibliographiques

Affolter, S., Fleitmann, D., Leuenberger, M., 2014. New-on-line method for water isotope analysis of speleothem fluid inclusions using laser absorption spectroscopy (WS-CRDS). Clim. Past 10, 1291–1304.

Akinfiev, N.N., Diamond, L.W., 2010. Thermodynamic model of aqueous CO2–H2O–NaCl solutions from −22 to 100°C and from 0.1 to 100MPa. Fluid Phase Equilibria 295, 104–124. https://doi.org/10.1016/j.fluid.2010.04.007

Amat, G., Pimbert, M., 1965. On Fermi resonance in carbon dioxide. J. Mol. Spectrosc. 16, 278–290. https://doi.org/10.1016/0022-2852(65)90123-2

Angus, S., Armstrong, B., de Reuck, K.M., 1978. International thermodynamic tables of the fluid state. 5. Methane.

Angus, S., Armstrong, B., De Reuck, K.M., Altunin, V.V., Gadetskii, O.G., Chapela, G.A., Rowlinson, J.S., 1976. International thermodynamic tables of the fluid state. Carbon Dioxide 3, 338–342.

Angus, S., Reuck, K.M. de, Armstrong, B., 1979. International thermodynamic tables of the fluid state - 6; nitrogen. Oxford : Pergamon Press.

Arienzo, M.M., Swart, P.K., Vonhof, H.B., 2013. Measurement of δ18O and δ2H values of fluid inclusion water in speleothems using cavity ring-down spectroscopy compared with isotope ratio mass spectrometry. Rapid Commun. Mass Spectrom. 27, 2616–2624. https://doi.org/10.1002/rcm.6723

Bakker, R.J., 1997. Clathrates: Computer programs to calculate fluid inclusion V-X properties using clathrate melting temperatures. Comput. Geosci. 23, 1–18. https://doi.org/10.1016/S0098-3004(96)00073-8

Bakker, R.J., Diamond, L.W., 2000. Determination of the composition and molar volume of H2O-CO2 fluid inclusions by microthermometry. Geochim. Cosmochim. Acta 64, 1753–1764. https://doi.org/10.1016/S0016-7037(99)00334-8

Bakker, R.J., Dubessy, J., Cathelineau, M., 1996. Improvements in clathrate modelling: I. The H2O-CO2 system with various salts. Geochim. Cosmochim. Acta 60, 1657–1681. https://doi.org/10.1016/0016-7037(96)00032-4

Banks, D.A., Yardley, B.W.D., 1992. Crush-leach analysis of fluid inclusions in small natural and synthetic samples. Geochim. Cosmochim. Acta 56, 245–248. https://doi.org/10.1016/0016-7037(92)90129-7

Ben-Amotz, D., Herschbach, D.R., 1993. Hard fluid model for solvent-induced shifts in molecular vibrational frequencies. Hard Fluid Model Solvent-Induc. Shifts Mol. Vib. Freq. 97, 2295–2306.

Ben-Amotz, D., LaPlant, F., Shea, D., Gardecki, J., List, D., 1992. Raman Studies of Molecular Potential Energy Surface Changes in Supercritical Fluids, in: Supercritical Fluid Technology, ACS Symposium Series. American Chemical Society, pp. 18–30. https://doi.org/10.1021/bk-1992-0488.ch002

Ben-Amotz, D., Lee, M., Cho, S.Y., List, D.J., 1992. Solvent and pressure-induced perturbations of the vibrational potential surface of acetonitrile. J. Chem. Phys. 96, 8781–8792. https://doi.org/10.1063/1.462285

Bendtsen, J., 1974. The rotational and rotation-vibrational Raman spectra of 14N2, 14N15N and 15N2. J. Raman Spectrosc. 2, 133–145. https://doi.org/10.1002/jrs.1250020204

Benson, S.M., Cole, D.R., 2008. CO2 Sequestration in Deep Sedimentary Formations. Elements 4, 325–331. https://doi.org/10.2113/gselements.4.5.325

Bergman, S.C., Dubessy, J., 1984. CO2-CO fluid inclusions in a composite peridotite xenolith: implications for upper mantle oxygen fugacity. Contrib. Mineral. Petrol. 85, 1–13. https://doi.org/10.1007/BF00380216

Bertrán, J.F., 1983. Study of the Fermi doublet ν1 — 2ν2 in the Raman spectra of CO2 in different phases. Spectrochim. Acta Part Mol. Spectrosc. 39, 119–121. https://doi.org/10.1016/0584-8539(83)80066-X

Bodnar, R.J., Lecumberri-Sanchez, P., Moncada, D., Steele-MacInnis, M., 2014. 13.5 - Fluid Inclusions in Hydrothermal Ore Deposits, in: Holland, H.D., Turekian, K.K. (Eds.), Treatise on Geochemistry (Second Edition). Elsevier, Oxford, pp. 119–142. https://doi.org/10.1016/B978-0-08-095975-7.01105-0

Bögözi, T., Popp, J., Frosch, T., 2015. Fiber-enhanced Raman multi-gas spectroscopy: what is the potential of its application to breath analysis? Bioanalysis 7, 281–284. https://doi.org/10.4155/bio.14.299

Bottrell, S., Yardley, B.W.D., Buckley, F., 1988. A modified crush-leach method for the analysis of fluid inclusion electrolytes. Bull. Minéralogie 111, 279–290. https://doi.org/10.3406/bulmi.1988.8048

Bouanich, J.-P., 1992. Site-site Lennard-Jones potential parameters for N2, O2, H2, CO and CO2. J. Quant. Spectrosc. Radiat. Transf. 47, 243–250. https://doi.org/10.1016/0022-4073(92)90142-Q

Boulliung, J., Caumon, M.-C., Tarantola, A., Randi, A., Robert, P., Mullis, J., 2017. A new relation between CO2 density and Fermi Diad Raman shift from experimental HPOC analyses. Application to natural CO2-H2O-NaCl fluid inclusions. ECROFI.

Bowen, N.L., 1928. Geological thermometry. Lab. Investig. Ores Wash. DC 172–219.

Brewster, D., 1845. III.—On the Existence of Crystals with different primitive forms and physical properties in the Cavities of Minerals; with additional Observations on the New Fluids in which they occur. Earth Environ. Sci. Trans. R. Soc. Edinb. 16, 11–22. https://doi.org/10.1017/S0080456800024868

Brewster, D., 1826. On the Refractive Power of the Two New Fluids in Minerals; with Additional Observations on the Nature and Properties of These Substances. By David Brewster. P. Neill.

Brewster, D., 1823. I. On the Existence of Two New Fluids in the Cavities of Minerals, which are immiscible, and possess remarkable Physical Properties. Earth Environ. Sci. Trans. R. Soc. Edinb. 101 1–41.

Buckingham, A.D., 1960. A theory of frequency, intensity and band-width changes due to solvents in infra-red spectroscopy. Proc. R. Soc. Lond. Ser. Math. Phys. Sci. 255, 32–39. https://doi.org/10.1098/rspa.1960.0046

Buric, M.P., Chen, K., Falk, J., Velez, R., Woodruff, S., 2009. Raman sensing of fuel gases using a reflective coating capillary optical fiber. Presented at the Fiber Optic Sensors and Applications VI, p. 731608. https://doi.org/10.1117/12.818746

Burke, E.A.J., 2001. Raman microspectrometry of fluid inclusions. Lithos, Fluid Inclusions: Phase Relationships - Methods - Applications. A Special Issue in honour of Jacques Touret 55, 139–158. https://doi.org/10.1016/S0024-4937(00)00043-8

Burruss, R.C., 1981. Analysis of fluid inclusions; phase equilibria at constant volume. Am. J. Sci. 281, 1104–1126. https://doi.org/10.2475/ajs.281.8.1104

Cabaço, M.I., Longelin, S., Danten, Y., Besnard, M., 2007. Local Density Enhancement in Supercritical Carbon Dioxide Studied by Raman Spectroscopy. J. Phys. Chem. A 111, 12966–12971. https://doi.org/10.1021/jp0756707

Carocci, E., Marignac, C., Cathelineau, M., Truche, L., Lecomte, A., Pinto, F., 2019. Rutile from Panasqueira (Central Portugal): An Excellent Pathfinder for Wolframite Deposition. Minerals 9, 9. https://doi.org/10.3390/min9010009

Cathelineau, M., Marignac, C., Marignac, L.-M., Boiron, M.-C., Dejean, M., Carocci, E., 2017. Are we sure to know the fluids responsible for W mineralization at Panasqueira (Portugal): the case for loss of information due to intense quartz recrystallization and FI natural decrepitation. ECROFI 98.

Caumon, M.-C., Dubessy, J., Robert, P., Tarantola, A., 2013. Fused-silica capillary capsules (FSCCs) as reference synthetic aqueous fluid inclusions to determine chlorinity by Raman spectroscopy. Eur. J. Mineral. 25, 755–763. https://doi.org/DOI: 10.1127/0935-1221/2013/0025-2280

Caumon, M.-C., Robert, P., Laverret, E., Tarantola, A., Randi, A., Pironon, J., Dubessy, J., Girard, J.-P., 2014. Determination of methane content in NaCl–H2O fluid inclusions by Raman spectroscopy. Calibration and application to the external part of the Central Alps (Switzerland). Chem. Geol. 378, 52–61. https://doi.org/10.1016/j.chemgeo.2014.03.016

Caumon, M.-C., Tarantola, A., Wang, W., 2019. Raman spectra of gas mixtures in fluid inclusions: Effect of quartz birefringence on composition measurement. J. Raman Spectrosc. 0. https://doi.org/10.1002/jrs.5605

Charlou, J.L., Donval, J.P., Fouquet, Y., Jean-Baptiste, P., Holm, N., 2002. Geochemistry of high H2 and CH4 vent fluids issuing from ultramafic rocks at the Rainbow hydrothermal field (36°14′N, MAR). Chem. Geol. 191, 345–359. https://doi.org/10.1016/S0009-2541(02)00134-1

Chi, G., Chou, I.-M., Lu, H., 2003. An overview on current fluid-inclusions research and applications. Acta Petrol. Sin. 19, 201–212.

Chou, I.-M., 2012. Optical cells with fused silica windows for the study of geological fluids. EMU Notes Mineral. 12, 227–247. https://doi.org/10.1180/EMU-notes.12.6

Chou, I.-M., Burruss, R.C., Lu, W., 2005. Chapter 24 - A new optical capillary cell for spectroscopic studies of geologic fluids at pressures up to 100 MPa, in: Chen, J., Wang, Y., Duffy, T.S., Shen, G., Dobrzhinetskaya, L.F. (Eds.), Advances in High-Pressure Technology for Geophysical Applications. Elsevier, Amsterdam, pp. 475–485. https://doi.org/10.1016/B978-044451979-5.50026-0

Chou, I.-M., Pasteris, J.D., Seitz, J.C., 1990. High-density volatiles in the system C-O-H-N for the calibration of a laser Raman microprobe. Geochim. Cosmochim. Acta 54, 535–543. https://doi.org/10.1016/0016-7037(90)90350-T

Chou, I.-M., Song, Y., Burruss, R.C., 2008. A new method for synthesizing fluid inclusions in fused silica capillaries containing organic and inorganic material. Geochim. Cosmochim. Acta 72, 5217–5231. https://doi.org/10.1016/j.gca.2008.07.030

Chueh, P.L., Prausnitz, J.M., 1967. Vapor-liquid equilibria at high pressures: Calculation of partial molar volumes in nonpolar liquid mixtures. AIChE J. 13, 1099–1107. https://doi.org/10.1002/aic.690130612

Collins, P.L.F., 1979. Gas hydrates in CO 2 -bearing fluid inclusions and the use of freezing data for estimation of salinity. Econ. Geol. 74, 1435–1444. https://doi.org/10.2113/gsecongeo.74.6.1435

Cuadros, F., Cachadiña, I., Ahumada, W., 1996. Determination of Lennard-Jones interaction parameters using a new procedure. Mol. Eng. 6, 319–325. https://doi.org/10.1007/BF01886380

Darimont, A., Heyen, G., 1988. Simulation des équilibres de phases dans le système CO2-N2. Application aux inclusions fluides. Bull. Minéralogie 111, 179–182. https://doi.org/10.3406/bulmi.1988.8083

Davy, H., 1822. XXVII. On the state of water and aëriform matter in cavities found in certain crystals. Philos. Trans. R. Soc. Lond. 112, 367–376. https://doi.org/10.1098/rstl.1822.0028

Deicha, G., 1955. Les lacunes des cristaux et leurs inclusions fluides: signification dans la genèse des gîtes minéraux et des roches. Masson.

Dhamelincourt, P., Beny, J.-M., Dubessy, J., Poty, B., 1979. Analyse d'inclusions fluides à la microsonde MOLE à effet Raman. Bull. Minéralogie 102, 600–610. https://doi.org/10.3406/bulmi.1979.7309

Diamond, L.W., 1994. Salinity of multivolatile fluid inclusions determined from clathrate hydrate stability. Geochim. Cosmochim. Acta 58, 19–41. https://doi.org/10.1016/0016-7037(94)90443-X

Diamond, L.W., 1992. Stability of CO2 clathrate hydrate + CO2 liquid + CO2 vapour + aqueous KCl-NaCl solutions: Experimental determination and application to salinity estimates of fluid inclusions ∗. Geochim. Cosmochim. Acta 56, 273–280. https://doi.org/10.1016/0016-7037(92)90132-3

Diamond, L.W., 1990. Fluid inclusion evidence for P-V-T-X evolution of hydrothermal solutions in late-Alpine gold-quartz veins at Brusson, Val d'Ayas, Northwest Italian Alps. Am. J. Sci. 912–958. https://doi.org/10.2475/ajs.290.8.912

Dijkman, F.G., van der Maas, J.H., 1977. Inhomogeneous broadening of Morse oscillators in liquids. J. Chem. Phys. 66, 3871–3878. https://doi.org/10.1063/1.434462

Dill, H.G., Siegfanz, G., Marchig, V., 1994. Mineralogy and chemistry of metalliferous muds forming the topstratum of a massive sulfide-metalliferous sediment sequence from East Pacific rise 18°S: Its origin and implications concerning the formation of ochrous sediments in cyprus-type deposits. Mar. Georesources Geotechnol. 12, 159–180. https://doi.org/10.1080/10641199409388260

D'Orazio, M., Hirschberger, R., 1983. Multichannel Raman Spectrometer For The Study Of Dynamical Processes In Analytical Chemistry. Opt. Eng. 22, 308. https://doi.org/10.1117/12.7973110

Dubessy, J., Audeoud, D., Wilkins, R., Kosztolanyi, C., 1982. The use of the Raman microprobe MOLE in the determination of the electrolytes dissolved in the aqueous phase of fluid inclusions. Chem. Geol., Current Research on Fluid Inclusions 37, 137–150. https://doi.org/10.1016/0009-2541(82)90073-0

Dubessy, J., Buschaert, S., Lamb, W., Pironon, J., Thiéry, R., 2001. Methane-bearing aqueous fluid inclusions: Raman analysis, thermodynamic modelling and application to petroleum basins. Chem. Geol., 7th Pan American Conference on Research on Fluid Inclusions 173, 193–205. https://doi.org/10.1016/S0009-2541(00)00275-8

Dubessy, J., Caumon, M.-C., Rull, F., 2012. Instrumentation in Raman spectroscopy: elementary theory and practice. EMU Notes Mineral. 12, 83–172. https://doi.org/10.1180/EMU-notes.12.3

Dubessy, J., Moissette, A., Bäkker, R.J., Frantz, J.D., Zhang, Y.-G., 1999. High-temperature Raman spectroscopic study of H2O-CO2-CH4 mixtures in synthetic fluid inclusions: first insights on molecular interactions and analytical implications. Eur. J. Mineral. 23–32. https://doi.org/10.1127/ejm/11/1/0023

Dubessy, J., Pagel, M., Beny, J.-M., Christensen, H., Hickel, B., Kosztolanyi, C., Poty, B., 1988. Radiolysis evidenced by H2-O2 and H2-bearing fluid inclusions in three uranium deposits. Geochim. Cosmochim. Acta 52, 1155–1167. https://doi.org/10.1016/0016-7037(88)90269-4

Dubessy, J., Poty, B., Ramboz, C., 1989. Advances in C-O-H-N-S fluid geochemistry based on micro-Raman spectrometric analysis of fluid inclusions. Eur. J. Mineral. 517–534. https://doi.org/10.1127/ejm/1/4/0517

Duschek, W., Kleinrahm, R., Wagner, W., 1990. Measurement and correlation of the (pressure, density, temperature) relation of carbon dioxide II. Saturated-liquid and saturated-vapour densities and the vapour pressure along the entire coexistence curve. J. Chem. Thermodyn. 22, 841–864. https://doi.org/10.1016/0021-9614(90)90173-N

Eckhardt, G., Wagner, W.G., 1966. On the calculation of absolute Raman scattering cross sections from Raman scattering coefficients. J. Mol. Spectrosc. 19, 407–411. https://doi.org/10.1016/0022-2852(66)90262-1

Edmond, J.M., Measures, C., Mangum, B., Grant, B., Sclater, F.R., Collier, R., Hudson, A., Gordon, L.I., Corliss, J.B., 1979. On the formation of metal-rich deposits at ridge crests. Earth Planet. Sci. Lett. 46, 19–30. https://doi.org/10.1016/0012-821X(79)90062-1

Ermakov, N., 1950. Research on mineral-forming solutions. Kharkov Univ Press 460, 1957–58.

Etheridge, M.A., Wall, V.J., Vernon, R.H., 1983. The role of the fluid phase during regional metamorphism and deformation. J. Metamorph. Geol. 1, 205–226. https://doi.org/10.1111/j.1525-1314.1983.tb00272.x

Fabre, C., Boiron, M.-C., Dubessy, J., Cathelineau, M., Banks, D.A., 2002. Palaeofluid chemistry of a single fluid event: a bulk and in-situ multi-technique analysis (LIBS, Raman Spectroscopy) of an Alpine fluid (Mont-Blanc). Chem. Geol. 182, 249–264. https://doi.org/10.1016/S0009-2541(01)00293-5

Fabre, C., Boiron, M.-C., Dubessy, J., Moissette, A., 1999. Determination of ions in individual fluid inclusions by laser ablation optical emission spectroscopy: development and applications to natural fluid inclusions. J. Anal. At. Spectrom. 14, 913–922. https://doi.org/10.1039/A809338E

Fabre, D., Couty, F., 1986. Etude, par spectroscopie Raman, du methane comprime jusqu'a 3 kbar. Application a la mesure de pression dans les inclusions fluides contenues dans les mineraux. Comptes Rendus Acad. Sci. Paris Ser. II 303, 1305–1308.

Fabre, D., Oksengorn, B., 1992. Pressure and Density Dependence of the CH4 and N2 Raman Lines in an Equimolar CH4/N2 Gas Mixture. Appl. Spectrosc. 46, 468–471.

Fall, A., Eichhubl, P., Cumella, S.P., Bodnar, R.J., Laubach, S.E., Becker, S.P., 2012. Testing the basin-centered gas accumulation model using fluid inclusion observations: Southern Piceance Basin, ColoradoBasin-Centered Gas Accumulation, Piceance Basin, Colorado. AAPG Bull. 96, 2297–2318. https://doi.org/10.1306/05171211149

Fall, A., Tattitch, B., Bodnar, R.J., 2011. Combined microthermometric and Raman spectroscopic technique to determine the salinity of H2O–CO2–NaCl fluid inclusions based on clathrate melting. Geochim. Cosmochim. Acta 75, 951–964. https://doi.org/10.1016/j.gca.2010.11.021

Fang, J., Chou, I.-M., Chen, Y., 2018. Quantitative Raman spectroscopic study of the H2─CH4 gaseous system. J. Raman Spectrosc. 49, 710–720. https://doi.org/10.1002/jrs.5337

Faulstich, F.R.L., Neumann, R., Pironon, J., Randi, A., 2013. Synthesis of Fluid Inclusion Reference Materials in the H2O–NaCl–CH4 System. Geostand. Geoanalytical Res. 37, 393–402. https://doi.org/10.1111/j.1751-908X.2013.00238.x

Fenner, W.R., Hyatt, H.A., Kellam, J.M., Porto, S.P.S., 1973. Raman cross section of some simple gases. JOSA 63, 73–77. https://doi.org/10.1364/JOSA.63.000073

Fermi, E., 1931. Über den Ramaneffekt des Kohlendioxyds. Z. Für Phys. 71, 250–259. https://doi.org/10.1007/BF01341712

Ferrando, S., Frezzotti, M.L., Orione, P., Conte, R.C., Compagnoni, R., 2010. Late-Alpine rodingitization in the Bellecombe meta-ophiolites (Aosta Valley, Italian Western Alps): evidence from mineral assemblages and serpentinization-derived H2-bearing brine. Int. Geol. Rev. 52, 1220–1243. https://doi.org/10.1080/00206810903557761

Fouche, D.G., Chang, R.K., 1972. Relative Raman Cross Section for O3, CH4, C3H8, NO, N2O, and H2. Appl. Phys. Lett. 20, 256–257. https://doi.org/10.1063/1.1654137

Fouche, D.G., Chang, R.K., 1971a. Relative raman cross section for n2, o2, co, co2, so2, and h2s. Appl. Phys. Lett. 18, 579–580. https://doi.org/10.1063/1.1653548

Fouche, D.G., Chang, R.K., 1971b. Relative raman cross section for n2, o2, co, co2, so2, and h2s. Appl. Phys. Lett. 18, 579–580. https://doi.org/10.1063/1.1653548

Frantz, J.D., Mao, H.K., Zhang, Y.-G., Wu, Y., Thompson, A.C., Underwood, J.H., Giauque, R.D., Jones, K.W., Rivers, M.L., 1988. Analysis of fluid inclusions by X-ray fluorescence using synchrotron radiation. Chem. Geol. 69, 235–244. https://doi.org/10.1016/0009-2541(88)90037-X

Frey, M., Teichmüller, M., Teichmüller, R., Mullis, J., Künzi, B., Breitschmid, A., 1980. Very low-grade metamorphism in external parts of the Central Alps: Illite crystallinity, coal rank and fluid inclusion data. Eclogae Geol Helvetiae 73, 173–203.

Frezzotti, M.L., Tecce, F., Casagli, A., 2012. Raman spectroscopy for fluid inclusion analysis. J. Geochem. Explor. 112, 1–20. https://doi.org/10.1016/j.gexplo.2011.09.009

Fu, Y., Dong, L., Li, C., Qu, W., Pei, H., Qiao, W., Shen, B., 2016. New Re-Os isotopic constrains on the formation of the metalliferous deposits of the Lower Cambrian

Niutitang formation. J. Earth Sci. 27, 271–281. https://doi.org/10.1007/s12583-016-0606-7

Fyfe, W.S., Thompson, A.B., Price, N.J., 1978. Fluids in the earth's crust : their significance in metamorphic, tectonic, and chemical transport processes. Amsterdam ; New York : Elsevier Scientific ; New York : distributions for the U.S. and Canada, Elsevier/North-Holland.

Gamo, T., Chiba, H., Yamanaka, T., Okudaira, T., Hashimoto, J., Tsuchida, S., Ishibashi, J., Kataoka, S., Tsunogai, U., Okamura, K., Sano, Y., Shinjo, R., 2001. Chemical characteristics of newly discovered black smoker fluids and associated hydrothermal plumes at the Rodriguez Triple Junction, Central Indian Ridge. Earth Planet. Sci. Lett. 193, 371–379. https://doi.org/10.1016/S0012-821X(01)00511-8

Garcia-Baonza, V., Rull, F., Dubessy, J., 2012. Raman Spectroscopy of Gases, Water and other Geological Fluids, in: Ferraris, G., Dubessy, J., Caumon, M.-C., Rull, F. (Eds.), Raman Spectroscopy Applied to Earth Sciences and Cultural Heritage. European Mineralogical Union, pp. 279–320. https://doi.org/10.1180/EMU-notes.12.8

Garrabos, Y., Chandrasekharan, V., Echargui, M.A., Marsault-Herail, F., 1989. Density effect on the raman fermi resonance in the fluid phases of CO2. Chem. Phys. Lett. 160, 250–256. https://doi.org/10.1016/0009-2614(89)87591-8

Garrabos, Y., Tufeu, R., Le Neindre, B., Zalczer, G., Beysens, D., 1980. Rayleigh and Raman scattering near the critical point of carbon dioxide. J. Chem. Phys. 72, 4637–4651. https://doi.org/10.1063/1.439706

Gasquet, D., Levresse, G., Cheilletz, A., Azizi-Samir, M.R., Mouttaqi, A., 2005. Contribution to a geodynamic reconstruction of the Anti-Atlas (Morocco) during Pan-African times with the emphasis on inversion tectonics and metallogenic activity at the Precambrian–Cambrian transition. Precambrian Res. 140, 157–182. https://doi.org/10.1016/j.precamres.2005.06.009

Gemery-Hill, P., Shanks, W., Balistrieri, L., Lee, G., 2007. Geochemical Data for Selected Rivers, Lake Waters, Hydrothermal Vents, and Subaerial Geysers in Yellowstone National Park, Wyoming and Vicinity, 1996–2004. Publ. US Geol. Surv.

Giuliani, G., Dubessy, J., Banks, D., Hoàng Quang, V., Lhomme, T., Pironon, J., Garnier, V., Phan Trong, T., Pham Van, L., Ohnenstetter, D., Schwarz, D., 2003. CO2–H2S–COS–S8–AlO(OH)-bearing fluid inclusions in ruby from marble-hosted deposits in Luc Yen area, North Vietnam. Chem. Geol., European Current Research on Fluid Inclusions 194, 167–185. https://doi.org/10.1016/S0009-2541(02)00276-0

Gordon, H.R., McCubbin, T.K., 1966. The 2.8-micron bands of CO2. J. Mol. Spectrosc. 19, 137–154. https://doi.org/10.1016/0022-2852(66)90237-2

Goubert, G., Chen, X., Jiang, S., Van Duyne, R.P., 2018. In Situ Electrochemical Tip-Enhanced Raman Spectroscopy with a Chemically Modified Tip. J. Phys. Chem. Lett. 9, 3825–3828. https://doi.org/10.1021/acs.jpclett.8b01635

Grundke, E.W., Henderson, D., 1972. Distribution functions of multi-component fluid mixtures of hard spheres. Mol. Phys. 24, 269–281. https://doi.org/10.1080/00268977200101431

Hacura, A., 1997. High pressure Raman study of Fermi resonance in CO2 in gaseous CO2□N2 mixtures. Phys. Lett. A 227, 237–240. https://doi.org/10.1016/S0375-9601(97)00010-8

Hacura, A., Bródka, A., Nikiel, L., Baglin, F.G., 1990. High pressure Raman study of fermi resonance spectrum in gaseous carbon dioxide. J. Mol. Struct. 218, 297–302. https://doi.org/10.1016/0022-2860(90)80283-P

Hanf, S., Bögözi, T., Keiner, R., Frosch, T., Popp, J., 2015. Fast and Highly Sensitive Fiber-Enhanced Raman Spectroscopic Monitoring of Molecular H2 and CH4 for Point-of-Care Diagnosis of Malabsorption Disorders in Exhaled Human Breath. Anal. Chem. 87, 982–988. https://doi.org/10.1021/ac503450y

Hanf, S., Keiner, R., Yan, D., Popp, J., Frosch, T., 2014. Fiber-Enhanced Raman Multigas Spectroscopy: A Versatile Tool for Environmental Gas Sensing and Breath Analysis. Anal. Chem. 86, 5278–5285. https://doi.org/10.1021/ac404162w

Hellmann, R., Bich, E., Vogel, E., Vesovic, V., 2014. Intermolecular potential energy surface and thermophysical properties of the CH4–N2 system. J. Chem. Phys. 141, 224301. https://doi.org/10.1063/1.4902807

Herczeg, A.L., Torgersen, T., Chivas, A.R., Habermehl, M.A., 1991. Geochemistry of ground waters from the Great Artesian Basin, Australia. J. Hydrol. 126, 225–245. https://doi.org/10.1016/0022-1694(91)90158-E

Herschbach, D.R., Laurie, V.W., 1961. Anharmonic Potential Constants and Their Dependence upon Bond Length. J. Chem. Phys. 35, 458–464. https://doi.org/10.1063/1.1731952

Herzberg, G., 1945. Infrared and Raman spectra of polyatomic molecules. Krieger Publishing Company.

Hirschfelder, J.O., Curtiss, C.F., Bird, R.B., 1964. Molecular theory of gases and liquids.

Hollister, L.S., Burruss, R.C., 1976. Phase equilibria in fluid inclusions from the Khtada Lake metamorphic complex. Geochim. Cosmochim. Acta 40, 163–175. https://doi.org/10.1016/0016-7037(76)90174-5

Howard-Lock, H.E., Stoicheff, B.P., 1971. Raman intensity measurements of the Fermi diad ν1, 2ν2 in 12CO2 and 13CO2. J. Mol. Spectrosc. 37, 321–326. https://doi.org/10.1016/0022-2852(71)90302-X

Huang, Y., Tarantola, A., Wang, W., Caumon, M.-C., Pironon, J., Lu, W., Yan, D., Zhuang, X., 2018. Charge history of CO2 in Lishui sag, East China Sea basin: Evidence from quantitative Raman analysis of CO2-bearing fluid inclusions. Mar. Pet. Geol. 98, 50–65. https://doi.org/10.1016/j.marpetgeo.2018.07.030

Hurai, V., Huraiova, M., Slobodnik, M., Thomas, R., 2015. Geofluids: Developments in Microthermometry, Spectroscopy, Thermodynamics, and stable isotopes.

Huraiova, M., Dubessy, J., Konecny, P., 1991. Composition and oxidation state of upper mantle fluids from southern Slovakia. Plinius 5, 110–111.

Hutchinson, E.J., Ben-Amotz, D., 1998. Molecular Force Measurement in Liquids and Solids Using Vibrational Spectroscopy. J. Phys. Chem. B 102, 3354–3362. https://doi.org/10.1021/jp9730656

Hyatt, H.A., Cherlow, J.M., Fenner, W.R., Porto, S.P.S., 1973. Cross section for the Raman effect in molecular nitrogen gas. JOSA 63, 1604–1606. https://doi.org/10.1364/JOSA.63.001604

Inaba, H., Kobayasi, T., 1969. Laser-Raman Radar for Chemical Analysis of Polluted Air. Nature 224, 170. https://doi.org/10.1038/224170a0

Irwin, J.J., Roedder, E., 1995. Diverse origins of fluid in magmatic inclusions at Bingham (Utah, USA), Butte (Montana, USA), St. Austell (Cornwall, UK), and Ascension Island (mid-Atlantic, UK), indicated by laser microprobe analysis of Cl, K, Br, I, Ba + Te, U, Ar, Kr, and Xe. Geochim. Cosmochim. Acta 59, 295–312. https://doi.org/10.1016/0016-7037(94)00285-T

Jochum, T., Fastnacht, A., Trumbore, S.E., Popp, J., Frosch, T., 2017. Direct Raman Spectroscopic Measurements of Biological Nitrogen Fixation under Natural Conditions: An Analytical Approach for Studying Nitrogenase Activity. Anal. Chem. 89, 1117–1122. https://doi.org/10.1021/acs.analchem.6b03101

Jochum, T., Rahal, L., J. Suckert, R., Popp, J., Frosch, T., 2016. All-in-one: a versatile gas sensor based on fiber enhanced Raman spectroscopy for monitoring postharvest fruit conservation and ripening. Analyst 141, 2023–2029. https://doi.org/10.1039/C5AN02120K

Jochum, T., von Fischer, J.C., Trumbore, S., Popp, J., Frosch, T., 2015. Multigas Leakage Correction in Static Environmental Chambers Using Sulfur Hexafluoride and Raman Spectroscopy. Anal. Chem. 87, 11137–11142. https://doi.org/10.1021/acs.analchem.5b03312

Jones, J.E., Chapman, S., 1924. On the determination of molecular fields. —II. From the equation of state of a gas. Proc. R. Soc. Lond. Ser. Contain. Pap. Math. Phys. Character 106, 463–477. https://doi.org/10.1098/rspa.1924.0082

Kajiya, D., Saitow, K., 2013. Investigation of attractive and repulsive interactions associated with ketones in supercritical CO2, based on Raman spectroscopy and theoretical calculations. J. Chem. Phys. 139, 054509. https://doi.org/10.1063/1.4817190

Kasemann, S., Meixner, A., Rocholl, A., Vennemann, T., Rosner, M., Schmitt, A.K., Wiedenbeck, M., 2001. Boron and Oxygen Isotope Composition of Certified Reference Materials NIST SRM 610/612 and Reference Materials JB-2 and JR-2. Geostand. Newsl. 25, 405–416. https://doi.org/10.1111/j.1751-908X.2001.tb00615.x

Kawakami, Y., Yamamoto, J., Kagi, H., 2003. Micro-Raman Densimeter for CO_2 Inclusions in Mantle-Derived Minerals. Appl. Spectrosc. 57, 1333–1339.

Keiner, R., Herrmann, M., Küsel, K., Popp, J., Frosch, T., 2015. Rapid monitoring of intermediate states and mass balance of nitrogen during denitrification by means of cavity enhanced Raman multi-gas sensing. Anal. Chim. Acta 864, 39–47. https://doi.org/10.1016/j.aca.2015.02.007

Kelley, D.S., 1996. Methane-rich fluids in the oceanic crust. J. Geophys. Res. Solid Earth 101, 2943–2962. https://doi.org/10.1029/95JB02252

Kennedy, G.C., 1950. Pressure-volume-temperature relations in water at elevated temperatures and pressures. Am. J. Sci. 248, 540–564. https://doi.org/10.2475/ajs.248.8.540

Kesler, S.E., Bodnar, R.J., Mernagh, T.P., 2013. Role of fluid and melt inclusion studies in geologic research. Geofluids 13, 398–404. https://doi.org/10.1111/gfl.12055

Kiefer, J., Seeger, T., Steuer, S., Schorsch, S., Weikl, M.C., Leipertz, A., 2008. Design and characterization of a Raman-scattering-based sensor system for temporally resolved gas analysis and its application in a gas turbine power plant. Meas. Sci. Technol. 19, 085408. https://doi.org/10.1088/0957-0233/19/8/085408

Kiipli, E., Kiipli, T., Kallaste, T., 2009. Reconstruction of currents in the Mid-Ordovician–Early Silurian central Baltic Basin using geochemical and mineralogical indicators. Geology 37, 271–274. https://doi.org/10.1130/G25075A.1

Klöckner, H.W., 1977. Dissertation,. University of Munich.

Kramida, A., Ralchenko, Y., Reader, J., NIST ASD Team, 2018. NIST Atomic Spectra Database (version 5.6.1).

Kunz, O. (Ed.), 2007. The GERG-2004 wide-range equation of state for natural gases and other mixtures, Als Ms. gedr. ed, Fortschritt-Berichte VDI Reihe 6, Energietechnik. VDI-Verl, Düsseldorf.

Kunz, O., Wagner, W., 2012. The GERG-2008 Wide-Range Equation of State for Natural Gases and Other Mixtures: An Expansion of GERG-2004. J. Chem. Eng. Data 57, 3032–3091. https://doi.org/10.1021/je300655b

Lamadrid, H.M., Moore, L.R., Moncada, D., Rimstidt, J.D., Burruss, R.C., Bodnar, R.J., 2017. Reassessment of the Raman CO2 densimeter. Chem. Geol. 450, 210–222. https://doi.org/10.1016/j.chemgeo.2016.12.034

Lamadrid, H.M., Steele-Macinnis, M., Bodnar, R., 2018. Relationship between Raman spectral features and fugacity in mixtures of gases. J. Raman Spectrosc. https://doi.org/10.1002/jrs.5304

Lammers, L.N., Brown, G.E., Bird, D.K., Thomas, R.B., Johnson, N.C., Rosenbauer, R.J., Maher, K., 2015. Sedimentary reservoir oxidation during geologic CO2 sequestration. Geochim. Cosmochim. Acta 155, 30–46. https://doi.org/10.1016/j.gca.2015.02.001

Le Van-Jodin, L., Rouchon, D., Le, V.-H., Chevalier, I., Brun, J., Secouard, C., 2019. Ex situ and operando study of LiCoO2 thin films by Raman spectroscopy: Thermal and electrochemical properties. J. Raman Spectrosc. 50, 1594–1601. https://doi.org/10.1002/jrs.5669

Le, V.-H., Caumon, M.-C., Tarantola, A., Randi, A., Robert, P., Mullis, J., 2020. Calibration data for simultaneous determination of P-V-X properties of binary and ternary CO2 - CH4 - N2 gas mixtures by Raman spectroscopy over 5–600 bar: Application to natural fluid inclusions. Chem. Geol. 552, 119783. https://doi.org/10.1016/j.chemgeo.2020.119783

Le, V.-H., Caumon, M.-C., Tarantola, A., Randi, A., Robert, P., Mullis, J., 2019. Quantitative Measurements of Composition, Pressure, and Density of Microvolumes of CO2–N2 Gas Mixtures by Raman Spectroscopy. Anal. Chem. 91, 14359–14367. https://doi.org/10.1021/acs.analchem.9b02803

Lee, B.I., Kesler, M.G., 1975. A generalized thermodynamic correlation based on three-parameter corresponding states. AIChE J. 21, 510–527. https://doi.org/10.1002/aic.690210313

Lee, M., Ben-Amotz, D., 1993. Pressure induced vibrational frequency shifts of ethane and methyliodide. Evidence for the formation of C–H hydrogen bonds in high density fluids. J. Chem. Phys. 99, 10074–10077. https://doi.org/10.1063/1.465513

Lemmlein, G.G., 1929. Sekundäre Flüssigkeit Scinschlüsse in Mineralien. Z. Für Krist.-Cryst. Mater. 71, 237–256.

Lemmon, E.W., Huber, M.L., McLinden, M.O., 2013. NIST Standard Reference Database 23: Reference Fluid Thermodynamic and Transport Properties-REFPROP, Version 9.1,

National Institute of Standards and Technology,. Stand. Ref. Data Program Gaithersburg.

Li, J., Chou, I.-M., 2015. Hydrogen in silicate melt inclusions in quartz from granite detected with Raman spectroscopy. J. Raman Spectrosc. 46, 983–986. https://doi.org/10.1002/jrs.4644

Lin, Bodnar, R.J., Becker, S.P., 2007a. Experimental determination of the Raman CH4 symmetric stretching (ν1) band position from 1–650bar and 0.3–22°C: Application to fluid inclusion studies. Geochim. Cosmochim. Acta 71, 3746–3756. https://doi.org/10.1016/j.gca.2007.05.016

Lin, Sum, A.K., Bodnar, R.J., 2007b. Correlation of methane Raman ν1 band position with fluid density and interactions at the molecular level. J. Raman Spectrosc. 38, 1510–1515. https://doi.org/10.1002/jrs.1804

Long, D.A., 2002. The Raman Effect : A Unified Treatment of the Theory of Raman Scattering by Molecules.

Lu, W., Chou, I.M., Burruss, R.C., 2008. Determination of methane concentrations in water in equilibrium with sI methane hydrate in the absence of a vapor phase by in situ Raman spectroscopy. Geochim. Cosmochim. Acta 72, 412–422. https://doi.org/10.1016/j.gca.2007.11.006

Lu, W., Chou, I.-M., Burruss, R.C., Song, Y., 2007. A unified equation for calculating methane vapor pressures in the CH4–H2O system with measured Raman shifts. Geochim. Cosmochim. Acta 71, 3969–3978. https://doi.org/10.1016/j.gca.2007.06.004

Mansoori, G.A., Carnahan, N.F., Starling, K.E., Leland, T.W., 1971. Equilibrium Thermodynamic Properties of the Mixture of Hard Spheres. J. Chem. Phys. 54, 1523–1525. https://doi.org/10.1063/1.1675048

Mavrogenes, J.A., Bodnar, R.J., 1994. Hydrogen movement into and out of fluid inclusions in quartz: Experimental evidence and geologic implications. Geochim. Cosmochim. Acta 58, 141–148. https://doi.org/10.1016/0016-7037(94)90452-9

McCreery, R.L., 2005. Raman Spectroscopy for Chemical Analysis. John Wiley & Sons.

Meléndez-Pagán, Y., Ben-Amotz, D., 2000. Intermolecular Forces and Bond Length Changes in High-Pressure Fluids. Vibrational Spectroscopic Measurement and Generalized Perturbed Hard Fluid Analysis. J. Phys. Chem. B 104, 7858–7866. https://doi.org/10.1021/jp0016479

Möller, D., Óprzynski, J., Müller, A., Fischer, J., 1992. Prediction of thermodynamic properties of fluid mixtures by molecular dynamics simulations: methane-ethane. Mol. Phys. 75, 363–378. https://doi.org/10.1080/00268979200100291

Morgan Vi, G.B., Chou, I.-M., Pasteris, J.D., Olsen, S.N., 1993. Re-equilibration of CO2 fluid inclusions at controlled hydrogen fugacities. J. Metamorph. Geol. 11, 155–164. https://doi.org/10.1111/j.1525-1314.1993.tb00137.x

Mullis, J., 1987. Fluid inclusion studies during very-low grade metamorphism. Frey M Ed Low Temp. Metamorph. Blackie 162–199.

Mullis, J., 1979. The system methane-water as a geological thermometer and barometer from the external part of the Central Alps. Bull Minéral 102, 526–536.

Mullis, J., 1975. Growth conditions of quartz crystals from the Val d'Illiez (Valais, Switzerland). Schweiz Min Petr Mitt 55, 419–430.

Mullis, J., Dubessy, J., Poty, B., O'Neil, J., 1994. Fluid regimes during late stages of a continental collision: Physical, chemical, and stable isotope measurements of fluid inclusions in fissure quartz from a geotraverse through the Central Alps, Switzerland. Geochim. Cosmochim. Acta 58, 2239–2267. https://doi.org/10.1016/0016-7037(94)90008-6

Murck, B.W., Burruss, R.C., Hollister, L.S., 1978. Phase equilibria in fluid inclusions in ultramafic xenoliths. Am. Mineral. 63, 40–46.

Murphy, W.F., Holzer, W., Bernstein, H.J., 1969. OSA | Gas Phase Raman Intensities: A Review of "Pre-Laser" Data [WWW Document]. URL https://www.osapublishing.org/as/abstract.cfm?uri=as-23-3-211 (accessed 6.25.18).

Musso, M., Matthai, F., Keutel, D., Oehme, K.-L., 2004. Critical Raman line shape behavior of fluid nitrogen. Pure Appl. Chem. 76, 147–155. https://doi.org/10.1351/pac200476010147

Musso, M., Matthai, F., Keutel, D., Oehme, K.-L., 2002. Isotropic Raman line shapes near gas–liquid critical points: The shift, width, and asymmetry of coupled and uncoupled states of fluid nitrogen. J. Chem. Phys. 116, 8015–8027. https://doi.org/10.1063/1.1468885

Noronha, F., Doria, A., Dubessy, J., Charoy, B., 1992. Characterization and timing of the different types of fluids present in the barren and ore-veins of the W-Sn deposit of Panasqueira, Central Portugal. Miner. Deposita 27, 72–79. https://doi.org/10.1007/BF00196084

Olijnyk, H., Däufer, H., Jodl, H. -J., Hochheimer, H.D., 1988. Effect of pressure and temperature on the Raman spectra of solid CO_2. J. Chem. Phys. 88, 4204–4212. https://doi.org/10.1063/1.453828

Pasteris, J.D., Kuehn, C.A., Bodnar, R.J., 1986. Applications of the laser Raman microprobe RAMANOR U-1000 to hydrothermal ore deposits; Carlin as an example. Econ. Geol. 81, 915–930. https://doi.org/10.2113/gsecongeo.81.4.915

Pasteris, J.D., Wopenka, B., Seitz, J.C., 1988. Practical aspects of quantitative laser Raman microprobe spectroscopy for the study of fluid inclusions. Geochim. Cosmochim. Acta 52, 979–988. https://doi.org/10.1016/0016-7037(88)90253-0

Pedeche, S., Simon, P., Matzen, G., Moulin, B., Blanchard, K., Querel, G., 2003. Probing gas bubbles inside industrial glasses by Raman scattering. J. Raman Spectrosc. 34, 248–252. https://doi.org/10.1002/jrs.984

Peng, D.-Y., Robinson, D.B., 1976. A New Two-Constant Equation of State. Ind. Eng. Chem. Fundam. 15, 59–64. https://doi.org/10.1021/i160057a011

Penney, Goldman, Lapp, 1972. Raman Scattering Cross Sections. Nat. Phys. Sci. 235, 110–112.

Petrov, D.V., Matrosov, I.I., 2016. Raman Gas Analyzer (RGA): Natural Gas Measurements. Appl. Spectrosc. 70, 1770–1776. https://doi.org/10.1177/0003702816644611

Petrov, D.V., Matrosov, I.I., Zaripov, A.R., Maznoy, A.S., 2019. Effects of pressure and composition on Raman spectra of CO-H2-CO2-CH4 mixtures. Spectrochim. Acta. A. Mol. Biomol. Spectrosc. 215, 363–370. https://doi.org/10.1016/j.saa.2019.03.006

Placzek, G., 1934. Rayleigh-Streuung und Raman-Effekt. Akad. Verlag-Ges.

Poling, B.E., Prausnitz, J.M., O'Connell, J.P., 2001. Properties of Gases and Liquids, Fifth Edition. McGraw-Hill Education: New York, Chicago, San Francisco, Athens, London, Madrid, Mexico City, Milan, New Delhi, Singapore, Sydney, Toronto.

Potter, J., Konnerup-Madsen, J., 2003. A review of the occurrence and origin of abiogenic hydrocarbons in igneous rocks. Geol. Soc. Lond. Spec. Publ. 214, 151–173. https://doi.org/10.1144/GSL.SP.2003.214.01.10

Poty, B.P., 1967. La croissance des cristaux de quartz dans le filons sur l'exemple du filon de La Gardette (Bourg d'Oisans) et des filons du massif du Mont-Blanc (phdthesis). Université de Nancy.

Poty, B.P., Stalder, H.-A., Weisbrod, A.M., 1974. Fluid inclusion studies in quartz from fissures of western and central Alps. Schweiz Min Petr Mitt 54, 54.

Raman, C.V., 1929. The production of new radiations by light scattering. —Part I. Proc. R. Soc. Lond. Ser. Contain. Pap. Math. Phys. Character 122, 23–35. https://doi.org/10.1098/rspa.1929.0002

Raveendran, P., Wallen, S.L., 2002. Cooperative C−H···O Hydrogen Bonding in CO_2 −Lewis Base Complexes: Implications for Solvation in Supercritical CO_2. J. Am. Chem. Soc. 124, 12590–12599. https://doi.org/10.1021/ja0174635

Rice, J.K., Niemeyer, E.D., Dunbar, R.A., Bright, F.V., 1995. State-Dependent Solvation of Pyrene in Supercritical CO2. J. Am. Chem. Soc. 117, 5832–5839. https://doi.org/10.1021/ja00126a023

Roedder, E., 1984. Fluid Inclusions. Reviews in Mineralogy. Mineral. Soc. Am. 12, 644.

Roedder, E., 1979a. Fluid Inclusion Evidence on the Environments of Sedimentary Diagenesis, A Review.

Roedder, E., 1979b. Fluid inclusions as samples of ore fluids. Geochem. Hydrothermal Ore Depos. 684–737.

Roedder, E., 1971. Fluid inclusion studies on the porphyry-type ore deposits at Bingham, Utah, Butte, Montana, and Climax, Colorado. Econ. Geol. 66, 98–118. https://doi.org/10.2113/gsecongeo.66.1.98

Roedder, E., 1967. Metastable Superheated Ice in Liquid-Water Inclusions under High Negative Pressure. Science 155, 1413–1417. https://doi.org/10.1126/science.155.3768.1413

Roedder, E., 1965. Liquid CO2 inclusions in olivine-bearing nodules and phenocrysts from Basalts. Am. Mineral. 50, 1746–1782.

Roedder, E., 1963. Studies of fluid inclusions; [Part] 2, Freezing data and their interpretation. Econ. Geol. 58, 167–211. https://doi.org/10.2113/gsecongeo.58.2.167

Roedder, E., 1962. Studies of fluid inclusions; Part 1, Low temperature application of a dual-purpose freezing and heating stage. Econ. Geol. 57, 1045–1061. https://doi.org/10.2113/gsecongeo.57.7.1045

Roedder, E., Bodnar, R.J., 1997. Fluid inclusion studies of hydrothermal ore deposits. Geochem. Hydrothermal Ore Depos. 657–698.

Roedder, E.W., 1958. Technique for the extraction and partial chemical analysis of fluid-filled inclusions from minerals. Econ. Geol. 53, 235–269. https://doi.org/10.2113/gsecongeo.53.3.235

Rosasco, G.J., Roedder, E., 1979. Application of a new Raman microprobe spectrometer to nondestructive analysis of sulfate and other ions in individual phases in fluid inclusions in minerals. Geochim. Cosmochim. Acta 43, 1907–1915. https://doi.org/10.1016/0016-7037(79)90004-8

Rosasco, Roedder, E., Simmons, J.H., 1975. Laser-Excited Raman Spectroscopy for Nondestructive Partial Analysis of Individual Phases in Fluid Inclusions in Minerals. Science 190, 557–560.

Rosso, K.M., Bodnar, R.J., 1995. Microthermometric and Raman spectroscopic detection limits of C02 in fluid inclusions and the Raman spectroscopic characterization of C02. Geochim. Cosmochim. Acta 59, 3961–3975. https://doi.org/10.1016/0016-7037(95)94441-H

Ryan, C.G., Cousens, D.R., Heinrich, C.A., Griffin, W.L., Sie, S.H., Mernagh, T.P., 1991. Quantitative PIXE microanalysis of fluid inclusions based on a layered yield model. Nucl. Instrum. Methods Phys. Res. Sect. B Beam Interact. Mater. At. 54, 292–297. https://doi.org/10.1016/0168-583X(91)95528-L

Saitow, K., Nakayama, H., Ishii, K., Nishikawa, K., 2004. Attractive and Repulsive Intermolecular Interactions of a Polar Molecule: Short-Range Structure of Neat Supercritical CHF3 Investigated by Raman Spectroscopy. J. Phys. Chem. A 108, 5770–5784. https://doi.org/10.1021/jp049225c

Schneider, G.M., 1979. Methane–International Thermodynamic Tables of the Fluid State, Bd. 5. Von S. Angus, B. Armstrong and K. M. de Reuck. Pergamon Press, Oxford–New York 1978. 1. Aufl., XXIV, 251 S., zahlr.Abb.u. Tab., geb. $ 38,00. Chem. Ing. Tech. 51, 766–766. https://doi.org/10.1002/cite.330510728

Schrötter, H.W., Klöckner, 1979. Raman Scattering Cross Section in Gases and Liquids, in: Topics in Current Physics. pp. 123–164.

Schweizer, K.S., Chandler, D., 1982. Vibrational dephasing and frequency shifts of polyatomic molecules in solution. J. Chem. Phys. 76, 2296–2314. https://doi.org/10.1063/1.443302

Seitz, J.C., Pasteris, J.D., Chou, I.-M., 1996. Raman spectroscopic characterization of gas mixtures. II. Quantitative composition and pressure determination of the CO2-CH4 system. Am. J. Sci. 296, 577–600.

Seitz, J.C., Pasteris, J.D., Chou, I.-M., 1993. Raman spectroscopic characterization of gas mixtures; I, Quantitative composition and pressure determination of CH 4, N 2 and their mixtures. Am. J. Sci. 293, 297–321.

Seitz, J.C., Pasteris, J.D., Wopenka, B., 1987. Characterization of CO2 CH4 H2O fluid inclusions by microthermometry and laser Raman microprobe spectroscopy: Inferences for clathrate and fluid equilibria. Geochim. Cosmochim. Acta 51, 1651–1664.

Sharp, Z.D., 2009. Application of Stable Isotope Geochemistry to Low-Grade Metamorphic Rocks, in: Low-Grade Metamorphism. John Wiley & Sons, Ltd, pp. 227–260. https://doi.org/10.1002/9781444313345.ch8

Shepherd, T.J., 1981. Temperature-programmable, heating-freezing stage for microthermometric analysis of fluid inclusions. Econ. Geol. 76, 1244–1247. https://doi.org/10.2113/gsecongeo.76.5.1244

Shepherd, T.J., Chenery, S.R., 1995. Laser ablation ICP-MS elemental analysis of individual fluid inclusions: An evaluation study. Geochim. Cosmochim. Acta 59, 3997–4007. https://doi.org/10.1016/0016-7037(95)00294-A

Sieburg, A., Jochum, T., Trumbore, S.E., Popp, J., Frosch, T., 2017. Onsite cavity enhanced Raman spectrometry for the investigation of gas exchange processes in the Earth's critical zone. Analyst 142, 3360–3369. https://doi.org/10.1039/C7AN01149K

Sieburg, A., Schneider, S., Yan, D., Popp, J., Frosch, T., 2018. Monitoring of gas composition in a laboratory biogas plant using cavity enhanced Raman spectroscopy. Analyst 143, 1358–1366. https://doi.org/10.1039/C7AN01689A

Sloan, E.D., Koh, C.A., Koh, C., 2007. Clathrate Hydrates of Natural Gases. CRC Press.

Smith, F.G., 1953. Historical development of inclusion thermometry. Univ. Tor. Press.

Soave, G., 1972. Equilibrium constants from a modified Redlich-Kwong equation of state. Chem. Eng. Sci. 27, 1197–1203. https://doi.org/10.1016/0009-2509(72)80096-4

Song, W., Biswas, R., Maroncelli, M., 2000. Intermolecular Interactions and Local Density Augmentation in Supercritical Solvation: A Survey of Simulation and Experimental Results. J. Phys. Chem. A 104, 6924–6939. https://doi.org/10.1021/jp000888d

Song, Y., Chou, I., Hu, W., Robert, B., Lu, W., 2009. CO2 Density-Raman Shift Relation Derived from Synthetic Inclusions in Fused Silica Capillaries and Its Application. Acta Geol. Sin. - Engl. Ed. 83, 932–938. https://doi.org/10.1111/j.1755-6724.2009.00090.x

Sorby, H.C., 1858. On the Microscopical, Structure of Crystals, indicating the Origin of Minerals and Rocks. Q. J. Geol. Soc. 14, 453–500. https://doi.org/10.1144/GSL.JGS.1858.014.01-02.44

Sublett, D.M., Sendula, E., Lamadrid, H., Steele-MacInnis, M., Spiekermann, G., Burruss, R.C., Bodnar, R.J., 2019. Shift in the Raman symmetric stretching band of N2, CO2, and CH4 as a function of temperature, pressure, and density. J. Raman Spectrosc. n/a. https://doi.org/10.1002/jrs.5805

Taquet, N., Pironon, J., De Donato, P., Lucas, H., Barres, O., 2013. Efficiency of combined FTIR and Raman spectrometry for online quantification of soil gases: Application to the monitoring of carbon dioxide storage sites. Int. J. Greenh. Gas Control 12, 359–371. https://doi.org/10.1016/j.ijggc.2012.10.003

Tarantola, A., Mullis, J., Vennemann, T., Dubessy, J., de Capitani, C., 2007. Oxidation of methane at the CH4/H2O–(CO2) transition zone in the external part of the Central Alps, Switzerland: Evidence from stable isotope investigations. Chem. Geol., New Results in Fluid and Melt Inclusion Research 237, 329–357. https://doi.org/10.1016/j.chemgeo.2006.07.007

Thiéry, R., Kerkhof, A., Dubessy, J., 1994a. vX properties of CH4 -CO2 and CO2 -N2 fluid inclusions; modelling for T<31 degrees C and P<400 bars. Eur. J. Mineral. 6, 753–771.

Thiéry, R., Vidal, J., Dubessy, J., 1994b. Phase equilibria modelling applied to fluid inclusions: Liquid-vapour equilibria and calculation of the molar volume in the CO2□CH4□N2 system. Geochim. Cosmochim. Acta 58, 1073–1082. https://doi.org/10.1016/0016-7037(94)90573-8

Thieu, V., Subramanian, S., Colgate, S.O., Sloan, E.D., 2000. High-Pressure Optical Cell for Hydrate Measurements Using Raman Spectroscopy. Ann. N. Y. Acad. Sci. 912, 983–992. https://doi.org/10.1111/j.1749-6632.2000.tb06853.x

Thomas, M.A., Welsh, H.L., 1960. The Raman Spectrum of Methane. Can. J. Phys. 38, 1291–1303. https://doi.org/10.1139/p60-135

Thompson, A.B., Connolly, J.A.D., 1992. Migration of metamorphic fluid: some aspects of mass and heat transfer. Earth-Sci. Rev. 32, 107–121. https://doi.org/10.1016/0012-8252(92)90014-K

Touret, J., 1984. Les inclusions fluides : histoire d'un paradoxe. Bull. Minéralogie 107, 125–137. https://doi.org/10.3406/bulmi.1984.7743

Touret, J.L.R., 2001. Fluids in metamorphic rocks. Lithos, Fluid Inclusions: Phase Relationships - Methods - Applications. A Special Issue in honour of Jacques Touret 55, 1–25. https://doi.org/10.1016/S0024-4937(00)00036-0

Truesdell, A.H., Thompson, J.M., 1982. The Geochemistry of Shoshone Geyser Basin, Yellowstone National Park 153–159.

Tsunogae, T., Dubessy, J., 2009. Ethane- and hydrogen-bearing carbonic fluid inclusions in a high-grade metamorphic rock. J. Mineral. Petrol. Sci. 104, 324–329. https://doi.org/10.2465/jmps.090622f

Uemura, R., Nakamoto, M., Asami, R., Mishima, S., Gibo, M., Masaka, K., Jin-Ping, C., Wu, C.-C., Chang, Y.-W., Shen, C.-C., 2016. Precise oxygen and hydrogen isotope determination in nanoliter quantities of speleothem inclusion water by cavity ring-down spectroscopic techniques. Geochim. Cosmochim. Acta 172, 159–176. https://doi.org/10.1016/j.gca.2015.09.017

Van den Kerkhof, 1988. The system CO2-CH4-N2 in fluid inclusions: theoretical modelling and geological applications.

Van den Kerkhof, A., Thiéry, R., 2001. Carbonic inclusions. Lithos 55, 49–68.

van den Kerkhof, A.M., 1990. Isochoric phase diagrams in the systems CO2 CH4 and CO2 N2: Application to fluid inclusions. Geochim. Cosmochim. Acta 54, 621–629. https://doi.org/10.1016/0016-7037(90)90358-R

Veirs, D.K., Rosenblatt, G.M., 1987. Raman line positions in molecular hydrogen: H2, HD, HT, D2, DT, and T2. J. Mol. Spectrosc. 121, 401–419. https://doi.org/10.1016/0022-2852(87)90058-0

Wagner, W., Pruss, A., 1993. International Equations for the Saturation Properties of Ordinary Water Substance. Revised According to the International Temperature Scale of 1990. Addendum to J. Phys. Chem. Ref. Data 16, 893 (1987). J. Phys. Chem. Ref. Data 22, 783–787. https://doi.org/10.1063/1.555926

Wang, C.H., Wright, R.B., 1973. Effect of density on the Raman scattering of molecular fluids. I. A detailed study of the scattering polarization, intensity, frequency shift, and spectral shape in gaseous N_2. J. Chem. Phys. 59, 1706–1712. https://doi.org/10.1063/1.1680252

Wang, W., Caumon, M.-C., Tarantola, A., Pironon, J., Lu, W., Huang, Y., 2019. Raman spectroscopic densimeter for pure CO2 and CO2-H2O-NaCl fluid systems over a wide P-T range up to 360 °C and 50 MPa. Chem. Geol. 528, 119281. https://doi.org/10.1016/j.chemgeo.2019.119281

Wang, X., Chou, I.-M., Hu, W., Burruss, R.C., Sun, Q., Song, Y., 2011. Raman spectroscopic measurements of CO2 density: Experimental calibration with high-pressure optical cell (HPOC) and fused silica capillary capsule (FSCC) with application to fluid inclusion

observations. Geochim. Cosmochim. Acta 75, 4080–4093. https://doi.org/10.1016/j.gca.2011.04.028

Wang, Z., Sun, S., Li, J., Hou, Q., Qin, K., Xiao, W., Hao, J., 2003. Paleozoic tectonic evolution of the northern Xinjiang, China: Geochemical and geochronological constraints from the ophiolites. Tectonics 22. https://doi.org/10.1029/2002TC001396

Werre, R.W., 1979. A novel gas-flow fluid inclusion heat/freezing stage[abst.]. Geol Soc Amer Abst Programs 11, 539.

Wilkinson, J.J., 2001. Fluid inclusions in hydrothermal ore deposits. Lithos, Fluid Inclusions: Phase Relationships - Methods - Applications. A Special Issue in honour of Jacques Touret 55, 229–272. https://doi.org/10.1016/S0024-4937(00)00047-5

Wilkinson, J.J., Rankin, A.H., Mulshaw, S.C., Nolan, J., Ramsey, M.H., 1994. Laser ablation-ICP-AES for the determination of metals in fluid inclusions: An application to the study of magmatic ore fluids. Geochim. Cosmochim. Acta 58, 1133–1146. https://doi.org/10.1016/0016-7037(94)90577-0

Wopenka, B., Pasteris, J.D., 1986. Limitations to Quantitative Analysis of Fluid Inclusions in Geological Samples by Laser Raman Microprobe Spectroscopy. Appl. Spectrosc. 40, 144–151.

Wopenka, Brigitte., Pasteris, J.Dill., 1987. Raman intensities and detection limits of geochemically relevant gas mixtures for a laser Raman microprobe. Anal. Chem. 59, 2165–2170. https://doi.org/10.1021/ac00144a034

Wright, R.B., Wang, C.H., 1974. Effect of density on the Raman scattering of molecular fluids. II. Study of intermolecular interaction in CO2. J. Chem. Phys. 61, 2707–2710. https://doi.org/10.1063/1.1682403

Wright, R.B., Wang, C.H., 1973. Density effect on the Fermi resonance in gaseous CO2 by Raman scattering. J. Chem. Phys. 58, 2893–2895. https://doi.org/10.1063/1.1679594

Yamamoto, J., Kagi, H., 2006. Extended Micro-Raman Densimeter for CO2 Applicable to Mantle-originated Fluid Inclusions. Chem. Lett. 35, 610–611. https://doi.org/10.1246/cl.2006.610

Yamamoto, J., Kagi, H., Kaneoka, I., Lai, Y., Prikhod'ko, V.S., Arai, S., 2002. Fossil pressures of fluid inclusions in mantle xenoliths exhibiting rheology of mantle minerals: implications for the geobarometry of mantle minerals using micro-Raman spectroscopy. Earth Planet. Sci. Lett. 198, 511–519. https://doi.org/10.1016/S0012-821X(02)00528-9

Yamamoto, J., Kagi, H., Kawakami, Y., Hirano, N., Nakamura, M., 2007. Paleo-Moho depth determined from the pressure of CO2 fluid inclusions: Raman spectroscopic barometry of mantle- and crust-derived rocks. Earth Planet. Sci. Lett. 253, 369–377. https://doi.org/10.1016/j.epsl.2006.10.038

Yang, Xiaoyong, Yang, Xueming, Zhang, Z., Chi, Y., Yu, L., Zhang, Q., 2011. A porphyritic copper (gold) ore-forming model for the Shaxi-Changpushan district, Lower Yangtze metallogenic belt, China: geological and geochemical constraints. Int. Geol. Rev. 53, 580–611. https://doi.org/10.1080/00206810903211906

Yuan, X., Mayanovic, R.A., Zheng, H., Sun, Q., 2017. Determination of pressure in aqueo-carbonic fluid inclusions at high temperatures from measured Raman frequency shifts of CO2. Am. Mineral. 102, 404–411. https://doi.org/10.2138/am-2017-5405

Zakin, M.R., Herschbach, D.R., 1988. Density dependence of attractive forces for hydrogen stretching vibrations of molecules in compressed liquids. J. Chem. Phys. 89, 2380–2387. https://doi.org/10.1063/1.455081

Zakin, M.R., Herschbach, D.R., 1986. Vibrational frequency shifts induced by molecular compression of pyridine in solution. J. Chem. Phys. 85, 2376–2383. https://doi.org/10.1063/1.451092

Zhang, J., Qiao, S., Lu, W., Hu, Q., Chen, S., Liu, Y., 2016. An equation for determining methane densities in fluid inclusions with Raman shifts. J. Geochem. Explor., Fluid and Melt inclusions 171, 20–28. https://doi.org/10.1016/j.gexplo.2015.12.003

Liste des figures

Figures of Supporting Information (Chapter 2)

Figures of Appendix A (Chapter 3)

Figures of Appendix B (Chapter 3)

Figures of Appendix C (Chapter 3)

Figures of Appendix D (Chapter 3)

Figures of Appendix E (Chapter 4)

Figures of Appendix F (Chapter 5)

Liste des tableaux

Tables of Supporting Information (Chapter 2)

Figures of Appendix D (Chapter 3)

Résumé: Les inclusions fluides naturelles peuvent fournir des informations quantitatives précieuses pour reconstruire les conditions de circulation des paléofluides. CO_2, CH_4 et N_2 sont les espèces gazeuses majoritaires le plus souvent rencontrées dans divers environnements géologiques. Cependant les données d'étalonnage des mélanges constitués de ces espèces pour une quantification de leurs propriétés *PVX* ne sont pas encore complètement établies. L'objectif central de ce travail de thèse est d'apporter des données d'étalonnage du signal Raman des gaz CO_2, CH_4, N_2 et de leurs mélanges, sur une gamme de pression de 5 à 600 bars, afin de pouvoir déterminer simultanément les propriétés *PVX* à une température fixée. Pour cela, des mélanges de gaz ont été préparés à haute pression par le biais d'un mélangeur couplé avec un système de pressurisation développé au laboratoire GeoRessources. Des analyses *in situ* Raman des mélanges de gaz ont été réalisées dans des conditions contrôlées en utilisant le système HPOC couplé avec un microcapillaire transparent placé sur une platine microthermométrique. L'incertitude des mesures des propriétés *PVX* à 22 ou 32 °C à partir de nos équations d'étalonnage est de < 1 mol%, ~ ± 20 bars et ~ ± 0,02 g·cm^{-3}, respectivement. Un autre objectif du projet est d'interpréter la tendance de variation de la position du pic du N_2 et CH_4 pour une compréhension approfondie. Deux modèles théoriques, i.e., le potentiel de Lennard-Jones 6-12 et le modèle « Perturbed hard-sphere fluid » ont été utilisés pour évaluer quantitativement la contribution des forces d'interaction intermoléculaire attractives et répulsives aux décalages des bandes de CH_4 et N_2. Un modèle prédictif a été proposé pour prédire la tendance de la variation de la position du pic du CH_4 jusqu'à 3000 bars en fonction des propriétés *PVX*. En fin, l'applicabilité de nos données d'étalonnage aux autres systèmes gazeux ou dans d'autres laboratoires est discutée et évaluée. Des nouvelles données d'étalonnage universelles applicables dans d'autres laboratoires sont fournies sous forme d'un programme de calcul « FRAnCIs » avec une interface utilisateur.

Abstract: Quantitative knowledge of species trapped within fluid inclusions provides key information to better understand geological processes as well as to reconstruct the conditions of paleofluid circulation. CO_2, CH_4, and N_2 are among the most dominant gas species omnipresent in various geological environments, but their quantitative *PVX* calibration data are not fully established yet. The aim of this work is to provide accurate calibration data for the simultaneous determination of *PVX* properties of pure gases or any binary and ternary mixtures of CO_2, CH_4, and N_2 over 5 to 600 bars, directly from Raman spectra. For this, gas mixtures were prepared using a mixer coupled with a homemade pressurization system. Raman *in situ* analyses of gas mixtures were performed at controlled conditions using an improved HPOC system coupled with a heating-cooling stage. The uncertainty of the measurement of the *PVX* properties from our calibration equations at 22 or 32 °C is < ± 1 mol%, ~ ± 20 bars, and ~ ± 0.02 g·cm^{-3}, respectively. The ensuing aim of the project is to interpret the variation trends of the peak position of the CH_4 and N_2 ν_1 band for an in-depth understanding. Two theoretical models, i.e., Lennard-Jones 6-12 potential energy approximation and Perturbed hard-sphere fluid model were involved to quantitatively assess the contribution of the attractive and repulsive intermolecular interaction forces to the pressure-induced frequency shifts. A predictive model was also provided to predict the variation trend of the CH_4 ν_1 band over a pressure range up to 3000 bars as a function of pressure and composition. Furthermore, the applicability of our calibration data to other laboratories and apparatus and to gas mixtures that contain a small amount of other species (e.g., H_2, H_2S) was discussed and evaluated. New universal calibration data applicable for other laboratories were then provided. A computer program "FRAnCIs" was also developed to make the application of our calibration data as convenient as possible via a user-friendly interface.